A Microgripper for Single Cell Manipulation

Belén Solano Hermosilla

School of Engineering

Durham University

A thesis submitted to Durham University for the Degree of Doctor of Philosophy

April 2008

ABSTRACT

This thesis presents the development of an electrothermally actuated microgripper for the manipulation of cells and other biological particles. The microgripper has been fabricated using a combination of surface and bulk micromachining techniques in a three mask process. All of the fabrication details have been chosen to enable a tri-layer, polymer (SU8) - metal (Au) - polymer (SU8), membrane to be released from the substrate stress free and without the need for sacrificial layers.

An actuator design, which completely eliminates the parasitic resistance of the cold arm, is presented. When compared to standard U-shaped actuators, it improves the thermal efficiency threefold. This enables larger displacements at lower voltages and temperatures. The microgripper is demonstrated in three different configurations: normally open mode, normally closed mode, and normally open/closed mode. It has been modelled using two coupled analytical models – electrothermal and thermomechanical – which have been custom developed for this application. Unlike previously reported models, the electrothermal model presented here includes the heat exchange between hot and cold arms of the actuators that are separated by a small air gap.

A detailed electrothermomechanical characterisation of selected devices has permitted the validation of the models (also performed using finite element analysis) and the assessment of device performance. The device testing includes electrical, deflection, and temperature measurements using infrared (IR) thermography, its use in polymeric actuators reported here for the first time.

Successful manipulation experiments have been conducted in both air and liquid environments. Manipulation of live cells (mice oocytes) in a standard biomanipulation station has validated the microgripper as a complementary and unique tool for the single cell experiments that are to be conducted by future generations of biologists in the areas of human reproduction and stem cell research.

To my parents.

ACKNOWLEDGEMENTS

First of all, I would like to express my gratitude to Durham University and, in particular, Professor David Wood for having given me the opportunity to pursue these studies. I would also like to thank Andrew Gallant and Mark Rosamond for all of their help in the cleanroom, the office and beyond. It is fair to say that without the help of my colleagues, this work would not have been possible. Finally, I must mention that the telephone calls, emails and visits from my family and friends have given me the strength to survive these years, and the northern latitudes.

DECLARATION

I declare that no material in this thesis has previously been submitted for a degree at this or any other university.

TABLE OF CONTENTS

CHAPTER 1

Introduction

Progress in biological and medical applications demands research at a cellular level. Every organism is the result of a series of single-cell proliferation and differentiation processes. Experiments performed directly on individual cells allow for a better and more selective study of cell functions and properties than conventional experiments where data is generally averaged over a large population of cells [1, 2]. This explains the growing interest within the medical, pharmacological and biological communities in techniques and tools which enable the individual manipulation of biological samples [3-7].

This thesis focuses on producing a microgripper which can be used for biomanipulation. Biomanipulation [8, 9] entails operations such as cell transportation, positioning, orienting, grasping or material injection. These actions could be of crucial importance for the future of different areas such as genomics and proteomics [7, 10, 11], human reproduction [12-14], medicine [15], and cancer research [16].

Current biomanipulation techniques and tools can be classified as non-contact or contact. The first group include systems that use optical forces, electric fields, magnetic fields, hydrodynamic flows and aerostatics. The second group include systems based on vacuum suction, adhesive forces, acoustic traps, cryogenic and mechanical forces

(microgrippers, AFM, etc.) [6, 9]. Two recent reviews [17, 18] give a detailed account of different manipulation techniques.

1.1. Microsystems Technology (MST)

Imagine a drug delivery system that permits the controlled delivery of insulin through the skin without pain or blood [19, 20]; a wireless pressure sensor implanted under the skin that can be used to monitor hypertension patients [21]; a cochlea implant that allows for hearing corrections that conventional hearing aids cannot fix (e.g. problems in inner ear) [22, 23]; a tiny gripper that can be inserted in arteries to treat aneurysms in the brain [24]; an accelerometer that gives the Nintendo Wii™ console its core ability to sense the motion in the controller [25-27]; a micromirror array that forms the basis of the technology used for high definition projectors and displays [28]; inkjet print heads that integrated in consumer electronics lead to the manufacturing of low cost computer printers.

What do all of these technologies have in common? They all use very small devices which not only have a reduced size compared to any existent counterpart but, in most of the cases, they open up new functionalities that at larger scales are simply not possible. They all belong to a class of devices described by Microsystems Technology (MST), also known as MicroElectroMechanical Systems (MEMS) in the USA, that use layer-by-layer batch manufacturing techniques similar to the ones used to make electronic chips.

The acronym MST denotes both a technology and a category of devices. MST is a technology that has been developing for the last 30 years. Microsystems are highly miniaturised devices, ranging in size from millimetres to submicrometres, that combine multiple disciplines such as biology, optics, fluidics, mechanics, or electronics in one single device and more importantly in a single silicon chip [29-32]. An MST device is often composed of two different conceptual parts: the microelectronics and the sensor/actuating structure. The latter enables physical or analytical functions to be performed in addition to standard microprocessor operations, and this is precisely what differentiates MST devices from standard microelectronic chips. MST assists to bridge the gap between the digital world of the computers and the physical world where we live. The sensors and actuators gather information from the environment by measuring

physical or chemical parameters, and through microelectronic processing they are able to respond by moving, positioning, pumping, filtering, etc.

One of the most important driving forces towards miniaturisation of devices (by MST) is the improvement in performance and cost that they can confer over their macroscopic counterparts. In some applications just the smaller size of the device itself can be advantageous, for example miniaturisation can enable the shortening of the mechanical and thermal response times [33], the manipulation of micro sized objects in confined spaces without interacting with surrounding elements, or the development of implantable devices such as retinal or neuronal implants, and microneedles.

In addition, improvement in device performance can also be achieved through the exploitation of some physical phenomena that only appear or dominate at the microscale [31, 34, 35]. Physical quantities (force, energy, etc.) do not necessarily scale linearly with dimensions and as they are reduced, new microscale phenomena appear or are favoured. This has been the focus of some theoretical studies [31]. A simple yet revealing technique was proposed by Trimmer [36] to determine how a given parameter, such as force, scales into the small domain. This scaling behaviour implies for example that at the microscale faster systems can be obtained at lower power consumption [37]. Thus surface effects (e.g. stiction and friction) become more important in the microscale whereas volume effects (e.g. gravitation or inertia) are relatively less important. One important implication of that is that inertial forces become insignificant while viscous forces and friction dominate. The latter can be exploited in the fabrication of a microfluidic device that separates and detects different particles with different size based on diffusion [30].

Finally, another major advantage of MST devices is the reduction in production cost per unit compared to equivalent macroscopic systems. Microfabrication techniques are inherently batch production techniques where hundreds of devices can be fabricated simultaneously on a single wafer in a single production run. In addition, most microfabrication processes and tools are compatible with IC processing. This implies that a large industrial base already exists and that initial production costs can be reduced further.

1.1.1. Applications and markets

The competitive advantage of MST devices over other options has already been demonstrated in various areas via the successful commercialisation of different MST devices. Since the first launch of a MST device, the technology has had a rapid expansion into many different fields of engineering, physical sciences, biology and medicine. Table 1.1 partially summarises some existing or envisaged areas of application for MST and the associated devices.

Table 1.1: MST devices and applications

Area of application	MST devices and applications
DEFENCE	Accelerometers (inertial navigation, image stabilisation), biochemical and chemical sensors, biochips, lab-on-a-chip (detection chemical weapons, drug administration), gyroscopes (inertial navigation), magnetometers, micro-bolometer (infrared imaging system), micro-displays, micromirrors, micro-power sources and smart dust (surveillance)
AUTOMOTIVE	Accelerometer (airbag system, active suspension), oxigen sensor (emission sensor), pressure sensor (active suspension), temperature sensor (air conditioning, engine management system), light sensor (automatic headlight control)
ENVIROMEMTAL	Accelerometers (seismic detection), biochemical and chemical sensors, biochips, lab-on-a-chip (pollutants control), geophones (oil detection)
IT AND ENTERTAINMENT	Acceleration sensors (joystick; hard disk stabilisation), inkjet printers, optical mouse, hard disk drive heads (data storage), micro-displays (portable systems)
MEDICAL AND BIOMEDICAL	Active patches (drug delivery), hearing aids, accelerometers (heart pacemakers), implantable insulin pumps (drug delivery), needle-less injectors (drug deliver), smart pill (drug delivery), pressure sensors (blood pressure)
PROCESS CONTROL AND INSTRUMENTATION	Acceleration and tilt sensors (vibration monitoring), biosensors (quality control in food), biosensors, gas sensors (oil platforms), magnetic sensors (rotation measurements), micro-pumps, pressure sensors, spectrometers, temperature sensors
TELECOMS	Micromirrors (switching, optical attenuation), V-grooves (optical fibre alignment), tunable filters, micro-optical benches, antennas, inductors, tunable capacitors, switches(signal routing)
HOME APPLIANCES	Acceleration sensor, tilt sensor (vibration washing machines), biochips (food control), chemical sensors water quality), flat panel displays, microfluidic ships (dosing systems in washing machines), temperature sensors (cooking), electronic noses (atmospheric monitoring)

Nowadays, numerous and diverse MST devices which could have a dramatic impact on everything from aerospace technology to biotechnology are being developed in R&D laboratories and in companies around the world [38, 39]. Some of the most renowned companies (other than the ones producing PC printers [28, 40]) are Texas Instruments [25, 41], Robert Bosch [42], and ST Microelectronics [43].

Fig.1.1 shows a recent forecast published by Yole Development [44] that announces a 14% compound annual growth for the MST market from 2007 until 2012. This forecast

takes into account the market of the 1st level packaged MST excluding the hard disk read-write heads. In 2009, four products will still make up 50% of the market: inkjet heads, pressure sensors, silicon microphones and accelerometers. The ratio at which the production of MST devices belonging to the various applications (see table 1) will grow is predicted to be variable, from a modest 3.5% growth of automotive applications to 18% and 40% in medical and life science applications and telecoms respectively.

Fig. 1.1: Market forecast in value for 1st level packaged MEMS, detail for product type [45].

1.1.2. MST for medical and life science

BioMEMS [4, 5] is an emerging research field which applies microsystems technology to medicine and the life sciences. In general, this category of devices deals with the fabrication of microscale devices that are used for processing, delivery, manipulation, analysis, or construction of biological and chemical entities. BioMEMS is now a heavily researched area in a wide variety of applications from diagnostics, such as DNA and protein arrays, to novel materials for BioMEMS, microfluidics (see Fig. 1.1), tissue engineering, implantable devices such as pacemakers, surface modification, biosensors or drug delivery. The appearance of commercially and scientifically successful BioMEMS devices, such as the lab-on-a chip of Caliper Technology [46], and many point-of-care devices like Micronics [47, 48] have increased the need and demand for MST in biology and medicine.

The device developed in this thesis will fall in this general category of devices, i.e. MST for medical and life science. In particular, it is intended to work as an instrument to assist biological researchers in the manipulation of biological specimens. The design of the tool is flexible enough to envisage other uses such as a tool in minimal invasive surgery. However, this and any other commercial issues like drivers, market entry barriers and the position in the value chain are out of the scope of this thesis.

1.2. Background and motivation

MST can also offer the possibility to biologists and other scientists to design and control experiments directly at the microscale [6, 9]. Until recently, those experiments remained a technological challenge. Nowadays, the combination of MST devices with conventional technologies is making these experiments not only possible, but affordable.

When studying complex interactions between and inside cells, it is often necessary to hold, sort and transport biological samples in dry or aqueous environments. Recent advances in microbiology demonstrate the need for complex micromanipulation strategies for the characterisation and manipulation of cells. This has become a challenging issue in biomedical applications [49] such as cloning, cell replacement therapy (CRT), gene injection, in vitro fertilization (IVF) or intracytoplasmic sperm injection (ICSI) [50]. Other applications such as minimal invasive surgery or research in fundamental biology [51] (e.g. research in cell apoptosis [10, 52], cell injection [7], single-cell force sensors, etc.) also require the manipulation of micro sized biological objects. Microrobotics and MST can then play an important role in manipulating biological cells, a field often referred to as biomanipulation [9].

MST technology, when used appropriately to address the right problems, can be the enabling technology for these kinds of experiments. Reference [53] gives a global overview of MST applications in biology and medicine and, in particular, experiments involving cells or cell biology.

1.2.1. Biomanipulation

1.2.1.1. Non-contact manipulation techniques

Non-contact techniques based on optical tweezers [54-56] have been around for more than thirty years and offer the possibility to manipulate particles from the size of few microns down to a single atom. Optical tweezers use the force (~ pN) generated when light interacts with matter, absorbing, refracting or reflecting photons and exchanging momentum. Optical tweezers have been used to manipulate some living cells that have particular sizes, shapes, and adherent properties (e.g. yeast cells, red blood cells, and spermatozoa) and provides a powerful method to investigate different aspects of cell biology [55]. They are more "cell friendly" than many alternative methods because of the non-invasive character of light. However cell photo damage remains an issue [18]. This problem seems to have been solved with the use of near infrared (780-950 nm) lasers, however the question as to whether the incident laser beam might induce abnormalities in the cell's genetic material still exists [57]. Another drawback of these systems is their cost, which is in the range of ~$10-100K. Overall, commercial optical tweezers are adequate for positioning and manipulating objects but are incapable, without further modification, of ultra-sensitive position or force measurement [58].

Other non-contact techniques use, for example, electric (e.g. dielectrophoresis (DEP) and electrophoresis) or magnetic fields and can be used for particular manipulation tasks. Different system configurations with high accuracy in cell positioning and separation have already been established. Dielectrophoresis is based on forces generated by the gradient of an electromagnetic field and it has been used in microfluidics to manipulate a variety of biological cells such as bacteria, yeast, and mammalian cells [9]. Electrophoresis is used to size-sort DNA strands and produce DNA fingerprints. Although the method works well for trapping and transporting over short distances, the heat generation can be an issue over longer distances. Biomanipulation using magnetic forces generally requires the adhesion or introduction of magnetic beads into the cells. This has been found not to damage the viability of the cells [59] and results in a very flexible manipulation system. However, they involve a detailed consideration of field strengths and their generation and confinement and even then equipment tends to be cell specific.

1.2.1.2. Contact manipulation techniques

The fact that non-contact biomanipulation techniques have certain limits in terms of applied forces, size of the samples, optical and electrical interaction, and cost makes contact manipulation techniques desirable.

Vacuum technology is a common contact technique. Tools such as glass micropipettes have been used for over one hundred years [60]. However, this manipulation technique requires a very skilled operator and it can easily damage the cell membrane or cytoskeleton [61, 62]. It can hold cells, but doesn't give real control, e.g. for cell discrimination, and is not easily scalable to all dimensions.

Also, a large number of what is called lab-on-a chip MST devices for the direct manipulation and transport of cells can be used. Such a device generally consists of a set of micro channels, pumps and valves, that direct, separate and hold cells in position for subsequent analysis.

Finally, the route involving microgrippers, which act as a pair of miniature tweezers, has been effectively demonstrated at very different lengths scales: from the manipulation of DNA and bacteria (<1 μm) to the manipulation of larger single cells and clusters. Microgrippers seem to be a promising approach to biomanipulation as they are cost effective, offer flexibility over the range of cells that can be manipulated, provide an intuitive tool for an average human operator, and offer robustness.

These microgrippers are distinguished from the grippers made by conventional machining by the overall small size. In an MST microgripper the size is comparable to the size of the objects to be manipulated and therefore they are able to operate in confined spaces or without greatly affecting the neighbouring objects (see Fig. 1.2)

Active research in contact techniques and microgripper for micro and biomanipulation is being carried out in different institutions in the UK, Europe and around the world. As will be shown in the review chapter, numerous MST prototypes exist. However, only a few among them can be used for the effective manipulation (pick and place and transport) of living cells in air as well as in liquid environments.

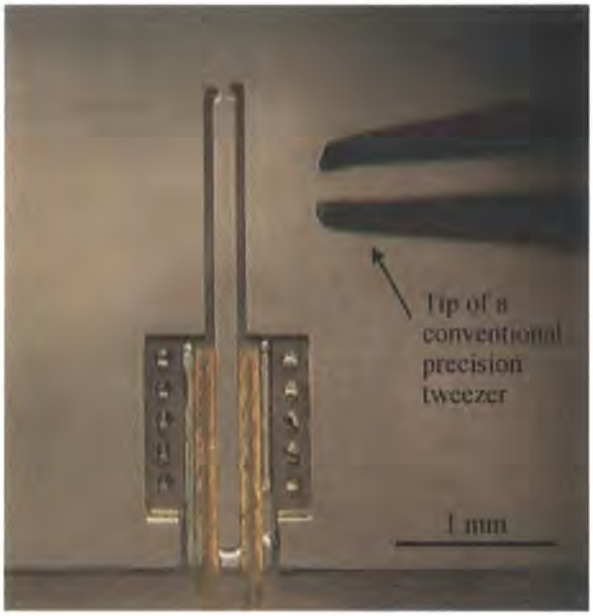

Fig. 1.2: Tips of precision conventional tweezers compared to a meso-scale microgripper fabricated in this work (The microgripper shown in this image could be further reduced in size by a factor of ten)

Although some of them show good manipulation capabilities, little effort has been paid to the thermal or geometrical optimisation of the structures. Thus no extra functionalities apart from the gripping action can be added to the microgripper tool. In this context, the microgripper design proposed in this thesis provides a thermally efficient device for biomanipulation, with bi-directional movement and with the possibility to integrate additional functionalities such as force sensors.

1.3. Thesis objectives and organisation

This dissertation focuses on the full development — design, modelling, fabrication, testing, and simulation optimisation — of a microgripper, and on the demonstration of the gripping operation by the manipulation of micro sized objects in air and liquid environments.

The thesis – containing 7 chapters – is organised as follows:

Chapter 1 presents a general introduction to microsystems and the different advantages that they confer over their macroscopic counterparts. It also includes background and motivation behind this work. The relevance of MST devices for biological and medical

applications, and in particular for biomanipulation, is highlighted. Different contact and non-contact techniques are presented.

Chapter 2 shows the state-of-the-art in microgrippers. The microgrippers have been classified as a function of their actuation mechanism. Quantitative and qualitative data about performance and overall adequacy of the tool for biological manipulation is provided. Each of the microgrippers presented has advantages and disadvantages which depend on the final manipulation application. At the end of the chapter a resume table is proposed with the grippers that have potential in biomanipulation. The increasing scientific effort in the field of microgrippers demonstrates the contemporary nature of this work.

Chapter 3 includes the description of the microgripper: design constraints, choice of actuation mechanisms and lay-out. For the microgripper presented here, in-plane electrothermal actuation has been adopted. An alternative in-plane polymeric thermal actuator that completely eliminates the heat generation in the cold arm has been designed and is described in detail. In the second part of the chapter, after a brief introduction to microfabrication techniques and materials, the particular fabrication of the microgripper is explained in detail. Two alternative fabrication flows have been designed. Both lead to a stress-free polymeric (SU8) microgripper with integrated resistors and accessible contact pads. Viable prototypes have been produced.

Chapter 4 proposes an analytical tool for the description of the behaviour of the microgripper. The complete tool consists of two different analytical models, electrothermal and thermomechanical. The electrothermal model predicts the temperature distribution along the parts of the microgripper for an initial input current or power. This temperature distribution, and in particular the difference established between the parts, is what ultimately determines the deflection of the system. Once this temperature is calculated and used as an input, the thermomechanical model can predict the in-plane deflection. As opposed to existing models, the thermal model includes the heat exchange between the hot and cold arm that are separated by a small gap. A set of semi-empirical formulae are proposed to calculate the heat losses to the ambient and between the arms by conduction, as opposed to convection. The construction of the model is validated using finite element software. In theory both models, electrothermal

and thermomechanical, are highly coupled through the dependency of the material properties with temperature. How this variation of the properties affects the final results is evaluated. This analytical model provides a simple and fast tool to simulate U-shaped thermal actuators. The model has a general validity and is not limited to the particular geometry used in this thesis.

Chapter 5 reports on the detailed electrothermomechanical characterisation of various microgrippers. The electrothermal characterisation is performed using infrared thermography, its use in polymeric thermal actuators reported here for the first time. After a brief introduction to different methods to measure temperature, infrared thermography is described with particular emphasis on its associated benefits and limitations. Overall, this technique provides a fast and reliable tool to obtain temperature measurements with high spatial resolution in both static and dynamic modes. High quality infrared experimental data is used in this chapter to present the thermal mapping of different devices, and to present the characterisation data. In the second part of the chapter the mechanical behaviour of the microgripper is reported. The deflection of the different non-loaded microgrippers is measured in air as well as in a liquid environment. In addition, a set of manipulation experiments are presented. Live testing, failure mechanisms and the difficulties associated with the manipulation tasks are explained.

In **Chapter 6**, the experimental results are compared to the predictions provided by the FEA and analytical models. The effect of the material properties and environmental conditions on the deflection results and the agreement with the analytical models is discussed. In the final part of the chapter, a set of simulation based predictions is presented. These simulations are based on both the electrothermal and thermomechanical model, and help to analyse the effect of different geometrical parameters (gap, shape and overall scale) on the performance of the microgripper, and ultimately to optimise the design.

Chapter 7 summarises the research carried out, highlighting the particular achievements and suggests a future research direction. First experiments manipulating single oocyte cells are also presented.

CHAPTER 2

A Microgripper survey

The main goal of this chapter is to present an overview of the state-of-the-art in microgripper technology. Previous reviews [63, 64] primarily account for the very first microgripper designs that appeared in the mid to late nineties. This review focuses on more recent advances, prototypes and commercial microgrippers developed since 2000.

2.1. Background

In recent years, research and development in systems and tools for the gripping, positioning and release of micro-sized objects has boomed. An essential component of these systems is the gripping unit and, in particular, the end effector or microgripper tool. The latter brings the macroscopic part of the system into contact with the microscopic object which is to be manipulated. Furthermore, it permits the handling and positioning of the object without inducing damage. The microgripper ultimately determines the reliability and effectiveness of the overall manipulation system. For this reason, there has been a dramatic increase in the number of published prototypes in recent years. This is illustrated in Fig. 2.1 which shows that more than two thirds of the published grippers have been developed since 2000.

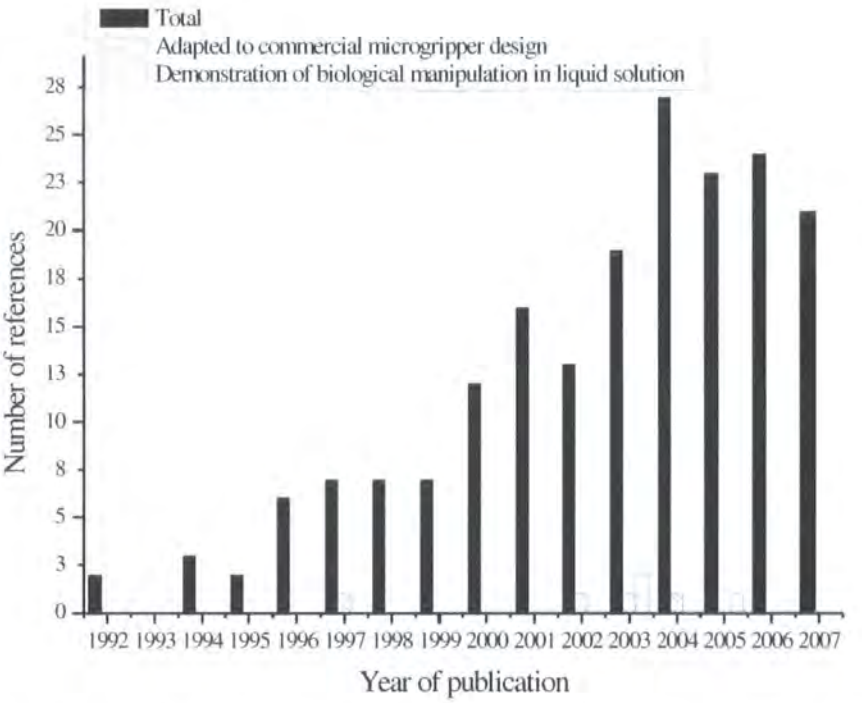

Fig. 2.1: Total number of published microgripper prototypes per year. (Source Web of Knowledge (Word search: Microgripper*); Number of prototypes that have become a commercial microgripper; and number of prototypes that have demonstrated the manipulation of biological particles in liquid solution.

The emergence of the research field of micromanipulation can be justified by an increase in the demand for (micro)manufacturing [64-67] and biomedical technology [7, 68-70].

From a medical and biological technology perspective microgripper devices have applications in many areas. In microsurgery (minimal invasive surgery) and drug delivery, catheters, endoscopes and "active pills" [71] may require the inclusion of clamping devices that permit them to be attached to different parts of the body such as the digestive tract [72]. In areas of assisted medicine such as in-vitro fertilisation (IVF) or intracytoplasmic sperm injection (ICSI), the manipulation of small biological cells and particles is also required. Some growing areas of more fundamental research such as genomics, proteomics and cancer research at a cellular level, require the manipulation of single cells and other biological particles such as DNA [7, 73]. All of these areas require that the manipulation is carried out in liquid environments in order to protect in vivo samples. Microgripper devices, when designed to operate in liquid environments, can offer a flexible, cost-effective alternative to other existing techniques.

However, the number of commercial microgrippers available is still very low when compared to the number of research prototypes. Table 2.1 shows a list of microgrippers that are commercially available [74-81]. This indicates that not all of the design and manufacturing challenges have been solved and, more importantly, that there is still room for research and exploration in this area.

Table 2.1: Characteristics of commercial microgrippers

Company	Actuation principle	Performance	Material	Ref.
Nascatec Nanoscale technologies GmbH	Electrostatic (Comb drive)	Displacements up to 170 μm	Silicon	[77]
Zyvex	Electrothermal (Chevron)	Displacements up to 30 μm for a voltage up to 10 V	Silicon	[79]
MEMS precision instruments	Electrothermal (linear expansion)	Displacements up to 100 μm for a voltage up to 18 V and 100 mA current.	Silicon	[74]
Bartels mikrorechnik	Shape memory alloy	-	Ni-Ti	[80]
Kleindiek Nanotechnick GmbH	Piezoelectric	Gripping area (4 ± 1μm); Force > 200 μN; temperature range (273-353 K); Resolution 15 nm	Tungsten probes	[76]
Kloche Nanotechnick GmbH	Piezoelectric	Size of the objects (20-5000 μm); maximum stroke 700 μm; gripping force 20 mN	-	[75]
Piezosystem Jena	Piezoelectric	Displacements up to 300 μm for a voltage up to 150 V and a temperature below 80 °C.(initial gap 300 μm)	-	[81]
Preiser Scientific	Piezoelectric	-	Polymer actuator + stainless steel tips	[78]

In the research arena more actuation mechanisms than the ones showed in Table 2.1 have been explored. The different microgripper prototypes can be classified in families and subfamilies based on their driving mechanism, and the particular choice of actuator. There are three main families which include microgrippers driven by electrical, magnetic and thermal effects. These three families contain subfamilies. For instance, microgrippers controlled by electrical effects include: electrostatic ([82-91]), piezoelectric[92-104], and electroactive polymer [7, 105-107] actuation. Thermally driven microgrippers include shape memory alloy (SMA) actuators [72, 108-115], thermal expansion actuators[73, 97, 116-128], and hydraulic and pneumatic microactuators[106, 129-134]. Magnetically driven microgrippers include: electromagnetic and magnetostrictive actuators [135-137].

The following sections will describe and discuss a selection of the most relevant prototypes and commercial microgrippers along with the principles of their various actuation mechanisms.

2.2. Microgripper review

2.2.1. Electrostatic microgrippers

Electrostatic actuation is the mechanism most commonly used in the design of microactuators. In industry, it is already used in microresonators, switches, micromirrors and accelerometers. There are several reasons for its popularity. First, scaling effects favour electrostatic force at the microscale. The devices can be fabricated using standard materials such as silicon or electroplated metals and therefore well mastered batch fabrication processes for high aspect ratio structures such as Deep Reactive Ion Etching (DRIE) can be used. This allows for IC compatible processes which enable microelectronic control systems to be fabricated on the same substrate as the electrostatic actuator.

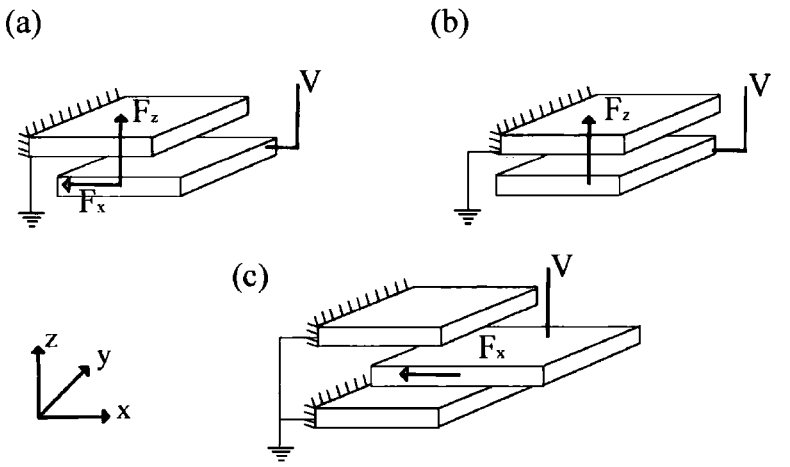

Fig. 2.2 : (a) Lateral (F_x) and perpendicular (F_z) forces experiences by two charged parallel plates. (b) Pure perpendicular force (c) Pure lateral force (Comb basic unit)

Electrostatic actuators are designed to exploit either the perpendicular force F_z (Fig. 2.2 (b)) or the lateral force F_x (Fig. 2.2 (c)) which is experienced by two charged plates, separated by a dielectric material and subject to a potential difference (V). There are different design configurations to generate and exploit electrostatic forces. These include lateral electrostatic comb drives, parallel-plate (PP), scratch drive actuators (SDA), curved electrodes and wobble motors.

The most common design of actuator is the lateral electrostatic comb drive where a number of elementary electrostatic actuators (Fig. 2.2 (c)) create a parallel structure of equally spaced fingers. This, in theory, results in a purely lateral force (F_x) [138]. The

magnitude of the force depends on the number of fingers, the gap in between them, the thickness and the applied voltage. The main advantage of this design is that the behaviour is linear with a constant force makes for easier control of the displacement. In addition, they have very good mechanical quality factors due to low internal damping and the lack of squeeze film air damping. The main downside, however, is the high voltage requirement (hundreds of volts) if large displacements are required.

In parallel-plate (PP) actuators, the positive charges on one plate/beam attract the negative charges on the other plate/beam with a Coulombic electrostatic force F_z which is in the direction of the electric field. Compared to the comb drive where the direction of movement is perpendicular to the electric field, they can produce more force per applied volt in a smaller chip area. However, they are less stable than comb drives due to the 'pull-in' effect which limits the maximum displacement and applied force. As the plates/beams approach one another, the electrostatic force increases faster than the restoring spring force, and at a critical distance (governed by a critical pull-in voltage) the plates become unstable and snap together. For a PP actuator, the displacement of the actuator is ultimately limited to one third of the unbiased gap before pull-in occurs. As with comb drives, and electrostatic actuators in general, actuation voltages are also relatively high for large displacements.

Comb drive actuators can also enter unstable control states. These instabilities appear because of the electrostatic forces that also act in the z direction of the fingers. If the interdigitated fingers are not equally spaced then this will cause an offset in the force and pull the fingers to one side. There are other electrostatic actuators such as the scratch drive actuator (SDA) which are relatively more stable and can produce higher forces [139].

Some general characteristics of electrostatic actuators are that they can produce large displacements (up to 150 μm [140]), low forces (μN-mN range) at low power and high driven speeds (kHz and above). Their inherently high mechanical quality factors make them excellent for resonant structures.

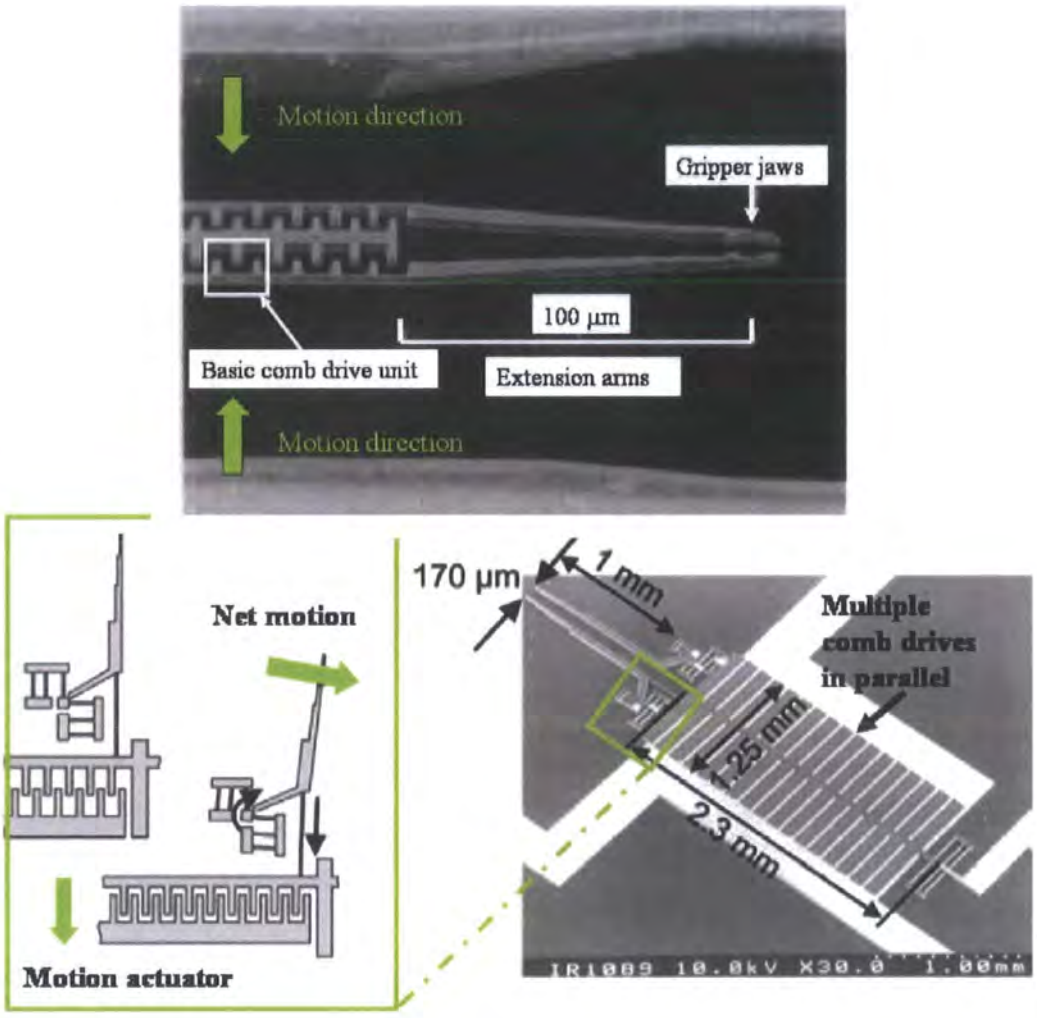

Fig. 2.3 : (Top) Electrostatic polysilicon microgripper [82] (Bottom) Electrostatic microgripper with amplification mechanisms [85]

The main disadvantage of electrostatic actuators is the high actuation voltage requirement. This, however, is not a fundamental limitation of the actuator since design improvements can be introduced which improve dramatically the displacement capabilities for a given voltage [141, 142]. In addition, recently proposed polymer-based electrostatic actuators, fabricated in PMMA or SU8, could further reduce the voltage requirements [143, 144].

Several microgrippers [82, 85, 89] have been developed which use an electrostatic comb drive as the actuation mechanism. Kim et al. [82] proposed the first microgripper of this type in the early nineties. The monolithic structure (Fig. 2.3 (top)) was composed of an electrostatic comb drive which consisted of one central electrode and two drive

electrodes that included the microgripper's jaw. The microgripper could only be operated in an open mode, i.e. it requires power during the manipulation operation. The two jaws in this design have an equipotential and this stops electric conduction occurring as the gap is reduced. This microgripper, in its overhanging configuration, grasped objects of approximately 2.7 μm of diameter for an applied voltage of 45 V. However, there are a few disadvantages to this particular design. First is the limited aspect ratio of the beams that can be produced in polysilicon using standard micromachining techniques (maximum thickness 2.5 μm). This in turn limits the size of the structures that can be grasped. In addition the structure was fragile and prone to breakage during various stages of operation and fabrication, especially during the bulk micromachining release step. Finally the jaws of the microgripper are an active part of the driving mechanism and have limited range of displacement. Volland [85] found the solution to some of these problems by designing a new electrostatic microgripper also based on a comb drive (Fig. 2.3 (Bottom)). First, the microgripper was built in thick silicon using silicon-on-insulator (SOI) technology (up to 10-40 microns) which provided better structural rigidity. Second, the linear motion of the comb drive was converted into a rotational motion by flexible hinges. This resulted in an amplification of the jaw displacement range that was not limited by the possible contact between jaws and electrodes. This microgripper provided 20 μm of in-plane displacement for an applied voltage of 80 V. The actuation voltage is still relatively high, but recent efforts by the same author include an optimisation of the design to obtain the same displacement at approximately half of the applied voltage [89]. The company Nascatec GmbH has adopted this design for its proposed microgripper [77].

Various microgrippers have been based on parallel plate/beam actuation ([145], [83], [86, 87]). Molhave et al. [86, 87] (Fig. 2.4 (a) and (b)) designed two nanogrippers based on parallel beam electrostatic actuation. In both cases, the beams deflect in-plane when a voltage is applied. In the second version of this design [87] the jaws are insulated from the electrodes. This allows not only the successful manipulation of single nanotubes but also enables electrical measurements to be performed on the samples

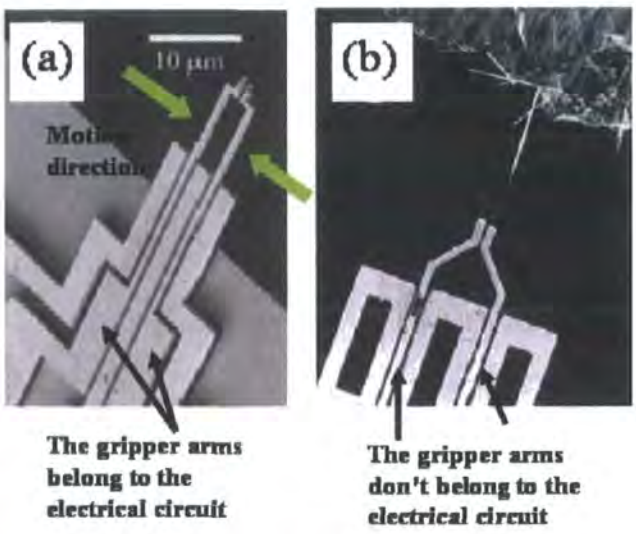

Fig. 2.4: Electrostatic microgrippers developed by Molhave et. al. for the manipulation of carbon nanotubes (a) The arms belong the electrostatic beams [86] (b) The gripping arms are independent of the electrostatic beams [87]

Another interesting, but less practical, microgripper uses a third type of electrostatic actuator, a scratch drive actuator (SDA) [139]. It is produced in an eight mask surface micromachining process. This actuator has some advantages such as highly precise quasi-static motion and demonstrates the principle of the actuator but the complicated fabrication flow and the slow speed of the jaws (less than 20 μm/s) make it impractical as a microgripper. In addition, SDAs are based on frictional effects which limit the lifetime of the system.

More recently, a microgripper (Fig. 2.5) has been published that not only seems to solve most of the existing problems but also adds some advantages to electrostatic microgrippers such as a force sensor [90]. The latter adds the possibility to measure in-situ the force applied in between the jaws. In this design an electrostatic comb drive moves one of the jaws permitting the grasping operation. At the same time the other jaw is connected to another comb drive that is used as a capacitive sensor to measure the force.

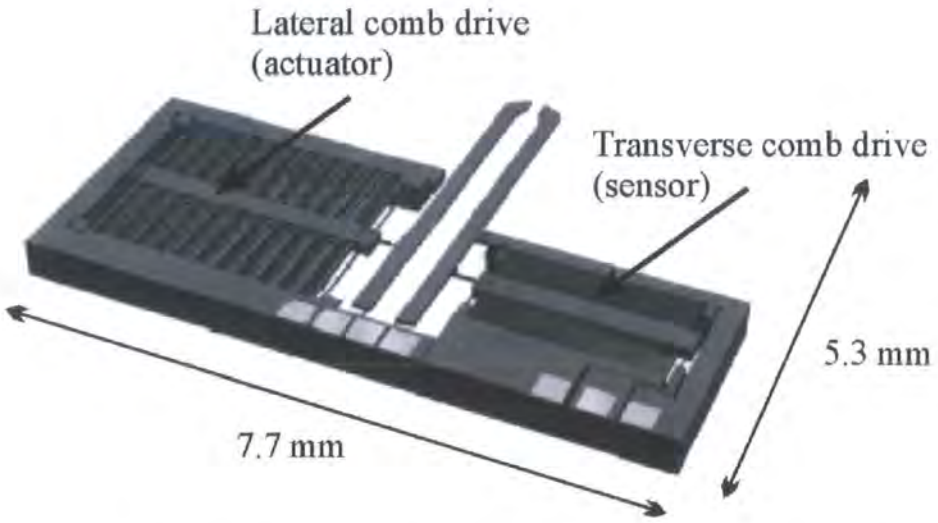

Fig. 2.5: Electrostatic microgripper with integrated sensor structure by Beyeler et al. [90]

None of the reported electrostatic based microgrippers has been demonstrated to function in liquid environments with total immersion of the gripper. This is due to the high voltage requirements. Electrostatic microgrippers cannot be operated in fluidic media when completely submerged due to reasons such as electrode screening and air trapped between the combs.

2.2.2. Piezoelectric microgrippers

A material property known as piezoelectricity allows certain materials to be used as sensors as well as actuators. On the one hand, piezoelectric materials can "sense" by generating an electrical response when they are mechanically stressed. On the other hand, they can move with a precise motion when an electric field is applied to them.

Thick and thin films of piezoelectric ceramics (most commonly lead zirconate titanate (PZT) or barium titanate) can be deposited using sputtering and sol-gel techniques. Piezoelectricity can also be displayed in polymers such as polyvinylidene fluoride (PVDF), which in addition is pyroelectric i.e. capable of converting changes in temperature into electrical output. Recent studies have reported the piezoelectric properties of conducting polymers such as polyaniline and polypyrrole. All of these polymers have the advantage of requiring one order of magnitude less input voltage than ceramic materials for equivalent displacements. This could have potential advantages in biological applications.

Piezoelectric actuation offers some advantages over other actuation mechanisms such as speed, resolution, accuracy, reliable positioning, output force and low power consumption. However, it can only generate displacements of a few microns and requires high voltages.

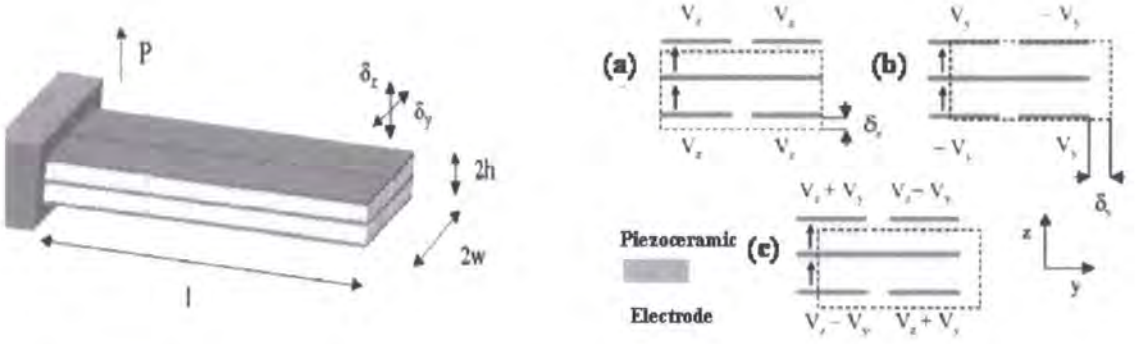

Fig. 2.6: (Left) Geometrical configuration of the duo-bimorph used in [100] (Right) Working principle duo-bimorph with the electrical configuration resulting in displacements δy, δz.

Actuators exist in different forms: multilayer stack, single or multilayer 1 DOF bending actuators, single or multilayer 2- DOF bending (see Fig. 2.6) actuators and monolithic bulk actuators with electrode stacking [100]. They are normally integrated in large scale devices but they are difficult to implement at the microscale and they require hybrid fabrication processes. This is a major disadvantage when compared to electrostatic actuators.

Most of the recently reported microgrippers require hybrid fabrication processes where the assembly of the piezoactuator to the end effector is one of the most difficult tasks. So far only one monolithic microgripper has been reported in the literature, designed by Breget et al. [146]. The gripper is 3 cm long and opens and closes 18 μm at the tip for a voltage of 150 V. Leaving aside fabrication and assembly complexity, the advantages of piezoelectric microgrippers as tools that provide more precise positioning of objects (compared to other actuation mechanisms) and less consumed power has been demonstrated on different occasions. Also, a few commercial microgrippers are already available in the market.

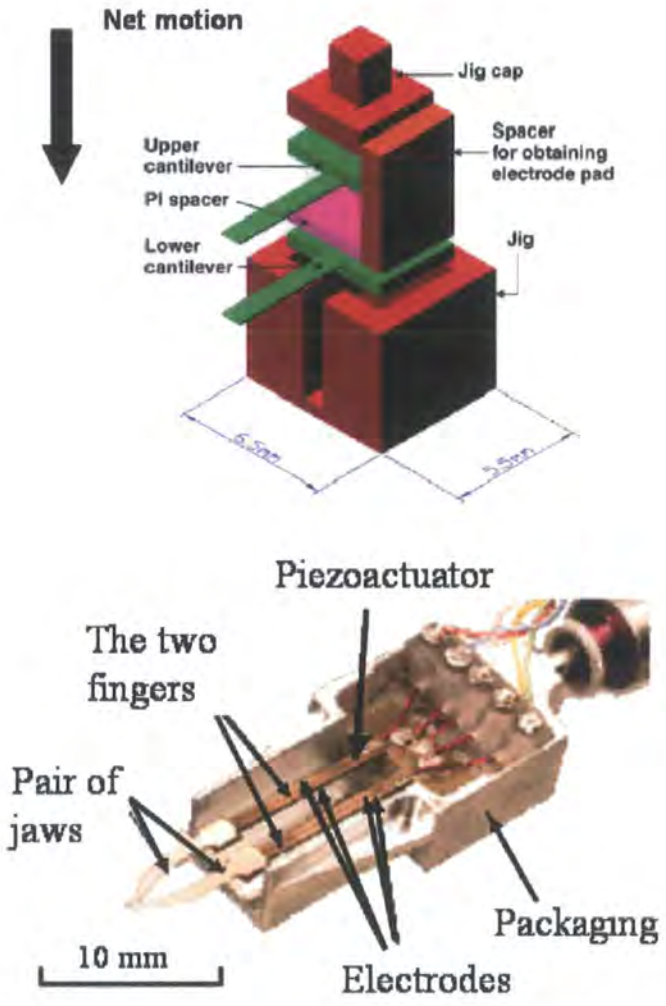

Fig. 2.7: (Top) Drawing of a microgripper composed of two micro PZT cantilevers [[101] (Bottom) Piezoelectric microgripper presented in [100]

Although none of the commercial microgripper companies report the integration of force sensors, four of the microgrippers found in the literature incorporate them in their designs [94, 96, 99, 104, 147]. Carrozza et al. showed the integration of strain gauge sensors in 2000 [104, 148]. In these papers, due to the relatively large size of the commercial sensors, the force was not measured at the tips of the microgripper. This was achieved by Park et al. [96] in the design of a two finger microgripper with incorporated piezoresistive sensors at the silicon tips. Perez et al. have also integrated silicon piezoresistors into a bi-directional microgripper composed of two piezoceramic parallel bimorphs [99]. In all of these design, however, the sensors have to be assembled to the microgripper structures manually, which can result in misalignments of the sensors and the piezoceramic fingers [149]. In addition to that, the sensing capabilities

of PVDF actuators, although not yet integrated in microgrippers, are also being investigated.

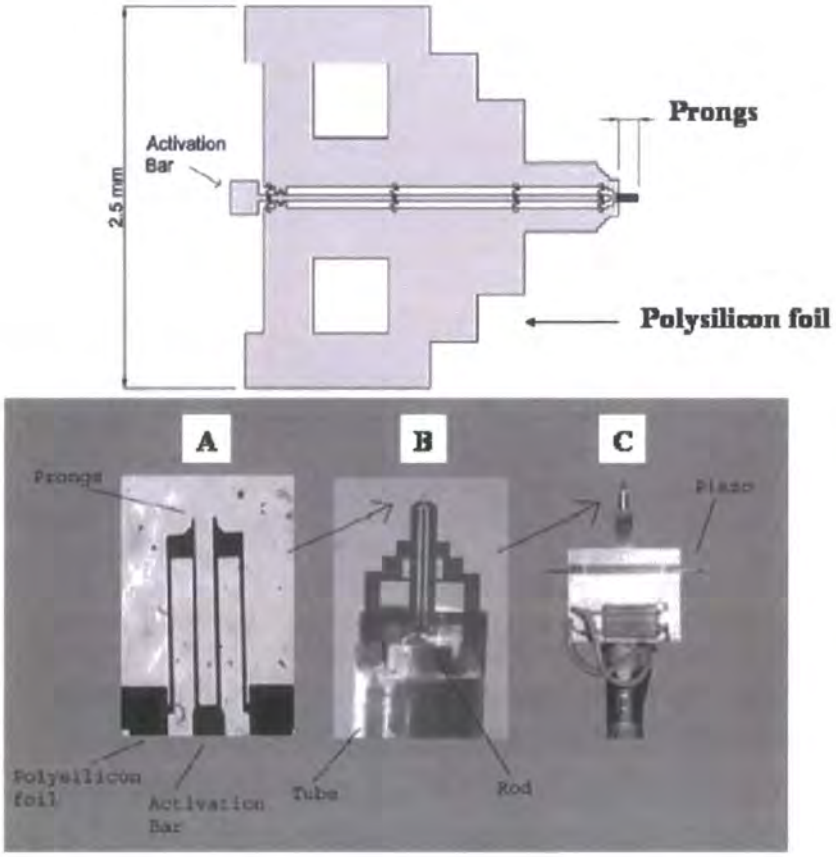

Fig. 2.8: (Top) Drawing of the Piezoelectric design proposed by Jericho et al. [98] for the manipulation of bacteria (Bottom) Fabricated microgripper

Biological manipulation has also been demonstrated with the use of piezoelectric microgrippers. Jericho et al. [98] proposed an interesting design of microgripper (Fig. 2.8) which could manipulate bacteria in a biological fluid. In this design, the end effector and the actuators were linked with the help of a long activation bar. In this way the extended arms are sufficiently far away from the actuator to make operation in fluidic media is possible. The design proposed by Jeon et al. [101] also showed promise in biomanipulation. It required low actuation voltages, and could be coated with appropriate polymers. The actuators could be deposited using standard microfabrication processes and possessed good displacement range (up to 50 μm). Potential problems with this design include the difficulty in controlling the actuator stresses accumulated during fabrication and the fact that the gripper obscures the view of the object during manipulation (Fig. 2.7).

2.2.3. Electromagnetic microgrippers

Electromagnetic actuators can provide several advantages when compared to piezoelectric and electrostatic actuators. They can produce larger displacements, at moderate forces and at low power, and can operate in ionic fluid environments. The main disadvantages are the heat dissipation in the coils while maintaining constant forces, and the difficulties presented in the miniaturisation of the electromagnet.

There are two main designs of electromagnetic actuators. One uses electrical currents to produce attractive forces between two solids, and the other uses permanent magnets to produce a magnetic flux through current carrying wires. Other magnetic field driven actuators include electrodynamic, magnetostrictive and magnetorheological [150].

The voice coil motor (VCM) is one of the secondary types of electromagnetic actuators. Once the difficulties in producing it on a small scale are overcome, it has several advantages which include large strokes, linear response (Force versus Current) making good control possible, and it requires simple cost effective electronic circuits.

VCMs are already widely used in optical data storage devices. A microgripper has been reported based on this principle [137]. The performance of this microgripper with operating voltages of a few volts and strokes and forces of up to 180 μm and 600 mN respectively is an ideal candidate for manipulation tasks such as tissue probing. The downside, however, is that it has an extremely complicated process flow.

Another interesting magnetic microgripper based on Lorentz forces is the one proposed by Suzuki in the early nineties [135, 136]. For a maximum voltage of 2.5 V, strokes of up to 450 μm in air and 150 μm in water could be achieved. Initial problems related to stiction during fabrication were also solved by the author developing a dry release method based on naphthalene [151].

2.2.4. Shape memory alloy microgrippers

In shape memory alloy (SMA) microactuators, the physical work is produced by a solid state phase transformation that occurs in the SMA material, generally Ti-Ni, when it passes through its transition temperature. When the material undergoes a phase

transformation (can plastically deform by up to 10%), it passes from a martensitic state (soft and deformable) at low temperatures to an austenitic state (hard and difficult to deform) at high temperatures.

To exploit the shape memory effect (SME), the material has to be trained first, by forcing a high stressed deformation at elevated temperatures. This can be achieved during fabrication by using stresses accumulated during deposition or by external means such as applying forces. Once this is done, every time the material is heated above the transition temperature, by external or internal (Joule) heating, it will recover its initial, trained, shape. Hence, it generates work. On some occasions, when using for example SMA wires, mechanisms such as springs to recover the coiled shaped are needed. This is also necessary when using one-way SME.

SMA actuators have several advantages in performance such as high force/weight ratio (able to produce stresses up to 500 MPa), large displacements, low operating voltages, superelasticity (the ability to sustain large recoverable strain and to resist stress without the occurrence of plastic deformation) and they can be fabricated in thin films. There are however, some processing and operation problems. These include [152]: low energy efficiency (typically less than 10% [153]), slow response, limited temperature range (up to 70 °C), high processing temperatures (500 °C), large hysteresis, non-linear complex thermomechanical behaviour (and therefore difficulty in controlling force and displacement), on some occasions mechanical biasing (providing recovery force) is required to enable cycling, high cost of the films, difficulties controlling material properties and, finally potential degradation and fatigue problems.

Some of these general disadvantages can be partially solved by using different fabrication techniques. For example, the large hysteresis can be reduced adding Cu to the composition of TiNi [108]. Fatigue issues can be avoided by using an intermediate R-phase transformation of the material [110, 154]. Despite the highlighted disadvantages SMA actuators are ideal for actuation purposes where high force is required. For example electrostatic actuators only exert a fraction of the force.

Two major types of microgrippers exist as a function of the role played by the SMA material. In the first type [109-111, 113] the SMA material is shaped into a compliant

structure and it provides both the actuation mechanism and the gripper operation. This type of design requires the SMA material in a thin film or a commercially available sheet film form. The thin film form is sputter deposited during fabrication. The material properties of the thin film depend highly on the deposition process and are difficult to control. Monolithic microgrippers are generally driven by current-induced thermal expansion, and have shown displacements of up to 400 μm for a gripping force of 50 mN.

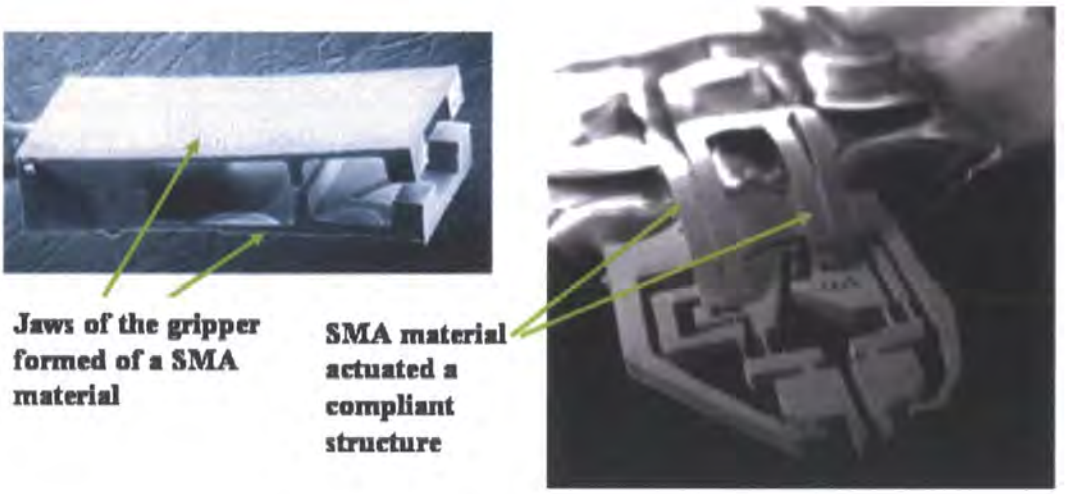

Fig. 2.9: (Left) Out-of-plane SMA microgripper by Lee et. al ([108]) (Right) Monolithic compliant microgripper by Buttgenbach [112]

In the second type of microgripper [108, 114, 155, 156], the design consists of two parts; the actuation structure and the gripping mechanisms. The SMA material is used exclusively to create the actuator mechanism whilst another material (e.g. Si or a polymer or even an SMA which exploits superelasticity) is used to create the end-effector of the microgripper. In this case, the choice of type of SMA material that can be used is wider as it is not restricted to thin film form, and it can be used in preformed sheets, wires or springs [72, 115, 157].

All of the SMA based grippers offer similar advantages such as high actuation forces, ranging from 13 to 50 mN, large displacements (ranging from 100 to 500 μm), and low voltages, generally between 2-5 V. The latter could be important when compatibility with CMOS is required.

Kohl et al. overcame the difficulties associated with the control of position and associated force [109]. They integrated a displacement photosensor and used a feedback control algorithm to improve the positioning accuracy from 25 μm in the first version of the microgripper [110] to 2 μm in the most recent one [109].

Despite some intrinsic limitations, SMA actuators and microgrippers continue to have great potential as an alternative to other mechanisms of actuation for applications where very high output forces and/or displacements are required. Menciassi et al. [72] reported clamping mechanisms to realise different tasks within the gastrointestinal tract using an SMA wire.

2.2.5. Micro-Pneumatic and micro-hydraulic microgrippers

Based on well known macroscopic hydraulic and pneumatic principles, these microactuators convert the pressure exerted by liquids or gases in a confined space into force and displacement. The main advantages of these kinds of actuators are the high energy density, the possibility to exert high forces, and the possibility to operate in any environment due to the passive nature. The main disadvantage is these actuators require an interface to an external macroscopic source of air and liquid.

The microgripper designed by Schlick et al. [129] and Buttenfisch [130] (see fig 2.10 left) are based in micro-pneumatics. The Schlick microgripper proved the principle but only permits the manipulation of relatively large parts with dimension of 200 to 3500 μm. Another structure based on micro-pneumatics, is the one developed by Ok et al. [132] where the fingers of a microcage are actuated by the pneumatic deformation of a membrane that is situated underneath the centre point of cage. When a pressure is applied the fingers open; when the pressure is released the fingers close.

Hydrostatic actuation has also been exploited in microgrippers designs. For example Mutzenich et al. [131] proposed a design based on a technique similar to a Bourdon Tube. In this design, pressure changes induced through the heating of a contained fluid act as the driving force. Modelling work [158] has been carried out recently but no prototype or experimental results have been published so far.

Finally, another hydrostatic actuator has demonstrated the use of phase change materials (PCM) (see fig. 2.10, right). In this case the hydraulic pressure is obtained by the volumetric expansion that PCM materials suffer when they change from solid to liquid [134]. Paraffin wax, already used in the past for other applications [159], is heated by a resistor and the volumetric expansion experienced during melting is used to move a pair of silicon prongs up or down. Displacements up to 300 μm can be achieved with an applied voltage of 10 V. This is an important design since it does not require macroscopic systems that provide air or fluid pressure.

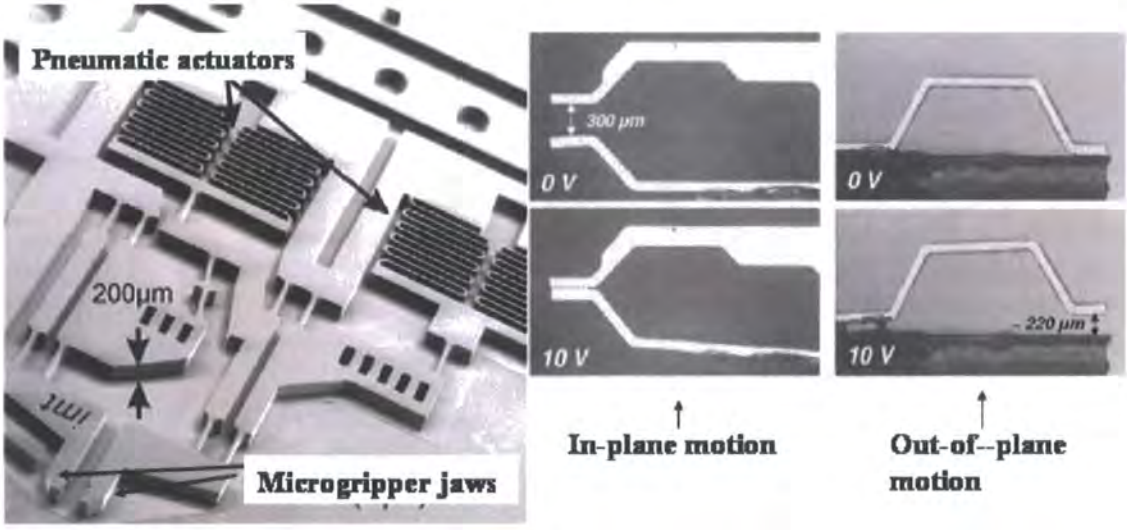

Fig. 2.10: (Left) Pneumatic microgripper [130] (Right) PCM microgripper [134]

2.2.6. Electroactive polymers microgrippers

There are several electroactive polymers (EAP) that can be used to produce actuators. They exist in dry and wet versions.

The main dry polymer is PVDF (fig. 2.11) since, as reported in section 2.2.2, it also exhibits piezoelectric behaviour. Another dry example is the polymer elastomers that, due to charge accumulation in the electrodes, suffer a longitudinal compressive stress when a voltage is applied across their thickness. The most critical issue for this kind of polymer is that they require an electrical field of the order of 100 V/μm.

There are two main wet polymers: Ionic polymer metal composite (IPMC) and conducting polymers such as polyaniline (PANI) and polypirrole (PPy). All of these polymers are characterised by a change of shape or size when they respond to an electrical stimulus.

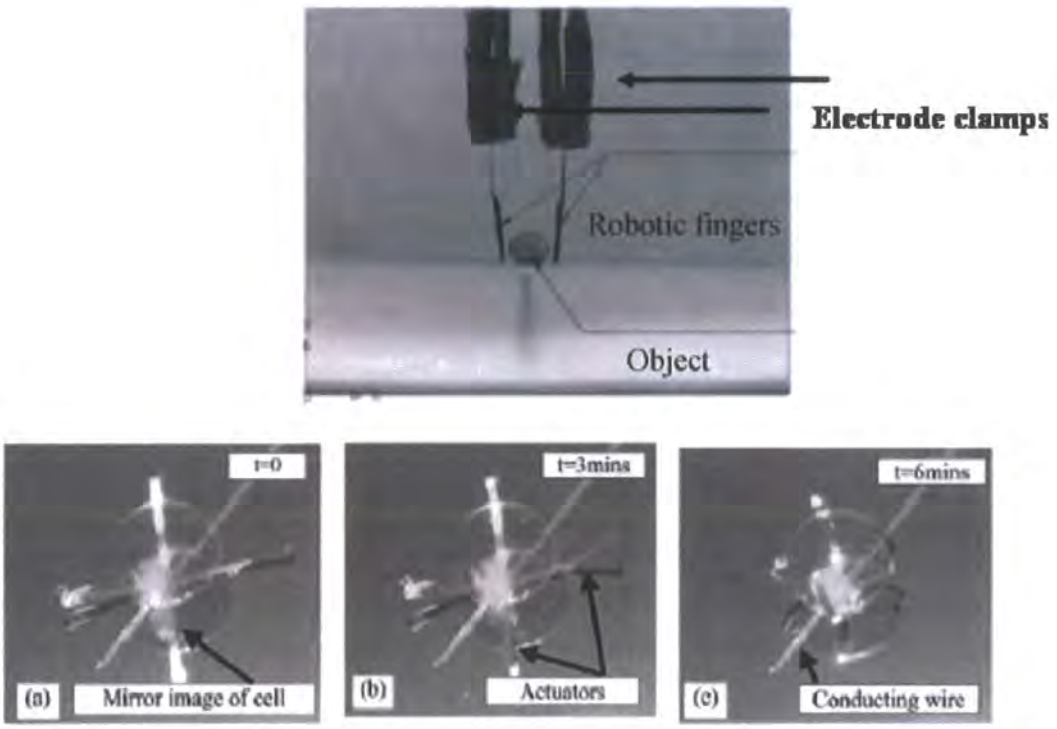

Fig. 2.11: (Top) PPy- Platinum- PVDF trilayer finger gripper [160] (Bottom) Sequence of Parylene C cage in water by increasing the temperature from 23 °C to 27 °C [106].

IPMC are materials that bend in response to an electrical stimulus as a result of the mobility of the cations in the polymer network. IPMC swell in water due to their ionic and hydrophilic nature. Anions are fixed in the polymer membrane, while cations are free to move in the fluid. When an electrical field is applied, the cations diffuse towards the negative electrode, which causes the composite polymer to deform. Thus strips of IPMC can bend dramatically when an electrical voltage is applied across their thickness and they can generate force and large displacements. On the other hand, they also show a change in voltage (~mV) across their thickness when they are bent. Thus, they can also be used as sensors. They only require a relatively low voltage (1-10 V) for activation at low frequencies. The main disadvantages is that the strain response to electrical stimulation is not linear and still needs to be understand better in order to control and improve these actuator designs. The typical two IPMC are Nafion® manufactured by Dupont and Flemion® manufactured by Asahi Glass.

Conducting polymers are thought to change in volume due to swelling of the polymer during oxidation reduction reaction. The polymer is normally in contact with an electrolyte and there is ion transport in and out of the conducting polymer. They require only a few volts to produce a few % size change (3% in-plane and 30% out-of-plane). Therefore they can be used for bending actuators (unimorph or bimorph layers) as well as linear actuators and can exert considerable force. They are perfectly suited for ionic media such as blood or other body fluids. Their main disadvantages are that they have a slow response time and poor efficiency. In addition, they cannot operate easily [69] without an electrolyte.

Electroactive actuators have also been incorporated in several microgrippers. The common feature of all of them is that they are very slow (~ 10's of s response time). But they all require on the other hand very low voltage, which makes them ideal for underwater applications. The actuators are always bending actuators. Different configurations of grippers have been published: cages (two three fingers), robotic arms and two finger tweezers.

2.2.7. Other microgrippers

Finally, a few microgrippers have been published that exploit other mechanisms such as opto-pneumatic [161], where the energy of a laser is used to expand a liquid and push a piston; opto-mechanic [162], where the energy of a laser is used to strain a layer of carbon nanotubes in a U-shaped configuration, and simple mechanic[163, 164].

In the latter case the objective is to produce a very rigid end-effector that does not require an actuation mechanism. This therefore does not have any failures associated with the actuator. In addition, the simplicity and passive structure allows an easier integration of sensor structures.

2.2.8. Electrothermal microgrippers

In recent years, a variety of thermal actuators that exploit the differential thermal expansion of heated microstructures have been demonstrated [165-172]. In most cases, the material used to build the actuator is a conductive material which can be used as a

self-heating element as well as an expansion material. In these cases, the geometry of the system is limited by the conduction path. Electrothermal actuators consume considerably more power than comparable electrostatic or piezoelectric actuators. However, the combination of conductor and polymeric materials enable the production of more efficient and flexible designs with, for example, geometries not limited by the conduction path. This method of actuation is used for the devices presented in this thesis. The mechanisms of actuation will be further discussed in chapter 3.

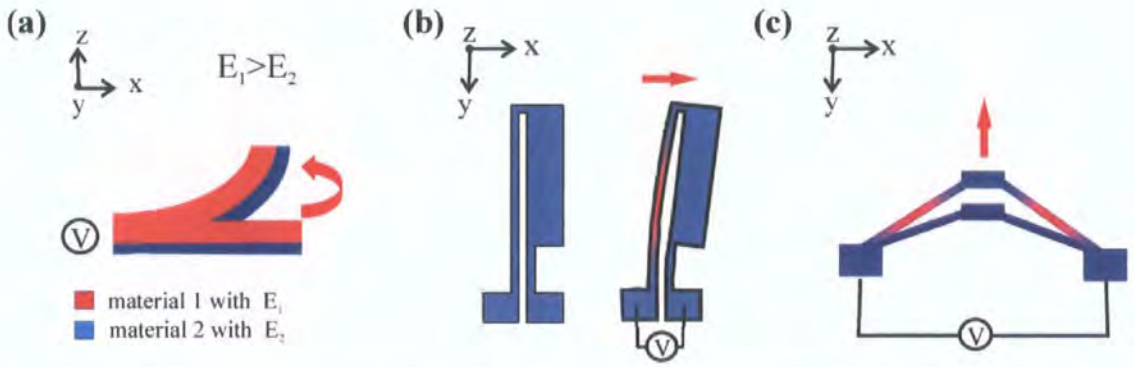

Fig. 2.12: The three main types of electrothermal actuators: (a) C-type (b) U-shaped (c) V-shaped (E ≡ Young's Modulus)

Typical thermal actuator designs that enable out-of-plane and/or in-plane displacements include: bimorph [166-169] (also known as C-shaped), pseudo-bimorphs (also know as U-shaped) [165, 167, 168, 172], chevron (also known as V-shaped) [171], and bidirectional (BTVA) designs [170]. Fig. 2.12 depicts the three main types of thermal actuators.

The first type, C-shaped (Fig. 2.12 (a)), relies on the asymmetric expansion in an isothermal multi-layer beam composed of materials with different coefficients of expansion. For a given temperature change in the structure, different induced expansions in the layers produce out-of-plane bending. Recent work includes the evaluation of new material combinations for the optimisation of force and displacement output parameters [173].

The second type, U-shaped (Fig. 2.12 (b)), rely on the asymmetrical heating and expansion of a materially homogenous structure. The beams composing this actuator, which have different lengths and/or cross-sections, are connected in a U-shaped configuration. When a current flows through the conducting path, resistive (Joule)

heating occurs and a temperature difference is established between parts with various geometries. For a typical U-shaped actuator, the thin hot arm expands more than the cold and flexure arms. This causes a net in-plane deflection. In general, the expansion of the actuators depends on the temperature difference established between opposite arms, the separation gap and the relationship between different geometrical parameters such as the total length and the length of the flexure compared to that of the hot arm. In recent years, numerous design variations have appeared which optimise the structure thermally and/or mechanically. Examples include the inclusion of two hot arms that eliminate the parasitic heating of the cold arm; the inclusion of a third arm that allows bi-directional movements; the shortening of the arms to produce larger forces. Many of these optimisation efforts have been intended to improve the thermal efficiency of the system.

The third type of actuator, V-shaped, also relies in the asymmetrical heating and expansion of a materially homogenous structure. In this case, the beams are fixed by two supports at an angle creating a V shaped structure. When a current passes from one support to the other, the beams expand due to Joule heating and an in-plane rectilinear motion is obtained. These actuators have also been subjected to optimisation, and spring-like actuators have appeared [120, 174]. This new type of spring like planar actuator consists of a number of chevron sections constrained by insulating beams. Different configurations of the insulating beam can produce outward and inward displacements. An original circular version has been proposed by [120].

Fig. 2.13: SEM picture of a cage microgripper capturing a 65 μm particle[118].

All of these actuators have been used in microgrippers. The C-shaped thermal actuator is normally used in a cage configuration. Chan et al. [117] were the first group to demonstrate a microgripper that could manipulate biological cells (Dario cells) in an aqueous environment. This was possible because low voltages (< 3 V) and low temperatures (~ 60 °C) were necessary to activate the Parylene C – Platinum fingers. The use of a high coefficient of expansion polymer maximises the amount of deflection per unit of input power. Earlier papers have used other combinations of materials such as polyimide-Au [169], but higher voltages (7 V) and temperatures (up to 260 °C) were required. Luo et al. [118] proposed a similar concept of microgripper in a cage configuration (Fig 2.13). The main difference with the previous microgrippers is that this design operates in closed mode where power is required only for the release operation. The use of diamond like carbon (DLC) and nickel fingers allows the fabrication of pre-curved fingers that become flat when the power is applied. By varying the thicknesses of the layers, different cage sizes can be obtained. Recently, this design has been further improved with the addition of a polymeric layer [127]. The fingers were composed of a trilayer structure SU8/DLC/Ni and required only 300 K to open compared to the 700 K needed for the DLC/Ni combination. The cage-based microgrippers have proven to be appropriate for holding micro-sized objects in position. However, for micromanipulation it is necessary to move the sample from one place to another.

From this perspective, microgrippers based on the U-shaped or V-shaped actuator are more flexible than cage-like structures. Two commercially available microgrippers distributed by Zyvex [79] and based on the developments published in [175, 176] are driven by a V-shaped actuator mechanism (Fig. 2.14). Their BB and SM-BB models operate in a closed and open mode respectively and are fabricated from silicon. They have recently added a high coefficient of expansion polymer (SU8) coated with nickel to their silicon grippers. A priori this would mean that lower voltages are required for actuation. Despite the fact that successful manipulation of cells (normal rat kidney cells) has been demonstrated in [177], these improved devices have not entered commercial production.

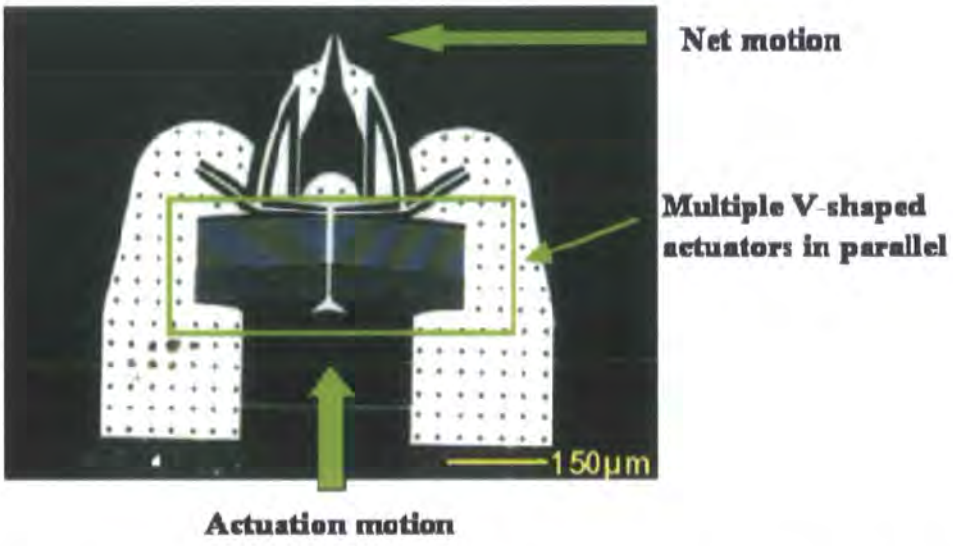

Fig. 2.14: Electrothermal microgripper using a V-shaped thermal actuator and commercialised by Zyvex [79]

Other microgrippers have been published using original variations of the V-shaped actuator. In these cases spring-like actuators are used [120, 125]. The design is original in both papers but they suffer from very high operating temperatures (300-1000 °C).

Finally, four other microgrippers have been published that exploit the U-shaped principle [73, 119, 122, 123]. Molhave et al. proposed a nanogripper fabricated in gold [122]. The main feature of this design is that it offers integrated piezoresistive force feedback. This was the first time that an electrothermal microgripper included a sensing structure. The design is however still at the early stage and improvements have to be made to the structure in order to obtain a practical microgripper. So far it lacks the necessary aspect ratio and enough sensitivity in the piezoresistor. Hashiguchi et al.[73] fabricated a silicon microgripper coated with Al at the tips. It demonstrated, for the first time, the ability to manipulate biological particles (DNA molecules) in aqueous solution. A power of 200 mW was necessary to open a 1 µm gap. On a larger scale, Chronis et al. [123] also demonstrated the manipulation of Hela cells. The microgripper made from SU8 polymer and gold, opened up to 12 µm for a low voltage (1.8 V) and a temperature change of 20 °C. These parameters make this microgripper an ideal candidate for single cell manipulation. Finally, Nguyen et Al. [119] also proposed a SU8 microgripper covered by a titanium/platinum layer. At slightly higher voltages (up to 10 V) than the previous one, it offers considerably larger displacements (up to

100 μm). In addition the temperature of actuation remains below 100 °C and it also offers bidirectional movement.

To finish this section, it would be interesting to cite another commercial microgripper ([74]) based on a developed reported by Keller et al. [178] in the late nineties. The Hexsil microgripper is formed by a linear thermal expansion structure plus an amplification compliant mechanism. Displacements of up to 100 μm were achieved with voltages up to 18 V and currents of 100 mA. Although not offered as a commercial product, manipulation of cells has been demonstrated on the company web page. Despite the requirements in terms of voltage, the manipulation is achieved by mounting the actuator in the handle of the manipulator.

2.3. Conclusion

This chapter has reported a multitude of different microgrippers with a wide range of properties and applications. Therefore to conclude, table 2.2 shows the best performing microgrippers in each actuation class.

Table 2.2: Summary of the best performing microgrippers per each mechanism of actuation

Actuation mechanism	Year	Ref.	Device description	Performance	Force/displacement sensor	Manipulation tests Air/Liquid
Electrostatic	2007	[90]	Linear comb drive. Monolithic structure fabricated in polysilicon.	Displacements of 50, 100, 200 μm for applied volatges of 50, 150 and 150 V respectivelly. Force = 8 μN	Yes (Capacitive)	Yes/Yes
Piezoelectric	2004	[98]	The jaws are connected to the actuator by an activation bar	Displacements of up to 9 μm for applied voltages of 9 V. Force = 0.7 μN	No	Yes/Yes
SMA	2002	[109]	Ni-Ti free standing film	Displacements of 300 μm for an applied power of 100mW. Force = 300 mN	Yes (optical)	No/No
Electrothermal (U-shape)	2005	[123]	Standard U-shaped actuator fabricated in polymer SU8 and Gold	Displacements up to 12 μm for applied volatges of 1.8 V.	No	Yes/Yes
Electrothermal (C-shape)	2003	[117]	Cage formated with various fingers of a bilayer composition Parylene + Pt	Close cage at inout voltage 3V and a temperature < 60 °C	No	Yes/Yes
Micro-pneumatic	2004	[130]	A Pyrex-Si-Pyrex sandwhich structure	Displacement up to 600 μm. Force 10mN at 400 mbar	No	Yes/No
Electromagnetic	2005	[137]	Thin Film cantilever of NiCr and Au.	Displacements uo to 210 μm for an applied voltages of 1 V respectivelly. Force = 29.9 nN	Yes (piezoresistive)	Yes/Yes (in see water urchin eggs)
EAP	2000	[7]	Bilayer actuator fabricated in Ppy-Au	Enclose a sample at 1V	No	No/yes

CHAPTER 3

Microgripper design and microfabrication

This chapter is divided into two main sections: one dedicated to the conceptual design of the microgripper, another dedicated to the physical fabrication of the device. In the first part, aspects such as the reasons for a particular choice of thermal actuator, optimisation strategies, and the description of the microgripper itself are treated. In the second part, after a brief introduction to microsystems technology, the choice of materials and the fabrication processes are presented.

3.1. Design criteria and choice of actuation mechanism

The starting point of this design is the realisation of a pair of miniaturised tweezers that can be used by a human operator under a microscope. As such they will be composed of an actuation mechanism and a pair of tightened arms (prongs). Through the application of electrical power the prongs will open or close, and therefore grasp. One of the main advantages of this design is the intuitive nature of the mechanism, which should minimise the learning time of any human operator. The microgripper should be attached to an XYZ micromanipulation stage which allows precise positioning.

The main objective of the microgripper design is to provide a tool for the manipulation (transport, and pick-and-place) of cells and other biological particles. As such, certain requirements have to be met by the design:

- Operation in air as well as in conductive liquid biological environments
- Operation at relatively low temperatures (T < 100 °C) to avoid the overheating of the sample and the surrounding media
- Operation at low voltages to avoid electrolysis which occurs at approximately 2 V.
- Suitable range of displacements determined by the minimum and maximum size of the samples to be manipulated. In the case of human cells, this range would be ~2 - 150 μm (±20 % of size variation within cells of the same type)
- Low handling forces in the order of nN to a few μN
- Prongs thermally and electrically insulated from the actuation mechanism.
- Dimensions of the order of the samples. Structural thickness between 10 and 150 μm.
- Biocompatibility
- Disposability
- Able to follow sterilisation protocols

In addition other attributes, such as ease of fabrication and ease of use by a human operator, also play a significant role in the viability of a prototype. From a fabrication point of view, monolithic solutions are therefore preferable to complicated hybrid designs which often require multiple sequential assembly steps. Equivalently, solutions that facilitate the manipulation task for a standard human operator, for example using transparent flexible materials, will be preferred. Finally, the possibility to include sensing capabilities, although non essential for all manipulation tasks, will be considered here as beneficial since it can improve the overall quality of a microgripper device. The inclusion of force sensors, for example, permits the accurate control of the grasping forces and therefore could be used to prevent potential damage to delicate samples. They could also provide extra manipulation functionalities such as the possibility to apply forces directly onto the samples in order to study their mechanical properties [13].

The actuation mechanism for the microgripper has to be chosen in order to satisfy all of the design requirements. It is now possible to discriminate between the actuation mechanisms briefly described in Chapter 2.

Generally, electrostatic and piezoelectric actuators have the advantage of low power consumption and high speeds, but they require high actuation voltages. The speed criterion is of less importance in biological manipulation because manipulation tasks are generally performed by human operators. High input voltages, however, can be a problem when manipulating specimens in a fluid environment. They produce electrolysis in water or any other conductive fluid and make the manipulation of particles extremely difficult due to, among other things, bubble formation. Electrolytic gas generation in conducting fluids is completely avoided at electrode potentials below 2 V and this must be the target in terms of actuation voltage for unencapsulated devices.

Electrostatic actuators also have other problems when operating in conducting ionic fluids. These include electrode potential screening and anodisation. To overcome this problem, the use of a high-frequency ac square wave signal (± V) with an average voltage of zero has been proposed [179, 180]. Since the square wave has the effect of rapidly alternating the anode and the cathode, there is no net build up of gas at either electrode. This can solve the problem in electrolytes with ionic strength of up to 10 mmol/L. However most biological media have strengths above 10 mmol/L and up to1 mol/L. In addition, if manipulation in and out of liquid was required, sticking problems would take place. Magnetic actuators integrate elements that are difficult to miniaturise, and result in expensive hybrid fabrication process with little flexibility[1]. Fluidic grippers produce large deformation and high forces but the models and techniques are still at the early stages of development. Electroactive polymers that deform by exchanging ions with the media are good candidates for fluid trapping (i.e. a cage), but have limited actuation control and are restricted to out of plane motion. In addition they cannot operate in air. SMA (shape memory alloy) actuated microgrippers could be used in biological media but they have poor actuation control, they often require hybrid fabrication processes, and have limited operating temperature range. They are ideal when high forces and displacements are necessary [72]. However, for single cell manipulation other mechanisms of actuation can be much more favourable.

Electrothermal actuation is the preferred mechanism for biological manipulation. Electrothermally driven microgrippers can be easily produced using standard

[1] Recent advances in magnetic actuators include the fabrication of polymer magnets which should provide an easier way to produce smaller magnets using standard microfabrication techniques [181]

microfabrication techniques in monolithic designs. When made out of conventional materials, such as single crystal silicon, polysilicon and metals, they operate at high temperatures and require high voltages. However, with the appropriate combination of polymeric and conductive materials, large deflections at low input voltages (<2 V) can be achieved. In addition, due to the low Young's modulus of polymers, only gentle forces are produced and the damage of delicate samples is unlikely. Polymeric electrothermal grippers demonstrate additional advantages such as good biocompatibility and transparency. The main drawback of this kind of actuation is the high power consumption, which can increase considerably in fluidic media due to increased heat losses to a fluidic ambient. That is why it is important to clearly understand during the design and modelling phase of a thermal actuator how to best raise the temperature using minimum power

3.1.1. Electrothermal actuators for microgripper applications

In Chapter 2, a general overview of thermal actuators integrated in different microgrippers was given. In general terms they can be divided as a function of the kind of motion they produce. Thus some actuators produce an out-of-plane motion (C-shaped or BVTA), two others produced in-plane motion (V- and U- shaped), and finally some of them combine in and out-of plane movement in a single device.

Out-of plane actuators have not been chosen for this work because, although they have demonstrated good holding capabilities, for example in cage-like devices [118], they cannot be used directly to move and position particles. This considerably reduces their flexibility and practical use as a manipulation tool.

Combined in- and out-of-plane motion, although potentially useful in some applications, has not been considered as an essential characteristic of a generic microgripper, and therefore is not developed in this work. Moreover it potentially has some disadvantages. On the one hand, the addition of a secondary degree of freedom can complicate the fabrication flow requiring many more mask processes. On the other hand, multiple degrees of freedom can add difficulties to real manipulation tasks. The latter is due to the limited focal depth of an optical microscope at high magnification that would require continuous refocusing as the actuator moved up and down.

In-plane actuators, however, generate an in-plane movement of the jaws of the microgripper that can facilitate, and be used directly for, any manipulation task. The reasons for that are twofold: First, the sample is always between the jaws and therefore in direct view of the objective of the microscope; second, for a given opening of the microgripper, the sample is always on the same focal plane as the jaws. For these practical reasons, it seems apparent that an in-plane actuator is a good solution for the design of a reliable microgripper able to hold, position and transport particles.

When looking at the main two types of in-plane actuators, U-shaped and V-shaped actuators, it can be seen that the main difference is the kind of motion that they produce. The first one rotates around a vertical axis at the anchors and induces an arc movement of the tips. This is essentially the movement required for a gripping action. The second type, however, produces a rectilinear motion. Thus, when using this kind of actuator for a microgripper application, the rectilinear motion has to be converted into rotational or gripping motion. This requires additional compliant mechanisms which complicates the design and fabrication.

In general, single V-shaped actuators produce smaller displacements when compared to U-shaped actuators. To some extend this is due to the fact that single chevron actuators are composed of long slender structures prone to buckling and stiction which limits the practical lengths of the beams. On the other hand, they produce more force than U-shaped actuators and, on some occasions, they are more thermally efficient as no heat is dissipated in a so called "cold arm". In terms of overall performance, both standard in-plane actuators have pros and cons [181, 182], and there is often a trade off between power consumption, ease of fabrication, peak temperature, generated force, and displacement. However, in both cases there is still room for optimisation [120, 174, 183, 184].

Leaving aside the typical V-shaped actuator, this work focuses on the thermal optimisation of a typical U-shaped actuator in order to produce a simple rotational, low temperature, and low power consumption driving mechanism that can be used in the design of a microgripper for biological manipulation.

3.1.2. Overview of the standard U-shaped actuator

The typical U-shaped actuator is generally built of a single conductive material that is used at the same time as a structural material and a current carrying resistor. This reduces considerably the choice of geometries which is limited by the conduction path.

The geometry of a standard U-shaped actuator is depicted in Fig. 3.1. The basic structure is composed of three beams called hot, cold and flexure arms. They have different lengths and cross-sections and are disposed in a parallel configuration, with the longer hot arm positioned facing the cold and flexure arms. Both beams are connected to each other at one end, and to an insulated substrate via the anchors at the other end. The hot arm is the active heating part of the structure whereas the other arm provides 1) a return path for the electrical current and 2) mechanical amplification and flexibility via the flexure.

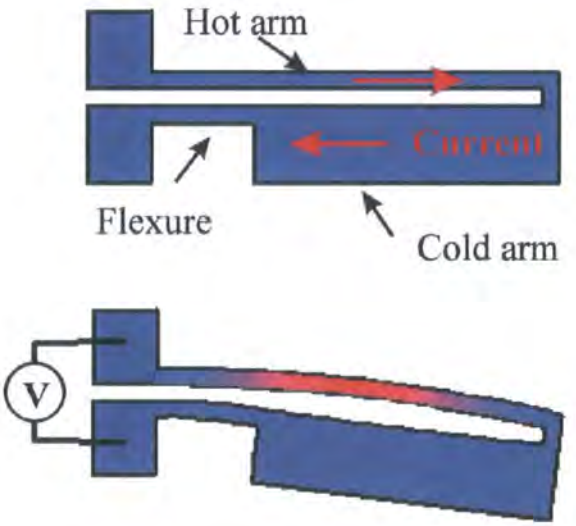

Fig. 3.1: Sketch of a standard U-shaped thermal actuator

When a current is applied to the anchors, the hot arm, which has a smaller cross section and is therefore more resistive, will heat more than the cold/flexure arm, and so will expand more. Since both arms are connected at one end, a differential expansion will result in a net rotational motion around the z axis. In order to keep the actuator in a particular position, a constant current has to be supplied to the system, which is dissipated in the form of heat.

The net expansion and deflection depends mainly on the temperature difference established between the hot and cold/flexure arms and it is a function of the driving power, the geometry, the environmental conditions, and the materials used. The exact relationship between all of these parameters is not simple and requires the solution of a highly coupled electro-thermo-mechanical problem. Thus, since Guckel proposed the first U-shaped actuator in 1992 [165], numerous authors have studied the behaviour of this type of actuator, trying to establish the best geometry and conditions to obtain maximum performance . This has been done using analytical as well as numerical approaches.

Key geometrical parameters are the total length of the actuator, the relationship between the lengths and widths of the arms, and the separation between them. For a given temperature change, the deflection of the actuator will be proportional to its total length, and will be larger for actuators with narrower hot arms and with smaller separations between hot and cold arms [185]. Also there will be a critical length for the flexure. If it is made too short, the device will become stiffer and will produce lower deflections. If the flexure is made too long and thin, the effective difference in temperature between the arms will be reduced due to extra heating generated in this region of the cold/flexure arm. Finally, particular geometrical configurations will affect the way the thermal actuator loses heat to the ambient, and this will have to be taken into account if thermally efficient devices are to be achieved.

Electrothermal actuators consume considerably more power than comparable electrostatic or piezoelectric actuators, and therefore it is important to look at the thermal efficiency of the device. Various works have been published that optimise the basic U-shaped actuator for different applications.

On some occasions, the optimisation consists of modifying some environmental conditions in order to improve the heat loss mechanism. An example of this is the inclusion of a trench in the substrate underneath the hot arm that reduces considerably the heat losses to the substrate. With this insulation, the temperature difference within the cold arm which readily loses heat to the substrate is maximised [186]. Another example demonstrated by Mankame et al. [187] is the inclusion of a thermal insulator material between the thermal ground and the base of the actuators. This increases the

overall temperature of the device but produces a more efficient structure as it minimises the heat losses along the actuator to the anchors. The latter is generally the dominant heat loss in thermal actuators.

In other implementations, optimisation through the modification of the basic design is proposed. These design modifications include the addition of low resistance materials on the cold arm that reduce the total resistance of the arm and therefore the heat generated [188], and the inclusion of two hot arms to eliminate the parasitic heating of the cold and flexure arm [167].

Finally, another way to increase the deflection for a given input power in electrothermal actuators is the use of materials with high coefficients of expansion. In this case, the combination during fabrication of conductive and polymeric materials is required but a major flexibility on the design is achieved. Due to the high CTE and relatively small Young's modulus, polymeric thermal actuators have the potential to generate larger displacements but at the expense of lower output forces. Different polymeric actuators have been successfully demonstrated in the works of [119, 123, 124, 169, 189, 190], where more efficient devices have been proposed. Polymers have been included in the design of nearly every thermal actuator: in a standard U-shaped actuator [123], a two hot arm actuator [119], a C-shaped actuator [169] and a chevron actuator [189].

3.2. Microgripper design

Fig. 3.2 shows the schematic of the microgripper proposed in this thesis. The design is a compliant mechanism that deforms in a particular controlled manner when a current is applied. The design consists of two parts: an actuation structure and a pair of extended arms (prongs). The actuation structure, composed of two thermal actuators positioned face-to-face, is able to move in-plane when a current is passed. The extended jaws are a pair of cantilever beams that amplify the motion of the actuators and act as end effectors. Both parts, the actuator and prongs, are built of the same structural material, the polymer SU8 [191], and are fabricated at the same time. This produces a single monolithic structure. The overall size of the structure will depend on the range of deflections and forces required for each application.

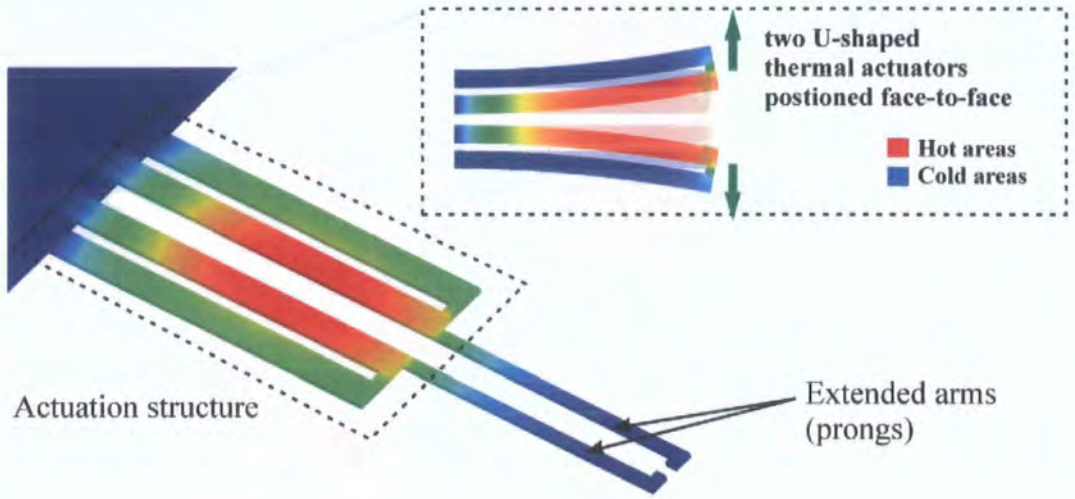

Fig. 3.2: Schematic of the proposed microgripper

3.2.1. New architecture of the thermal actuators

The principle of operation of the microgripper is basically the well established U-shaped thermal actuator. The actuators are made of a multi-layer structure which encapsulates a conductor between two or more layers of dielectric material.

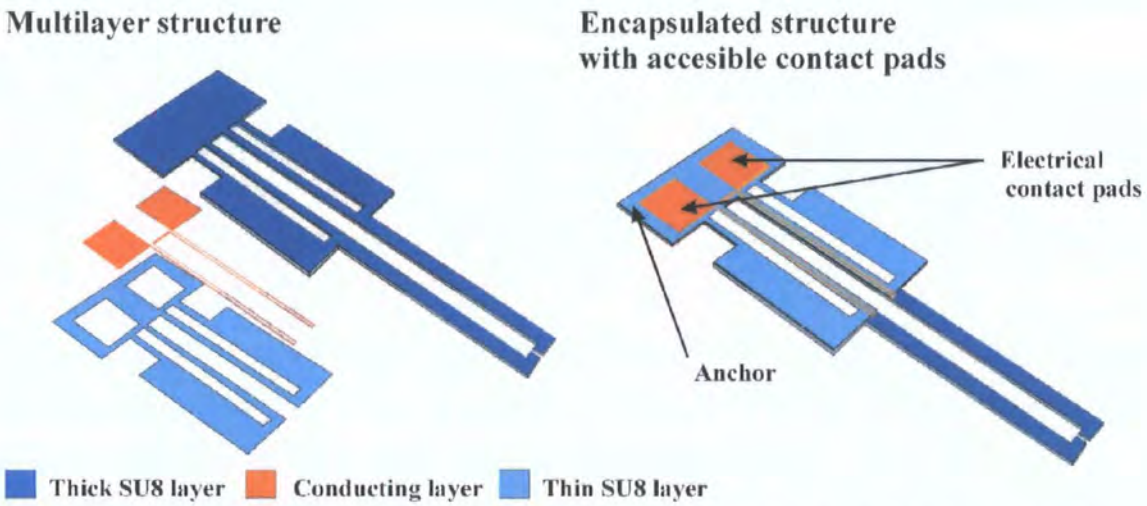

Fig. 3.3: Basic 3-layer structure composed of SU8-metal-SU8 (left). In the final device (right), the metallisation is encapsulated between two layers of SU8.

A generic multi-layer structure (Fig. 3.3) would consist of a thick layer of polymer (SU8) which forms the anchors and the microgripper and gives structural rigidity to the whole structure, one or more thin conducting metallic layers (gold) patterned into heating electrodes, and finally one or more thin polymer layers (SU8) that encapsulate and insulate different metallic layers.

The choice of this particular combination of dielectric and conductive materials has enabled the design of a much more flexible actuator geometry which is not limited anymore to a particular conduction path. As opposed to standard U-shaped actuators (Fig. 3.4 (a)), with the new architecture (Fig. 3.4 (b)) the asymmetrical heating is achieved by embedding a resistor in just one arm of the actuator and not entirely relying on the geometry of wide and narrow beams (arms). This, for example, makes it possible to design a microgripper such as the one shown in Fig. 3.2 where both arms have identical external dimensions. When a current is passed through the conducting layer, the arm containing the resistor (hot arm) will heat more than the other arm (cold arm) and so will expand more. As no heat is generated in the cold arm, the difference in temperature between both arms will be maximised. In addition, the fact that the structure is polymeric minimises the heat losses to the anchors, which increases the overall temperature of the system per watt of input power.

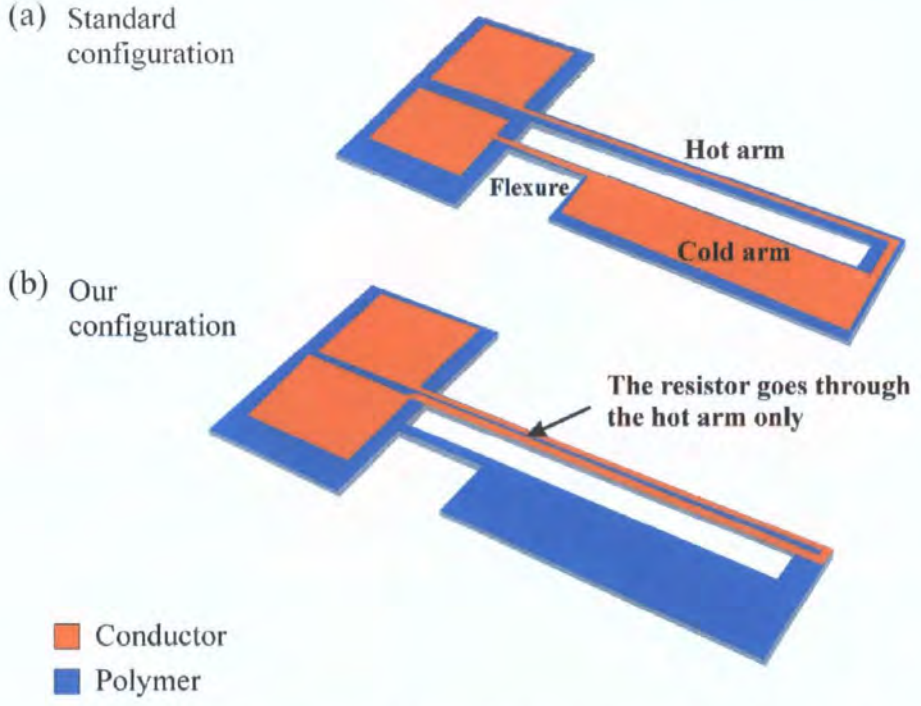

Fig. 3.4: (a) Standard U-shaped configuration actuator where the resistor goes through hot and cold/flexure arms; (b) Actuator configuration where the resistor goes through the hot arm only.

3.2.2. Microgripper operation

Multiple configurations exist for the microgripper, some examples are shown in Fig. 3.5.

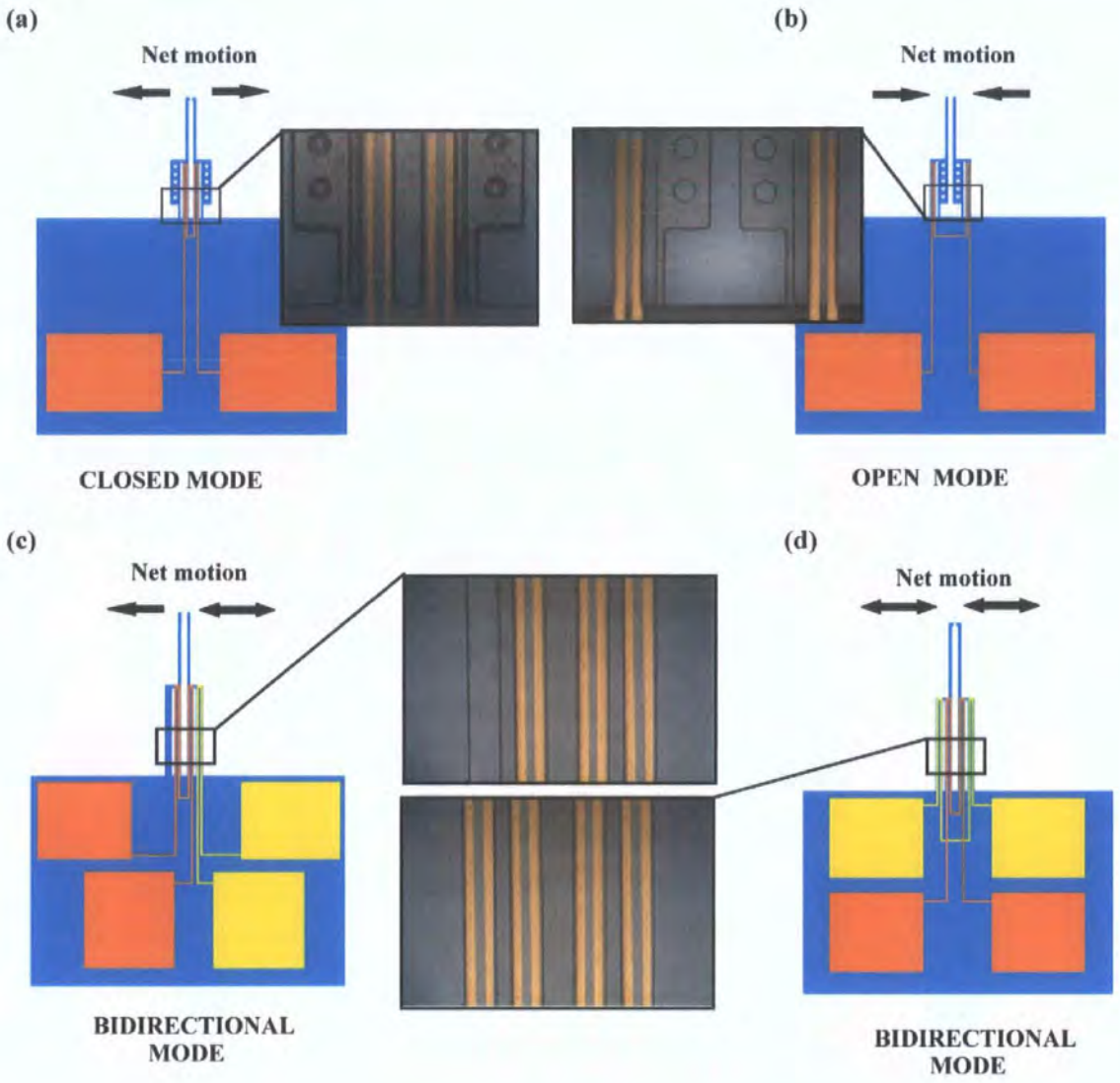

Fig. 3.5: (a) Microgripper in closed mode configuration (photo detail of the resistors embedded in the internal beams of the structure); (b) Microgripper in open mode configuration (photo detail of the resistors embedded in the external beams of the structure); (c) Microgripper in bidirectional mode configuration (photo detail of the resistors embedded in the internal beams of the structure and in one of the external beams); (d) Microgripper in bidirectional mode configuration (photo detail of the resistors embedded in both the internal and external beams of the structure).

Fig. 3.5(a) shows a configuration where the two hot arms of the actuators are facing each other in the internal part of the structure. Thus when a current is passed, the microgripper opens from its original position increasing the gap between the prongs. With this closed mode configuration, the electrical power is needed only for the gripping and release operations and no actuation is needed when holding the object. Fig. 3.5(b) shows a second possible layout. In this case, the two cold arms which have the common flexure/cold arm structure are facing each other in the internal part of the structure. When a current is passed, the microgripper closes from its initial position, reducing the gap between the prongs. With this open mode configuration, the actuators

need to be operated continuously to ensure the gripping of the sample. Fig. 3.5(c) shows a layout that combines both open and closed mode configurations, and produces a microgripper with bidirectional motion, at least in one of the prongs. The orange circuit in the image allows for the opening of the prongs when a current is passed. The yellow circuit in the image allows for the closing of the right hand prong when a current is passed. Finally, Fig. 3.5(d) shows a layout that combines both open and closed mode configurations, and produces a microgripper with bidirectional motion in both prongs. When a current is passed, the orange circuit allows for the opening of the prongs while the yellow circuit allows for the closing of the prongs. It is worth noting the orange and yellow circuits are electrically independent. In Fig. 3.5 (c) and Fig. 3.5 (d) the cold arms, in the external part of the structure, have the same overall geometry as the hot arms.

In the configurations presented so far (except Fig. 3.5(c)), the hot arms of both actuators of the microgripper belong to the same circuit. However another set of configurations could be conceived which use independent electrical circuits for each arm.

Particular in-plane and out-of-plane geometries have been chosen for the tri-layer structures (polymer–metal–polymer) fabricated in this thesis (more detail in the fabrication section). However, larger deflections would be obtained at the same power by increasing the total length (e.g. increasing the length of the prongs) and/or changing some of the materials, and there is clearly scope for further optimisation.

At first sight, four main advantages are provided by this new configuration of the thermal actuator:

- Bidirectional movement
- Free volume/ surface space to incorporate force sensors, micro channels or other systems that increase the functionality of the microgripper
- Increased power efficiency due to the insulation of the anchors (reducing the overall heat losses to the thermal ground)
- Increased thermal efficiency of the system through the elimination of the heat produced in the cold/flexure arm. A thermally efficient device maximises the

asymmetrical heating for a given input power. (The thermal efficiency of different devices is discussed in detail in Chapter 5 section 5.5.2)

The last point is of particular relevance because the maximum achievable deflection of the microgripper is ultimately limited by the thermal damage of the heated parts of the device.

3.3. Microsystems technology overview

Microsystems technology enables the fabrication of complex 3D systems using batch fabrication techniques. With dimensions in the meso-, micro- and nanoscales, this technology combines multiple engineering disciplines such as electronics, mechanics, optics and fluidics. In the early years, microfabrication was almost exclusively based on thin and thick film processes and materials borrowed from the IC industry. Nowadays, however, new materials, processing techniques and design methods are developed specifically for microsystems devices.

3.3.1. Techniques and material selection for electrothermal microgrippers

In microfabrication there are three main standard routes to create three dimensional structures: bulk micromachining, surface micromachining and replication techniques. Bulk micromachined structures are fabricated by removing material directly from the substrate. In surface micromachining the structures are created by sequentially depositing and etching layers of different materials on top of a substrate. Replication techniques involve the casting or imprinting and subsequent peeling away of a material from a microfabricated mould.

Microfabricated structures are formed using a sequence of individual fabrication steps. These steps can include wafer cleaning, lithography, doping, thin film metal deposition, etching, electro-deposition, soft lithography, injection moulding and hot embossing. A variety of materials can be used during the fabrication process.

A typical IC fabrication flow uses a limited number of materials. These are chosen primarily based upon their electrical properties. Microsystems devices however,

integrate multiple and novel materials that can be used as substrates as well as structural materials (see Table. 3.1).

Table 3.1: Microfabrication materials

MEMS materials	
Substrate	Silicon
	GaAs
	Metals
	Glass
	Sapphire
	Ceramics
	Plastics (polymers and other organics)
Deposition	Silicon
	Silicon compounds
	Metals
	Ceramics
	Plastics
	Other biomaterials

When designing a prototype, it is important to bear in mind that the choice of material is determined as much by the design of the device itself as by the possible microfabrication routes. The materials must allow the device to work within the technical specifications (range of displacements, temperature, voltage requirements, etc.). The materials must also allow for a reliable fabrication process, and be cost effective. This common sense approach to the design process is the main difference between a 'one-off' demonstrator prototype that intends to prove a fundamental principle, and a prototype with a commercial aim.

Furthermore, in the design of microtools for biological application aspects such as biocompatibility or chemical compatibility have to be taken into account. Biocompatibility is the ability of a material to interface with a natural substance without provoking a natural response. There are a few studies about the biocompatibility of MEMS materials that can be used as guidelines.

3.3.1.1. Silicon

Silicon is used as both a substrate and a structural material. Silicon microfabrication was a well established technique in IC processing and was used to produce the first microgripper in 1990 [192]. Nowadays, silicon in its different forms is still the most

widespread material used in microfabrication because, in addition to its excellent physical properties [193] and the wide range of existing and well known silicon based processes (eg. MUMPs [194]) it opens up the possibility of integrating microelectronic and microfabricated devices on a single die. Silicon is easy to etch using both wet and dry processes which can show either anisotropic or isotropic etching.

As shown in the review chapter, a few silicon (or polysilicon) based microgrippers have been reported. The main problem when using silicon based thermally actuated microgrippers for biological applications is the relatively high operating temperatures which are required, the electrical conductivity of the structure and the high output forces associated with a high Young's modulus. As shown in [124], these problems could be overcome to some extent by using Si-polymer composites, where the added complexity to the fabrication processes could counteract some of the potential benefits.

3.3.1.2. Metals

Commonly used metals such as gold, platinum, nickel and aluminium can be easily deposited by evaporation, sputtering and/or electroplating. In microfabricated devices they can be used for electrical interconnects or electrodes, and as structural materials.

Metallic thermal actuators provide several advantages when compared to silicon devices. They have a higher CTE and therefore undergo larger deformations for a given temperature difference, or equivalently for a given stroke they require less power. They have more stable electrical properties which are independent of doping levels. They are simpler and less expensive to fabricate, and they can be deposited readily on a wide range of substrates, e.g. a circuit board.

However, there are three main reasons why metallic thermal actuators are not integrated in microgrippers for biological manipulation. The first one is that the structure is intrinsically conductive. Thus, when closing the prongs a potential difference is created across, and a current flows through, a biological sample. This could damage the specimen. The second is that metals are generally good conductors of heat. This means that in an all-metal device, it is difficult to thermally isolate the actuators from the jaws.

It is therefore possible that the jaws can reach relatively[2] high temperatures [195] which could also damage any specimen. Finally, in order to make practical microgrippers, high metal thicknesses up to 150 μm are required. These require high aspect ratio polymers moulds for an electroplating process.

3.3.1.3. Polymers

Polymer fabrication has several advantages over silicon and glass micromachining. From a commercial perspective, polymers are highly cost effective mainly because their bulk price is cheaper, and because of the ease and the speed with which they can be processed. Furthermore, in many biological and medical applications disposable devices are mandatory, which stresses the need for low cost materials and processes.

There are two main routes to polymer fabrication: replication techniques and direct fabrication (i.e. photolithography on a solid substrate). Replication techniques include processes such as injection moulding, hot embossing or casting and are mainly based on macroscopic manufacturing processes adapted to the microscale. These are very good techniques for producing large volumes of relatively simple chips. However they are typically not compatible with silicon processing and this can be difficult for the production of hybrid structures.

Table 3.2: Some material properties of a sample of polymers used in microfabrication

Material	Tg [°C]	Melting /degradation [°C]	CTE [ppm/°C]	Thermal conductivity [W/mK]	UV-transparency	Visible light transparency	Effect organic solvents
PMMA	106	205	70	0.19	opaque	good	soluble to many
PDMS	-125	400	310	0.15	>230 nm	good	swelling with many
SU8	240	>340	50-102	0.2	>350 nm	good	mostly no effect
Polyimide	400	620	3	0.2	opaque	good	mostly no effect

Polymers can be spin deposited with a wide range of thicknesses (sub micron to millimetre). They can act as standard photoresists (e.g. for etch masking) or as a structural material in a microsystems device. Polymers which can be patterned for

[2] Relative to the maximum temperature that a biological specimen can resist. (generally temperatures above 60 ° C would produce irreversible damage)

structural applications are particularly useful for microfabrication. The general material properties of commonly used polymers can be found in Table 3.2

PMMA (polymethylmethacrylate) behaves as a positive resist and is widely used in different areas of microfabrication particularly in hot embossing. However, it cannot be patterned using UV lithography and requires X-ray, electron beam or ion exposures via expensive and specialised equipment.

Polyimides (PI) resists can also be used as structural components for microdevices. Some polyimides are photodefineable using standard lithography and etching techniques. Photodefineable PIs are however more limited when compared to other negative resist such as SU8 that allow for higher aspect ratios and layer thicknesses.

PDMS is an elastomeric polymer with good biocompatibility and is biodegradable. One of its main drawbacks is its poor chemical stability against organic solvents [196].

SU8 is now a widely used negative resist for high resolution/ aspect ratio applications. It has good mechanical properties, is chemically stable and is biocompatible. Various microgrippers have been reported which use SU8 as a structural material [97, 119, 123, 124]. SU8 has been selected for the fabrication of the microgripper in this thesis. A more detailed description of the material, properties and processing is given in the following section.

3.4. Microgripper fabrication

The operation of the microgripper described in section 3.2 requires that the actuators and prongs are completely overhanging, i.e. that the substrate underneath the device is eliminated. In addition, it is desirable that the range of displacements is as large as possible. Longer actuators can be used to produce larger displacements but apply less force. This is not a problem since the microgripper is intended to work primarily in low or zero handling force situations.

The actuator lengths chosen for the different designs presented in this thesis are 2000 μm and 1500 μm with a gap between the arms of 60 μm. The thicknesses of the devices have to be consistent with the size of the samples to be manipulated (20 –

150 μm). In this thesis two thicknesses have been chosen, 30 μm and 100 μm. Finally, in order to optimise the use of the device layout and be able to incorporate additional features such as force or displacement sensors, the metallisation layer (heater) should be insulated from other parts of the device. Moreover to avoid undesired out-of-plane bending of the devices the resistor should be ideally centred within the thickness of the device. Both things can be achieved by encapsulating the resistor within the SU8 polymer. The fabrication processes in this thesis have been chosen to accommodate all of these geometrical and operational requirements.

In this thesis, two fabrication processes that produce stress-free polymeric SU8 structures with encapsulated gold resistors and accessible electrical contacts pads are presented. Three sets of polymeric microgrippers using three different fabrication flows will work as a demonstrator for the manufacturing processes.

3.4.1. SU8 as structural material

The polymer SU8 is the structural material for the microgripper and is responsible for giving mechanical robustness and chemical stability to the whole structure and in particular to the support anchors. The viability and overall quality of the fabricated microgrippers relies upon the successful processing of this polymer

3.4.1.1. SU8 background

SU8 is a chemically amplified solvent-developed, near-UV, negative photoresist that was first developed and patented by IBM [197] in 1989 for the fabrication of printed circuit boards and packaging. A few years later, in 1996, SU8 was successfully adapted for microsystems fabrication [198, 199]. Now, SU8 is broadly used in a range of applications. It is used either used structurally or as a mould in micromolding [200], for the fabrication of microparts [201], microvalves, protective layers for surface acoustic wave devices [202], inkjet printer heads, image sensors, AFM probes, microchannels in microfluidics [203], biosensors [204], and microreactors to name but a few. This diversity of applications has been possible because SU8 combines very good physical and chemical properties with the ease of processing and a low cost.

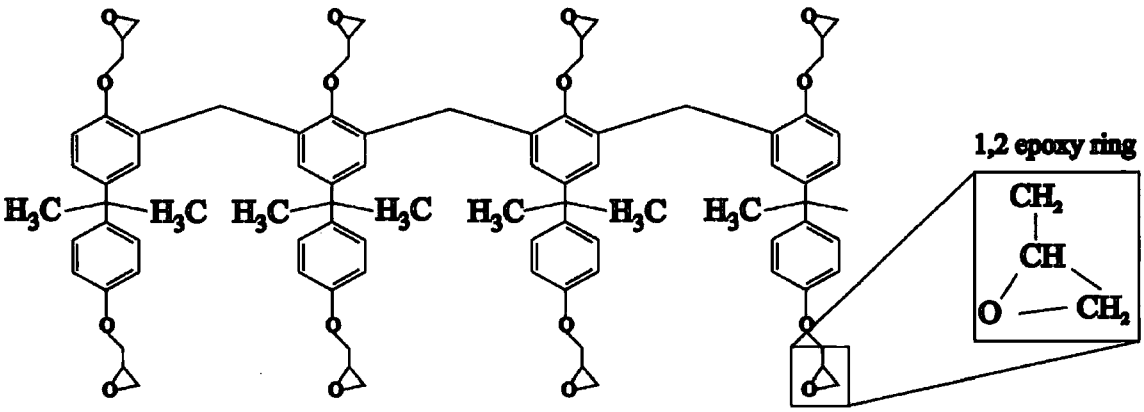

Fig. 3.6: Idealised structure of the SU8 monomer

SU-8 photoresist consists of an epoxy resin (EPON®) dissolved in an organic solvent, along with an onium salt which acts as a photoacid generator.

- The epoxy resin EPON® SU8[3] is the main constituent of the material and it consists of a multifunctional glycidyl ether bisphenol-A novolac [199]. The idealised structure for a single molecule of the polymer is shown in Fig. 3.6. On average, a single molecule contains 8 reactive epoxy groups, hence the "8" in SU8. The 8 functional side groups provide a very dense three dimensional network of crosslinking when the resin is cured.

- Two organic solvents can be used for the formulation of SU8: gamma-butyrolacetone (GBL) for the standard SU-8 and cyclopentanone for the SU8-2000 series supplied by MicroChem [191].The quantity of solvent determines the viscosity and thereby the range of thicknesses achievable with a single spin [198].

- The photoacid generator (PAG), present in a low mass percentage (2-10% of the weight of the SU8), consists of a mixture of triarylsulfonium (TSS)/hexafluoroantimonate salt4. This salt mixture is the initiator of the photo transformation of the SU8 from a low-molecular-weight material to a highly crosslinked network. Upon UV-exposure, the triarylium-sulfonium based salt is converted into a strong acid and some side products. Then, during post-exposure

[3] Available from Shell Chemical

[4] CYRACURE® UVI from Union Carbide

baking (PEB), the strong acid catalyses the polymerization (or crosslinking) of the polymer. The baking is necessary to accelerate the crosslinking reaction. The glass temperature (Tg) of the uncured SU8 is approximately 50°C and therefore, at ambient temperature (Tambient < Tg) the molecular motion would be effectively frozen and any reaction would be very slow. In the case of SU8, the polymerisation is achieved by a process called cationic polymerisation [199] where the epoxy rings are opened and cross-linked using an acid as a catalyser.

- During PEB the acid reacts with the epoxy side groups producing radicals attached to the backbone of the SU8 molecule. Upon a cross-linking reaction between two such radicals, from the same or a different molecule, the acid molecule is regenerated and can induce further polymerisation (chemical amplification) [205, 206].

SU8 has a high functionality, which yields good sensitivity, and a low molecular weight, providing high contrast and high solubility. These properties combined with a low optical absorption in the near UV spectrum range makes SU8 an ideal candidate for the fabrication of high aspect ratio structures using standard UV lithography. Layers of polymer up to 2 mm [201] in a single spinning process, with high aspect ratios of up to 190:1 have been demonstrated [207]. The use of SU8 allows the production of thick and high aspect ratio structures faster and less expensive than other techniques such as X-Ray LIGA [208], microstereolithography [209], and DRIE [210].

Although, the best properties of the SU8 polymer were found in thick and ultra-thick photoresist applications where it is used as a mould for etching or electroplating [201, 211] its potential as a structural material is also well recognised.

Once the SU8 is crosslinked it becomes mechanically and thermally stable and resistant to most organic solvents and acids. Unlike other polymers, SU8 is compatible with standard Si processing which adds great flexibility to the kind of devices that can be produced at a reasonable cost [212]. It is also compatible with most of the chemicals used in analytical applications, which is why it is used widely in microfluidics.

SU8 can also have very good optical properties. Pure SU8 exhibits an optical transparency greater than 98% from 500 to 850 nm. Its transparency enables relatively good optical detection [213] through the layers and in some cases, the creation of optical planar waveguides and lenses [214].

Finally, the surface of the SU8 includes some unreacted epoxy groups that can be used to functionalise it. This, together with its low Young's modulus (30 times smaller than silicon) and its biocompatibility makes it interesting as a cantilever material in biological sensors.

The downside is that SU8 does suffer from some noteworthy fabrication limitations which include adhesion selectivity, mechanical stress, resist stripping difficulties, a large coefficient of expansion, and a low degradation temperature. However, as will be shown in the following sections, these limitations can also be positively exploited by the careful choice of device design, process flow and materials.

3.4.1.2. Single layer SU8 processing and material properties

Fig. 3.7 illustrates a basic process flow for the fabrication of a single SU8 layer. A typical SU8 process consists of five steps: deposition, soft baking, exposure, post exposure baking (PEB), and development. The easiest way to deposit SU8 on a substrate is by spin coating. The spin curves depend on the composition and viscosity of the type of SU8 used. The soft baking step is necessary to drive off the solvent in the layer and the bake time depends on the intended layer thickness. After baking, the SU8 is exposed to UV light through a mask which includes clear and opaque areas. Once the crosslinking of the layer is initiated by this exposure, the process is catalysed with a PEB. Finally, the unexposed resist is removed with a developer (GBL or PGMEA), whilst the exposed crosslinked SU8 remains insoluble.

Although conceptually simple, the processing of SU8 is a challenging task because the overall quality and properties of the fabricated structures are very sensitive to the processing conditions [215-223].

It has been reported that soft-baking conditions of a thick SU8 film are critical for its lithographic quality [223, 224]. It has been demonstrated that low soft-bake temperatures increase the exposure sensitivity, reduce the stress between the SU8 and the substrate and minimise crack formation [217]. Also, although the level of solvent retained in the layer is identical, a two step soft-baking produces better results than a single baking step [225].

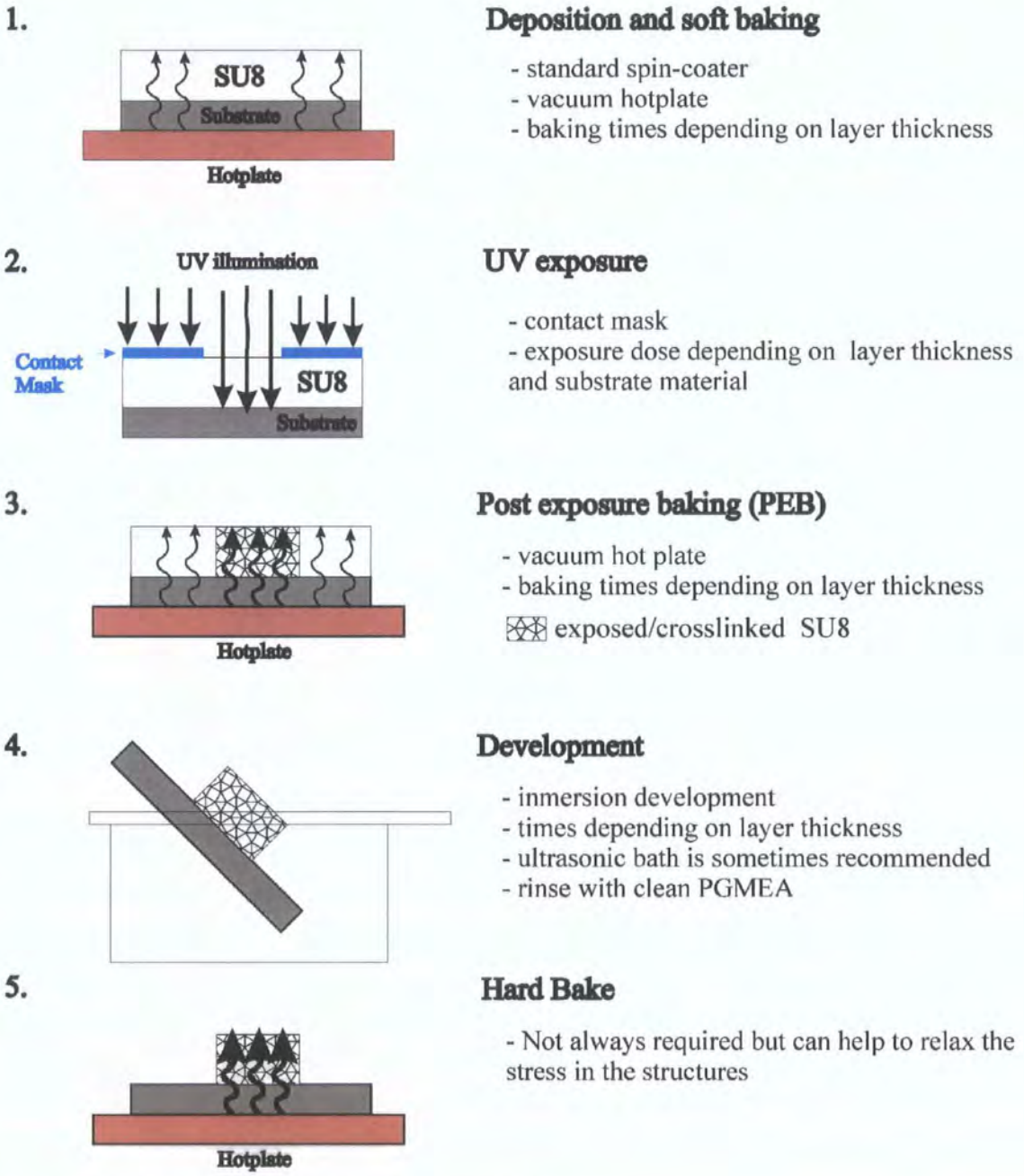

Fig. 3.7: Typical process flow for a single layer of SU8

The energy and the uniformity of the exposure is also an important parameter to control for good pattern quality [219-221, 223, 226]. If long and high exposure doses (> 300 mJ/cm^2) are applied to the layer, a thin solid crust due to the heating can form on the top surface, causing loss of resolution (Fig. 3.8). A way to alleviate the problem is to divide the exposure in 10 to 15 seconds intervals with a 60 seconds resting time in between.

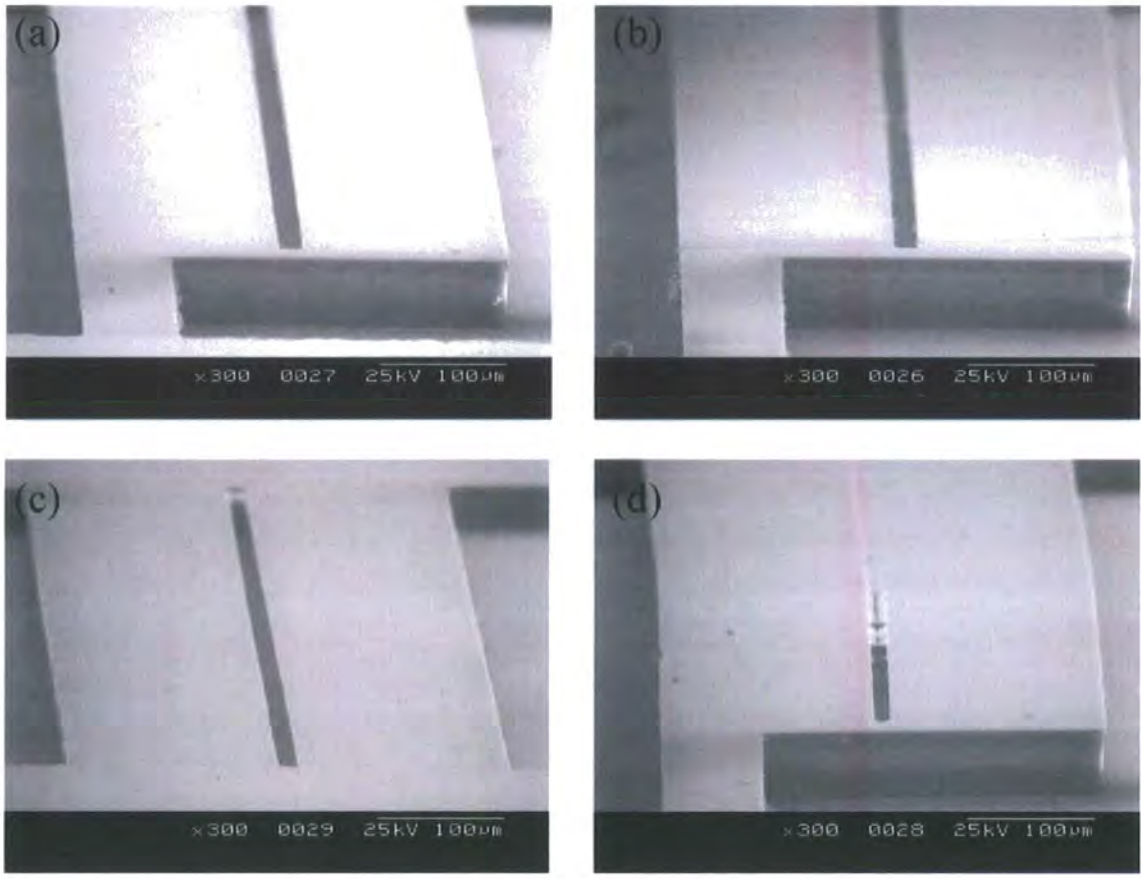

Fig. 3.8: Same feature processed with the same masks and parameters except the time of the UV exposure. (a) 12 seconds (b) 15 seconds (c) 18 seconds (d) 21 seconds. Samples (c) and (d) started to detach from the substrate.

As with other photoresists, the exact exposure time and dose is chosen to depending on the thickness of the layer, the quality of the mask and the substrate reflectivity. Overexposure can lead to "reflective notching" which is caused by the reflection of light from the substrate underneath the exposed areas into the adjacent non-exposed ones. Low exposures can induce a low level of crosslinking at the substrate layer interface which causes poor adhesion.

Finally, thickness variations within the layers due to "edge bead" and soft bake conditions, can also affect the contact between the mask and the SU8 layer which can cause exposure non-uniformities. This causes residual stress, cracks and poor adhesion. The PEB is the heating process that accelerates the crosslinking of exposed areas rendering them insoluble to organic developers.

To obtain the desired SU8 microstructures, it is important to understand how the temperature affects the crosslinking and development of the resist. In principle, the use of temperatures above the T_g of the unexposed SU8 should be avoided in order to decrease the diffusion of the acidic centres into unexposed areas, which would affect the accuracy of thin line pattern.

However, the value of the polymer's T_g begins to grow rapidly as it cross-links and consequently the diffusion rate of the acid decreases dramatically. For a fully cross-linked polymer the T_g exceeds 200 °C [227]. Using a two step PEB can help to ensure that the polymerisation process happens in the areas where the initial acid concentration was exceeding a certain threshold.

The development is an important step in features with a high aspect ratio which often requires optimisation of the time, and strong agitation. A hard baking process is sometimes added to completely finish the crosslinking of the SU8 and guarantee the size stability of the structures [198]. All of these processing aspects have been taken into account during the development of the fabrication processes presented in this thesis.

Another important question is how the processing conditions affect the material properties of the SU8 [228]. This has been extensively studied by Feng et al. in [216, 229] where the planar and volumetric thermomechanical properties have been calculated. Table 3.3 shows some values of the material properties calculated by different authors. Leaving aside the particular testing equipment and methodologies, the noticeable spread of values reported by different authors can be mainly attributed to the differences in the fabrication conditions. However the affect of a variation of the CTE on the performance of the microgrippers will be studied in Chapter 6.

Table 3.3: Thermomechanical properties of SU8

Property	Type	Value	Ref.
Young's Modulus [GPa]	in-plane	4.02	[198]
	in-plane	4.95	[254]
	in-plane	3.2	[130, 216]
	out-of-plane	5.9	[216]
Poisson ratio	in-plane	0.33	[216]
	out-of-plane	0.29	[216]
Shear Modulus [GPa]	in-plane	1.21	[216]
	out-of-plane	0.3	[216]
Tensile strength [MPa]		34	[130, 254]
(yield stress)		106	[216]
Elongation at break [%]		8	[216]
Residual stress on Silicon [MPa]		19-16	[198]
Coefficient thermal expansion (CTE) [ppm/K]	in-plane	87.1	[228]
	in-plane	102	[216]
	out-of-plane	278	[216]
	volumetric	452	[216]
Thermal conductivity [W/ mK]		0.3	[229]
		0.2	[206]
Density [Kg/m^3]		1218	[216]

3.4.2. Multilayer metal/polymer processing

The main goal of this fabrication work was to produce completely released SU8 structures with integrated electrodes using standard surface micromachining processing and equipment. In order to reduce the complexity of the fabrication process, a key aim was to minimise the number of masks required.

Two different fabrication flows have been developed and will be presented in the following sections. In essence, the two fabrication processes consist of 4 fabrication steps in a 3-mask surface micromachining process. The two processes are illustrated in Fig. 3.9 and Fig. 3.10. The deposition and patterning of the 3 active layers is qualitatively the same. Only the pre-coating of the wafer and the release steps are different between the processes.

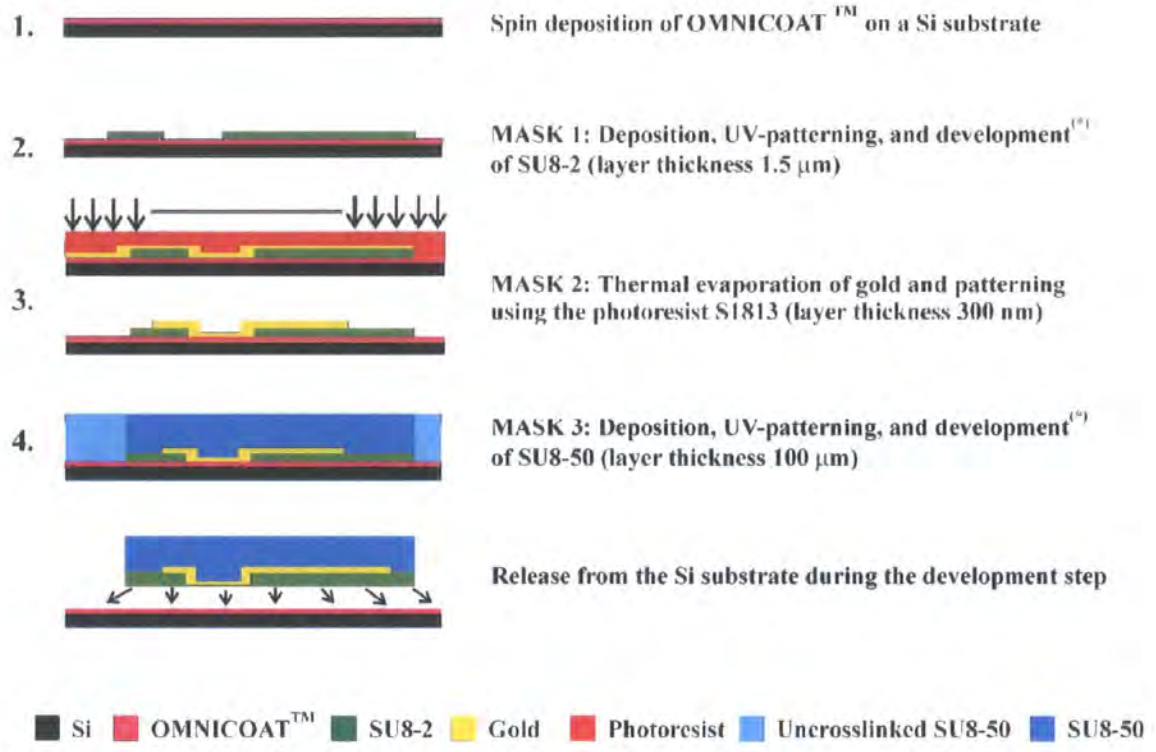

(*)The SU8-2 and SU8-50 are processed as explained in Fig. 3.7

Fig. 3.9: Process 1: Fabrication process based on diminished adhesion.

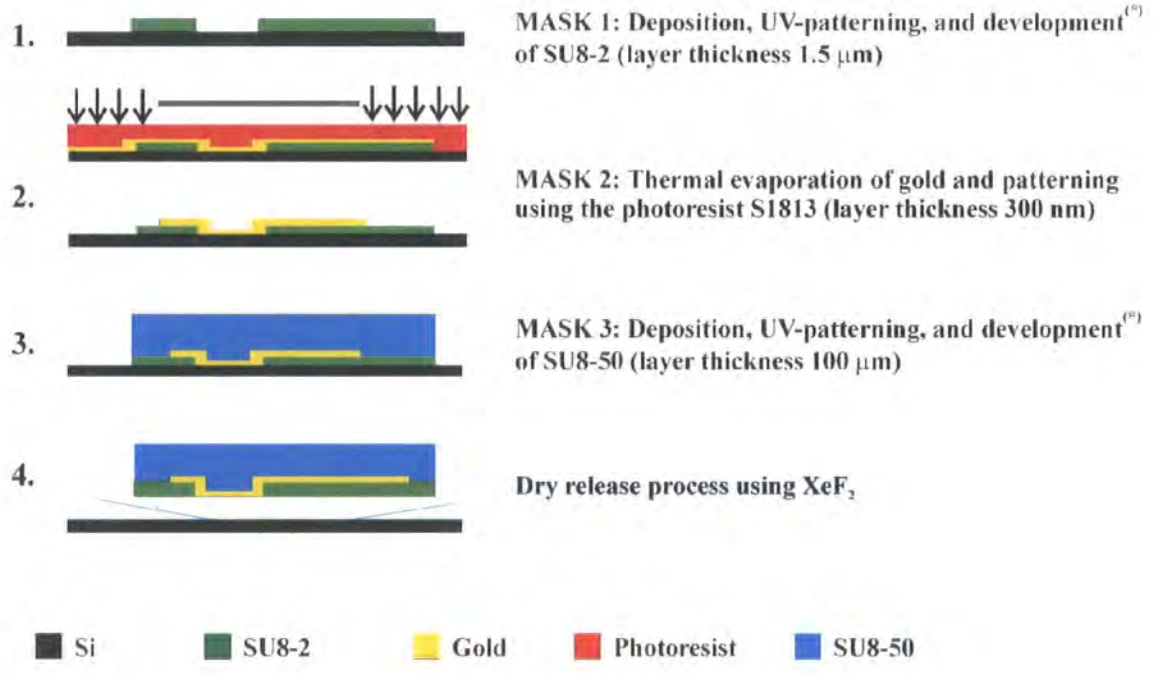

(*)The SU8-2 and SU8-50 are processed as explained in Fig. 3.7

Fig. 3.10: Process 2: Fabrication using XeF_2 release.

3.4.2.1. Mask fabrication

Both processes use the same mask patterns. Mask 1 and Mask 3 define the whole structure of the microgripper and Mask 2 defines the contact pads and the heaters. Fig. 3.11 shows a 3D representation of the processes and the patterns defined with each mask.

Mask 1 and Mask 3 are identical in the layout of the actuators but differ in the layout of the anchor. Mask 1 defines the access holes for the electrical connection whilst Mask 3 provides the mechanical support to the contact pads and a stress release path. Mask 2 defines the contact pads and the heaters embedded in the SU8 structure. SU8 is a negative tone resist and therefore the structure of the microgripper will be defined by the clear areas in the mask whilst the dark areas will protect the SU8 from UV exposure. The masks used in this thesis have been made in-house [230], using a camera that photoreduces a macroscale printed pattern into a microscale one on a glass emulsion plate with a minimum feature size of 20 μm.

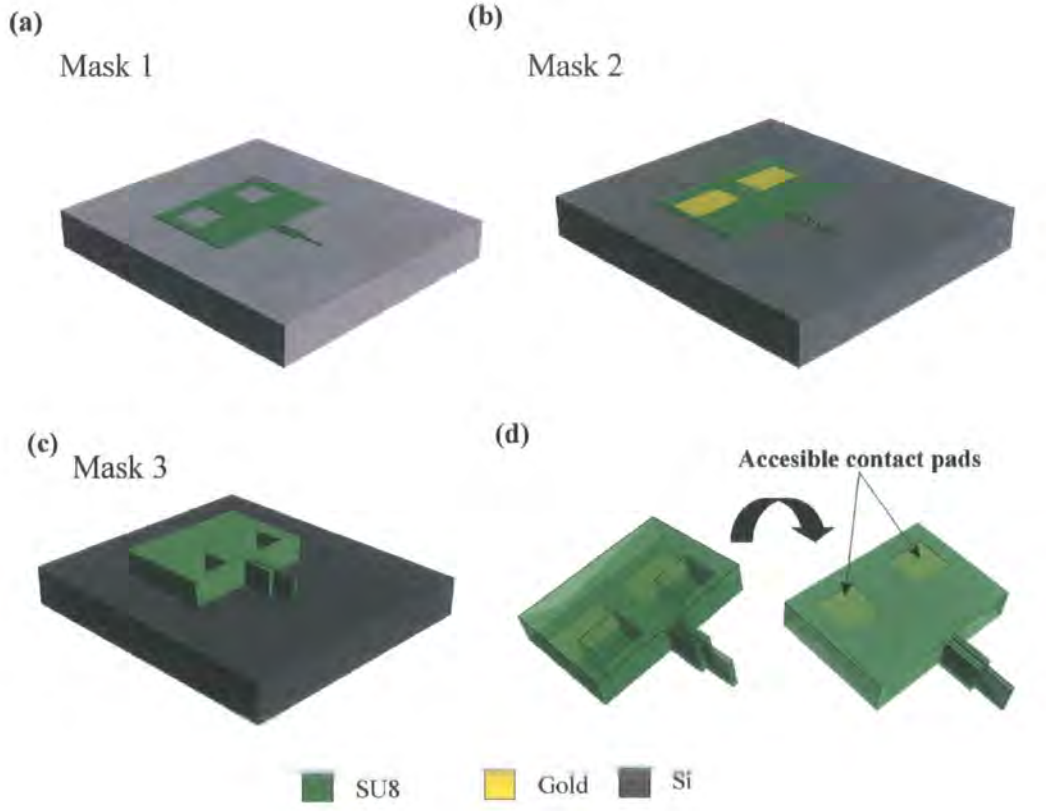

Fig. 3.11: (a) Silicon substrate with thin SU8-2 patterned on top (mask 1); (b) Conformal deposition of evaporated gold and patterning (mask 2); c) Deposition and patterning of the thick SU8-50; (d) Release of the structure leaving the contact pads accessible (note that the contacts pads are placed on what before was the bottom of the structure in contact with the Si wafer)

3.4.2.2. Conducting layer

In order to produce electroactive devices, the SU-8 polymer (which is intrinsically a dielectric), has to be provided with electrically conducting elements. Different approaches can be used to achieve this.

One is the incorporation of conductive particles in the SU8 polymer to create a conductive composite. This has been reported in the literature by adding silver particles [231], multiwalled carbon nanotubes [232] and gold nanoparticles [233] to the SU8. Apart from processing difficulties that can reduce the overall quality of the conductive SU8 structures (e.g. light scattering during patterning); the use of conductive composites implies that the SU8 itself has to define the structure and the conductive path. This limits considerably the design possibilities.

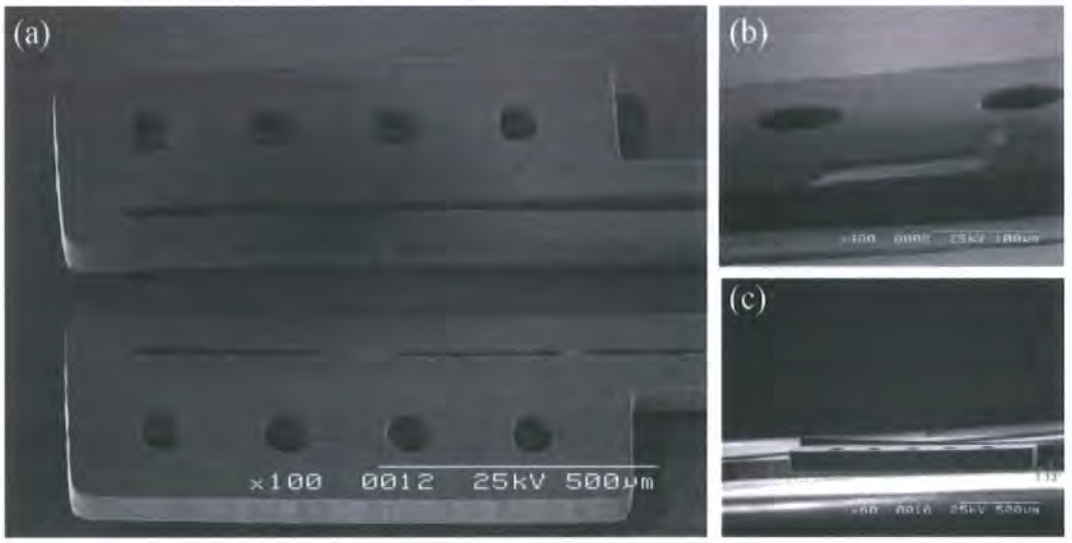

Fig. 3.12: (a) Gold coated microgripper after delamination of the metallisation layer (b) detail of the delamination (c) Out-of-plane deflection due to accumulated thermal stresses during the metal deposition.

A second option is the deposition of a metal film over an already patterned SU8 structure. This is a very fast and easy way to produce initial prototypes. However, the functionality of devices produced in this way is often limited by the low adhesion between the SU8 and some metals [234] and, as in the case of conducting polymer composites, by the fact that the conductive path has to be defined by the SU8 itself. This approach has been used to create polymeric thermal actuators [119, 189, 235]. In these cases, the delamination of the metallisation due to the mismatch between the

coefficients of expansion at the SU8/metal interface as the devices heat up is a clear limiting factor. Deposition of gold through a stencil mask and over an already detached SU8 structure was used to produce one of the first microgripper prototypes of this thesis. Fig. 3.12 shows an image of the microgripper after the metallisation has cracked and detached from the SU8.

Finally, the last approach is to pattern the metal heaters prior to the patterning of the thicker SU8 layers. This allows the conducting paths to be defined independently from the polymer structure and leads to more design possibilities. In some cases the resistor can be patterned directly onto a sacrificial layer and remains adhered to the SU8 after processing [236, 237]. However, as in the previous case, this method is again prone to delamination of the metallisation due to the low adhesion and accumulated stresses. A way to minimise this problem is to encapsulate the metallisation between two layers of SU8 [204]. This is the approach used in this thesis. Gold was used because of some good material properties such as good biocompatibility [238], a low Young's modulus, a high coefficient of expansion compared to other metals, ductility and reasonably good adhesion to SU8 without the need for adhesion promoters [234, 239].

The thin SU8 layer has a double purpose:

- to work as an adhesion layer for the gold metallisation
- to encapsulate the resistors of the microgripper.

Encapsulation is important because it can stop the mechanical failure of the device due to resistor delamination. It is worth noting that the precise failure mechanisms of thin metallic interconnect on elastic and deformable substrates is still an active research area [240-246]. What seems to be clear is that metal films when "well adhered" to a flexible substrate can withstand higher strains (>20% [247]) than free standing films (1%-2% [248]). The fact that the metallic film is adhered on both sides to a deformable substrate could further improve this stretchability of the films.

It has been found that during the testing of the microgrippers that in general the failure of the metallisation originates from localised heating rather than excessive stretching. The gold metallisation works well until the device reaches the glass transition

temperature of the device. At that stage the reflowing of the polymer can induce cracks in the metallisation which in turn can generate either an effective reduction of the resistor section and therefore localised hot and highly resistive areas or complete breakage of the conductive path and direct electrical failure

A 2" Si wafer with a patterned SU8 layer of 1.5 µm thickness was used as a substrate. A filament evaporator Edwards 306 was used for the deposition of a 300 nm thick gold layer. Standard photolithography with a positive photoresist (Shipley S1813) was used to pattern the conductor lines and the contact pads. No electroplating of the contact pads was performed for the microgrippers. All of the samples tested in this thesis were wire bonded and these bonds reinforced with conductive silver paste.

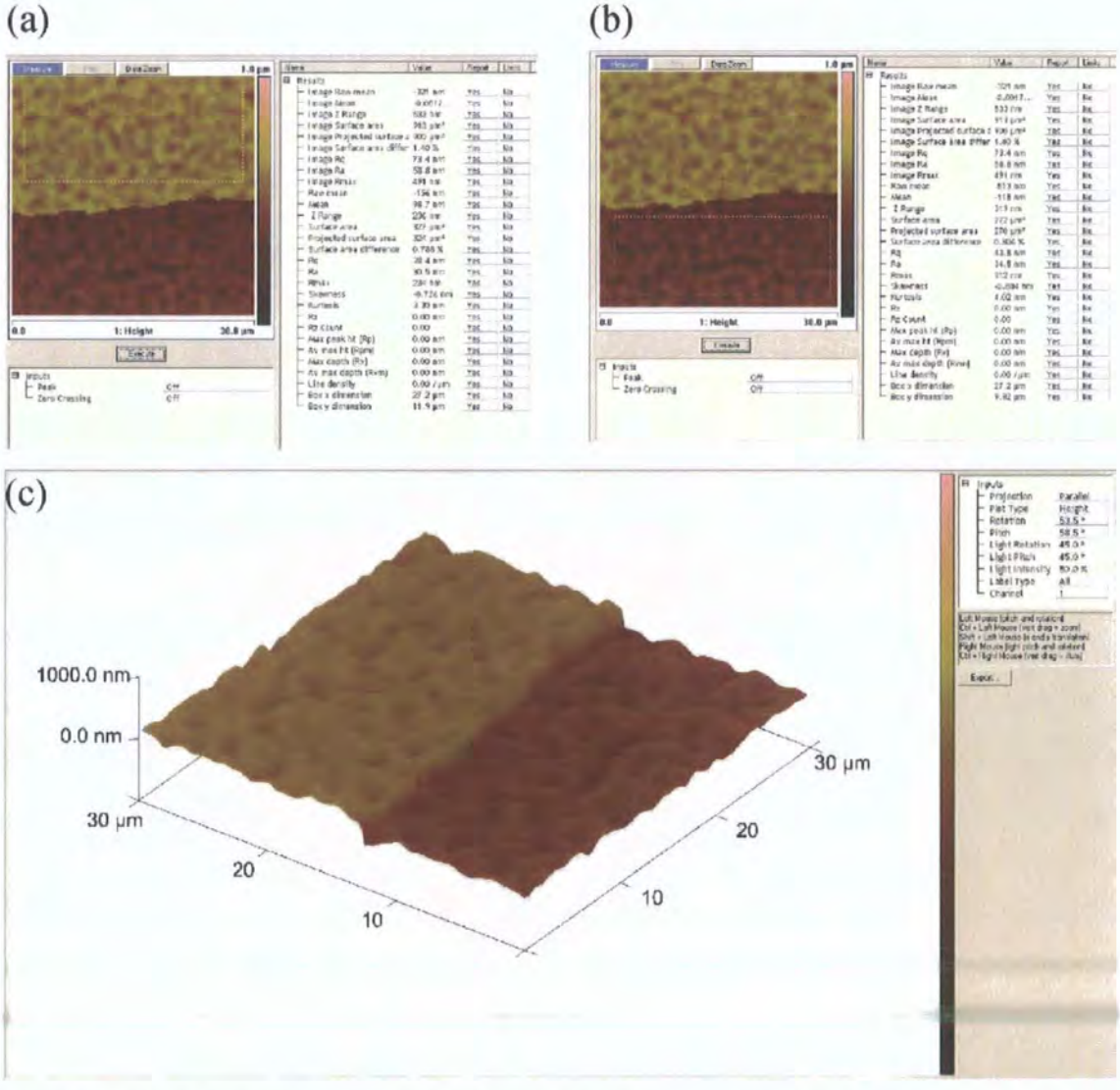

Fig. 3.13: (a) Surface measurement on Gold (b) Surface measurement on SU8 (c) 3D view of the roughness of the metallisation on SU8

The AFM images in Fig. 3.13 show that the gold metallisation follows the relief of the underlying SU8 with an average roughness of 32 nm. It will be shown in chapter five that the electrical properties resulting from the deposition are consistent with standard reported values for thin films.

3.4.2.3. Multilayer SU8 processing

One of the advantages of SU8 is that, using standard UV-photolithography, it can be easily processed with multiple layers and hence mask patterns. This can be done using several techniques.

One is based on the definition of photolithographic masks that contain overlapped and ever smaller clear areas in successive layers [249]. When the design of the device prevents this particular configuration of the masks, it is also possible to add an embedded mask of another material to act as a UV shield. In this case the SU8 is used as a structural and sacrificial material. This is a very reliable technique when the metallisation is incorporated in the first layer. The inclusion of metallisation layers in the middle of the structure, i.e. fully encapsulated, will risk the crosslinkage of undesired areas due to the radiation generated during metal evaporation, especially when using e-beam evaporation. Embedded masks have been created to block UV rays at different stages of the patterning. Materials such as the SU8 2010 coated on top of SU8 2100 [249], SU8 with an added absorber of UV radiation SC1827 resist [250], the positive resist AZ4562 [251], copper [252] or aluminium [235] have been used. Bridged structures can be also obtained by controlling the exposing dose for a particular layer thickness [253] or by controlling wavelength used for the UV exposure [235]. Finally the use of other materials as sacrificial layers that fill the patterns is also possible. Fig. 3.14 shows different suspended stress-free structures using AZ5462 as sacrificial layer.

A common difficulty with all of these multilayer processes is the adjustment of the processing conditions in order to obtain features without distortions, accumulated stresses or cracks as the number of layers increase.

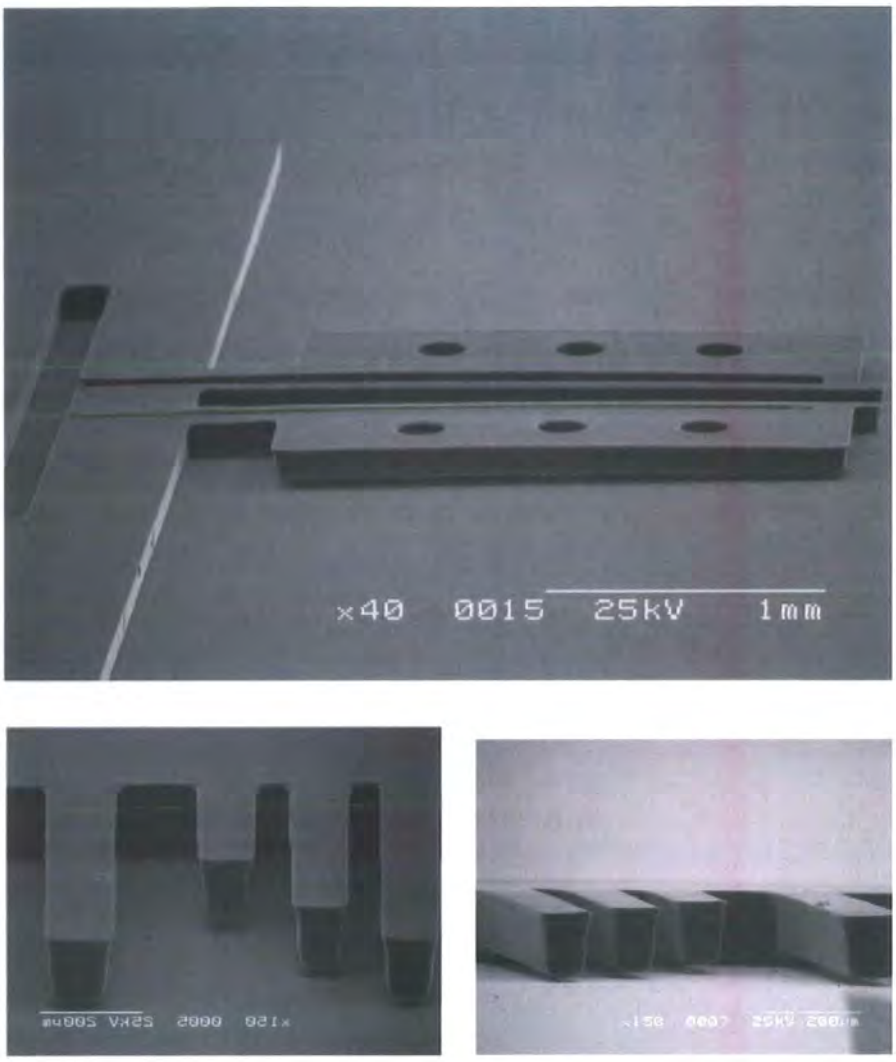

Fig. 3.14: Suspended structures realised with AZ4562 resist sacrificial layer

The microgrippers were produced using two layers of SU8. However, as shown in Fig. 3.15, multiple layers can be required when adding bi-directional movement to the microgripper. In that case the multilayer structure will be composed of thin SU8/Au/Thin SU8/Au/Thick SU8. In all of the cases the layers of SU8 are developed as they are patterned. In the basic microgripper (only one resistor) the thin layer of SU8 (~1.5 μm) composes the first structural layer. This layer is directly patterned and developed. Due to the small thickness of the layer it is possible to reliably spincoat another thick layer of SU8 without requiring the presence of an unexposed SU8 sacrificial layer. As no risk of UV exposure of the sacrificial layer exists, the second structural SU8 layer can be patterned with the most convenient design layout.

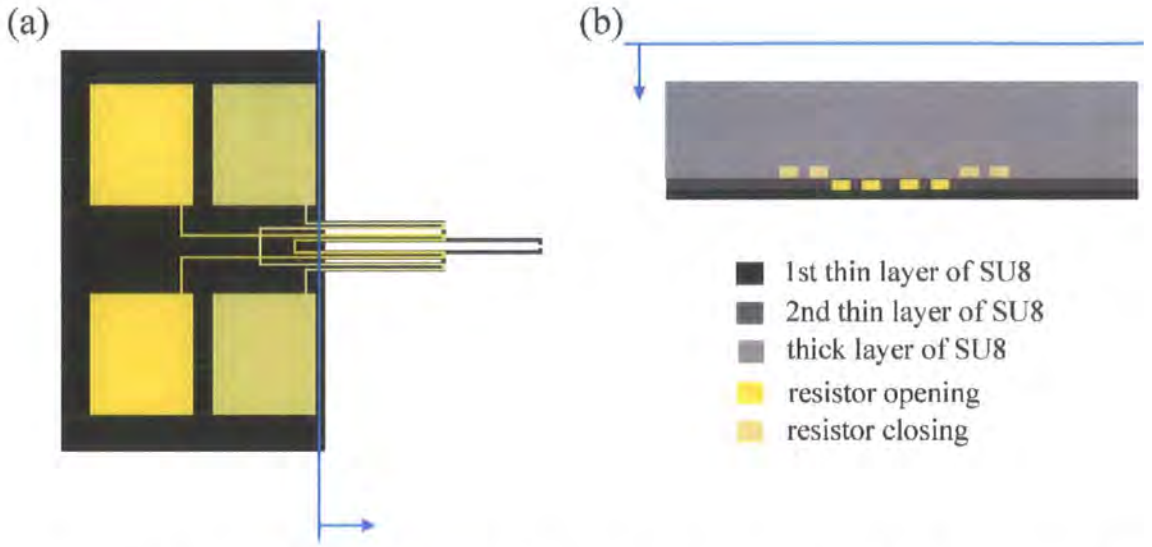

Fig. 3.15: (a) Top view of the microgripper with bidirectional movement (b) Cross sectional view

3.4.3. Release of the devices

A necessary step for many applications is the complete release of the fabricated structures from the substrate. One of the standard techniques is the wet etching of sacrificial layers composed of materials such as Ti [254], Cr/Au/Polystyrene [189], Cu [255], KOH [256], Ti/Cu/Ti, polymers [222, 257]. If the choice of the geometry is right, the wet release process gives good results. However it is normally time consuming [258] and the release of several square millimetres can take a few hours. Dry techniques have also been developed to release SU8 structures and membranes. These include the dry etching of a polysilicon layer using SF_6 in a plasma reactor[237] or XeF_2 [123], and the use of reduced adhesion layers such as self assembled monolayers (SAM) [236], fluorocarbons [259] or Omnicoat™ (Microchem Corp., MA, USA) [260].

In this thesis two release mechanisms are used after fabrication. This includes the controlled peeling of the structures during development of the SU8 using Omnicoat™, and also the dry etching of the silicon substrate using XeF_2. The first process is faster and cheaper but requires careful control of the geometry of the devices in terms of surface and thicknesses to work reliably. The second process is more expensive but is independent of the geometry. In both cases suspended free structures of SU8 with minimal stress and out-of-plane deflection are produced.

3.4.3.1. Process 1: Peel-off of SU8/Au/SU8 structures from Si

Process 1 is a release process based on the diminished adhesion that is induced between the substrate and the SU8/Au/SU8 membrane. The addition of an Omnicoat™ seed layer and a particular choice of processing parameters for the SU8 allows the membrane to peel away from the substrate during the final development step. This process is based on previous work by Bohl et al. where suspended membranes of SU8 were successfully released [260]. In the case of the microgripper an additional metallisation layer is required and the processing parameters have to be carefully controlled.

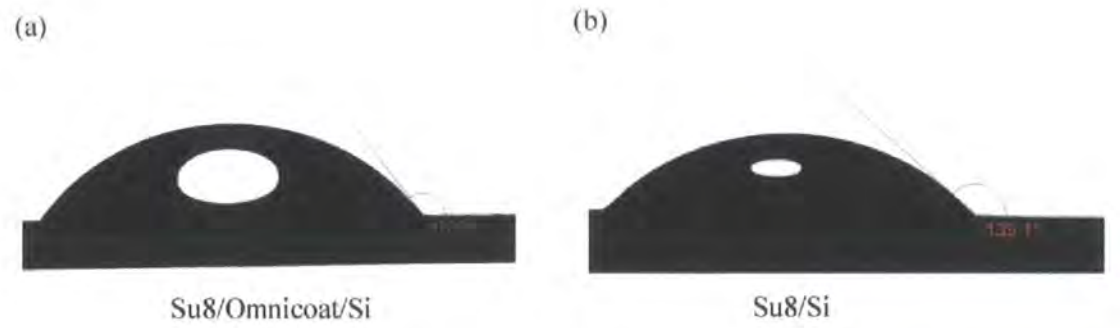

Fig. 3.16: Black and white optical photos through a microscope (a) SU8 drop on a silicon wafer coated with an Omnicoat™ layer (Contact angle = 127.5 °) (b) SU8 drop directly on a silicon wafer (Contact angle = 139.1 °)

Omnicoat™ is normally used to improve the adhesion between metals and the SU8; however it also reduces the adhesion between the SU8 and silicon (Fig. 3.16).This adhesion reduction alone does not produce a reliable release. It is also necessary to control and maximise the stress in the structure. Delamination of the SU8 due to the mismatch of the coefficient of thermal expansion between SU8 and the substrate, to the large amount of tensile stress generated during the crosslinking process (16-19 MPa), or due to inhomogeneous exposure is a well know problem of the SU8 processing. This fabrication process exploits these problems beneficially.

The stress in the membrane depends on the size of the surface in contact with the substrate and the thickness of the layers. However it is also know that in large exposed areas the SU8 is likely to crack during development. Thus in order to maximise the contact between the membrane and the substrate without increasing the surface of the

microgrippers the masks were designed with an external frame (see Fig. 3.17). The corners of the frame are the point where the delamination starts.

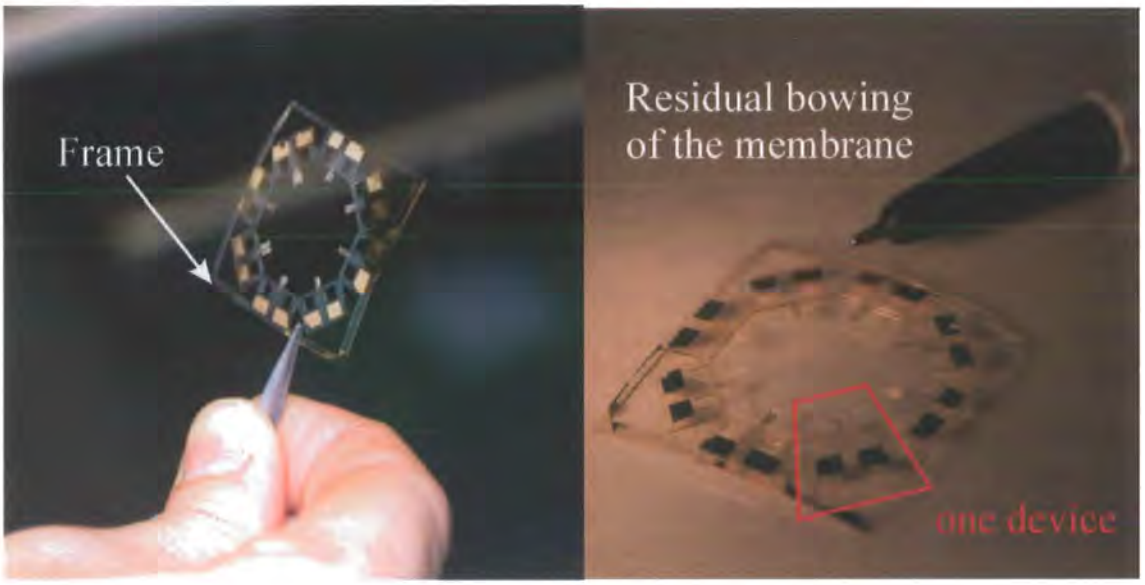

Fig. 3.17: Peel-off structure using diminished adhesion. Detail of the residual bowing of the membrane and frame. The stress is minimal at the actuator tips. The masks used for the final devices enable the fabrication of eight devices per fabrication run.

Gold is a noble metal that does not generate an oxide and has poor adhesion to silicon. The gold contact pads are directly in contact with the Omnicoat/silicon and it is important that they delaminate from the substrate whilst still attached to the SU8. During the fabrication of the microgripper the contact pads (2 x 3 mm) stick preferentially to the top SU8. This is consistent with recent studies where it was demonstrated that the order of the processing affects the adhesion of SU8 to gold [239]. For the final device layout, perfect adhesion is achieved between the SU8/Au/SU8. However when the surface of the resistors on the anchors was increased the membrane delaminated preferentially between the two layers of SU8. The reason for that could be the mismatch between the gold and the SU8 that increases the internal stress and depends on the size of the surface, and also the level of exposure used. Overexposures and very low exposures will improve the adhesion between gold and SU8 whilst medium range exposures will weaken the bond [239].

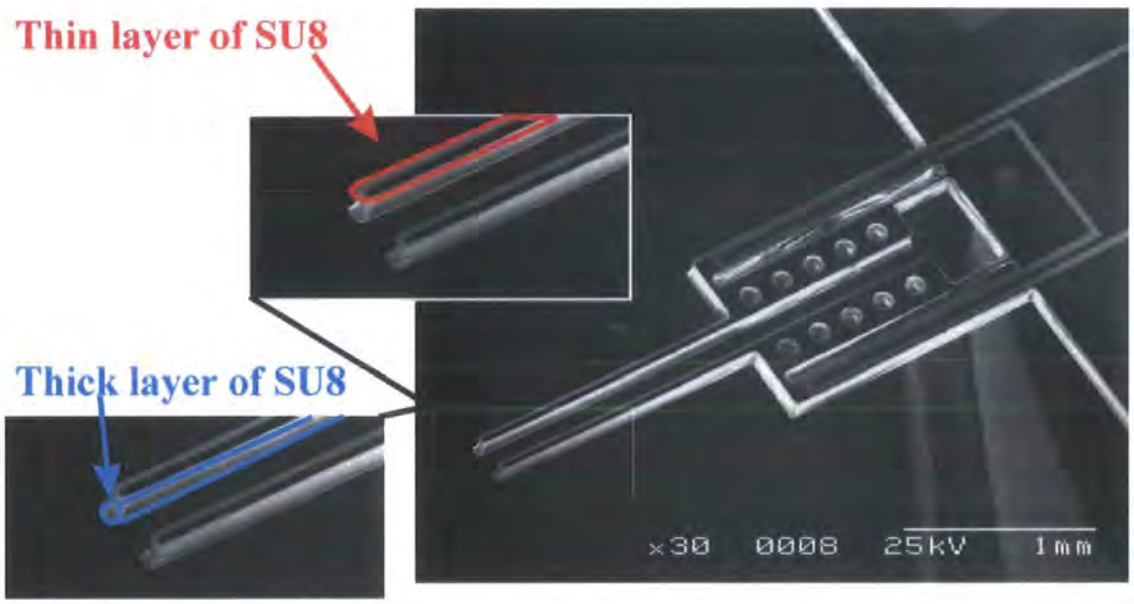

Fig. 3.18: Detail of the tips of the jaws with a marked negative side wall in the thick SU8 layer

An increase of the stress accumulated in the layers is also obtained by underexposing the thick layer of SU8 (last[5] deposited layer during the fabrication process and blue in Fig. 3.18). This underexposure will cause a variation in the degree of cross-linking through the thickness of the layer. This in turn will produce a differential shrinkage between the thin (red in Fig. 3.18) and thick layers and a differential surface stress that will help during the release. The exposure however has to be high enough to provide a good bonding between the two layers of SU8. Excessively low exposures will produce low concentration of crosslinking at the interface and there is the risk of the developer attacking the interface and inducing unwanted delamination. A low exposure also generates negative sidewalls that can be clearly seen in the profile of the thick layer in Fig. 3.18. This does not have a negative impact on the operation of the microgripper and in some occasions can be beneficial to minimise the contact surface between the samples to be manipulated and the jaws.

It is also known that the rate of cooling after the PEB has an impact in the accumulation of thermal stress; the slower the rate the lower the stresses. Thus for a reliable peeling of the structure a fast cooling is desired. A critical step for the success of the release

[5] When the microgripper is mounted and tested the device is turned up-side-down leaving the thin layer of SU8 and the gold on the top of the structure.

technique is to keep the sample at ambient temperature for approximately 5 minutes before the development step.

During the fabrication trials it was also noted that when the three layers of the membrane are processed in quick succession in one single fabrication run the rate of success is higher than when the substrate is left for a few hours before the deposition of the thick layer of SU8. The reason for that could be the moisture on the surface would diminish the adhesion between the gold and the SU8 and the relaxation of the stress in the first thin layer of SU8.

Fig. 3.17 shows a released structure using the peeling process. The advantage of this process versus other wet or dry alternatives is that it is faster, simpler and cheaper because it only requires the deposition and processing of Omnicoat™ which is achieved with a standard spin coater and baked on a hot plate for 2 minutes. In addition, the silicon substrate can be cleaned and reused for subsequent processing. The limitations of the process reside in the determination of the exposure doses, and heating steps of the layers for different thicknesses and contact surfaces. In the case of the geometry of the microgrippers and the masks used, only the membranes with a thickness of approximately 100 μm are reliably and consistently released.

3.4.3.2. Process 2: Dry release using XeF_2

The release process using XeF_2 is extremely reliable and does not depend on geometry but takes longer and is more expensive.

Fig. 3.20: (left) Top view of the released SU8-gold membrane after the dissolution of the Si wafer. The membrane is still attached to a Silicon ring that was protected with a metal mask. (Right) Side view of the release membrane. As with process 1, eight devices are fabricated simultaneously.

All of the microgrippers with an overall layer thickness of 30 μm were released by completely etching away the Si wafer in XeF_2 (Fig. 3.20). However, with a careful design of the masks only the silicon around and below the microgrippers would need to be etched to release the cantilevers. As in the previous fabrication process there is a slight out-of-plane bending of the microgrippers (Fig. 3.20 (right)) which indicates an accumulated residual stress during the processes. This out-of plane bending however does not affect the correct operation of the microgripper. Since with this second process, the requirement of inducing stress during the fabrication of the SU8 layers is eliminated, the parameters of the fabrication can be optimised to obtain vertical side walls (Fig. 3.21).

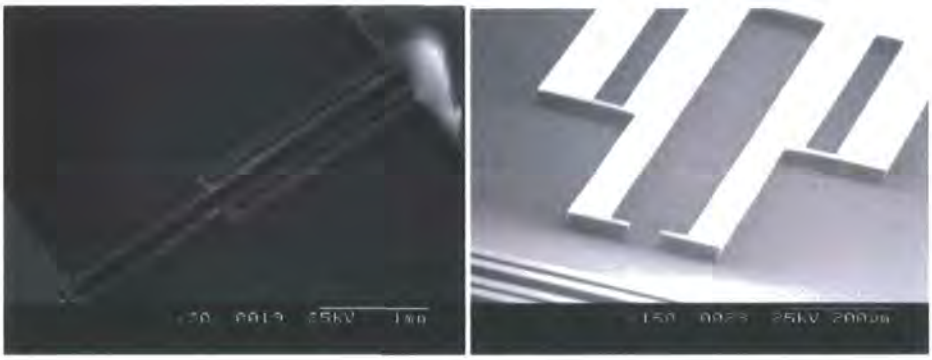

Fig. 3.21: Microgrippers processed using process 2 before the release step. Approximately vertical sidewalls between the substrate and the SU8 can be observed.

3.4.4. Post-processing

After the release step, the microgrippers are separated from the frame by manually cutting with a scalpel at the connecting points. The microgrippers are glued and wire bonded to a PCB board that is used as attachment to the manipulation station. The gold metallisation is at the same level of the SU8 and other electrical connections could be envisaged between the PCB and the microgripper. For example, the use of conducting tape could serve for two tasks: attaching the microgripper to a harder substrate, and also to provide electrical connection to the contact pads.

No hard baking steps have been performed on the tested microgrippers. The hard baking step before release was tried for some samples but it resulted in high crack generation and failure of the metallisation during testing. The reason for that could be the reflowing of the SU8 during hard baking affecting the morphology of the metallic film.

CHAPTER 4

Microgripper models: electrothermal and thermomechanical

This chapter focuses on the development of an analytical tool which consists of two different models, electrothermal and thermomechanical, that are coupled in an iterative manner. The electrothermal model predicts the temperature distribution developed along the beams of the actuators for an initial input current or power. This temperature distribution determines the deflection of the system and is used as an input for the thermomechanical model, which provides data on the in-plane deflection. The chapter is organised as follows.

In the first section, a literature survey on different models describing the behaviour of typical U-shaped thermal actuators is presented. This survey highlights that the area of modelling of thermal actuators is not fully characterised yet. In particular, two aspects deserve a more detailed investigation: the dependence of heat dissipation coefficients with the scale and configuration of the system, and the characterisation of the heat exchange between microbeams that are separated by a small fluid gap. In the second section, these two aspects are treated and a thermal analysis of a generic microbeam system is presented. The analysis is also extended to cover multiple beams which lose heat to the ambient as well as between each other. Different heat transfer mechanisms are considered in turn and their relative importance as a function of dimensions is established. In addition, empirical formulae are provided to calculate heat losses to the

ambient and in between internal parts through conduction, as opposed to convection or radiation. In the last part of the chapter a thermomechanical model is proposed. Both models will be validated using a commercial finite element analysis program.

4.1. Modelling thermal actuators: a literature survey

The principle of actuation of the microgripper is based on a U-shaped thermal actuator (see Chapter 3), which has been studied extensively in its embedded actuation version i.e. where the same material is used to produce the heating and the desired expansion. Usually fabricated from polysilicon, it has been demonstrated in many previous studies, and different analytical and finite element (FE) approaches have been used to model its response [116, 165, 168, 185-187, 261-267].

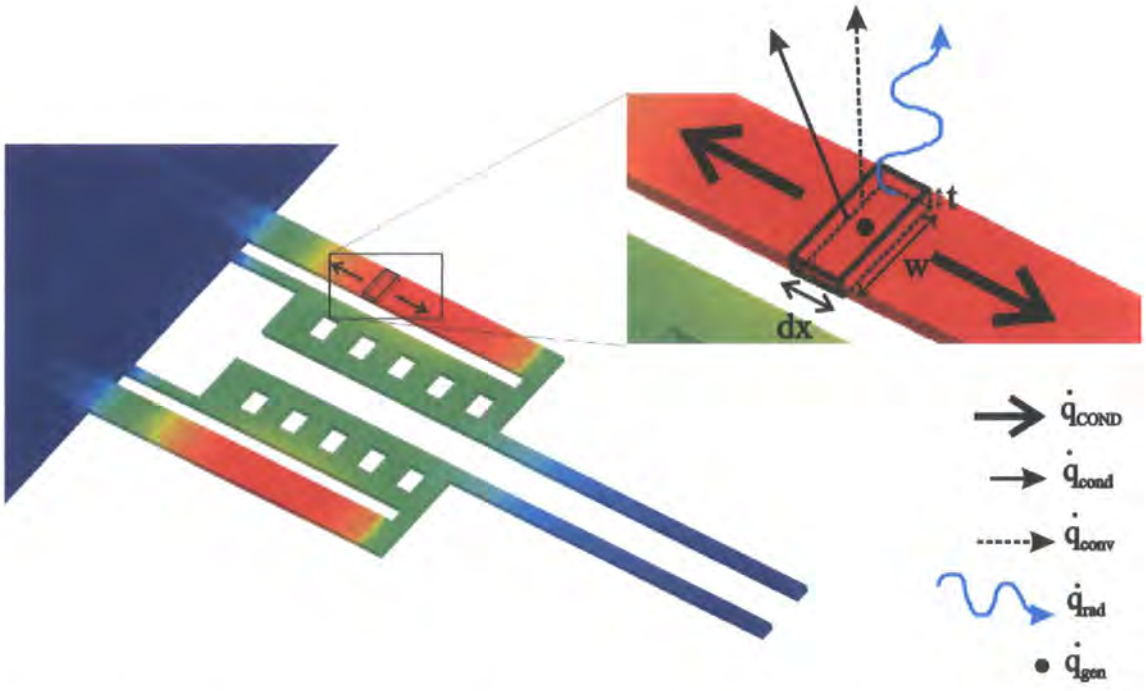

Fig. 4.1: Detail of heat dissipation routes of a volume element of the hot arm. The heat generated within the hot arm is dissipated through conduction to the anchors along the beam, and to the surrounding atmosphere by conduction, convection and radiation.

Modelling and simulating thermal actuators requires the knowledge of the heat input to the device via Joule heating, and also the mechanisms by which this heat is dissipated within the system. All three heat dissipation mechanisms, i.e. conduction, convection, and radiation, should be considered when fully calculating the steady state temperature distribution.

At steady state, the heat generated within the device has to be balanced by the heat conducted through the solid beams to the anchors and by the heat lost to the environment. For the volume element shown in Fig. 4.1, this heat balance can be expressed[6] as follows

$$q_{gen} = q_{COND} + q_{cond} + q_{conv} + q_{rad} \tag{4.1}$$

where q_{gen} is the heat generated within the volume element, q_{COND} is the net heat conducted through the volume element, and q_{cond}, q_{conv}, q_{rad} are respectively the heat rate lost into the ambient by conduction, convection, and radiation. The contribution of each of these mechanisms to the overall heat loss process is an important part of the heat transfer analysis and has to be assessed carefully. As will be shown, the relevance of each mechanism can be considerably different depending on multiple factors such as the configuration of the actuator and the surrounding media.

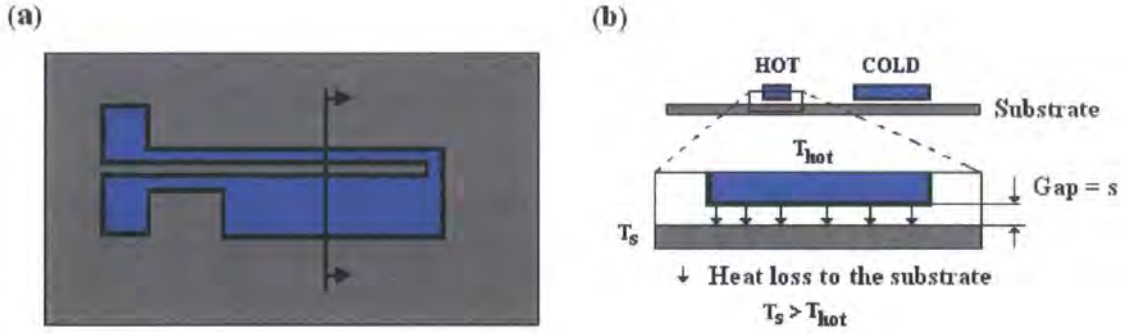

Fig. 4.2: (a) Top view and cross-section of an actuator suspended a few microns above the substrate (b) Cross-section view.

Most of the existing analytical models describe actuators that are mainly fabricated in thin structural layers (~1-3 μm), separated from the substrate by a small fluid gap (~1-2 μm) [170, 171, 185, 263, 265, 267-270]. This particular configuration (Fig. 4.2) greatly influences the thermal behaviour of those systems and the associated models have limited generic applicability. Heat loss from these actuators is generally dominated by conduction across the device to the anchors[7], which are considered as heat sinks, and by conduction through the thin air gap from the device to the substrate.

---

[6] "q" denotes in this work heat rate but for simplicity in the notation the dot above the q has been omitted.

[7] This is true for short actuators and for very good thermal conductors

The heat conducted through the air gap to the substrate, q_{cond}, is taken to be proportional to the difference in temperature between the substrate, T_s, and the actuator, T, with a constant of proportionality related to the size of the fluid gap, s, the conductivity of the fluid atmosphere, κ_∞, and the particular geometry of the microbeam.

$$q_{cond} = \frac{F\, w\, dx\, \kappa_\infty}{s}(T - T_s) \tag{4.2}$$

where w multiple by dx (Fig. 4.2) is the area of the beam facing the substrate. F is a geometrical shape factor which accounts for the heat loss to the substrate by the other dimensions not facing the substrate [116, 269]. It is dependent on geometry, and the value is found either numerically for particular geometries and shapes [271], or using an empirical expression first proposed by Lin et al. in [263] and shown in equation (4.3)

$$F = \left[t / w * ((2 * \frac{s}{t}) + 1)\right] + 1 \tag{4.3}$$

where t is the thickness of the beam.

The convective heat loss from the faces not facing the substrate, q_{conv}, is described by Newton's law of cooling as in equation (4.4). The heat loss is characterised by a constant called the convection coefficient, h.

$$q_{conv} = h\ (w + 2t)\, dx\, (T - T_s) \tag{4.4}$$

In principle, h is dependent on multiple parameters such as the geometry of the actuator or the ambient conditions, and is difficult to determine. In these models, however, the particular value of h does not crucially modify the result of the analysis as the contribution of convection to the overall heat dissipation process is usually small. Table 4.1 shows the contribution of convective heat losses at different values of h = 10, 100 and 1000 W m^{-2} K^{-1}. Also shown in Table 4.1, is the contribution of radiation, where heat losses are expressed as

$$q_{rad} = \varepsilon_\infty \varepsilon\ \sigma (w + 2t)\, dx (T^4 - T_\infty^4) \tag{4.5}$$

where ε and ε_∞ are the emissivities of the actuator and the ambient respectively, and σ is the Stefan-Boltzmann constant with a value of 5.67×10^{-8} W m^{-2} K^{-4}.

From Table 4.1, it can be concluded that for a typical configuration of U-shaped thermal actuator above a substrate and a particular length scale, neglecting convection and radiation, while keeping only conduction through the air gap, is justified. The values in Table 4.1 have been calculated integrating *dx* over the length of a generic beam.

Table 4.1: Energy and heat losses at different temperatures and different values of *h* for a typical thermal actuator fabricated in polysilicon with dimensions and conditions t = 2.5 μm, w = 2 μm, s = 2 μm, length 200 μm and $T_s = T_\infty = 293$ K.

h = 10 W m^{-2} K^{-1}

Heat loss [mW]	q_{cond}	q_{conv}	q_{rad}	E_{gen}
at 300 K	2.57E+00	1.28E-03	3.26E-04	1.82E+01
at 600 K	7.37E+00	3.68E-03	3.16E-03	2.46E+01
at 1000 K	1.70E+01	8.48E-03	4.73E-02	3.33E+01

h = 100 W m^{-2} K^{-1}

Heat loss [mW]	q_{cond}	q_{conv}	q_{rad}	E_{gen}
at 300 K	2.57E+00	1.28E-02	3.26E-04	1.82E+01
at 600 K	7.37E+00	3.68E-02	3.16E-03	2.46E+01
at 1000 K	1.70E+01	8.48E-02	4.73E-02	3.33E+01

h = 1000 W m^{-2} K^{-1}

Heat loss [mW]	q_{cond}	q_{conv}	q_{rad}	E_{gen}
at 300 K	2.57E+00	1.28E-01	3.26E-04	1.82E+01
at 600 K	7.37E+00	3.68E-01	3.16E-03	2.46E+01
at 1000 K	1.70E+01	8.48E-01	4.73E-02	3.33E+01

Even though this analytical approach has led to relatively accurate predictions in device performance, it seems to break down for:

a) very thin air gaps [272] where the shape factor F overestimates by a factor of 2 the heat losses to the substrate.

b) particular actuator geometries [273] where neglecting radiation and convection lead to unrealistic predictions of the maximum temperature, exceeding the melting point of the material.

c) overhanging configurations [187], where the actuator is suspended from the anchors in a fluid atmosphere. In those cases, heat losses to the surrounding ambient gain significance.

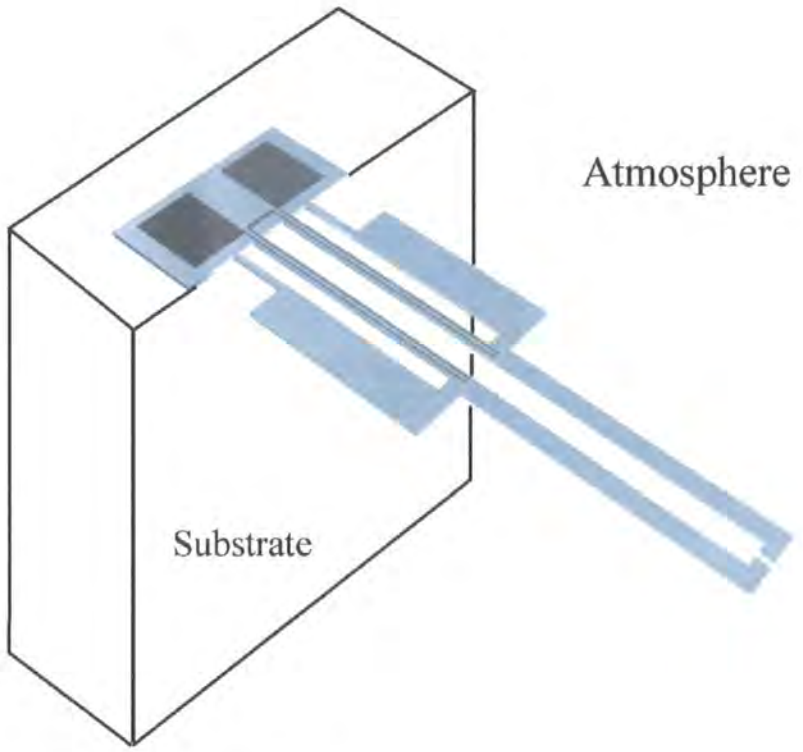

Fig. 4.3: Overhanging microgripper

The microgripper has an overhanging configuration (Fig. 4.3), and so an assessment of whether the existing analytical and FEA models can describe the system is particularly relevant. In overhanging actuators, the heat loss to the ambient has been treated differently by different authors.

- In some analytical models, it has been treated as a mass transport (convection) phenomenon [171, 187]. These models have been generally extrapolated from larger scale analysis, with heat losses into the ambient described by global convective heat transfer coefficient h (see equation (4.4)) whose value has been extracted from standard macroscopic engineering tables (See Table 4.2). Implicit

in the use of these convection values is the assumption that macroscopic thermal analysis is directly applicable at the microscale. However, caution needs to be exercised in applying techniques developed for larger scale structures to the microscale [274, 275].

- In other cases, as in the metallic mesoscale device presented in [255], both convection and conduction to the ambient are neglected, and it is assumed that conduction to the anchors is the main heat loss mechanism. This is mainly valid for metallic actuators where the thermal conductivity is much higher than the thermal conductivity of the surrounding media. However its applicability to poor heat conductors has to be assessed.

- Finally, some authors include values for heat losses to the ambient that have been fine tuned with experiments. Those values of heat transfer are valid only for a particular experiment and system configuration. Therefore, once again, the general applicability remains uncertain.

Table 4.2: Typical values of the convection heat transfer coefficient (h) [276]

PROCESS	h [$W m^{-2} K^{-1}$]
Free convection	
Gases	2-25
Liquids	50-1000
Forced convection	
Gases	25-250
Liquids	50-20000
Convection with phase change	
Boiling or condensation	2500-100000

FE modelling techniques have also been used to model thermal actuators, especially when complex geometries, temperature dependent material properties and temperature dependent heat transfer coefficients have to be modelled. In those cases, the correct implementation of the thermal boundary conditions is crucial. Two main approaches have been proposed to take into account heat losses to the atmosphere.

- First, to apply to all of the exposed faces of the devices an effective heat transfer coefficient that accounts for any kind of heat loss. In these cases, heat coefficients are extracted either from standard macroscopic engineering tables or

from semi-empirical formulae derived from macroscopic thermal analysis. As explained earlier, this assumes the direct scaling of macroscopic theories.

- Second, to place conductive air elements in the gaps within the actuator and between the actuator and the substrate and to apply a convection coefficient to the exposed air surfaces and/or actuator surfaces [277, 278]. This is an important technique because it not only accounts for the heat loss through conduction to the surrounding ambient, but also for the heat exchange between tightly spaced parts at different temperatures. However, once again, it is not clear in the literature to which boundaries those conditions apply, and how to obtain the heat transfer coefficients at the exposed surfaces. Geisberger et al. [278] calculated these heat transfer coefficients and applied them to the exposed surfaces of the actuator and the air. At 300 K, the temperature dependent convection coefficient for an infinite flat plate has been calculated to be 1101 W m^{-2} K^{-1}. However, Artre [277] calculated the heat transfer coefficients for a similar structure as being approximately half of this value, i.e. 500 W m^{-2} K^{-1}.

In conclusion, both analytical and finite element models have used a broad range of values for the convection coefficient h from 10 – 1000 W m^{-2} K^{-1}. This coefficient characterises the heat losses to the ambient, and its correct implementation in the models is crucial, especially when downsizing the actuators where the surface to volume ratio increases.

Leaving aside the manner in which different authors treat heat losses to the ambient, there are two other parameters that are rarely treated in the models:

- Most of the existing thermal models are applicable only to thermal actuators where the boundary conditions at the device anchors are considered to be identical to the conditions at the anchors, i.e. either with constant temperature equal to the ambient temperature or with identical thermal resistance [187]. Sometimes, however, fabrication limitations, or design requirements demand larger flexibility in the models. This is particularly important when different thermal boundary conditions at the anchors and material properties have to be modelled. First attempts to integrate these features in analytical electrothermal models can be found in [279].

- In addition, even if the effects of the heat exchange between closely spaced arms has been observed [123, 188], it has never been explicitly formulated in the models.

In the case of the microgripper, the actuators are not an embedded U-shaped type. In this design, the conducting layer is intended only to provide heating and not to produce any mechanical effects which, unlike the standard U-shape, have to be avoided. Second, the microgripper has an overhanging configuration, high aspect ratio beam structures and a relatively small air gap separating the arms. This can affect considerably the thermal behaviour of the system. Finally, the two actuators integrating the microgripper belong to the same electrical circuit and the same well-insulated anchor. This will introduce boundary conditions at the beginning of each actuator that will have an impact on the overall performance.

In this context, there exists the need to develop further the existing analytical and FEA models to characterise the microgripper more accurately. A good understanding of the physics underlying the thermal behaviour of the device should provide more complete and accurate simulations. Moreover, this understanding should promote a more efficient use of those simulations, and consequently a better performance of the overall modelling process.

4.2. Development of analytical models for the microgripper

Describing the behaviour of the microgripper (Fig. 4.4) requires the solution of a highly coupled electrothermomechanical problem. The power input to the system is a function of the electrical current and the resistance, which in turn is dependent on temperature. Even though the temperatures of operation of the microgripper are low or moderate, as will be shown later, the impact of the temperature dependency of the resistivity is non-negligible. Therefore a coupled electrothermal model is needed to solve the power and temperature distribution simultaneously. The thermomechanical behaviour (strain) appears through the dependency of the Young's modulus and the thermal coefficient of expansion with temperature. The strain is dependent on the temperature distribution but the temperature is not dependent of the strain. This allows the decoupling of the problem into two separate problems and models. Once the steady-state temperature is

calculated from the electrothermal model, it can be used as an input for the mechanical model and for the calculation of the strain field.

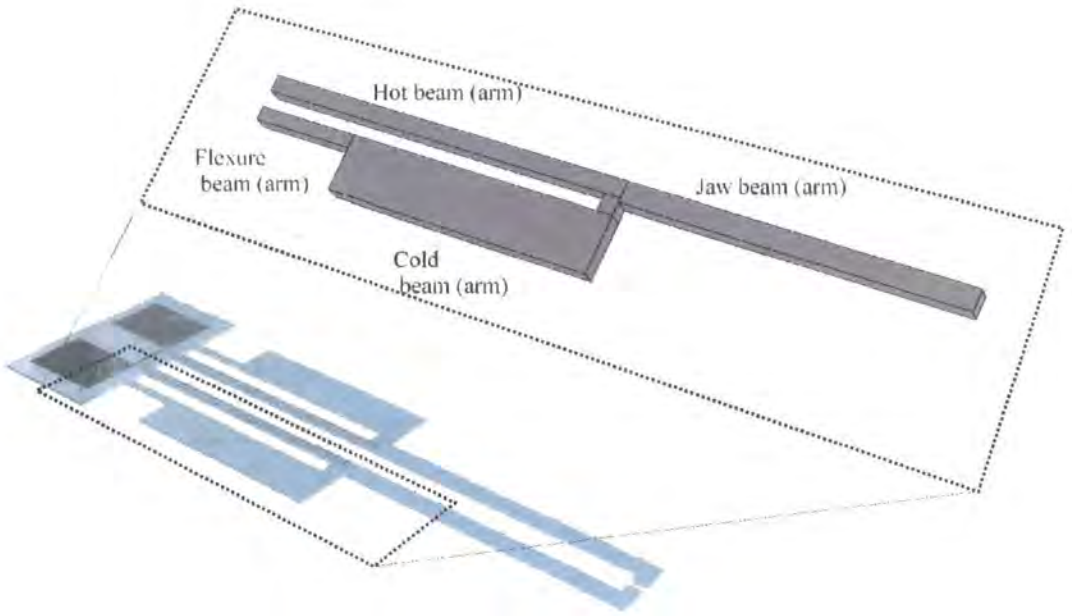

Fig. 4.4: Simplified representation of a thermal actuator as an assembly of microbeams: hot, cold, flexure and jaw beams (also called arms)

A number of simplifying assumptions have to be made to obtain a closed form solution of both models. First, the analytical electrothermal model for the microgripper will be reduced to a 1 dimensional (1D) problem. At the core of this model is the representation of the microgripper as an assembly of 1D slender structures, i.e. microbeams (Fig. 4.4), with different constant lengths and cross sections. Hence, the underlying assumption is that for all elements, the width and thickness of the beams are considerably smaller than their length, and that any variation of the temperature across the section of the beam is not significant compared to its length variation. Moreover, the beams are considered to be constructed of a single effective material. The geometry and thermal conductivity of the effective material is calculated considering that the thermal resistances of all the layers of the beam are connected in a parallel circuit, i.e. the thermal conductance of the beam is given by an aggregate term expressed as

$$\kappa A = \sum_i \kappa_i A_i \tag{4.7}$$

where i is the layer number, κ_i is the thermal conductivity and A_i is the cross-sectional area.

In addition, the temperature dependence of the resistivity and the thermal conductivity are taken in an iterative manner, i.e. for each input power. The segments that have embedded resistors are also treated as one-dimensional electrical resistors.

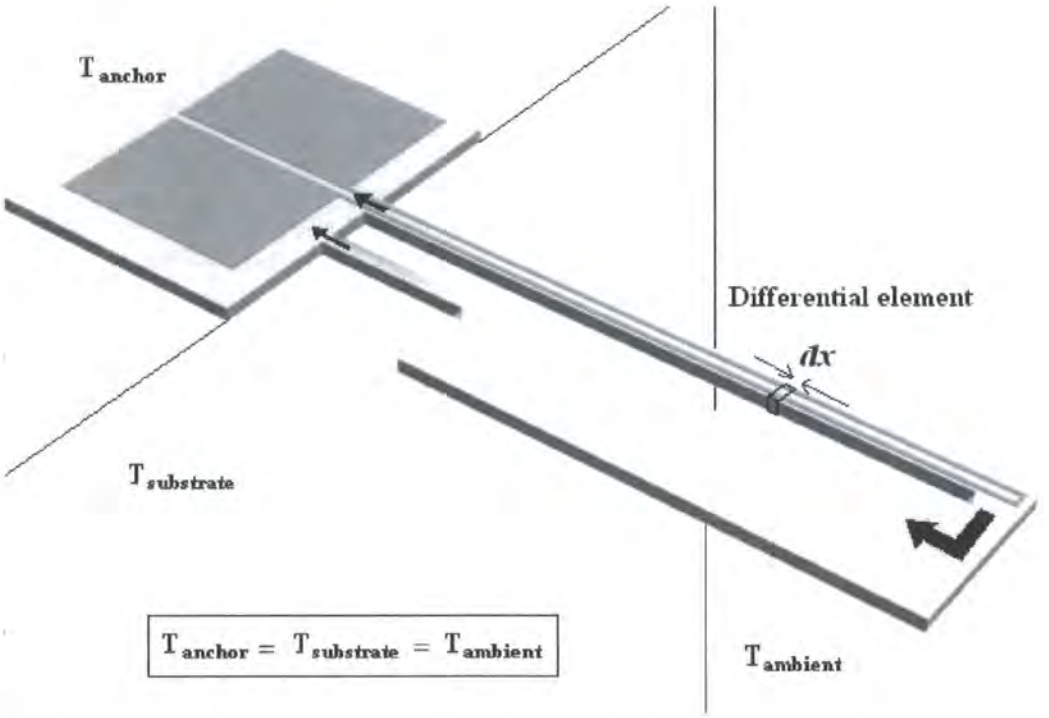

Fig. 4.5: Overhanging configuration of one of the actuators to be modelled in detail. Detail of the differential element on the hot arm.

Fig. 4.5 shows a more detailed representation of the configuration of the system. Due to symmetry only one half of the microgripper will be modelled (Fig. 4.4). Current is injected into the gold metallisation and joule heating leads to differential heating and expansion of different parts of the structure. Typical dimensions for the width, w, thickness, t, and length, L, of the arms of the microgripper are defined in Table 4.3. These values will be used through this analysis.

Table 4.3: Typical dimensions of a single actuator of the microgripper

Parameter Units	w [μm]	t [μm]	L [μm]
Hot arm	140	30	2000
	140	100	2000
Cold arm	250	30	1640
	250	100	1640
Flexure	40	30	360
	40	100	360

As can be seen, the actuator is attached to the substrate at its anchors in an overhanging configuration surrounded by a quiescent fluid atmosphere. For the purpose of this preliminary thermal analysis, the anchors will be considered here as perfect heat sinks with an infinite thermal conductivity to the substrate. Moreover, their temperature, T_a, will be considered to be equal to the ambient, T_∞, and substrate temperature, T_s. This is not necessarily correct because of the thermally insulating nature of the material of the anchors which would probably lead to a localised heating but, at this point, we assume that this condition describes the heat transfer mechanisms reasonably well. Later, during the development of the detailed analytical models, the particular case where the temperature of the anchors is different to the temperature of the substrate and the ambient ($T_a \neq T_s = T_\infty$) will be examined in detail (Chapter 6, section 6.1.6).

A 1D model enables a meaningful, yet simple, analytical model to be constructed. It confers several advantages. It reduces the computation time during the simulations, especially when a number of design iterations are necessary. It also allows for the formulation of a simplified set of coupled equations with a closed form solution that are suitable for optimisation purposes and for the identification of problems. Its main disadvantages however might be the intrinsic limitations in the assessment of the temperature distribution within the cross-section of the beams, the impact of the heat exchange between the two sides of the microgripper actuators when the hot arms of opposite actuators are in close proximity, and the second order deflection upwards due to the bimorph effect. These aspects should be verified by a combination of 3D FEA simulations and experiments, which are given later.

4.3. Heat transfer analysis overhanging configuration

From the system configuration, the relevant heat transfer mechanisms are (Fig. 4.5 and Fig. 4.6):

- Heat generation via Joule heating, q_{gen}
- Heat conduction along the microbeam structures to the anchors on the substrate, q_{COND}
- Radiation heat exchange with cooler surroundings, q_{rad}
- Heat transport into the ambient by conduction, q_{cond}, convection, q_{conv} or a coupling of both mechanisms, q_{cond}/ q_{conv}

- Intra device heat exchange (heat transfer between closely spaced bodies), q_{ex}

Here it will be considered that the upper, bottom and external sides of the beams dissipate heat only into the ambient while the internal faces of the beam exchange heat between each other.

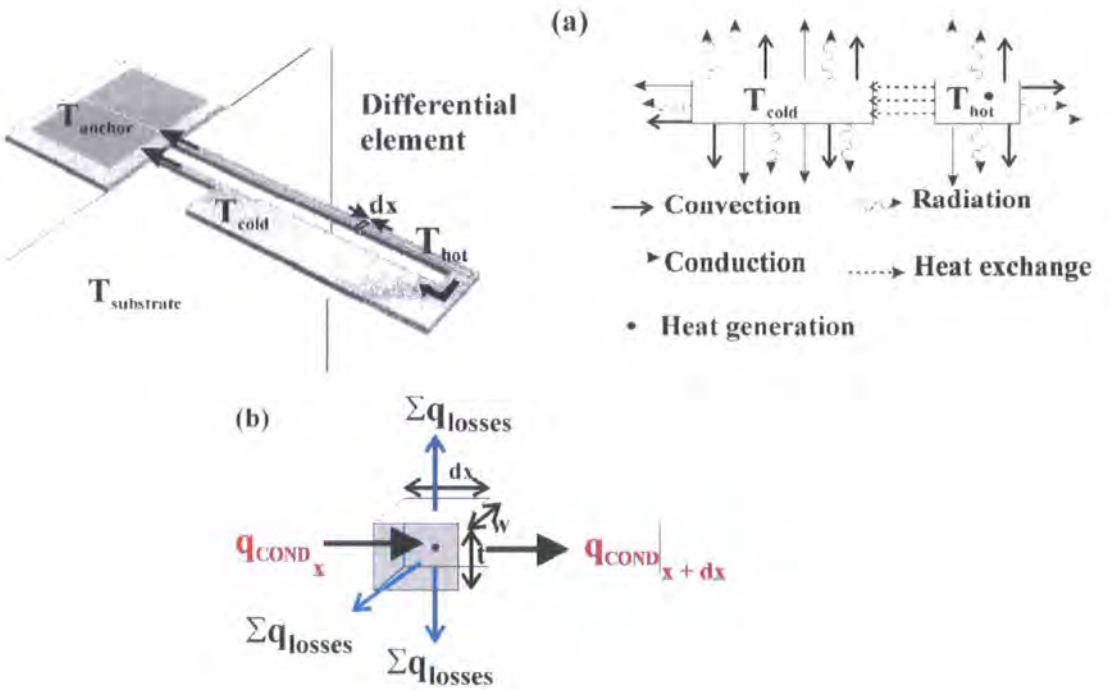

Fig. 4.6: (a) Cross-sectional scheme of the heat transfer mechanisms taking place between two beams at temperature T_{hot} and T_{cold} ($T_{hot} > T_{cold}$). Joule heating generated in the hot arm is dissipated by conduction, convection, radiation and heat exchange (b) Heat losses in a differential element of the hot beam

The temperature distribution along the arms of the actuator and the associated heat equations are obtained by applying an energy balance to a generic differential element, *dx*, of the beams. At thermal equilibrium, the heat generated within the differential element has to be entirely dissipated to maintain the steady-state temperature. For the differential element, shown in Fig. 4.6 (b), with thickness, *t*, width, *w*, and total length of *dx*, the energy balance gives

$$q_{gen} = (q_{COND}|_x - q_{COND}|_{x+dx}) + q_{cond} + q_{conv} + q_{rad} \tag{4.8}$$

where q_{gen} is the heat generated within the infinitesimal volume element, ($q_{COND}|_x$-$q_{COND}|_{x+dx}$) is the net conduction heat rate flowing through the volume.

As explained earlier, the absence of the substrate underneath the actuator, and its associated conductive heat losses, can mean that other heat dissipation mechanisms such as convection gain significance.

4.3.1. Heat generation within the hot arm

The heat generated within the differential element, q_{gen}, is due to the current (I) flowing through the conductor layer and is given by

$$q_{gen} = \frac{I^2 \rho}{A_{Au}} dx \tag{4.9}$$

where ρ and A_{Au} are the resistivity and cross-sectional area of the conductor metallisation respectively.

In equation (4.9) other heat generation terms such as the one resulting from the coupling of electrical and heat transport in the presence of a thermal gradient, have been deliberately omitted. In [274, 280] it is shown however that there is a relevant second order phenomenon called Thomson heating that could perturb the thermal behaviour of microscale heaters at certain length scales. This effect occurs in a conductor that is exposed to a temperature gradient. The flow of current along the conductor when a constant temperature gradient is maintained results in either generation or absorption of additional heat. This effect competes with the Joule heating and, for the volume element in Fig. 4.6 (b), it can be expressed as

$$q_{th} = I \beta \Delta T \tag{4.10}$$

where β is the Thomson coefficient (= 2 $\mu V K^{-1}$ for gold [281]).

Using equation (4.9) and (4.10) the ratio between the Joule heating and the Thomson heating can be estimated and is given by

$$\frac{Joule}{Thomson} = \frac{I R}{\beta \Delta T} \tag{4.11}$$

Given the low value of the Thomson coefficient for gold ($\sim 10^{-6}$) it can be seen that for voltages <2 V (design requirement for the microgripper) the ratio is of the order of 10^3. Therefore the Thomson heating can be safely neglected. This result is also consistent with the fact that the Thomson effect is significant when dealing with materials such as doped semiconductors where an excess of holes and electrons can induce large positive or negative values of the thermopower depending on the charge of the excess carriers [282].

4.3.2. Conduction along the arms of the microgripper

Using Fourier's law of heat conduction, the heat conducted through the volume element can be expressed as

$$q_{COND} = -\Sigma \kappa_i A_i \left(\frac{d^2T}{dx^2}\right) dx \tag{4.12}$$

where κ_i and A_i are the thermal conductivity and the cross-sectional, and $\sum \kappa_i A_i = \kappa A$ is an aggregate conduction path for the beams composed of i layers. This describes the heat loss along the actuators beams to the anchors.

4.3.3. Radiation heat dissipation

Any matter with a temperature above zero Kelvin emits electromagnetic radiation. The amount of radiation emitted by a body per unit area depends on its absolute temperature T and the temperature of the surrounding ambient T_∞ (equation (4.5) in section 4.1). When the temperature difference ($T-T_\infty$) is small compared to T, as it is the case of polymeric actuators, equation (4.5) can be expressed by the first term of a Taylor expansion centred at T_∞.

$$q_{rad} = 4\sigma(2w*t)\,dx\,T^3(T-T_\infty) = h_{rad}(2w*t)dx(T-T_\infty) \tag{4.13}$$

where h_{rad} is defined as the coefficient of radiation.

4.3.4. Heat dissipation into the surrounding ambient

When modelling thermal actuators, it is generally assumed that the global heat loss into the ambient is proportional to the temperature difference. As explained earlier, it is modelled using Newton's law of cooling with a simple constant of proportionality, h, named the coefficient of convection. When h is known, the calculation is straightforward using equation (4.14). However, one of the key difficulties of any convection problem is the determination of h because it depends on numerous parameters related to different fluid properties, flow conditions, object surface geometry and size, etc. For the infinitesimal element dx shown in Fig. 4.6 (b), the heat lost by convection from the sides of the beams not facing each other (q_{conv}) will be given by

$$q_{conv} = h\ (2w + t)\ (T - T_{\infty})\, dx \tag{4.14}$$

This is often referred to as 'convective heat loss' and modelled accordingly. This modelling approach that uses a constant value for h independently of the particular geometry of the system, derives from a scaling down of models used in larger geometries where true mass transport (convective) heat dissipation is an important heat loss mechanism. However, as will be shown later, great care needs to be exercised in applying models appropriate for one length scale to another. Indeed a closer inspection of semi-empirical models for convective heat loss suggests that mass transport effects in air are negligible in systems with the dimensions characteristic of the microbeams. This is why, in the next two subsections, the impact of size and geometry of the actuators in the values of the coefficient of convection h will be analysed.

4.3.4.1. Convection heat transfer in microbeams: background theory

Convection heat transfer occurs between a moving fluid (gas or liquid) over a surface when there is a temperature difference. Assuming that no forced external flows exist, the motion of the fluid is caused by buoyancy forces due to density changes near the heated surface, and heat transfer is described by the natural convection.

Hot objects, however, transfer heat into the ambient by a coupled conduction-convection mechanism and not by convection only. This coupled mechanism arises from the fact that the heat is transferred into the ambient by a conduction mechanism at the limit of the hot surface and, that it is the resulting energy from this conduction

mechanism that is carried away by convection (mass transport). In principle, convection is essentially determined by the boundary layers developed around the heated surfaces (Fig. 4.7 (a) and (b)). In this particular case, it is mainly dependent on the characteristics of the thermal layer.

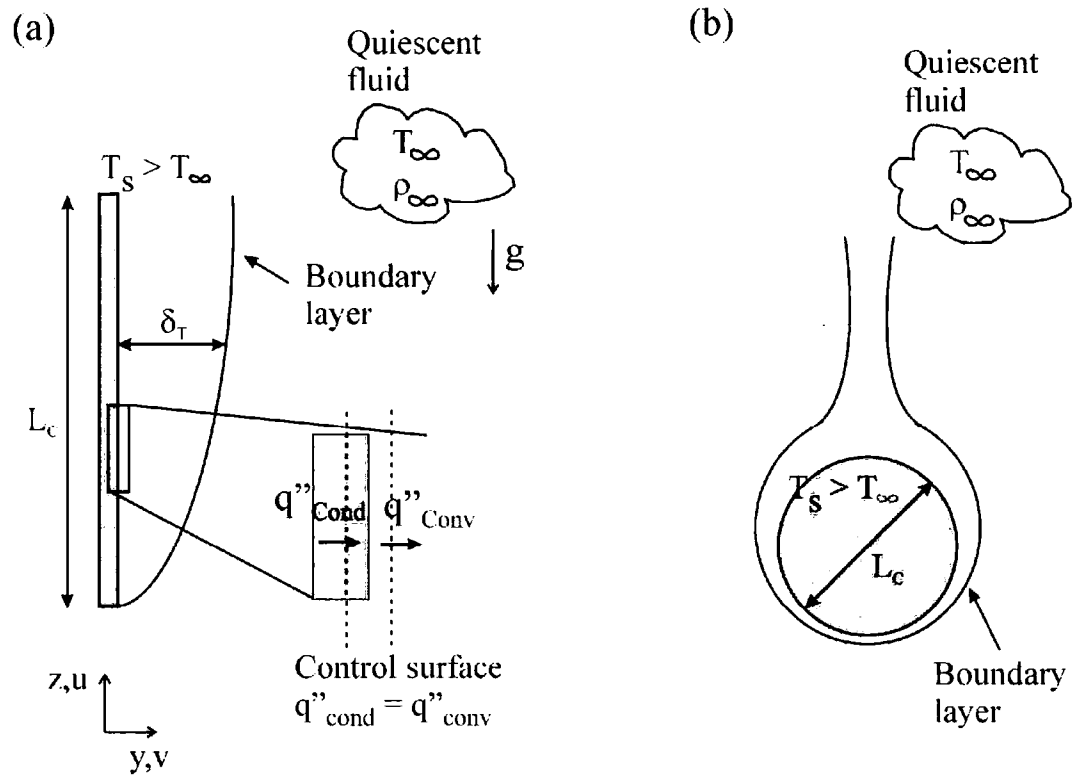

Fig. 4.7: (a) Boundary layer development on a vertical heated plate and detail of a control surface where δ_T is the thickness of the thermal boundary layer, L_c is the characteristic dimension of the surface, and q''_{Cond} and q''_{Conv} are the heat flux entering and leaving the control surface. (b) Boundary layer development around a heated horizontal cylinder.

If we could determine the temperature distribution, T (0, y, *u*, *v*), in the boundary thermal layer, the determination of *h* and therefore the determination of the heat lost will be possible using equation (4.15) [276]

$$h = \frac{\kappa_\infty * \partial T / \partial y \mid_{y=0}}{T_s - T_\infty} \qquad (4.15)$$

where $\partial T/\partial y \mid_{y=0}$ is the temperature gradient perpendicular to the surface (x=0) (see Fig. 4.7 (a)).

However, the equations that provide a complete account of the physics in the boundary layers in steady-state (Navier-Stokes equations[8]), and provide the velocity vectors, u, v, and the temperature, T, are highly non-linear and coupled; analytical solutions for the variables are extremely difficult unless some simplifying approximations are applied. Boundary layer approximations can be applied to the solution of the buoyancy driven flow for particular length scales and geometries. These assume that the thickness of the thermal boundary layer is much smaller than any characteristic length of the system defined in the streamwise direction, i.e. that the changes in physical properties in the direction parallel to the surface are small compared to the corresponding changes in the perpendicular dimension. Flow conditions within the medium are largely undisturbed, except in a very thin boundary layer close to the heated surface.

In macroscopic applications, the "boundary layer approximations" are applicable to the solution of the heat and fluid equations and standard values of the coefficient of convection e.g. the ones provided in Table 4.2 can be used. In those cases, the thickness (δ_T) of the thermal boundary layer is much smaller than any characteristic length, and the heat conducted through the thin thermal layer is generally neglected taking only into account the heat transferred to the surrounding fluid by mass transport.

In boundary layer theory, the coefficient of heat loss can be expressed by terms of a boundary layer thickness, δ_T, and a fluid thermal conductivity, κ_∞, as

$$h = \frac{\kappa_\infty}{\delta_T} \tag{4.16}$$

For free convection, δ_T shows a weak dependence upon both ΔT and the characteristic length of the surface L. For most macroscopic convection problems (ΔT = 10-1000 °C); L = 0.1–1 m) and δ_T is of the order of a few millimetres.

In the case of microscale objects however, the 'boundary layer approximations' are not always justified since the size of the thermal layer is likely to be of the same order as the object itself (Fig. 4.8). Therefore, the applicability of the convection coefficients obtained from classical boundary theory remains uncertain.

---

[8] The explicit form of these equations is not presented here but can be found however in any heat transfer book.

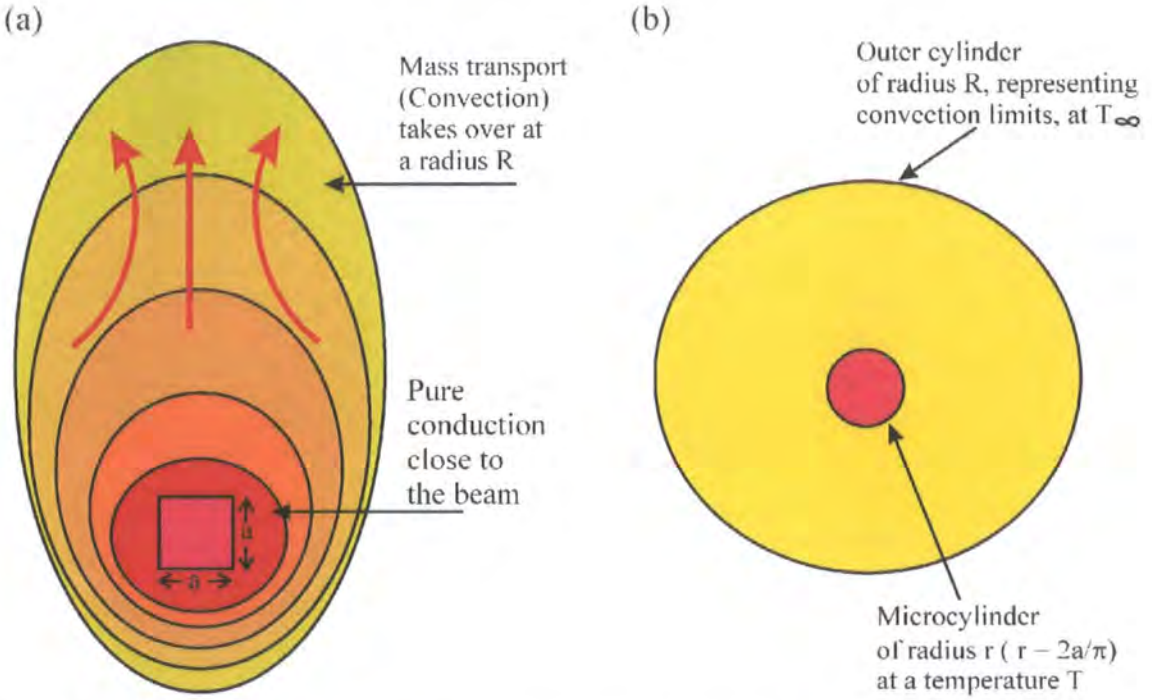

Fig. 4.8: (a) Heat dissipation (conduction + convection) from a microbeam (b) Redefinition of the problem as a pure conduction problem.

4.3.4.2. Scale dependence of the coefficient of convection

To gain some understanding of the underlying heat convection theory, the device will be treated here as an assembly of horizontal cylinders of the same overall dimensions of the rectangular microbeams. This geometry is more straightforward to analyse and has been treated extensively in the literature, e.g. [283].

The study of fluid motion and its interaction with immersed solids is characterised by a number of extremely useful dimensionless parameters. Table 4.4 lists and defines the ones particularly relevant to this discussion. Using the formulae in Table 4.4, and the values appearing in Table 4.5 and Table 4.6, the values of the dimensionless parameters can be estimated for different geometries and media.

Table 4.4: Selected dimensionless groups of heat and mass transfer

Dimensionless group	Definition	Interpretation
Grashoff number (G_r)	$g \beta L_c^3 \Delta T / \nu^2$	Ratio of buoyancy to viscous forces
Prandtl number (P_r)	ν / α	Ratio of the momentum and thermal diffusivities
Rayleigh number (Ra)	$P_r G_r$	Relative importance of heat transfer by convection and conduction
Nusselt number (Nu)	$h L_c / \kappa_\infty$	Dimensionless temperature gradient at the surface
Biot number (Bi)	$h L_c / \kappa$	Heat transfer resistance inside and at a surface of the body

Table 4.5: Variables for AIR at atmospheric pressure and T=293 K and 373 K

Symbol	Value at 293 K	Value at 373 K	Units	Interpretation
P_r	0.71	0.7	-	Value for most gases
L_c	-	-	m	Characteristic length (For cylinders L_c = Diameter)
ν	15.1 E-6	23.1 E-6	m^2s	Kinematic viscosity
α	21.2 E-6	32.8 E-6	m^2s	Thermal diffusivity
κ_f	25.7 E-3	31.4 E-3	$Wm^{-1}K^{-1}$	Thermal conductivity
β	3.43 E-3	2.68 E-3	K^{-1}	Volumetric thermal expansion coefficient

Table 4.6: Variables for WATER at atmospheric pressure and T=293 K and 373 K

Symbol	Value at 293 K	Value at 373 K	Units	Interpretation
P_r	7.01	1.75	-	Value for most gases
L_c	-	-	m	Characteristic length (For cylinders L_c = Diameter)
ν	1.00E-06	0.295 E-6	m^2s	Kinematic viscosity
α	1.43E-07	1.69E-07	m^2s	Thermal diffusivity
κ_f	5.61E-01	0.679	$Wm^{-1}K^{-1}$	Thermal conductivity
β	0.207 E-3	0.752 E-3	K^{-1}	Volumetric thermal expansion coefficient

A key parameter in convection problems is the Rayleigh number which describes the relative importance of mass transfer (convection) to simple conduction through the medium in contact with the surface.

For a microbeam of an equivalent diameter of 20 μm and for a temperature difference in air of 20 K, the Rayleigh number is about 1.7×10^{-5}. For a similar problem where water is the ambient fluid and the average temperature is 40 K, the Rayleigh number is about 4.6×10^{-3}. By contrast, for a more typical macroscopic problem, such as convective loss from a central heating radiator panel where the length might be of the order of 1 m, the Rayleigh number is of the order of 10^{10}.

This difference in 15 orders of magnitude suggests that in microsystems, where the Rayleigh is likely to be always of the order of 10^{-5}-10^{-3}, the contribution of mass transport is negligible compared to pure conduction at the surface.

There are a number of semi-empirical models describing convection heat loss [276, 284-286]. The heat loss to the ambient can be described by the Nusselt number, which relates the coefficient of convection, h, to the ratio of the characteristic length, L_c, and the thermal conductivity of the medium, κ_∞. The Nusselt number gives a measure of the heat transfer that occurs from a surface in a "real" situation, i.e. conduction enhanced by convection, compared to the heat that would be transferred if just conduction took place.

$$Nu = \frac{Convection}{Conduction}\bigg|_{\perp flow} = \frac{h\Delta T}{\kappa_\infty \Delta T / L_c} = \frac{hL_c}{\kappa_\infty} \tag{4.17}$$

From equation (4.17) a simple expression of the coefficient of convection, h, can be obtained

$$h = \frac{\kappa_\infty Nu}{L_c} \tag{4.18}$$

In these semi-empirical formulae, the Nusselt number is only a function of the Rayleigh and Prandtl numbers.

Fig. 4.9 summarises a number of empirical models [284-286] that cover a wide range of Rayleigh numbers ($10^{-6} < R_a < 10^{12}$) together with the values extrapolated from classical macroscopic boundary layer theory.

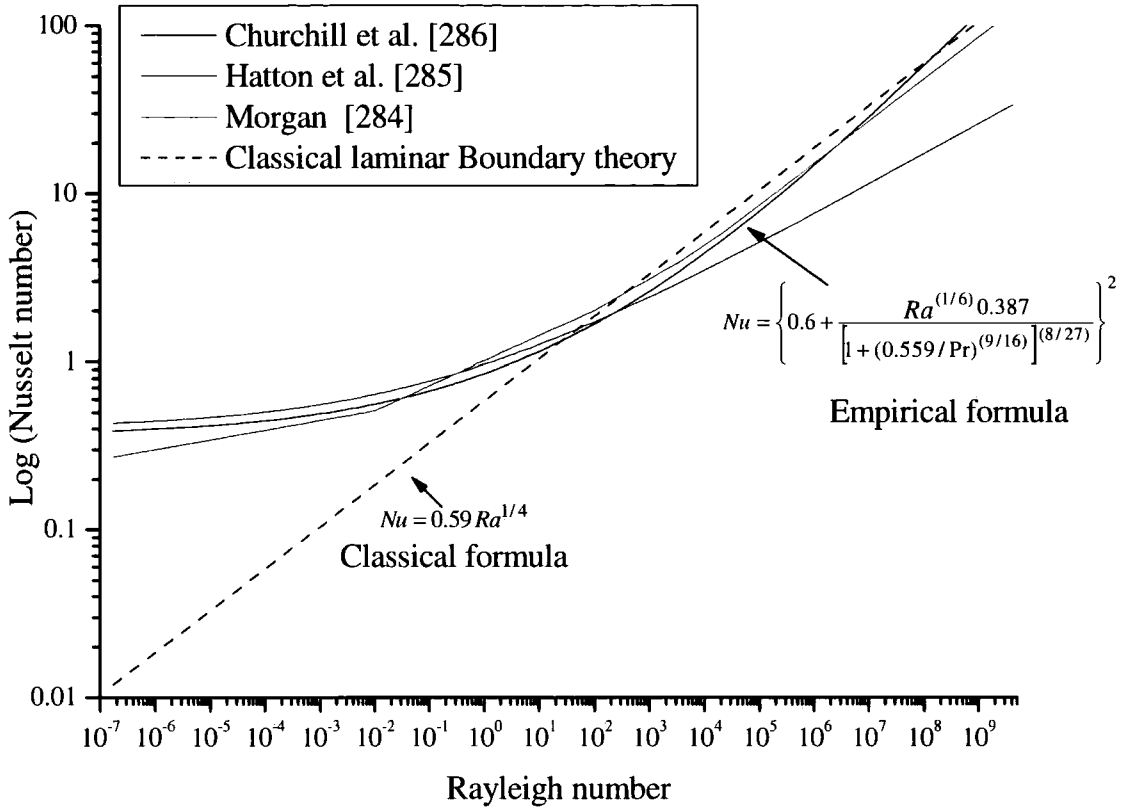

Fig. 4.9: Log_{10} (Nusselt number) versus Rayleigh number (logarithmic scale) (References [284-286])

As can be seen from Fig. 4.9, in the models that have been developed specifically for micro cylinders the Nusselt number reaches a steady value (of about 0.4) at low Rayleigh numbers. This is consistent with a purely conductive mechanism of heat transport.

However, classical laminar boundary theory assumes that the Nusselt number is proportional to $R_a^{1/4}$ and as a result, there is a tendency to underestimated heat loss. This approach has been recently used in [123], and as a result the heat loss may have been significantly underestimated. This is an example of where care needs to be taken in the extrapolation of physical models and heat transfer coefficients, $h=h\ (N_u)$, from one length scale to another.

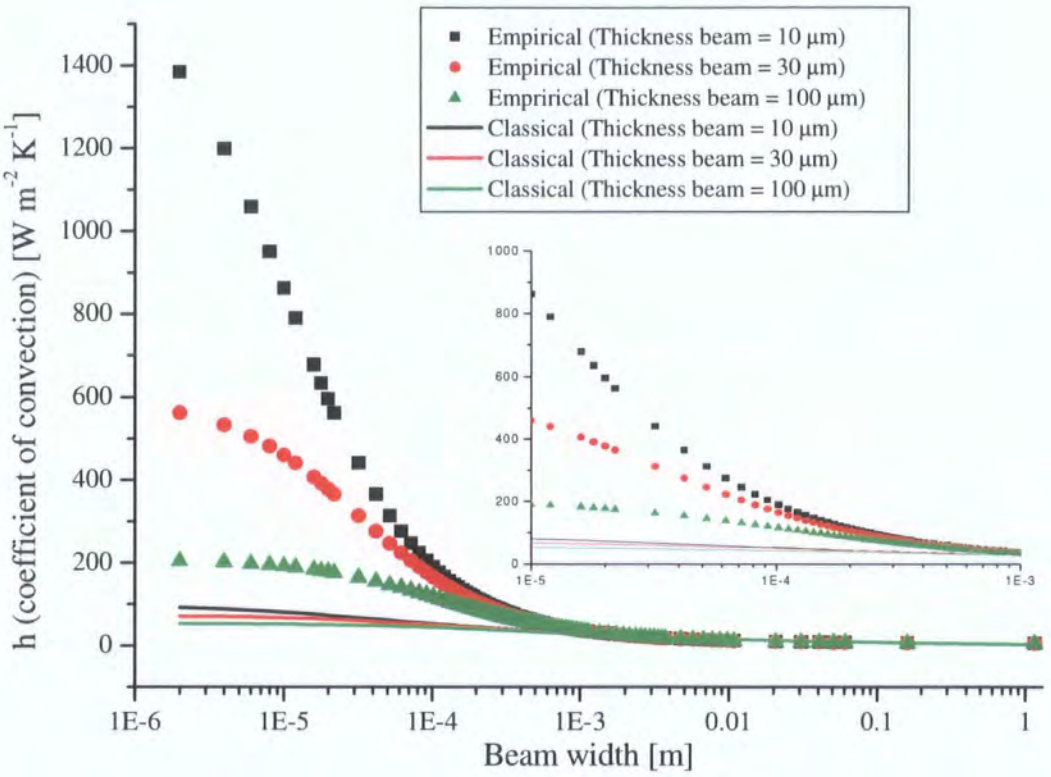

Fig. 4.10: h calculated in AIR from empirical and classical formula (microbeams thicknesses = 10, 30 and 100 μm and a ΔT of 100 K)

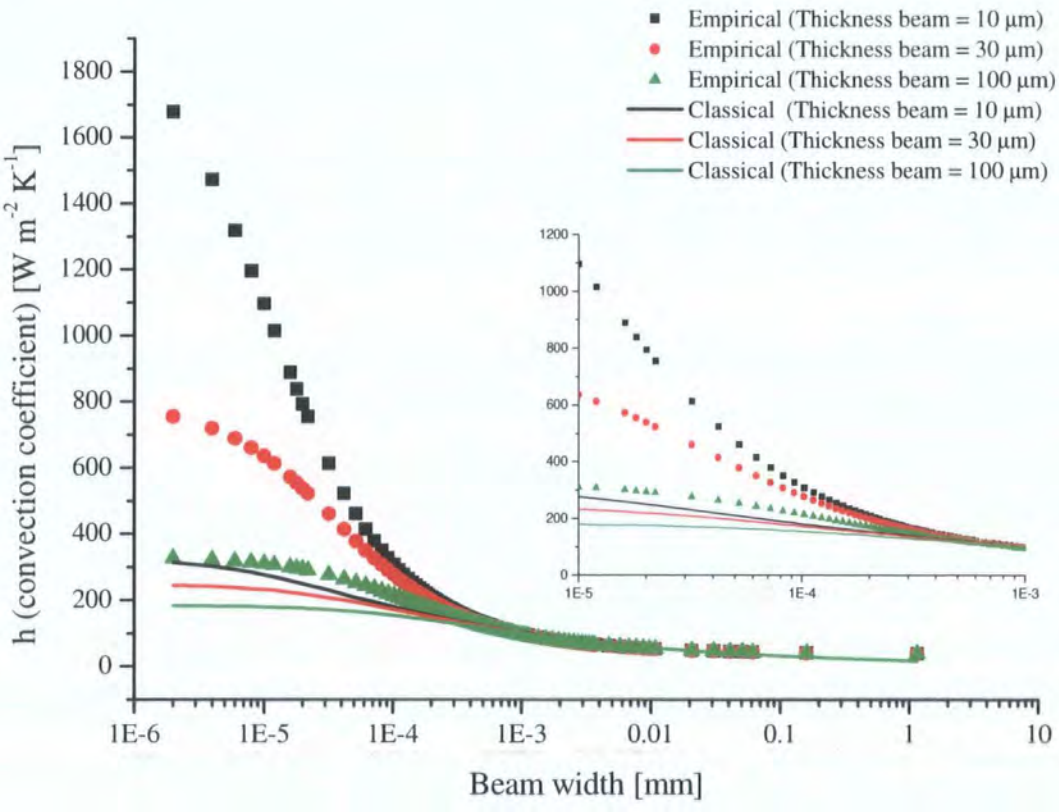

Fig. 4.11: h calculated in WATER from empirical and classical formula (microbeams thicknesses = 10, 30 and 100 μm and a ΔT of 100 K)

To give a general view of how the values of *h* can vary from one beam geometry to another, and from one scale to another, the values of h as a function of the width for three different thicknesses (10, 30 and 100 μm) have been calculated in air and water environments, and are shown in Fig. 4.10 and Fig. 4.11. Also appearing in these figures is the comparison of the values obtained with classical boundary layer theory. Both figures demonstrate that *h* may be underestimated significantly when using classical boundary theory. In some cases, such as for example, a beam of characteristic length 10 μm, the extrapolation from macro to microscale models or the use of standard values for *h* (Table 4.2) provides an underestimation of nearly two orders of magnitude (h =1500 W m^{-2} K^{-1} versus h = 95 W m^{-2} K^{-1} or h = 10 W m^{-2} K^{-1}).

An interesting point to highlight from Fig. 4.10 and Fig. 4.11 is that using classical formulae the difference between the average *h* in air and water at the scale of the figure inserts, 10 - 1000 μm, is around 70 %, whereas using semi-empirical microscale formulae, the difference is reduced to 40 %.

This difference could explain the reason why, in reference [123], the deflections measured under water relative to the ones measured in air, are higher than the FEA model predicted. There, it is considered that the difference in *h* between air and water is of the order of 95%. Hence the underestimation of the deflection in their models.

Table 4.7: Coefficient of convection calculated in air for different geometries using different convection models: semi-empirical formula (*h micro*) and classical boundary theory (*h macro*). ΔT = 40 K.

Parameters	t	w	Diameter	Rayleigh	Nusselt *micro*	Nusselt *macro*	*h micro*	*h macro*
Units	[μm]	[μm]	[m]	–	–	–	[W / m² K]	[W / m² K]
Formula	–	–	–	$Ra = \frac{g \beta L_c^3 \Delta T}{\alpha \nu}$	$Nu = \left\{0.6 + \frac{Ra^{(1/6)} 0.387}{\left[1 + (0.559/\mathrm{Pr})^{(9/16)}\right]^{(8/27)}}\right\}^2$	$Nu = 0.59\, Ra^{1/4}$	$h = \frac{\kappa_\infty Nu}{L_c}$	$h = \frac{\kappa_\infty Nu}{L_c}$
hot arm	30	140	1.08E-04	5.33E-03	5.39E-01	1.59E-01	128	38
cold arm	30	250	1.78E-04	2.38E-02	5.97E-01	2.32E-01	86	33
flexure arm	30	40	4.46E-05	3.72E-04	4.71E-01	8.19E-02	272	47
Jaw	30	60	5.73E-05	7.91E-04	4.87E-01	9.89E-02	218	44
hot arm	100	140	1.53E-04	1.50E-02	5.77E-01	2.06E-01	97	35
cold arm	100	250	2.23E-04	4.65E-02	6.28E-01	2.74E-01	72	32
flexure arm	100	40	8.91E-05	2.98E-03	5.21E-01	1.38E-01	150	40
Jaw	100	60	1.02E-04	4.44E-03	5.33E-01	1.52E-01	135	38

Table 4.7 and Table 4.8 show the values of the coefficients of convection calculated for microbeams with geometries (*t* and *w)* and different length scales. The *micro* values

have been obtained using the semi-empirical formulas proposed in [286] under the approximation of considering the microbeams as a cylinders of the same equivalent perimeter. Also shown in Table 4.7 is the comparison with the *macro* values extrapolated from classical boundary theory.

Table 4.8: Coefficient of convection calculated in air for different geometries using different convection models: semi-empirical formula (h micro) and classical boundary theory (h macro). ΔT = 40 K.

Parameters	t	w	Diameter	Rayliegh	Nusselt *micro*	Nusselt *macro*	*h micro*	*h macro*
Units	[μm]	[μm]	[m]	–	–	–	[W / m² K]	[W / m² K]
Formula	–	–	–	$R_a = \frac{g\,\beta\,L_c^3\,\Delta T}{\alpha\,\nu}$	$Nu = \left\{0.6 + \frac{Ra^{(1/6)}0.387}{\left[1+(0.559/\mathrm{Pr})^{(9/16)}\right]^{(8/27)}}\right\}^2$	$Nu = 0.59\,Ra^{1/4}$	$h = \frac{\kappa_\infty\,Nu}{L_c}$	$h = \frac{\kappa_\infty\,Nu}{L_c}$
hot arm	30	7	2.36E-05	5.49E-05	4.39E-01	5.08E-02	479	55
cold arm	30	20	3.18E-05	1.36E-04	4.53E-01	6.37E-02	366	51
flexure arm	30	7	2.36E-05	5.49E-05	4.39E-01	5.08E-02	479	55
Jaw	30	7	2.36E-05	5.49E-05	4.39E-01	5.08E-02	479	55

Both tables show that the values of h are different when using classical and microscale formulae and that this difference becomes more accentuated when reducing the characteristic dimension (Table 4.8). Hence, to correctly model the convective heat losses in electrothermal microbeams the coefficients of convection, h, have to be calculated for the particular geometry of the problem in each case.

4.3.4.3. Use of conduction coefficients as opposed to convection coefficients

A microscale approach to calculate convective losses to the ambient has been proposed in the previous section. However, it was argued earlier in the chapter that, given the low Rayleigh numbers at the microscale, the contribution of convection (mass transport) was negligible compared to the heat losses to the environment by conduction. Thus in this section, an alternative route to calculate the heat losses to the ambient by conduction only is proposed (Fig. 4.8 (b)). This approach will not only enable the calculation of the heat losses from independent beams but also from beams separated by a small fluid gap.

A pure thermal conduction problem could be analysed by finite element analysis (FEA), treating the surrounding medium as a solid and ignoring its fluid properties. The analysis presented here however, is intended to circumvent the requirement for full FEA in preliminary calculations.

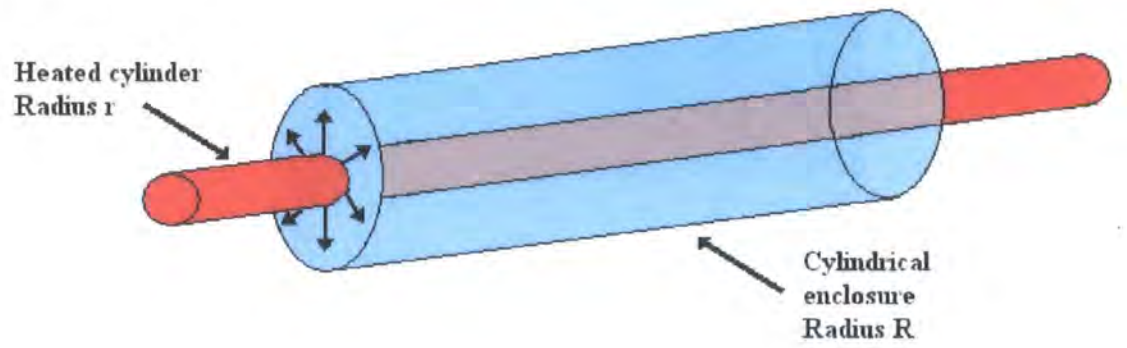

Fig. 4.12: Heat loss in a cylindrical geometry

In order to model the heat loss from a microbeam into the ambient, it is assumed that the problem is 1D and that the lateral variation in temperature, T, is negligible within the microbeams. It is then further assumed that the radial temperature gradient into the ambient fluid is substantially greater than the longitudinal gradient.

For a microbeam, the heat loss into the ambient by conduction, q_{cond}, can be characterised [276] as

$$q_{cond} = f\,\kappa_{\infty}\,\Delta T\,dx = h_{cond}(2w+t)\Delta T\,dx \tag{4.19}$$

where f is a geometrical factor (shape factor) that takes into account the geometry and configuration of the system, h_{cond} is an effective coefficient of conduction defined as $f\kappa_{\infty}/(2w+t)$.

The simplest case for a geometrical factor, f, is where an infinite beam of radius r is surrounded by an isothermal cylinder of radius R, representing the ambient (Fig. 4.12). In this case the geometrical factor is simply $2\pi/\ln(R/r)$. Another example might be that of a ground plane where a beam of radius r is suspended at a height h above a conducting substrate. Here the geometrical factor is $2\pi/\ln(2h/r)$ assuming $h >> r$. A range of examples is set out in Table 4.9.

Table4.9: Conduction geometrical factor empirical formula

	Concentric Cylinders	Cylinder above infinite plane (h>>r)	Rectangle inside cylinder (a, b<<R)	Rectangle above infinite plane (a, b <<R)
Configuration	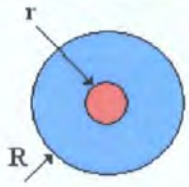	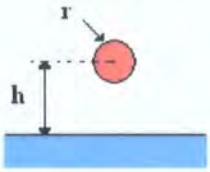	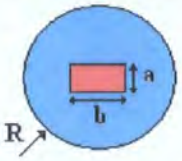	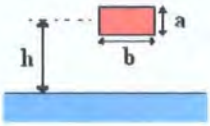
Geometrical factor	$f=\frac{2\pi}{\ln(R/r)}$	$f=\frac{2\pi}{\ln(2h/r)}$	$f=\frac{2\pi}{\ln(R/r')}$ $r'=\frac{0.53ab}{\sqrt{-0.1a^2+ab-0.1b^2}}$	$f=\frac{2\pi}{\ln(2h/r')}$ $r'=\frac{0.53ab}{\sqrt{-0.1a^2+ab-0.1b^2}}$
Equation	(4.20)	(4.21)	(4.22)	(4.23)

In practice, in order to estimate conductive heat losses into the ambient, a number of simplifying assumptions need to be made. For example, that the heat loss into a semi-infinite air mass can be modelled as a coaxial heat loss problem with the ambient being represented by a cylinder of some nominal radius *R*. Intuitively, the radius of this air cylinder may be thought as being the radius at which mass transport effects start to play a role, i.e. where R_a~1 (Fig. 4.8). In the context of the current problem, *R* is approximately 1 mm (~ΔT = 10 K).

Table 4.10: Geometrical factors based on convection and on conduction for a single beam.

Parameters	t	w	Diameter	Nusselt *micro*	*f* convection	*h* convection	*f* conduction	*h* conduction
Units	[μm]	[μm]	[m]	–	–	[W / m² K]	–	[W / m² K]
Formula	–	–	–	–	$f=\pi N_u$	$h=\frac{\kappa_\infty Nu}{L_c}$	$f=\frac{2\pi}{\ln(R/r)}$ $R=1mm$	$h=\frac{\kappa_\infty f}{p}$
	30	140	1.08E-04	5.72E-01	1.80	136	1.89	145
	30	250	1.78E-04	6.41E-01	2.01	92	2.23	103
	30	40	4.46E-05	4.91E-01	1.54	283	1.49	277
	30	60	5.73E-05	5.10E-01	1.60	229	1.59	229
	100	140	1.53E-04	6.18E-01	1.94	104	2.11	114
	100	250	2.23E-04	6.80E-01	2.14	78	2.42	90
	100	40	8.91E-05	5.51E-01	1.73	159	1.79	166
	100	60	1.02E-04	5.65E-01	1.78	143	1.86	151

It is now interesting to compare the values of *h* calculated in the previous section (4.3.4.2), i.e. based on dimensionless numbers and convection, with the ones calculated

in this section where the model is based on cylindrical thermal conduction in air. These values are shown in Table 4.10.

The small difference between the values obtained for h (~10%) with a microscopic convection approach and a pure conduction approach suggests that the analysis presented in this section, although somewhat empirical, is substantially correct, and encourages the use of this approach to calculate heat loss into the ambient from more complex structures such as the microgripper.

4.3.4.4. Determination of the conduction heat loss coefficients for adjacent beams

When trying to model thermal actuators, it is important to be able to model microbeams that are adjacent, i.e. separated by a small gap of air. In this instance, heat transfer occurs into the ambient as well as in between the beams.

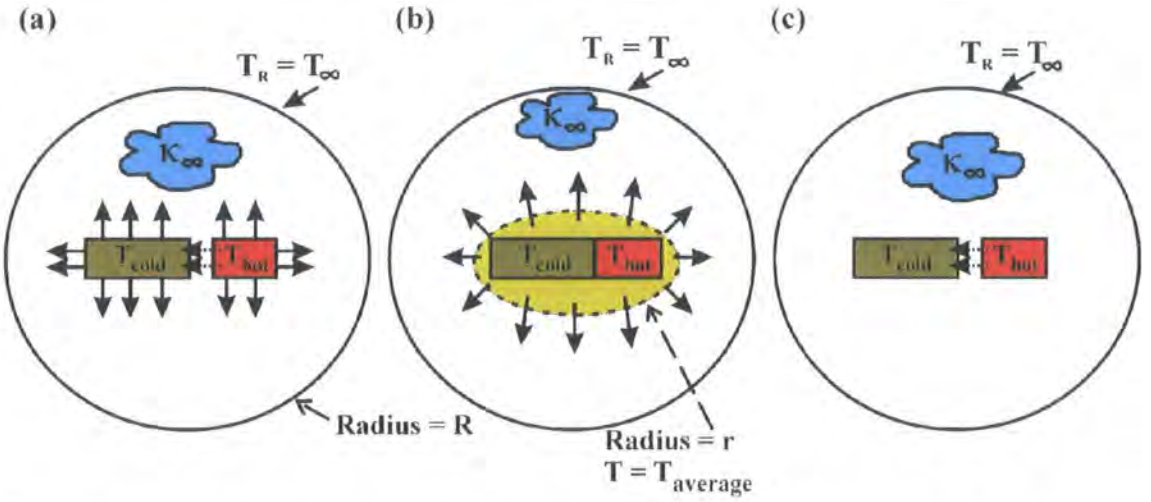

Fig. 4.13: (a) Total heat losses from coupled microbeams (b) Cooperative heat losses into the ambient (c) Intra device heat exchange by conduction.

For dual beams, calculations of the geometrical factors for heat transfer into the ambient from each individual beam rest upon further simplifying assumptions. It does not seem appropriate to calculate the geometrical factors for each beam of the actuator (hot and cold) as in Table 4.10 where it is assumed that they are thermally independent. Instead it is proposed that both beams transfer heat into the environment cooperatively (Fig. 4.13). Initially, an aggregate geometrical factor is calculated for both beams by "combining" them geometrically. The equivalent size of the beam will be given by its overall rectangular envelope. This geometrical factor is then apportioned between the two

beams in proportion to the exposed circumference. Inevitably, this implies that the geometrical factor for a dual beam is less than the one for two similar single beams in isolation.

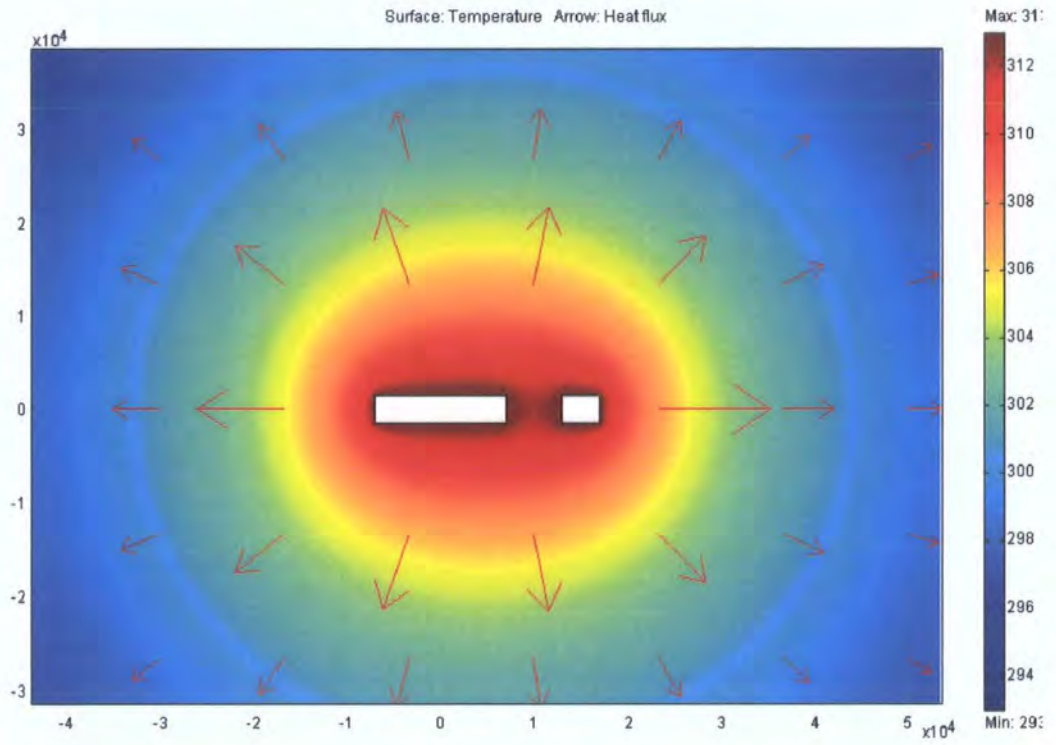

Fig. 4.14: 2D simulation for the validation of the heat transfer coefficients from two beams losing heat cooperatively.

Various geometrical factors have been calculated using equation (4.20), i.e. considering a microbeam of equivalent radius r surrounded by an isothermal cylinder of radius R (= 1 mm), and are shown in Table 4.11. Due to the empirical nature of this approach, the calculated coefficients have been verified by 2D FEA (Femlab) thermal analysis integrating beams with rectangular shape (Fig. 4.14). The comparison between both results indicates that the proposed geometrical factors are accurate within ± 3%; this accuracy is comparable to that inherent in the assumptions of the 1D model itself. Furthermore, the use of empirical relations, whilst trading accuracy to a limited extent, does enable the rapid assessment of design variants before comprehensive 3D FEA modelling is carried out.

Table4.11: Adjacent beams: Apportioned geometrical factors calculated using equation (4.20), and FEA software (ΔT = 40K)

t [μm]	w_h [μm]	w_c [μm]	gap [μm]	r [μm]	*f total*	f_h *apportioned*	f_c *apportioned*	*f 2D FEA total*	*f 2D FEA apportioned*	*f 2D FEA apportioned*	*deviation [%]*
30	140	140	60	5.41E-05	2.47	1.24	1.24	2.41	1.20	1.20	-2.81
30	140	250	60	8.91E-05	2.81	1.04	1.77	2.86	1.19	1.67	1.75
30	140	40	60	2.23E-05	2.15	1.58	0.56	2.10	1.37	0.73	-2.10
100	140	140	60	7.64E-05	2.69	1.35	1.35	2.70	1.35	1.35	0.30
100	140	250	60	1.11E-04	3.02	1.17	1.85	3.05	1.29	1.76	1.00
100	140	40	60	4.46E-05	2.38	1.61	0.76	2.35	1.45	0.90	-1.14

Comparing the values in Table 4.10 and Table 4.11, it can be seen that in the case of a beam thickness of 100 μm and a width of 140 μm the geometrical factor in isolation would be 2.11. If it is considered now as adjacent to another beam of the same dimensions (140 x 100 μm) and separated by a gap of 60 μm the partitioned geometrical factor is 1.35.

4.3.4.5. Determination of the conduction heat exchange coefficients

Two microbeams at different temperatures that are reasonably close to each other in comparison to their characteristic dimensions will exchange heat between them. The heat exchange between the surfaces is characterised by

$$q_{ex} = f_{ex} \kappa_{\infty} (T_h - T_c) dx \tag{4.24}$$

where T_c and T_h are the temperatures of the hotter and colder beams respectively, and f_{ex} is a geometrical factor that will depend on the temperature difference between the opposite beams, the gap dimensions, the fluid contained in the gap and the geometry of the surfaces.

For simplicity, consider that the heat transferred between the two surfaces of the coupled beams is similar to the heat exchange between two planar parallel plates at different temperatures. Provided that the beams are reasonably close to each other in comparison to their characteristic dimensions, then the geometrical factor is relatively straightforward to estimate, as the problem is similar to that of the capacitance of a semi-infinite strip line.

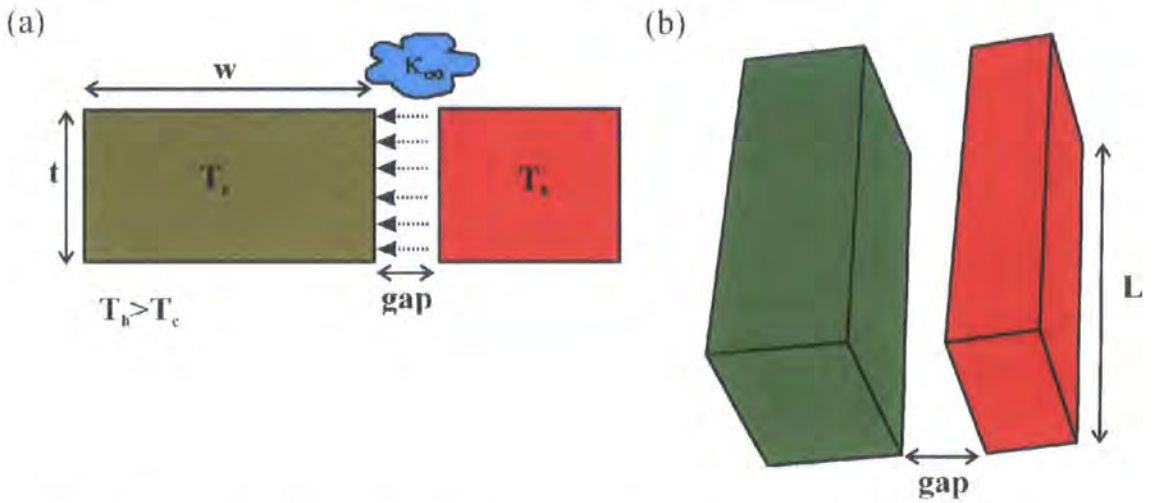

Fig. 4.15: Schematic heat transfer between beams. (a) Cross-sectional view of the adjacent beams (b) 3D view.

In the approximation where the separation, *gap*, is smaller than the thickness of the beams, t, the geometrical factor, *f*, can be given by

$$f_{ex} = \frac{t}{gap} \tag{4.25}$$

In the case where *gap* is larger than the thickness *t* (Fig. 4.15), then the following approximation, based upon geometrically equivalent formula for stripline capacitance, can be used to determine the geometrical factor [287].

$$f_{ex} = 1.21 + \frac{t}{gap} - 0.11\frac{gap}{t} + \frac{(1-\frac{gap}{2t})^6}{2} \tag{4.26}$$

However, the above formula does not consider the finite thickness of the beam and treats them as thin planes. Following a number of 2D FEA trials (Fig. 4.16), an empirical approximation has been derived that takes into account the thickness of the beam. The formula relies on the transformation of the real beam thickness, t, to a nominal value, t', to be applied in equation (4.26). If the width of the beam is w, then the transformation is

$$t' = t\left[\frac{1+1.4\frac{w}{t}+0.384\frac{w}{g}}{1+0.325\frac{w}{t}+0.55\frac{w}{g}}\right] \tag{4.27}$$

In the case of two coupled beams with different widths, then the value used is the average of the two.

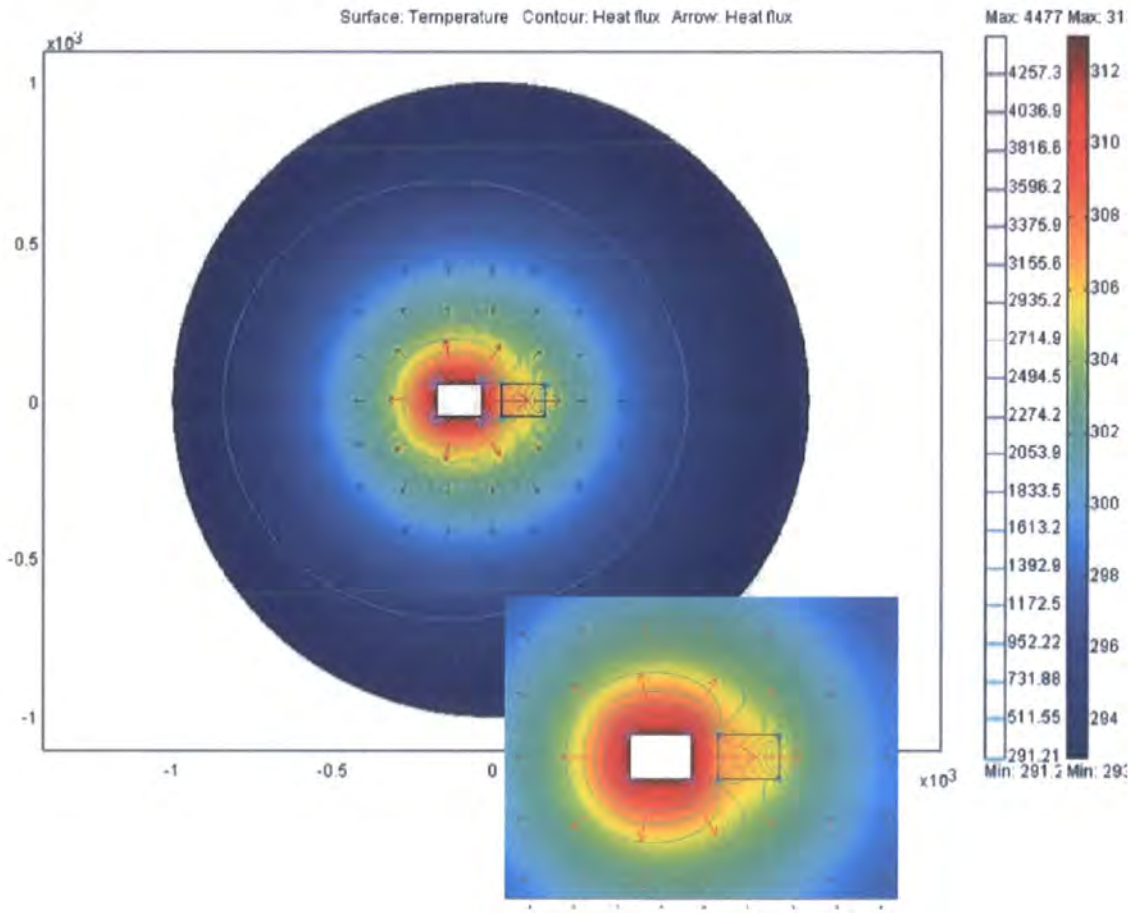

Fig. 4.16: 2D simulation for the validation of the heat exchange coefficients.

In this section, the possible contribution of radiation heat exchange between the beams has been ignored. The reason for this is that, at the scale of the microgripper (or in particular for the size of the gap ~60 μm), the intra-device radiation is negligible compared to conductive heat exchange.

Radiative heat exchange can exist between close proximity objects when there is a temperature difference. This might occur in between the cold and hot arms at temperatures T_c and T_h respectively. The radiative heat between bodies could be calculated using equation (4.28) [276], a modified version of the Stefan-Boltzmann law.

$$q_{ex\_rad} = \varepsilon\sigma F_{hc} t(T_h^4 - T_c^4)dx \approx 4\varepsilon\sigma F_{hc} t T_h^3 (T_h - T_c)dx \approx h_{ex\_rad} t(T_h - T_c)dx \qquad (4.28)$$

where F_{hc} is a radiation shape factor that takes into account the geometry of the beams and the gap. For the characteristic dimensions of the hot arm and a gap separation of 60 μm the values of F_{hc} have been calculated to be 0.25 and 0.5 for a beam thickness of 30 and 100 μm respectively [276]. For the length of the microgripper L= 2000 μm this leads to values of the radiation heat exchange between the surfaces two orders of magnitude smaller than the ones due to conduction heat exchange.

This result however is not valid for any size of gap. A general comparison between different heat mechanisms between surfaces separated by a fluid gap of different length scales was recently performed by Han et al. [288]. There it was demonstrated that thermal radiation between surface dominates at the macroscale (gap > 1 mm) and has an inflection point at approximately the micron range. Thermal radiation reduces with diminishing gap size from the macroscale to the microscale, but starts growing when microscale effects such as interference and tunnelling start having a major impact (gap < 1 μm) [288, 289]. When the size of the gap is equivalent or smaller than the dominant radiative wavelength at the temperature, the radiation heat transfer is intensified. In practice, this dimension is likely to be less than 100 nm.

These results suggest that for the scale of the microgripper the dominant phenomenon in between the hot and cold arm is a pure conduction mechanism, and that the use of conduction shape factors is justified.

4.3.5. Quantitative validation of the thermal analysis

Table 4.12 shows the comparison of the magnitude of the heat losses for a typical hot arm of the microgripper in the mesoscale (w =140 μm, t =100 μm) and for an eventual hot arm of the microgripper in the microscale (w = 14 μm, t = 20 μm). The contribution of conduction proportional to $f\kappa_{\infty}$, classical convection (mass transport i.e. h ~ $R_a^{1/4}$) proportional to h, and radiation proportional to h_{rad} at different temperatures, T=300, 350 and 400 K, has been calculated based on equations (4.13), (4.14), (4.18), (4.19) and (4.20).

Table 4.12: Comparison of the magnitude of the heat losses due to conduction, intra-device heat conduction, convection, and radiation at different temperatures T=300, 350 and 400 K.

Mesoscale

UNITS [W m^{-1} K^{-1}]	h_{cond}	h_{conv} ($\sim R_a^{1/4}$)	h_{rad}	h_{conv}/h_{cond} (%)	h_{rad}/h_{cond} (%)
300	106.6	22.0	6.1	20.6	5.7
350	106.6	38.0	9.7	35.7	9.1
400	106.6	44.0	14.5	41.3	13.6

Microscale

UNITS [W m^{-1} K^{-1}]	h_{cond}	h_{conv} ($\sim R_a^{1/4}$)	h_{rad}	h_{conv}/h_{cond} (%)	h_{rad}/h_{cond} (%)
300	443.8	30.0	6.1	6.8	1.4
350	443.8	52.0	9.7	11.7	2.2
400	443.8	60.0	14.5	13.5	3.3

At the microscale, for the range of temperatures between 293 K and 400 K, neglecting radiation and convection seems to be a good approximation as the heat losses represent in both cases less than 13% of the total heat lost by conduction.

At the mesoscale, for the range of temperatures between 293 K and 400 K, neglecting radiation heat losses seems a reasonably good approximation since the radiative heat losses represent less than 13% of the total heat by conduction. Convective heat losses, however, represent in some cases up to ~40% of the heat losses. The question is now whether it is reasonable to add the losses of convection (mass transfer) to the losses of conduction. This will be verified experimentally during the validation of the models in Chapter 6 (validation in section 6.3)

Based on these results, the analytical model presented in this thesis will not take into account the effects of heat radiation. However the contribution of conduction and convection heat losses will be considered. Hence, for an arbitrary infinitesimal volume of the microgripper, the balance 1D heat equation (4.8) defined in section 4.3, can be rewritten as

$$q_{gen} = (q_{COND}\big|_x - q_{COND}\big|_{x+dx}) + q_{cond} + q_{conv} \tag{4.29}$$

or

$$q_{gen} = -\Sigma \kappa_i A_i (\frac{d^2T}{dx^2})dx + (h_{cond} + h_{conv})(2w*t)\Delta T dx \quad (4.30)$$

Before concluding the thermal analysis a last hypothesis must be checked. The thermal behaviour of the microgripper has been described using a 1D model along the x-axis. Intrinsic to this assumption is that the heat flow along the beam length is relatively large in comparison to the heat flow in the orthogonal directions, i.e. y and z.

To check this hypothesis it is possible to calculated the Biot number, Bi, in the y and z direction using the formulae

$$Bi = \frac{h_{cond} L_j}{\kappa} \quad (4.31)$$

where h_{cond} is the conduction coefficient of heat transfer to the ambient and L_j (j=y, z) is the characteristic length along the y- and z-directions, and κ is the thermal conductivity of the beam.

The Biot number relates the heat transfer resistance inside and at the surface of a body. Using the values of h_{cond} shown in Table 4.12, and a value of 0.2 W m^{-1} K^{-1} for the thermal conductivity of SU8 it can be seen that the values of Bi are much smaller than unity, generally of the order of 10^{-2}-10^{-3}. Therefore a 1D thermal conduction model is appropriate to describe the thermal behaviour of the microgripper.

4.4. 1D electrothermal analytical model

The end goal of the analytical model is to be able to calculate the steady state temperature distribution, *T(x),* along the device under Joule heating.

4.4.1. General electrothermal definitions

A simplified representation of a generic microgripper to be modelled is shown in Fig. 4.17. In order to further simplify the calculations, only one half of the microgripper around its symmetry plane will be modelled. Current is injected into the metallisation

layer and joule heating leads to differential heating and expansion in the different parts of the structure.

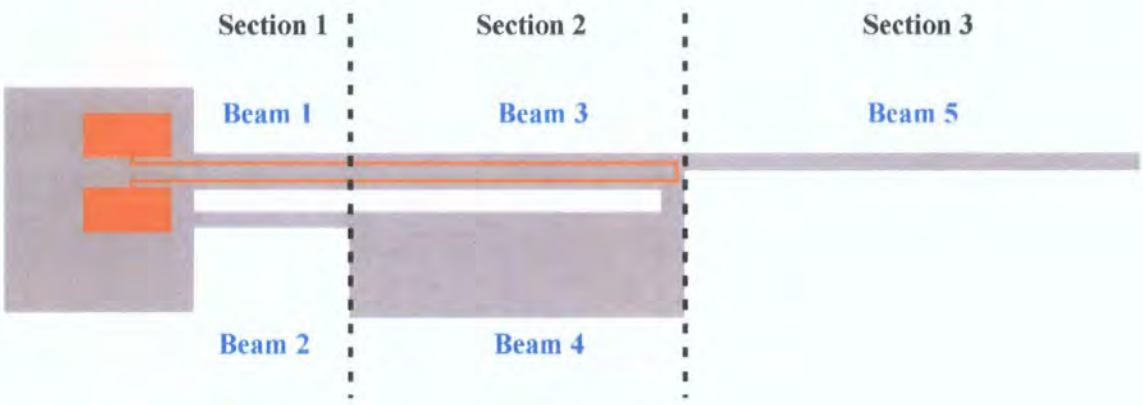

Fig. 4.17: Sketch of the actuator to be modelled.

For the purposes of modelling, the microgripper is split into 3 sections. Section 1 comprises part of the "hot arm", labelled Beam 1 and the flexure, labelled Beam 2. In Section 2, the remaining portion of the hot arm (Beam 3) lies adjacent to the cold arm (Beam 4). The reason the hot arm is given two distinct identities despite being uniform across both cross sections, is that the heat transferred from adjacent flexure or cold arm regions gives the hot arm distinct thermal profiles in each section. Finally, section 3 includes the unheated gripper arm (Beam 5).

When developing the model the following aspects will be considered:

- All temperatures, T(x), in the model are taken to be relative to the ambient.

  $$T(x) = \Delta T_{abs}(x) = T_{abs}(x) - T_{\infty} \tag{4.32}$$

  where $T_{abs}(x)$ is the absolute temperature.

- For the hot arm of the microgripper, the thin metal layer provides a substantial contribution to the overall thermal conduction path. Therefore, in line with the approach underlying the 1-D model, the metal and dielectric conduction paths are simply aggregated under the assumption that the temperatures are uniform within the section (see equation (4.7)).

- The temperature dependence of the resistivity will not be explicitly included in the model. For practical purposes, the resistivity will be considered a constant parameter $\rho(T,x) = \rho$, along the length of the hot arm and for a given current level. The latter will permit obtaining a closed form solution for the heat equation. During the simulations, this dependency will be considered in an iterative manner i.e. using an adjusted value of the resistivity for each range of current and expected average temperatures.

- The temperature dependence of the thermal conductivity of the surrounding ambient will not be explicitly included in the models. For practical purposes, the thermal conductivity will be considered as a constant parameter, $\kappa(T) = \kappa$, for a given current level. During the simulations, this dependency will be considered in an iterative manner i.e. using a look-up table of property values of the thermal conductivity at corresponding current levels and expected temperature ranges.

The combination of equations (4.9), (4.12), (4.19) and (4.24), expressed in heat per unit length, yields the following second-order partial differential equation

$$\kappa A \frac{d^2T}{dx^2} - f\,\kappa_\infty T - f_{ex}\kappa_\infty (T - T_c) = \frac{I^2\rho}{A_{Au}} = q'_{gen} \tag{4.33}$$

where q'_{gen} is the heat generated per unit length.

Equation (4.33) defines the governing 1D steady-state heat equation for a typical microbeam of temperature T separated by a distance, gap ($f_{ex} = f_{ex}(gap)$), from another microbeam of temperature T_c. This equation can be used to solve the thermal behaviour of a Joule heated beam.

In the following sections, equation (4.33) will be solved considering different boundary conditions at the anchor points and different system configurations. In particular, the analysis performed for a single microbeam will be extended to cover multiple beams.

4.4.2. Single beam model

To illustrate the working principle of the simple analytical model, a single beam system will be simulated before dealing with more complex structures. This case, $f_{ex} = 0$, and the general solution to equation (4.33) is given by

$$T(x) = T_0 + A'\cosh(\frac{x}{l_{th}}) + B'\sinh(\frac{x}{l_{th}}) \tag{4.34}$$

where

$$l_{th} = \sqrt{\frac{\kappa A}{\kappa_\infty f}} \tag{4.35}$$

$$T_0 = \frac{q'_{gen} l_{th}^2}{\kappa A} = \frac{q'_{gen}}{\kappa_\infty f} \tag{4.36}$$

and A' and B' are constants of integration dependent on the boundary conditions.

The parameter, l_{th}, is very useful, as it is a characteristic parameter that describes the useful length of a thermal beam. For a given q'_{gen}, the average temperature of the beam increases with increasing length, l, and then reaches a saturation value T_0, where $l>l_{th}$. That is to say, for $l<l_{th}$, thermal conduction to the anchors dominates; for $l>l_{th}$ thermal conduction to the ambient dominates. If the device efficiency was measured by the total length expansion of the beam, then for a given geometry, the device increases linearly with length for $l<l_{th}$, but saturates at higher values of l, where $l>l_{th}$.

It is instructive to calculate l_{th} for different materials. For example, nickel and SU8 (gold resistor) for a representative value of the section A = 1800 μm^2. Assuming that f is 1.16, then for nickel l_{th}= 1887 μm in air and for SU8 it is considerably smaller, l_{th}= 109 μm. The implication of this is that efficient devices in SU8 can be created using smaller structures than would be the case for nickel. Where the surrounding medium is water, the characteristic lengths are about a factor of five lower.

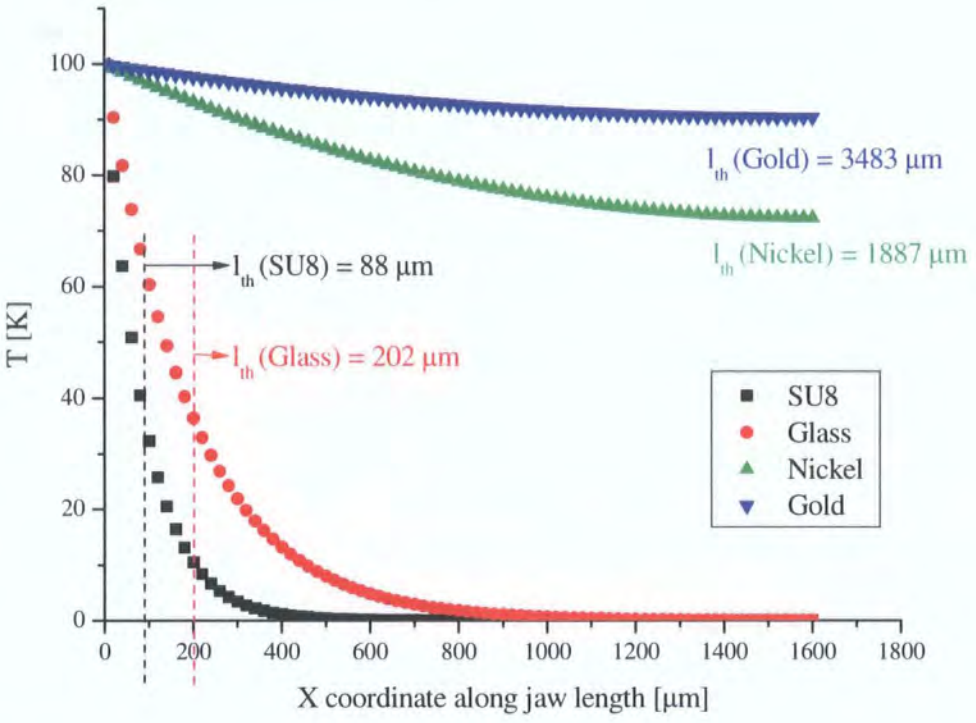

Fig. 4.18: Temperature decay along the length of the jaw for different beam materials. T_0 = 100 °C

Equation (4.34) can be directly used to solve the temperature distribution and the heat conducted into the Beam 5, the extended prong of the microgripper, in Fig. 4.17. In this case $q'_{gen} = 0$. Assuming that one end of the beam is maintained at a constant temperature, $T_5(0)=T_{50}$, that the beam length is L_5, and that the temperature gradient is zero, at the remote end $dT_5/dx\ |_{x=L}=0$ (no longitudinal heat conduction into air at the end). The temperature is given by

$$T_5(x) = A'\cosh(\frac{x}{l_{th}}) + B'\sinh(\frac{x}{l_{th}}) \tag{4.37}$$

where

$$A' = T_{50} \tag{4.38}$$

and

$$B' = -T_{50}\tanh(L_{50}/l_{th}) \tag{4.39}$$

The temperature gradient at the origin is B'/l_{th} and it is easy to calculate the heat conducted into the beam at the origin:

$$q_5 = \frac{\kappa A \tanh(L_5 / l_{5th}) T_{50}}{l_{5th}} \tag{4.40}$$

For this particular configuration l_{th} indicates the length along the jaw at which the initial temperature has decayed by 63%. Fig. 4.18 shows the decay of temperature from an initial temperature of 100 °C above ambient. As can be seen, the length of the jaws built in metals such as nickel, commonly used in thermal actuators, should be at least 1887 μm in order to remain close to ambient temperature at the ends.

4.4.3. Coupled beam model

In the structure to be modelled in detail, it is important to be able to model beams that are adjacent. In this instance, heat transfer occurs between the beams as well as into the ambient. Equations (4.41) is a set of coupled equations describing the behaviour of two adjacent beams

$$\begin{aligned} \kappa A_h \frac{d^2 T_h}{dx^2} - C_h T_h - C_{hc}(T_h - T_c) + P_{hl} = 0 \\ \kappa A_c \frac{d^2 T_c}{dx^2} - C_c T_c + C_{hc}(T_h - T_c) + P_{cl} = 0 \end{aligned} \tag{4.41}$$

where κA_h and κA_c are the aggregate thermal conduction for the hot and cold arms respectively, T_h is the temperature (above ambient) of beam 1 (hot arm) and T_c is the temperature of beam 2 (cold arm), $C_h = f_h \kappa_\infty$ and $C_c = f_c \kappa_\infty$ are the heat loss coefficients to the ambient from the beams 1 and 2 respectively, $C_{hc} = f_c \kappa_\infty$ is the heat transfer coefficient that characterises the heat exchange between the two beams. Finally, P_{hl} and P_{cl} are the heat generated per unit length for each arm.

The above equation system can be solved by matrix algebra and choosing a linear superposition of T_h and T_c. Equation (4.41) can be expressed in a matrix form as

$$\frac{d^2}{dx^2}\begin{bmatrix} T_h \\ T_c \end{bmatrix} = \begin{bmatrix} \left(\frac{C_h + C_{hc}}{\kappa A_h}\right) & \left(-\frac{C_{hc}}{\kappa A_h}\right) \\ \left(-\frac{C_{1hc}}{\kappa A_c}\right) & \left(\frac{C_c + C_{hc}}{\kappa A_c}\right) \end{bmatrix} \begin{bmatrix} T_h \\ T_c \end{bmatrix} - \begin{bmatrix} \left(\frac{P_{hl}}{\kappa A_h}\right) \\ \left(\frac{P_{cl}}{\kappa A_c}\right) \end{bmatrix} \tag{4.42}$$

Or equivalently,

$$\frac{d^2}{dx^2}\mathbf{T} = \mathbf{MT} - \mathbf{P} \tag{4.43}$$

The above matrix representation can be diagonalised by a suitable transformation

$$\begin{bmatrix} T_h \\ T_c \end{bmatrix} = \begin{bmatrix} \varepsilon_{11} & \varepsilon_{21} \\ \varepsilon_{12} & \varepsilon_{22} \end{bmatrix} \begin{bmatrix} T_h \\ Tc \end{bmatrix}' \tag{4.44}$$

By solving for the eigenvalues of the matrix described by equation (4.44), the coupled equations can be separated giving two solvable equations in T'_h and T'_c.

$$\frac{d^2}{dx^2}\boldsymbol{\varepsilon}\mathbf{T}' = \mathbf{M}\boldsymbol{\varepsilon}\mathbf{T}' - \mathbf{P} \quad \text{and} \quad \frac{d^2}{dx^2}\boldsymbol{\varepsilon}^{-1}\boldsymbol{\varepsilon}\mathbf{T}' = \boldsymbol{\varepsilon}^{-1}\mathbf{M}\boldsymbol{\varepsilon}T' - \boldsymbol{\varepsilon}^{-1}\mathbf{P} \tag{4.45}$$

By choosing ε to be a matrix of column eigenvectors for M we can rewrite the above equation:

$$\frac{d^2}{dx^2}\mathbf{T}' = \boldsymbol{\varepsilon}^{-1}\mathbf{M}\boldsymbol{\varepsilon}T' - \boldsymbol{\varepsilon}^{-1}\mathbf{P} = \boldsymbol{\lambda}\mathbf{T}' - \boldsymbol{\varepsilon}^{-1}\mathbf{P} \tag{4.46}$$

where λ is a diagonal matrix of eigenvalues:

$$\boldsymbol{\lambda} = \begin{bmatrix} \lambda_1 & 0 \\ 0 & \lambda_2 \end{bmatrix} \tag{4.47}$$

and finally

$$\frac{d^2T'_h}{dx^2} = \frac{T'_h}{l_h^2} - \varepsilon_{11}^{-1}\frac{P_{hl}}{kA_h} - \varepsilon_{21}^{-1}\frac{P_{cl}}{kA_c} \quad \text{where} \quad \lambda_1 = \frac{1}{l_h^2} \tag{4.48}$$

$$\frac{d^2T'_c}{dx^2} = \frac{T'_c}{l_c^2} - \varepsilon_{12}^{-1}\frac{P_{hl}}{kA_h} - \varepsilon_{22}^{-1}\frac{P_{cl}}{kA_c} \quad \text{where} \quad \lambda_2 = \frac{1}{l_c^2} \tag{4.49}$$

To which the solutions are:

$$T'_h = A\cosh\left(\frac{x}{l_h}\right) + B\sinh\left(\frac{x}{l_h}\right) + \varepsilon_{11}^{-1}\frac{P_{hl}l_h^2}{kA_h} + \varepsilon_{21}^{-1}\frac{P_{cl}l_h^2}{kA_c} \tag{4.50}$$

$$T'_c = C\cosh\left(\frac{x}{l_c}\right) + D\sinh\left(\frac{x}{l_c}\right) + \varepsilon_{12}^{-1}\frac{P_{hl}l_c^2}{k\,A_h} + \varepsilon_{22}^{-1}\frac{P_{cl}l_c^2}{kA_c} \tag{4.51}$$

A, B, C, D are constants which are required to fit the initial boundary conditions of continuity of temperature and heat flux.

The original (untransformed) temperatures, T_h and T_c, are calculated using $\boldsymbol{\varepsilon}$, the matrix set out in equation (4.44). All 1D calculations presented in the following sections are performed using a simple spreadsheet tool.

4.4.4. Modelling the microgripper

The complete modelling of the microgripper requires 3 sets of equations: 2 coupled beam model (equation 4.41) and one single beam model (equation (4.34), corresponding to each of the three sections illustrated in Fig. 4.17. In total there are five separate temperature distributions to calculate, T_1, T_2, T_3, T_4, T_5.

Fig. 4.19: Summary of boundary conditions used in the simulations.

The link between the separate equations describing each zone is defined by a set of boundary conditions assuming a continuous temperature distribution and continuity of heat flow (Fig. 4.19). Furthermore it is assumed that the anchor is thermally grounded with respect to the ambient. From solutions (4.37) and (4.50), (4.51), the single beam equation carries two unknowns, A', B' and the two coupled equations four each, A, B, C, D (E, F, G, H). In total there are 10 unknowns to be determined to define the temperature distribution absolutely and these correspond to the 10 defining boundary conditions set out below in Table 4.13.

Table 4.13: Summary of boundary conditions.

Number	Location	Boundary condition	Comment
1	At the anchor	$T_1 = 0$	Anchor thermally grounded
2	At the anchor	$T_2 = 0$	Anchor thermally grounded
3	Boundary Zone 1: Zone 2	$T_1 = T_3$	Continuous temperature distribution
4	Boundary Zone 1: Zone 2	$T_2 = T_4$	Continuous temperature distribution
5	Boundary Zone 1: Zone 2	$k_1 A_1 \frac{dT_1}{dx} = k_3 A_3 \frac{dT_3}{dx}$	Continuity of heat flow
6	Boundary Zone 1: Zone 2	$k_2 A_2 \frac{dT_2}{dx} = k_4 A_4 \frac{dT_4}{dx}$	Continuity of heat flow
7	Boundary Zone 2: Zone 3	$T_3 = T_5$	Continuous temperature distribution
8	Boundary Zone 2: Zone 3	$T_4 = T_5$	Continuous temperature distribution
9	Boundary Zone 2: Zone 3	$k_3 A_3 \frac{dT_3}{dx} = k_4 A_4 \frac{dT_4}{dx} k_5 A_5 \frac{dT_5}{dx}$	Continuity of heat flow
10	End of extended arm	$k_5 A_5 \frac{dT_5}{dx} = 0$	Continuity of heat flow - negligible axial flow of heat into the ambient

4.4.5. Validation of the 1D electrothermal model using FEA simulation

The results provided by the proposed 1D electrothermal model can be compared with the results obtained from finite element analysis (FEA) using the commercial software CoventorWare™ [290]. This software is able to solve highly coupled electrothermal problems, however, the options available to implement the heat losses to the surrounding ambient (e.g. air) are limited. The only way of representing those heat losses by conduction as opposed to convection is by simulating a sufficiently big mass of air around the structure. The air has to be modelled using conductive elements and therefore ignoring its fluidic properties. Although this method provides reasonably good results, this process is highly time consuming (> 6 hours per simulation) compared with the analytical model.

The geometry and characteristic dimensions of the microgripper and material properties used in the analytical and FEA simulations are shown in Fig. 4.20, and in Table 4.14 and Table 4.15. The FEA simulations were performed using a Manhattan meshing with hexahedral second order elements. The elements were rectangular in shape with dimensions 100 x 100 x 100 μm and with a maximum and minimum number of elements per edge of 20 and 2 respectively. The air has been modelled with approximately 85000 volume elements.

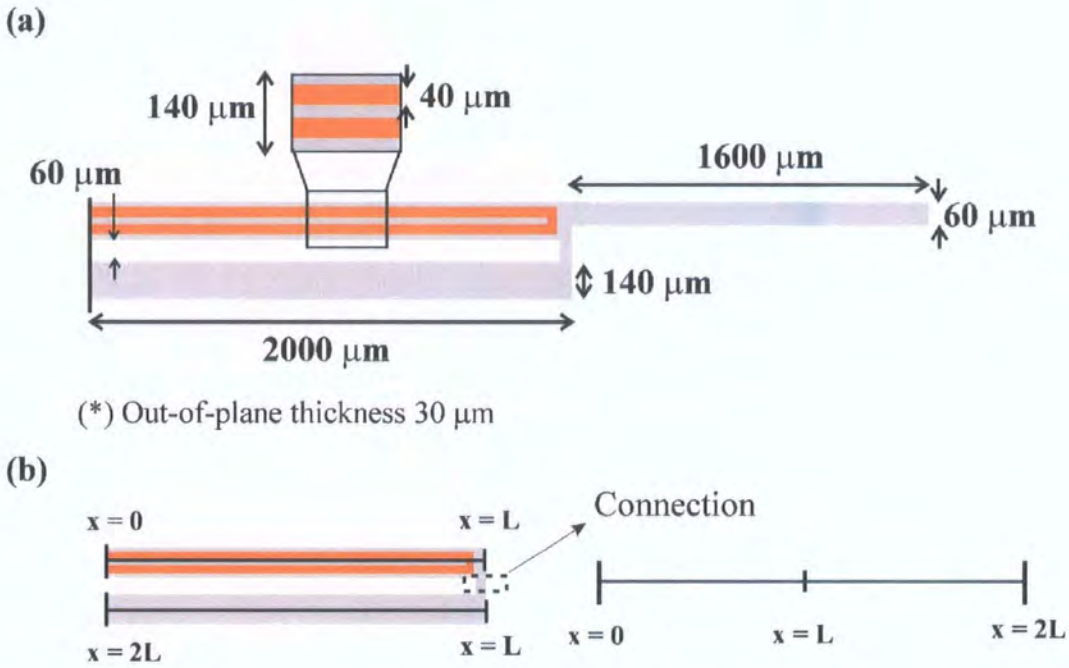

Fig. 4.20: (a) Geometry and characteristic dimensions used during the FEA validation of the analytical model (b) Unfolded coordinate system for x.

Table 4.14: Material properties used during the FEA (CoventorWare™) simulations.

Material properties FEA	SU8	Au	Air
E [MPa]	$4.4 * 10^3$	$5.7 * 10^4$	-
Poisson	0.22	0.35	-
TCE [1/K]	$5.2 * 10^{-5}$	$1.2 * 10^{-6}$	-
κ [pW/ μm K]	$2 * 10^5$	$297 * 10^5$	-
σ_0 [pS/ μm]$^{(*)}$	-	$5.022 * 10^{13}$	-
κ_0 [W/ m K]$^{(**)}$	-	-	0.025642

$^{(*)}$ $4*10^{-11} T^4 - 1*10^{-7} T^3 + 1*10^{-4} T^2 - 0.0647 T + 16.011$

$^{(**)}$ $72 * 10^{-6} + 0.025642 T$

Table 4.15: Parameters used during the analytical simulations.

Analytical model parameters	Values
f_h	1.23
f_c	1.23
f_{ex}	1.49
f_{jaw}	1.8
ρ_0[W m]$^{(*)}$	$2.53*10^{-8}$
κ_0 [W/ m K]$^{(**)}$	0.025642

$^{(*)}$ TCR = 0.0039 K^{-1}

$^{(**)}$ $72 * 10^{-6} + 0.025642 T$

Fig. 4.21 and Table 4.16 show the comparison between the values obtained for the characteristic temperatures of the microgripper model by FEA and analytical simulation under different system configurations. The reason why, in the FEA models, the temperature seems not to be continuous between the hot and cold arms is because the decay of the temperature along the connection has not been represented in the graphs (see coordinate system in (Fig. 4.20 (b)).

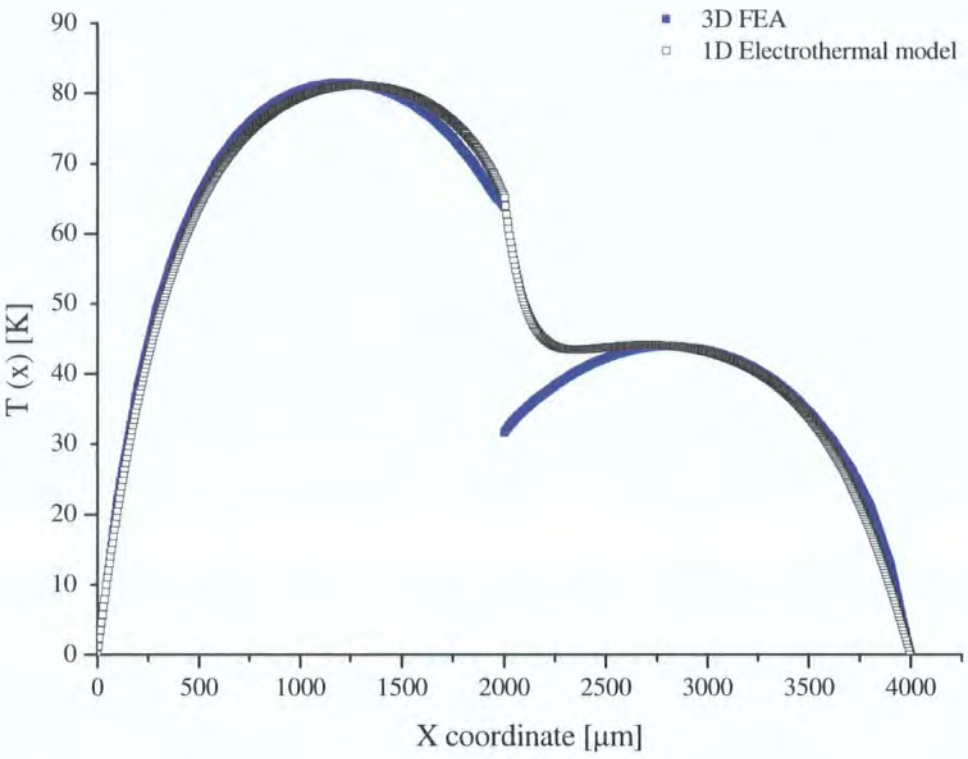

Fig. 4.21: Simulated (FEA vs. Analytical) temperature profile developed along the hot and cold arms of a single heated arm actuator (I = 30 mA). (X coordinate unfolded (Fig. 45.20 (b))

The results in Fig. 4.21 have been obtained by applying 30 mA of input current and using

- in the FEA analysis, a constant value of the thermal conductivity of the ambient, i.e. $\kappa_\infty = constant$, and a variable value of the resistivity that depends on the temperature and therefore on the position x along the length of the hot arm, *i.e.* $\rho = \rho(x, T)$.

- in the analytical model, constants values of the thermal conductivity of the ambient and the resistivity. They both will depend on the temperatures of the device (T_{ave_FEA}) calculated by FEA as in the previous bullet point, i.e. $\kappa_\infty = \kappa_\infty (T_{ave\ FEA}) = constant$, and $\rho = \rho\ (T_{av\ FEA}) = constant$.

The results obtained from the FEA simulations are interesting because they enable one to check how the variation of temperature along the length of the hot arm affects the value of the resistivity and therefore, the final temperature distribution.

Table 4.16: Average temperatures calculated for the hot and cold arms of the actuators calculated with analytical and FEA models.

	20 mA			30 mA			40 mA		
Model [K]	T_h	T_c	ΔT	T_h	T_c	ΔT	T_h	T_c	ΔT
FEA $\rho=\rho(x,T)$; κ_∞ = **Constant**	26	15	11	68	39	29	159	92	67
FEA $\rho=\rho(x,T)$; $\kappa_\infty = \kappa_\infty(x,y,z,T)$	25	14	11	64	37	27	131	79	52
Analytical $\rho=\rho(T_{ave\_FEA})$; $\kappa_\infty = \kappa_\infty(T_{ave\_FEA})$	29	16	13	72	38	34	143	76	67
IR measurements	30	16	14	73	40	33	144	81	63

As can be seen from Fig. 4.21, at moderate temperatures (<80 °C above ambient), there is a good agreement between analytical and FEA models even if the variation of the thermal conductivity in the FEA model is not considered, i.e. if $\kappa_\infty(x, y, z, T) = \kappa_0$. At higher temperatures obtained using 40 mA current (Table 4.16), however, if thermal conductivity is kept constant in the FEA simulations, the results start to diverge, giving higher temperature in the FEA analysis. The opposite happens when the value of the thermal conductivity to the ambient depends on temperature ($\kappa_\infty = \kappa_\infty(x, y, z, T)$ (second line Table 4.16). In this case, the overall temperatures provided by the FEA simulations are lower than the ones predicted by the analytical model. Actually, the

analytical model seems to provide temperatures in the range between both FEA models. As an indication, IR measurements of the temperature[9] are also included in Table 4.16.

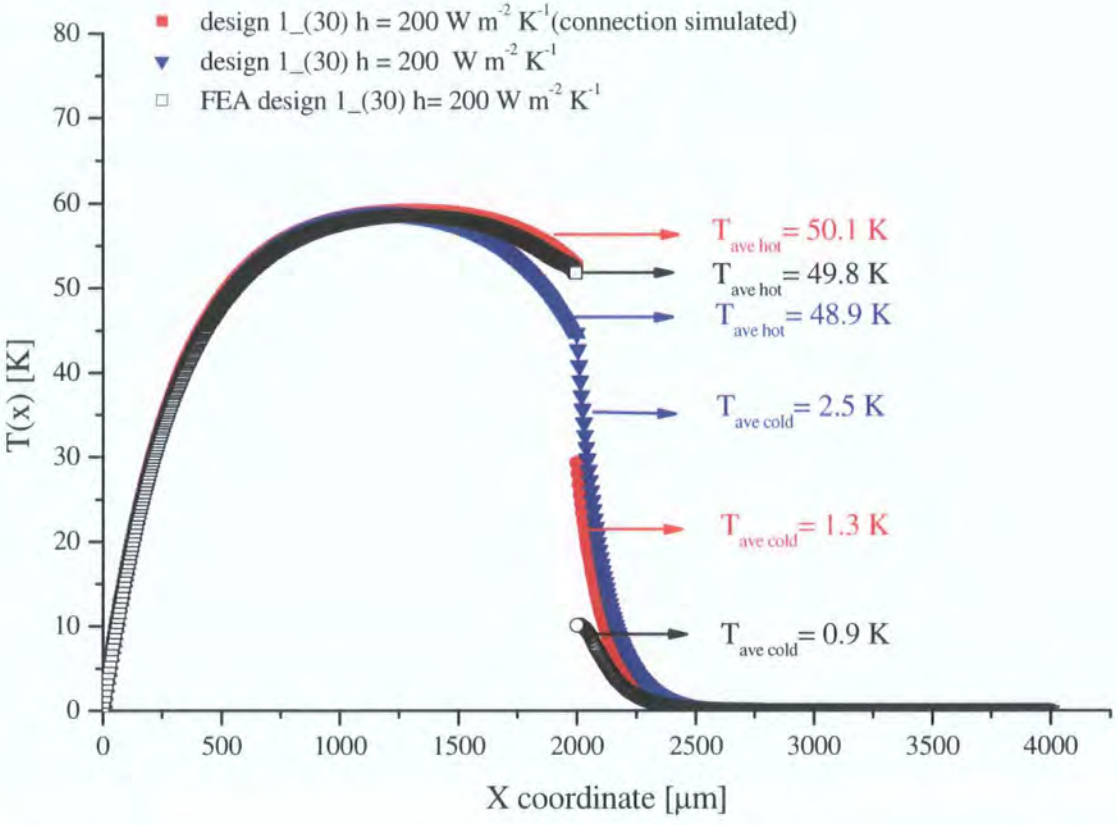

Fig. 4.22: Simulated (FEA vs. Analytical) temperature profile developed along the hot and cold arms when the heat exchange between the arms is not considered actuator (I = 30 mA).

In the final part of this section, the agreement between FEA and analytical models has also been checked under the assumption that there is no heat exchange between the arms (Fig. 4.22). The validation of the 1D model in this way is necessary if the model is intended to be used for the simulation of a device built in a highly electrical and thermally conductive material where heat losses to the anchors are dominant. Under those assumptions, the heat exchange coefficient becomes $f_{ex} = 0$, and the heat transfer coefficients f_i $(i = h\ c)$ are calculated as explained in section 4.3.4.3. When there is not air in between the arms of the actuators, the FEA simulations can be done faster without simulating the air but instead just introducing a convection coefficient as a boundary condition.

[9] The measurements will be explained in detail in Chapter 5.

Also shown in Fig. 4.22 is the comparison of the results when the connection bridge (see Fig. 4.20 (b)) is considered. The connection can be included in the analytical model by slightly modifying the boundary conditions to the equation system (4.41) (Table 4.13). In all the simulations, an input value of the current of 30 mA and a constant value of the heat losses to the air has been considered (h = 200 W m^{-2} K^{-1}). All of the models show a very good agreement but it can be seen that the results provided by the analytical model are slightly more accurate when the connection bridge is taken into account. In all of the simulations in this thesis the connection bridge will be considered.

4.4.6. Proposed electrothermal modelling technique

During the validation of the analytical model (section 4.4.5), the value of the material properties, resistivity of the metallisation and thermal conductivity of air, were fixed and based on the average temperatures predicted by the FEA model, at a given input current (T_{ave_FEA}). However, for a useful analytical tool it is important that the electrothermal model is able to correctly predict the temperature without the requirement of any external FEA or experimental data.

In the following points, a modelling methodology is proposed to include, in an iterative manner, the dependency of the material properties with temperature.

1. The simulations start at the minimum current level, I_0, or where relatively small temperatures are expected, in the case presented here I_0 = 20 mA. Initially standard properties of the conductive layer and ambient air are introduced. Three initial property values are required in the model: the resistivity of the metallisation at ambient temperature, ρ_0, the temperature coefficient of resistance, TCR, and the thermal conductivity of the surrounding atmosphere at ambient temperature, κ_0.

2. At I_0 = 20 mA, the model will generate different temperature outputs (ΔT, T(x), T_{max}, etc.) among which are the average temperature of the hot arm, T_h, and the average temperature of the cold arm, T_c. These values will be then used to calculate, $\rho(T_h, I_0)$ and $\kappa_\infty(T_c, I_0)$. These new property values will be introduced,

in a second run of the model, and the definitive values for the temperature distribution at I_0 will be calculated and recorded.

3. A new current level, I_1, 2 mA apart from the initial value, will be introduced as a second input to the model. The last values used for the resistivity and the thermal conductivity i.e. $\rho(T_h, I_0)$ and $\kappa(T_c, I_0)$, will be used as material properties for the first run. As in point 2, the resulting temperature outputs will be used to recalculate $\rho(T_h, I_1)$ and $\kappa(T_c, I_1)$, and the new temperature distributions will be calculated and recorded.

4. The same procedure can be repeated until the upper limit of input currents for the simulations is reached.

4.5. 1D mechanical model

4.5.1. Basic analysis and background

The analysis presented in this section is used to calculate the static deflection of a beam and apply that to the more complex situation where multiple beams are connected.

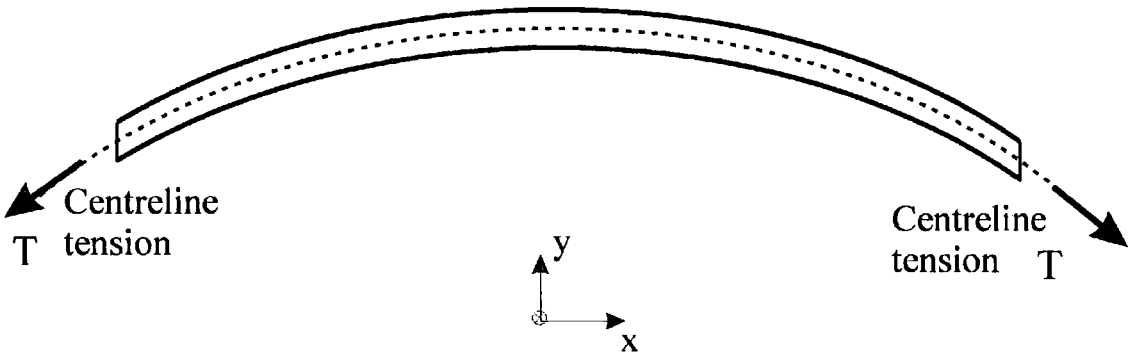

Fig. 4.23: Mechanics of a simple beam

Since the problem is a static one, then in the case of equilibrium all forces and moments on the beam must necessarily be equal to zero. It is also assumed that beam theory can be applied, i.e. that the thickness (y direction (Fig. 4.23)) of the beam is small compared to the length, and therefore certain simplifying assumptions may be made.

For a simple cantilever beam of thickness, t, whose centreline tension is T (Fig. 4.23), the force per unit volume is given by [291] (beam-column equation)

$$F = T\frac{\partial^2 y}{\partial x^2} + \frac{Et^2}{12}\frac{\partial^4 y}{\partial x^4} = 0 \tag{4.52}$$

where E is the Young's modulus and T the centreline tension.

The thickness term, t, is always defined to be in the same direction as that of the deflection. The first term in equation (4.52) is essentially a buckling term, as the centreline tension itself is proportional to any distortion for a beam that is constrained in some way. Thus it is a non-linear term. The second term is the linear flexure term (Euler-Bernoulli equation). That the first term is a non-linear term can be seen as follows:

For a beam constrained at both ends then the centreline tension can be approximated to when the deflections are small compared to the length of the beam

$$T = \frac{E}{2}\left\langle\left(\frac{\partial y}{\partial x}\right)^2\right\rangle \tag{4.53}$$

Thus the overall force can be rewritten as

$$F = \frac{E}{2}\left\langle\left(\frac{\partial y}{\partial x}\right)^2\right\rangle\frac{\partial^2 y}{\partial x^2} + \frac{Et^2}{12}\frac{\partial^4 y}{\partial x^4} = 0 \tag{4.54}$$

To appreciate the order of contribution of each of the terms we can assume that there is a small deflection of Δy in a beam of length l. Then the forces are of the following order

$$F \approx \frac{E}{2}\frac{\Delta y^3}{l^4} + \frac{Et^2}{12}\frac{\Delta y}{l^4} \tag{4.55}$$

Clearly the centreline tension produces a non-linear or buckling term. It can, however, be ignored if the deflection is small. The ratio of the two terms is given by:

$$\frac{F_{buckling}}{F_{flexure}} \approx 6\frac{\Delta y^2}{l^2} \tag{4.56}$$

The conclusion is therefore that the problem can be reduced to a simple linear flexure problem, if the deflection is small compared to the thickness of the beam. With this assumption, the force is given by

$$F = \frac{Et^2}{12}\frac{\partial^4 y}{\partial x^4} \tag{4.57}$$

The solutions to this are:

$$y = Ax^3 + Bx^2 + Cx + D \tag{4.58}$$

Otherwise, the more general solution to (4.52) is of the form

For positive T, (i.e. tensile stress and positive strain (ε>0))

$$y = A\cos kx + B\sin kx + Cx + D \qquad \text{where} \quad k = \sqrt{\frac{12T}{Et^2}} = \frac{1}{t}\sqrt{12\varepsilon} \tag{4.59}$$

For negative T (i.e. compressive stress and negative strain ((ε<0))

$$y = A\cosh kx + B\sinh kx + Cx + D \qquad \text{where} \quad k = \sqrt{\frac{-12T}{Et^2}} = \frac{1}{t}\sqrt{-12\varepsilon} \tag{4.60}$$

In order to calculate the boundary conditions at specific interfaces, it is useful to know the bending moment (couple) and shear force contributed by the beam

$$Bending\ Moment = -\frac{Et^3 w}{12}\frac{\partial^2 y}{\partial x^2} \tag{4.61}$$

where w is the width of the beam (perpendicular dimension)

$$Shear\ Force = -\frac{Et^3 w}{12}\frac{\partial^3 y}{\partial x^3} \tag{4.62}$$

4.5.2. Problem Definition

In this section the mechanical modelling of the microgripper, or rather the modelling of a single actuator element, will be presented. The simplest method for obtaining a closed solution is to impose a centreline strain on the hot arm, ε_h. Ultimately, this leads to a solution for the deflection of the entire system. This solution can then be analysed to determine the unstrained relative expansion of the two arms, which in turn can be used to calculate the average temperature difference between the two arms. Ideally, the average temperature difference itself would be the starting point of the solution, since this represents the output of any thermal modelling. However, it is much more difficult to produce a closed form solution from this starting point.

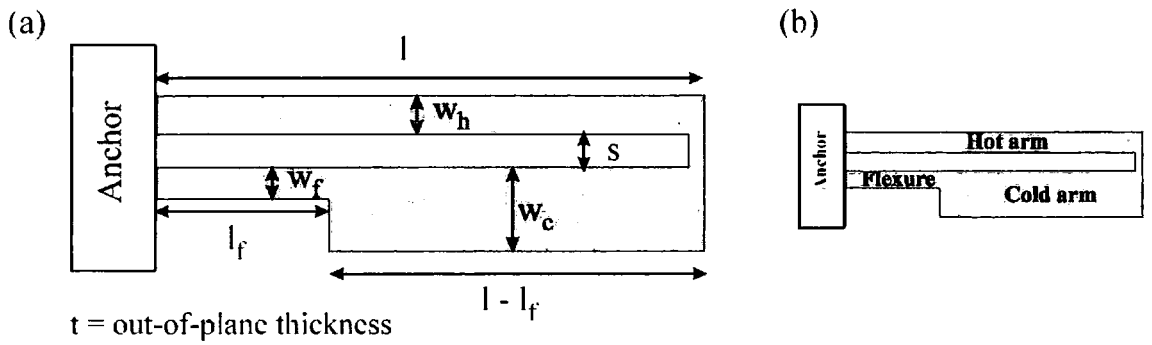

Fig.4.24: Sketch of the actuator for the mechanical model (a) Characteristic dimension (b) Actuator sections

In modelling the actuator shown in Fig. 4.24, the beam thickness, *t*, of the three beam elements, is the dimension in the direction of the deflection. So in the case of the microgripper, with an in-plane deflecting actuator, the thickness represents the horizontal dimension i.e. the width *w* of the beams.

Overall the solution of the problem is split into three separate regions (Fig. 4.24 (b)): hot arm, flexure, and cold arm each defined by the equations (4.59) or (4.60) with *t* substituted by *w*. In total there are 12 unknowns of integration.

The general solution for the hot arm ($\varepsilon<0$)

$$y = A_h \cos k_h x + B_h \sin k_h x + C_h x + D_h \qquad \text{where} \quad k = \frac{1}{w_h}\sqrt{-12\varepsilon_h} \tag{4.63}$$

The general solution for the flexure (ε>0)

$$y = A_f \cos k_f x + B_f \sin k_f x + C_f x + D_f \qquad \text{where} \quad k = \frac{1}{w_f}\sqrt{12\varepsilon_f} \tag{4.64}$$

The general solution for the cold arm (ε>0)

$$y = A_c \cos k_c x + B_c \sin k_c x + C_c x + D_c \qquad \text{where} \quad k = \frac{1}{w_c}\sqrt{12\varepsilon_f} \tag{4.65}$$

Boundary conditions are necessary to define the values of the coefficients. Where beams join, static equilibrium dictates there should be no net bending moment or shear force and continuity may require that where beams join (e.g. flexure and cold arm) the relevant deflections and gradients are continuous. The point at the anchors where the hot arm and flexure start represents the origin, i.e. x = 0.

4.5.3. Boundary conditions

In this problem, it is assumed that the strain in the hot arm is negative, i.e. it is under compression. The corresponding strain at the flexure, ε_f, is governed by the fact that the net force on the anchors must be zero for a static problem.

$$Ew_h t\varepsilon_h + Ew_f t\varepsilon_f = 0 \qquad \text{and} \quad \varepsilon_f = -\frac{w_h}{w_f}\varepsilon_h \tag{4.63}$$

i.e. the flexure arm is under tension.

At the anchors, which we define as being at x = 0, there are a total of six boundary conditions. Both hot arm and flexure are established to have zero displacement and zero gradient at the anchors, i.e.

$$y_h(0) = 0 \tag{4.64}$$

$$y_f(0) = 0 \tag{4.65}$$

$$\frac{\partial y_h}{\partial x}\Big|_{x=0} = 0 \tag{4.66}$$

$$\frac{\partial y_f}{\partial x}\Big|_{x=0} = 0 \tag{4.67}$$

The fifth boundary condition at the origin establishes that there should be no net bending moment on the system. The couple acting about the flexure consists of three terms: two terms relating to the bending of the two beams and an additional couple arising from the centreline tension of the hot beam.

$$Couple = -\frac{Ew_h^3 t}{12}\frac{\partial^2 y_h}{\partial x^2} - \frac{Ew_f^3 t}{12}\frac{\partial^2 y_f}{\partial x^2} + E\varepsilon_h w t_h \frac{(2s + w_w + w_f)}{2} = 0 \tag{4.68}$$

The final (sixth) boundary condition at the origin is for the shear:

$$Shear = -\frac{Ew_h^3 t}{12}\frac{\partial^3 y_h}{\partial x^3} - \frac{Ew_f^3 t}{12}\frac{\partial^3 y_f}{\partial x^3} = 0 \tag{4.69}$$

From (4.63) - (4.69) the following set of equations is obtained.

$$A_h = -D_h \tag{4.70}$$

$$B_h k_h = -C_h \tag{4.71}$$

$$A_f = -D_f \tag{4.72}$$

$$B_f k_f = -C_f \tag{4.73}$$

$$A_f = A_h + \frac{(2s + w_h + w_f)}{2} \tag{4.74}$$

$$A_h = \left(\frac{w_f}{w_h}\right)^{3/2} B_h \tag{4.75}$$

This partly defines the solution for the regions of the hot arm and flexure. Now it is necessary to consider the solutions for the third region, the cold arm. Thus the boundary conditions at the junction of flexure and cold arm have to be established.

As with the other arms, the cold arm has a centreline tension and, for the forces to balance, at the interface between flexure and cold arm the following must apply:

$$F = Etw_f\varepsilon_f = Etw_c\varepsilon_c \qquad \text{and} \qquad \varepsilon_c = \frac{w_f}{w_c}\varepsilon_f \tag{4.76}$$

Continuity in displacement at $x = l_f$ implies:

$$A_f \cos k_f l_f + B_f \sin k_f l_f + C_f l_f + D_f = A_c \cos k_c l_f + B_c \sin k_c l_f + C_c l_f + D_c \tag{4.77}$$

Similarly, continuity in the gradient at $x = l_f$ implies:

$$A_f k_f \sin k_f l_f + B_f k_f \cos k_f l_f + C_f = A_c k_c \sin k_c l_f + B_c k_c \cos k_c l_f + C_c \tag{4.78}$$

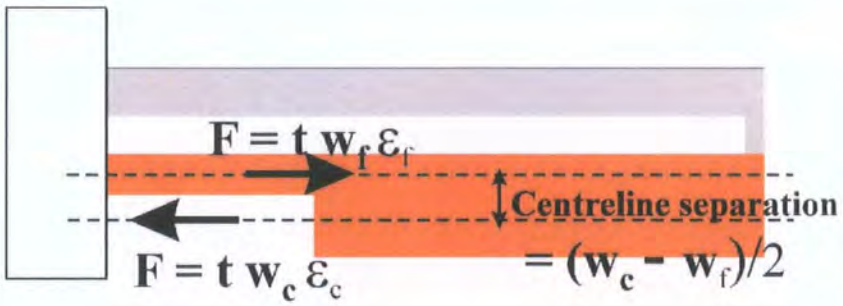

Fig. 4.25: Flexure/cold arm interface

For the impact of bending moment at this interface, it is instructive to sketch out the interface and the central forces. The net couple at the interface is comprised of the bending moment forces (second derivative) and the couple provided by the centreline forces (Fig. 4.25)

The overall couple is then given by:

$$Couple = \frac{Ew_f^3 t}{12}\frac{\partial^2 y_f}{\partial x^2} - \frac{E w_c^3 t}{12}\frac{\partial^2 y_c}{\partial x^2} - E\varepsilon_f t w_f \frac{(w_c - w_f)}{2} = 0 \tag{4.79}$$

evaluated at x = l_f

$$A_f \cos k_f l_f + B_f \sin k_f l_f = A_c \cos k_c l_f + B_c \sin k_c l_f - \frac{w_c - w_f}{2} \tag{4.80}$$

The condition for shear at the interface becomes:

$$Shear\ Force = \frac{E w_f^3 t}{12} \frac{\partial^3 y_f}{\partial x^3} - \frac{E w_c^3 t}{12} \frac{\partial^3 y_c}{\partial x^3} = 0 \tag{4.81}$$

evaluated at x = l_f gives

$$A_f w_c^{3/2} \sin k_f l_f + B_f w_c^{3/2} \cos k_f l_f = A_c w_f^{3/2} \sin k_c l_f + B_c w_f^{3/2} \cos k_c l_f \tag{4.82}$$

The final two boundary conditions derive from the end of the actuator where hot arm and cold arm meet. At that point displacements and gradients for the hot arm and cold arm must be identical

$$y_f = y_c \tag{4.83}$$

$$\frac{\partial y_f}{\partial x} = \frac{\partial y_c}{\partial x} \tag{4.84}$$

from where

$$A_h \cos k_h l + B_h \sin k_h l + C_h l_h + D_h = A_c \cos k_c l + B_c \sin k_c l + C_c l + D_c \tag{4.85}$$

$$A_h k_h \sin k_h l + B_h k_h \cos k_h l + C_h = -A_c k_c \sin k_c l + B_c k_c \cos k_c l + C_c \tag{4.86}$$

The twelve equations (4.70)-(4.75), (4.77)-(4.78), (4.80), (4.82), and (4.85)-(4.86) can be solved for the twelve coefficients using matrix methods and are incorporated in the design tool.

4.5.4. Temperature difference versus deflection

The next step is to calculate the unstrained difference in length between the hot arm and the cold arm/flexure combination. Initially, the lengths can be calculated by integrating length elements

$$L_{hh} = \int_0^l \sqrt{1+\left(\frac{dy_h}{dx}\right)^2}\,dx \tag{4.87}$$

where L_{hh} is the length of the hot arm

$$L_{fc} = \int_0^{lf} \sqrt{1+\left(\frac{dy_f}{dx}\right)^2}\,dx + \int_{lf}^{l} \sqrt{1+\left(\frac{dy_c}{dx}\right)^2}\,dx \tag{4.88}$$

where L_{fc} the length of the combined flexure cold arm region. These equations however do not consider the strain. The unstrained lengths become

$$L_{hh} = \int_0^l \sqrt{1+\left(\frac{dy_1}{dx}\right)^2}\,dx - l\varepsilon_h \tag{4.89}$$

$$L_{fc} = \int_0^{lf} \sqrt{1+\left(\frac{dy_f}{dx}\right)^2}\,dx + \int_{lf}^{l} \sqrt{1+\left(\frac{dy_c}{dx}\right)^2}\,dx - Fl\varepsilon_f - (1-F)l\varepsilon_c \tag{4.90}$$

where F * l = lf and (1-F)*l = (l – lf).

An additional consideration is that because the beams are deflected, one should not integrate to the same point in x, as illustrated in:

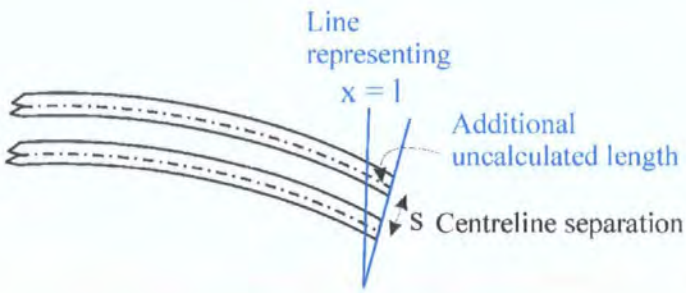

Fig. 4.26: Additional uncalculated length element

Fig. 4.26 shows that there is an uncalculated length, for the hot arm which is simply given by:

$$\Delta l = -\frac{(2s + t_h + t_c)}{2}\frac{\partial y_h}{\partial x} \tag{4.91}$$

So the final expression for L_{hh} should be

$$L_{hh} = \int_0^l \sqrt{1+\left(\frac{dy_h}{dx}\right)^2}\,dx - \frac{(2s+t_h+t_c)}{2}\frac{\partial y_h(l)}{\partial x} \tag{4.92}$$

Hence the effective temperature induced differential expansion is given by:

$$\frac{\Delta L}{L} = \frac{L_{hh} - L_{fc}}{l} \tag{4.93}$$

If the thermal expansion of the material is α then the difference in the average temperature between the two arms is:

$$\langle T_h \rangle - \langle T_{fc} \rangle = \frac{L_{11} - L_{23}}{\alpha l} \tag{4.94}$$

Equation (4.92) finally determines the average temperature difference between the two arms. This quantity drives the deflection and can be derived from any thermal model.

4.5.5. Validation of the 1D thermomechanical model

The results provided by the 1D analytical model can be compared with the results obtained from the commercial finite element software CoventorWare™ [290]. Two models with dimensions, design 1 and design 2, shown in Table 4.17 have been analysed with it.

Fig. 4.27 shows the comparison between the FEA and analytical modelling results of the actuator with dimensions design 1 (Table 4.17) in two different thicknesses t = 30 and 100 μm and for a difference in temperature between hot and cold arm ΔT = 60 K.

Table 4.17: Characteristic dimensions of the actuators modelled using the FEA and analytical thermomechanical model.

[μm]	design 1	design 2
l	2000	1500
l_f	2000	360
w_h	140	140
w_h	140	40
w_f	140	250
s	60	60

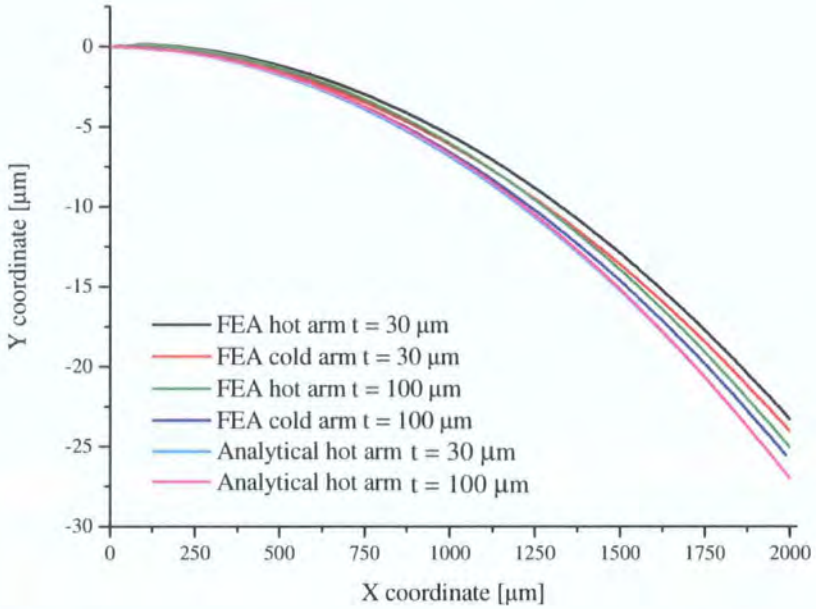

Fig. 4.27: Comparison of FEA and analytical model results for the deflection of the same actuator (see in two layer thicknesses 30 and 100 μm).

As can be seen, the agreement between FEA and analytical models is reasonably good with a maximum deviation of 3 μm in a 26 μm total deflection (at x = 2000). A characteristic of the analytical model is that the out-of-plane thickness of the device and the Young's modulus of the beams have dropped out of the equations. Even though the FEA simulations show a slight difference in the deflection between actuators of different thicknesses the overall results confirm that the approximations provide accurate enough results. Design 1 is the simplest geometry for a thermal actuator, where hot and cold arms have the same width. It is interesting to show how the model simulates a typical flexure actuator (design 2 in Table 4.17). The results are shown in Fig. 4.28. As can be seen overall, the FEA and analytical models results are in good agreement with a deviation in the results between 2.5 – 4 μm at low and high

temperatures respectively. Initially, it could be thought that the difference in the results comes from the fact that the analytical model does not take into account the bimorph effect generated by the gold layer embedded in the hot arm. However, Fig. 4.29 demonstrates that the gold layer has a minimal effect on the modification of the in-plane deflection value.

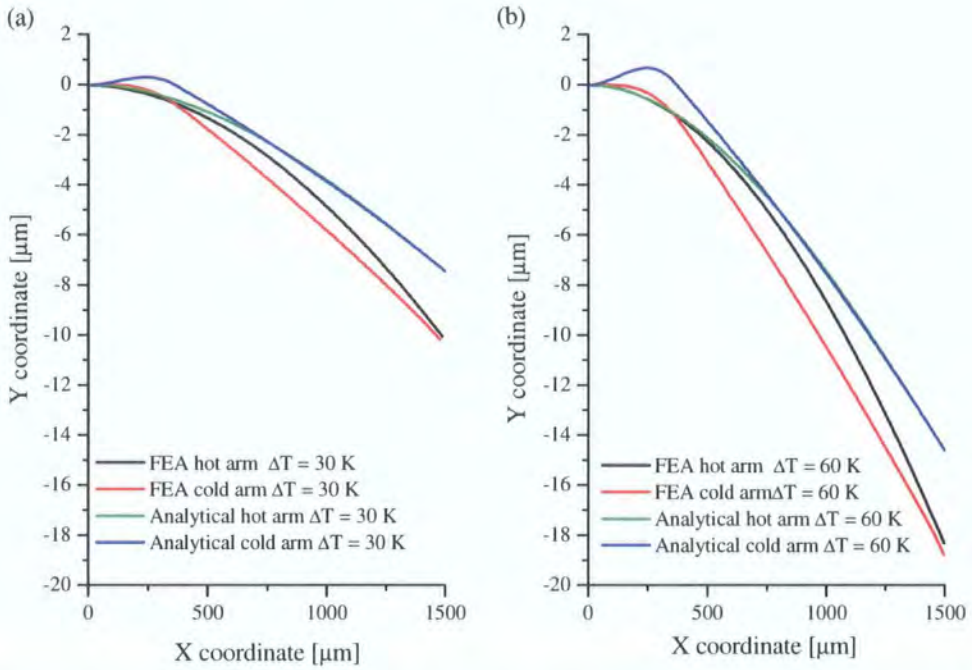

Fig. 4.28: Comparison of FEA and analytical modelling results for the deflection of design 2 (Table 4.17) for two different range of temperatures: ΔT = 30 K and ΔT = 60 K.

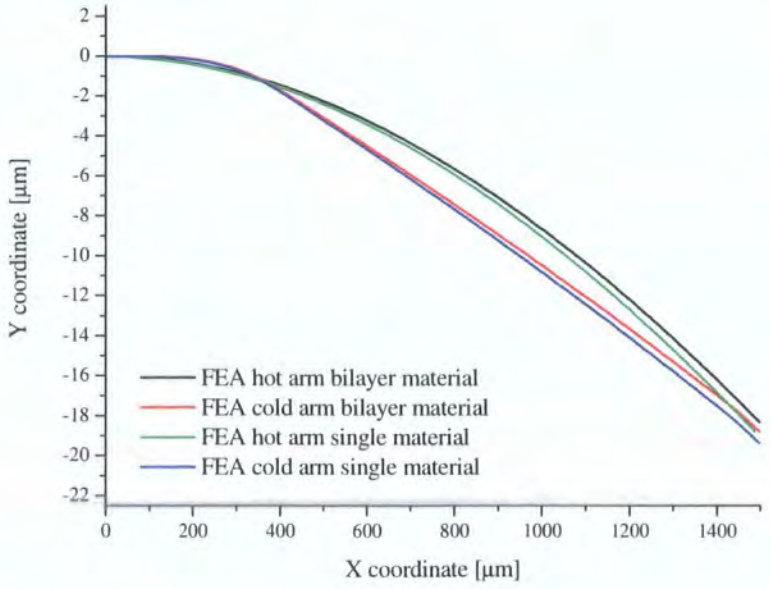

Fig. 4.29: Comparison between the FEA model of design 2 composed of a bilayer actuator and a single layer actuator for a ΔT = 60 K.

4.6. Conclusion

In this chapter, analytical models describing the electrothermomechanical behaviour of the microgripper have been provided.

First, a comprehensive electrothermal model describing the thermal behaviour of the microgripper has been proposed. A preliminary thermal analysis performed in section 4.3, has permitted the identification of the relevant heat transfer mechanisms taking place within the system and the suppression from the model of those that have the smallest contribution i.e. convection by mass transfer (referred as classical convection) and radiation. In addition, an alternative approach to calculate heat transfer into the ambient has been proposed. This approach utilises conduction heat transfer coefficients as opposed to standard convection coefficients. A few semi-empirical relationships for these coefficients which take into account the particular geometry of the beams and the separation in between adjacent beams have been proposed.

Second, a mechanical model that predicts the in-plane deflection of the actuator for a given difference in temperature between the arms has been provided. The model relates the initial strain in the hot arm to the strain in the cold and flexure arms and therefore to the geometry of the beams. Once this is done the result is used to calculate the elongation of the system and the induced temperature difference between the arms.

Both models have been combined to create a design tool for the design of different microgrippers. All the analytical simulations realised in this chapter has been done with a simple spreadsheet tool. The results have been validated by means of commercial FEA software. Good agreement between both FEA and analytical models has been demonstrated.

4.7. Summary

In this chapter the following generic analytical tools[10] have been provided:

[10] The analytical tool provided in this chapter not only is applicable to the thermal actuator developed in this thesis (resistor embedded in the hot arm only) but also to standard thermal actuators.

1. A set of semi-empirical formulae for the calculation of the heat transfer coefficients to the surrounding ambient by conduction. Departing from existing 2D conduction shape factors [276], a set of new formulas has been proposed to calculate the heat losses by conduction from a single rectangular beam, and from two closely spaced beams that lose heat conjointly. In the latter case, different formulas have been proposed depending on the relative size of some characteristic dimensions of the system: thickness and width of the beams, and the spacing between them. All of the coefficients have been validated by FEA.

2. A single beam 1D electrothermal model that takes into account the overhanging configuration of the beam, and the heat losses into the ambient by conduction as opposed to convection. This can be used to obtain the temperature distribution along the extended arm (jaw) of the microgripper.

3. A coupled beam 1D electrothermal model that takes into account the overhanging configuration of the system, the heat losses into the ambient by conduction as opposed to convection, and the heat exchange between closely spaced beams. This has been used to model the behaviour of the actuators which compose the microgripper.

4. A modelling technique that includes, in an iterative manner, the dependency of the material properties, resistivity and thermal conductivity of the air, with temperature.

5. A 1D thermomechanical model that predicts the deflection of the actuator for a given temperature difference between the arms.

CHAPTER 5

Microgripper experimental characterisation

This chapter reports on the experimental characterisation of various microgripper devices. Three different geometrical configurations, each consisting of two thicknesses, have been fabricated and tested. The characterisation study combines electrical testing with deflection and spatially resolved temperature measurements. The latter has been carried out using infrared (IR) thermography, its use in polymeric thermal actuators reported here for the first time.

The in-plane deflection of the microgripper (opening/closing) as a function of the driving voltage and temperature is the key focus of this characterisation study. Three types of experiments will be carried out for all of the microgrippers. The first one is a DC characterisation experiment where the voltage drop across the device is measured for a range of applied constant currents. This experiment also provides the measurement of the resistance change versus current. The second characterisation experiment is IR thermography and it has been used to obtain, in static and transient mode, accurate two dimensional mappings of the surface temperature of the devices over a range of input currents. Relevant thermal variables such as the temperature profile developed along the arms of the actuators, the maximum temperature or the thermal response time will be reported here. The final experiment consists of measuring the deflection of the unloaded microgrippers, and of carrying out a set of manipulation experiments. The manipulation of microsized pillars and cell clusters is demonstrated and qualitatively assessed. Other aspects such as lifetime and failure mechanisms are also discussed.

5.1. Test devices

Fig. 5.1 shows the three microgripper configurations that have been fabricated and tested.

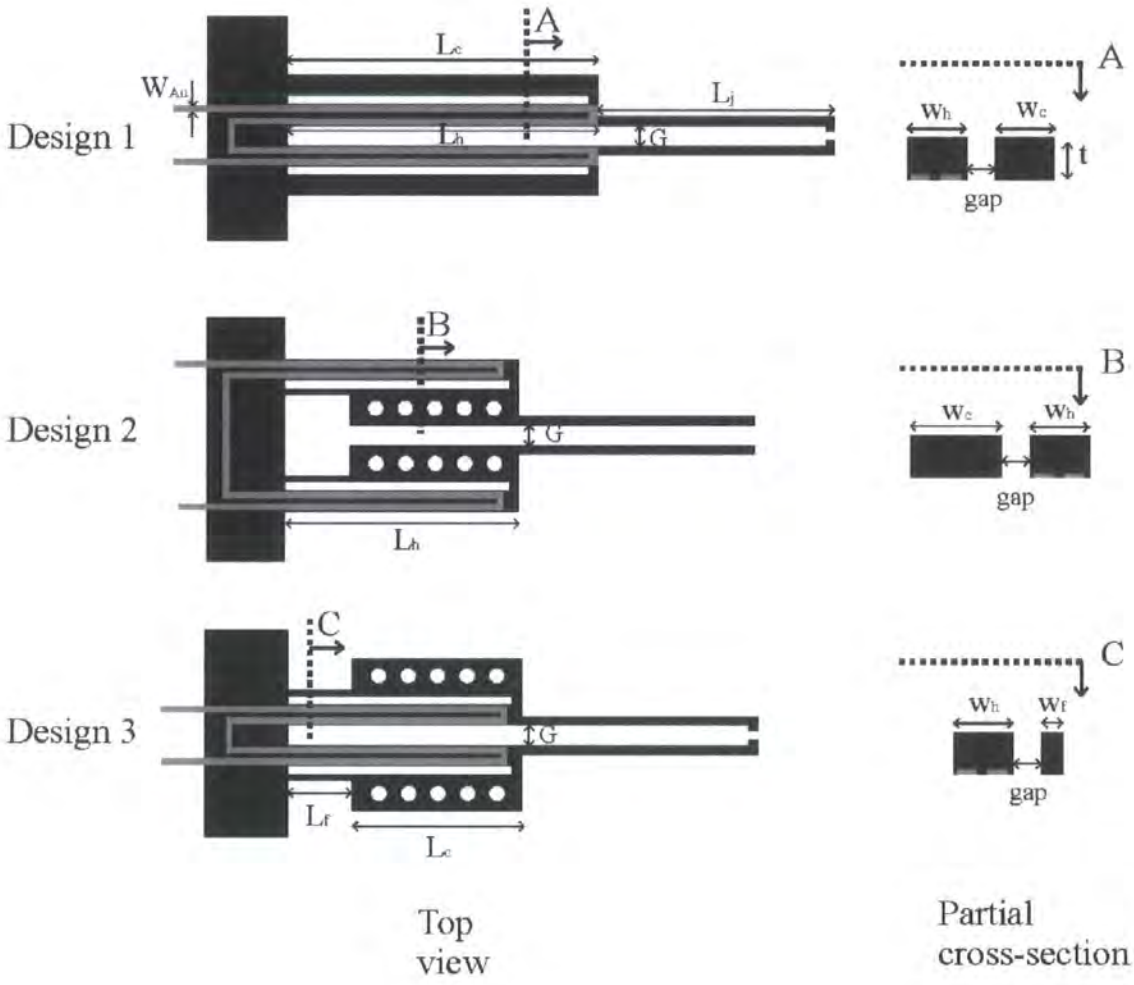

Fig. 5.1: Schematic of the tested microgrippers (design 1, design 2 and design 3) (Left) top view (Right) Partial cross-sectional view.

As can be seen from Table 5.1, some geometrical features are common to all of the microgripper configurations, i.e. the width of the resistors, w_{Au}, the spacing between the actuators, G, the gap between the individual arms of the actuators, *gap,* and the length of the jaws, L_j. The geometry of the individual actuators, however, is slightly different in each case. In design 1, the overall geometry of the hot and cold arms is identical. In design 2, the cold arms of the actuators are twice the width of the hot arms and are connected to the anchor with a thin beam called a flexure. This flexure is 3 times thinner than the hot arm and acts as a hinge. The holes appearing in design 2 are a fabrication

requirement and not a design feature. Design 3 has the same individual actuator geometry as design 2 but the actuators are positioned differently. In design 3 the hot arms are facing each other whilst in design 2 the hot arms are placed in the external sides of the device. When a current is applied, design 1 and design 3 will increase the gap between the jaws (i.e. opening) whilst design 2 will reduce the gap between the jaws (i.e. closing).The geometry of the resistors is given in Fig. 5.2.

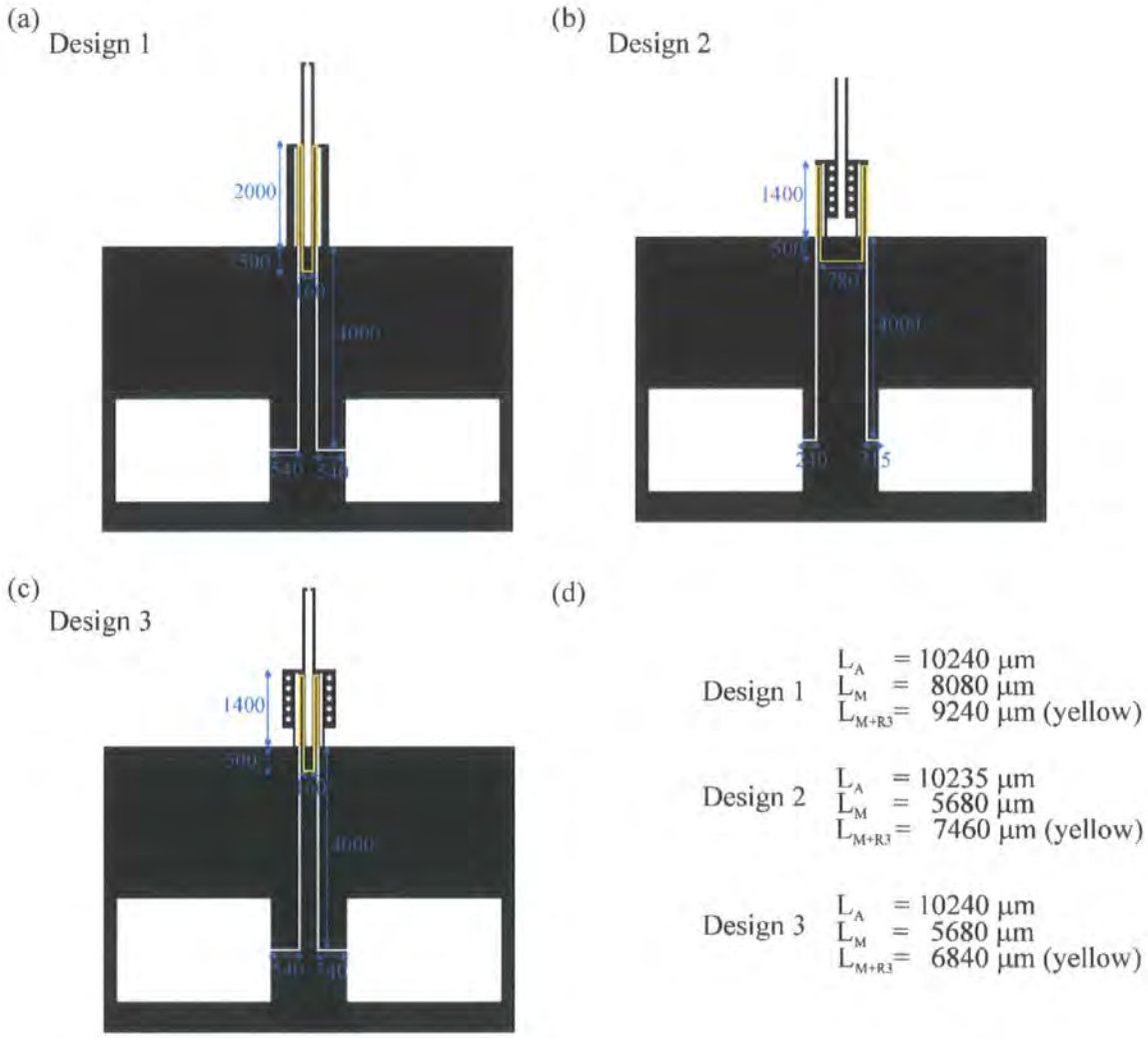

Fig. 5.2: Dimensions of the resistor lengths (a) design 1 (b) design 2 (c) design 3 (d) summary of the values.

For each configuration, two different thicknesses of the polymer layer, 30 and 100 μm, have been fabricated. In total, five different microgripper devices have been characterised and constitute the experimental foundation of this thesis. The different devices are named design 1_(30), design 2_(30), design 1_(100), design 2_(100), and design 3_(100). The number in brackets indicates the thickness of the device (polymer

layer) in microns. The first four designs will be used for the characterisation in air only, design 3_(100) will be used to characterised the microgripper in air as well as in water. For design 3, only the device with a layer thickness of 100 μm has been tested.

Table 5.1: Characteristic dimensions in microns: L_h, L_c, L_f ≡ length of hot, cold and flexure arms; w_h, w_c, w_f ≡ width of hot, cold and flexure arms; g ≡ spacing between hot and cold arms; G ≡ spacing between the actuators; t ≡ thickness of the beams; t_{Au} ≡ thickness of the metallisation layer.

	L_h	L_c	L_f	L_j	w_h	w_c	w_f	w_{Au}	g	G	t	t_{Au}
Design 1_(30)	2000	2000	-	1600	140	140	-	40	60	140	30	0.239
Design 1_(100)	2000	2000	-	1600	140	140	-	40	60	140	100	0.289
Design 2_(30)	1500	1140	360	1600	140	250	40	40	60	140	30	0.239
Design 2_(100)	1500	1140	360	1600	140	250	40	40	60	140	100	0.289
Design 3	1500	1140	360	1600	140	250	40	40	60	140	30	0.289

The initial values given to the characteristic dimensions of the microgrippers were fairly arbitrary. However, the configuration of the microgripper itself (open or closed mode, i.e. two hot arms facing each other vs. two cold arms facing each other), the configuration of the individual actuators (two equal beams vs. standard hot-cold-flexure actuators), and the thicknesses of the designs have been chosen with a purpose. The different geometries will help to evaluate various aspects of the overall microgripper design and their corresponding models. Some of the relevant aspects of the design include the effect of the ratio between the beam's width and thickness and the gap separating them in the intra-device heat exchange and the heat losses to the ambient, the impact in the overall performance of the configuration of the hot arms placed in the external or internal part of the device. All of these aspects will be qualitatively and quantitatively discussed in remainder of this thesis.

5.2. Electrical DC experiments

During the experiments, a constant current source (Keithley 2200) was used to actuate the microgrippers in air. The total voltage drop, *V*, and the effective current, *I*, flowing through the gold circuit were measured using two multimeters (Fluke 77III). Current levels ranging from 5 to 40 mA were applied to design 1_(30), design 1_(100), design 2_(30) and design 2_(100).

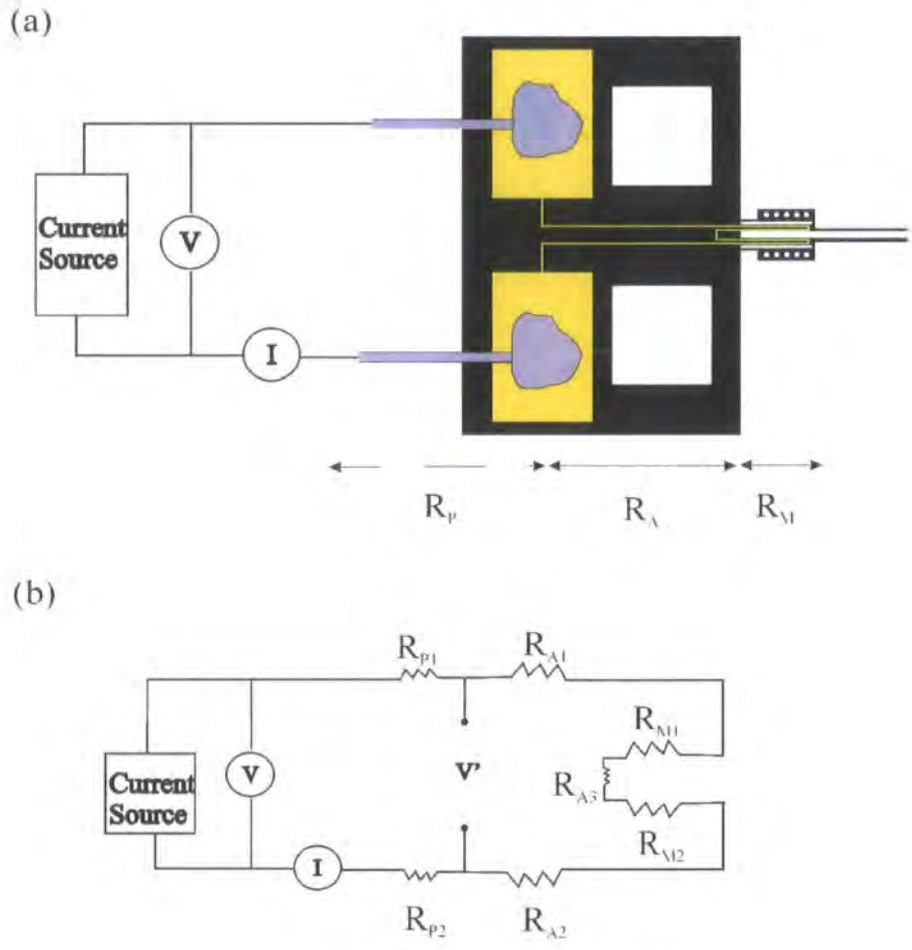

Fig. 5.3: Schematic of the electrical set-up: (a) experimental set up, (b) equivalent resistive circuit.

Fig. 5.3 shows the experimental electrical set-up and the equivalent resistive circuit. The total resistance measured for the device, R_T, can be considered as an assembly of independent resistances connected in series. Those resistances are: the parasitic resistance (wiring, multimeters), $R_P = R_{P1} + R_{P2}$, the anchor resistance (portion of the electrical circuit on the anchor), $R_A = R_{A1} + R_{A2} + R_{A3}$, and the two actuator resistances (heaters), $R_M = R_{M1} + R_{M2}$. The length of each resistance, parasitic, anchor and microgripper, are respectively L_P, L_A, and L_M (see Fig. 5.2)

Table 5.2 shows the estimated values of the resistances in the circuit. The total resistance, R_T, was obtained directly from the I-V measurements at different currents. The parasitic resistances, R_P, were calculated by subtracting the resistance of the microgrippers at the contact pads, measured prior to the wiring process, from the total resistance measured at 5 mA. At low currents, the contribution of the self heating of the resistor to the total resistance should be minimal and is therefore neglected. The values

of the anchor and microgripper resistances were estimated based on the geometry of the metal tracks and the value of the resistivity of the gold layer at 20 °C with a value of 2.04×10^{-8} Ω m [292].

Table 5.2: Resistances [Ω] accounted for the different parts of the electrical circuit at ambient temperature (20 °C): Total, R_T; wiring, R_P; anchor, R_A; and microgripper, R_M.

Device	R_T	R_P	R_A	R_M
design 1_(30)	38.3	2.5	21.4	16.9
design 1_(100)	31.3	2.9	17.5	13.8
design 2_(30)	32.2	2.2	21	11.1
design 2_(100)	26.8	3.9	17.5	9.3

In order to guarantee similar electrical properties within the models, the four microgrippers (in two different substrate wafers) were fabricated using the same metal evaporation process. However it can be seen from Table 5.2 that different resistances appear for identical designs e.g. design 1_(30) and design 1_(100). This is due to the thickness of the metal tracks, which are larger for design 1_(100) and design 2_(100) and has been caused by the location of the wafers in the evaporator during deposition.

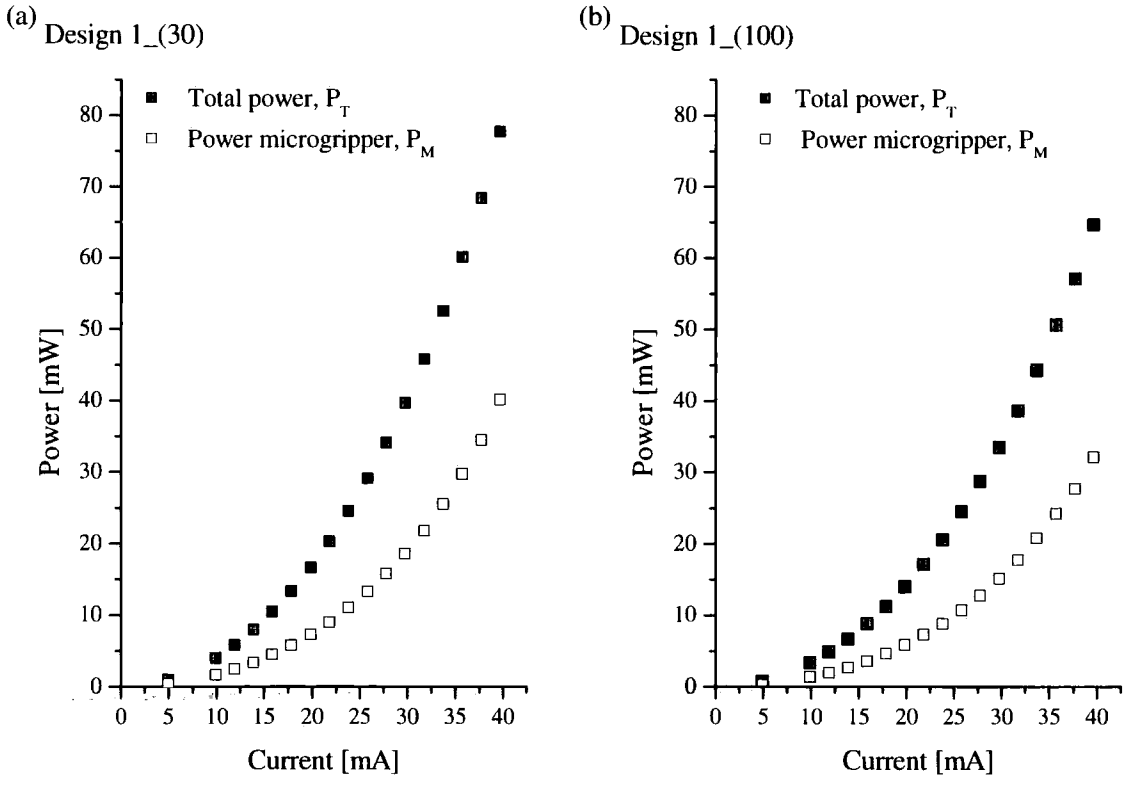

Fig. 5.4: Total power (black squares) and power consumed by the microgrippers only (white squares) versus input current. (a) design 1_(30); (b) design 1_(100).

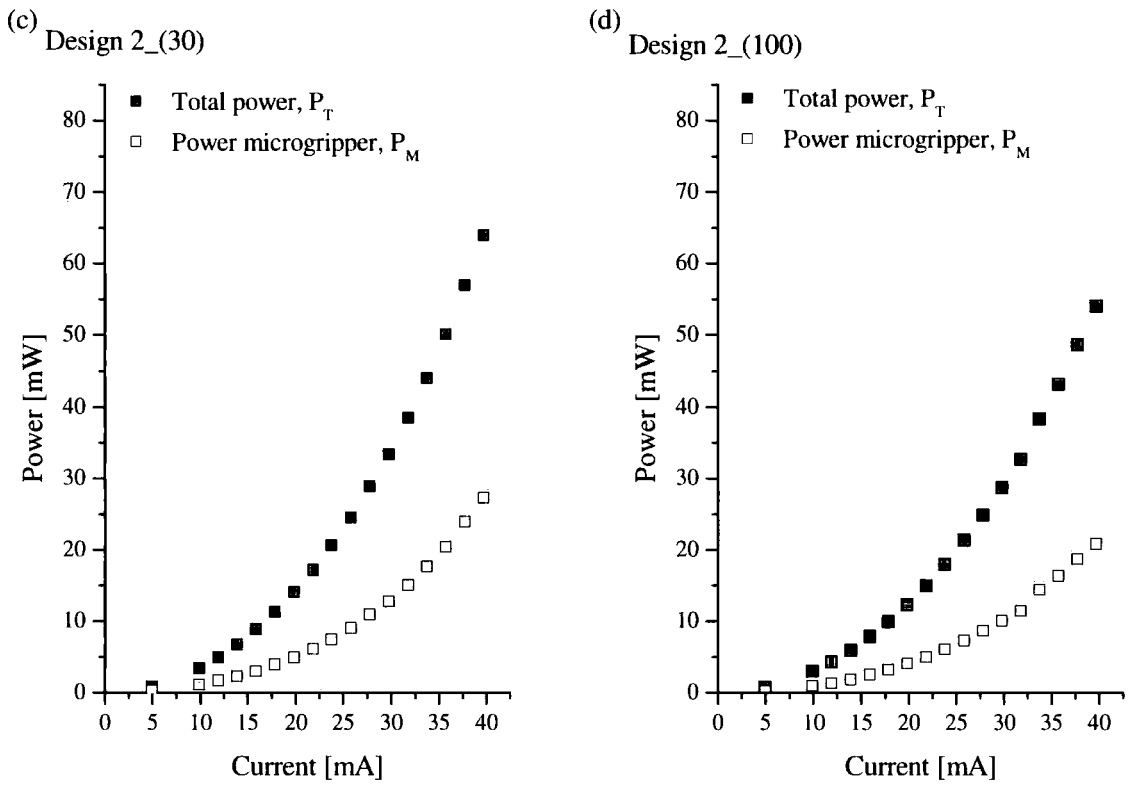

Fig. 5.5: Total power (black squares) and power consumed by the microgrippers only (white squares) versus input current. (c) design 2_(30); (d) design 2_(100).

Given the differences in the initial resistance values, and in order to cross-compare the devices and their performances, it is convenient to relate the results to an equivalent parameter such as the power. The consumed electrical power seems to be appropriate as it is ultimately responsible for the heating and therefore the actuation. In particular, for model comparison, the parameter of interest is the power consumed by the microgripper only, P_M. This is shown in Fig. 5.4 and Fig. 5.5.

The total power, P_T, consumed by each device can be found easily using equation (5.1)

$$P_T = IV_T \tag{5.1}$$

Ideally, the total electric power injected into the system should be dissipated entirely in the form of heat at the actuators' heaters and contribute correspondingly to the increase in temperature of the hot arms. However, due to the relatively small resistance of the active part of the heaters, R_M, parasitic resistances associated to experimental and fabrication constraints become relatively important and consume a non-negligible part of the input power that in some cases reaches more than 50%. The reduction of the

power consumed in the anchors and tracks would be a clear first modification for the electrical optimisation of the device.

The measured V-I characteristics of the devices together with their corresponding total resistance change, ΔR, are shown in Fig. 5.6 (a-b) and Fig. 5.7 (c-d).

From the discontinuous lines included in the graphs, it can be observed that the voltage deviates from the linear trend at higher powers. This typically indicates a non-ohmic behaviour of the resistors integrated in the microgripper. In a pure metal resistor such as the integrated gold heaters, the increase in resistance, ΔR, with power (joule heating), is mainly caused by the change in the resistivity of the metallisation due to an overall increase of the average temperature.

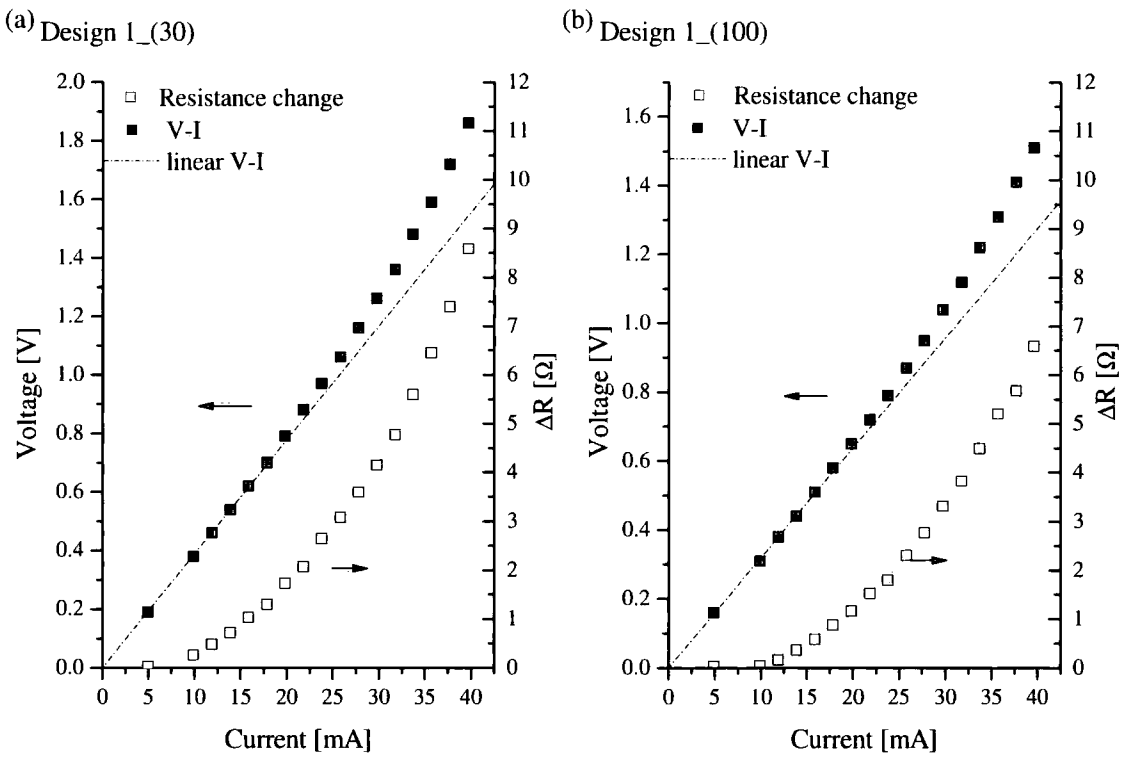

Fig. 5.6: V-I curve (right axes), Resistance change (left axes) versus input current; (a) design 1_(30), (b) design 1_(100). The discontinuous line indicates the trend expected from a linear V-I relationship.

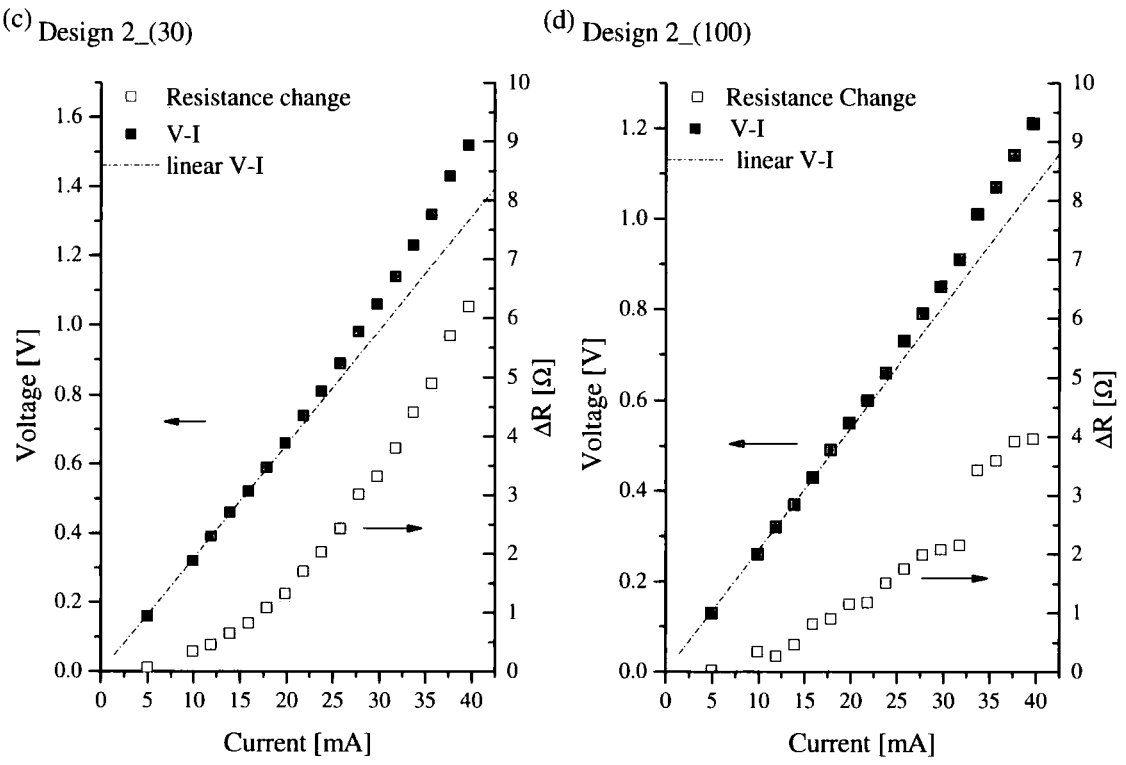

Fig. 5.7: V-I curve (right axes), Resistance change (left axes) versus input current; (c) design 2_(30), and (d) design 2_(100). The discontinuous line indicates the trend expected from a linear V-I relationship.

As a first approximation, within a relatively limited temperature range, the resistance of a metal resistor of length, l_0, cross section, a, and resistivity ρ_0, varies linearly with temperature as

$$R - R_0 = \Delta R = R_0 TCR(\Delta T) \qquad \text{with} \qquad R_0 = \frac{\rho_0 l_0}{a} \tag{5.2}$$

where R_0 represents the total resistance measured at the temperature T_0, ΔT is the average temperature increase of the resistor, and TCR is the temperature coefficient of resistance at T_0.

Given the boundary conditions of the system where it is assumed that the anchor is thermally grounded, it is more appropriate to rewrite equation (5.2) as:

$$R - R_0 = \Delta R = R_M TCR\,(\Delta T_h) \qquad \text{with} \qquad R_M = \frac{\rho_0 l_M}{a} \tag{5.3}$$

where R_0 (defined as in equation (5.2)) represents the total resistance measured at the temperature T_0, l_M is the length of the resistors in the hot arms only, ΔT_h is the average temperature increase experienced by the resistors in the hot arms only, and TCR is the temperature coefficient of resistance at T_0.

Equation (5.3) relies on the assumption that most of the resistors integrated in the anchors (R_A in Fig. 5.3) remain thermally grounded (i.e. experience no net difference in temperature, $\Delta T = 0$) and that only the resistors on the actuators (R_M in Fig. 5.3) experience a considerable change in resistance due to temperature.

Equation (5.3) could be used to calculate the temperature increase in the hot arms of the actuators. However some potential problems exist:

- Standard values of TCR and ρ_0 for bulk gold exist in the literature. However, the material properties of thin films, especially when they have been deposited or embedded in polymers, can differ considerably from the bulk values. They are highly dependent on fabrication conditions, grain size, roughness, and the thickness and boundaries of the layer. Even for samples produced on the same wafer considerably different values can be obtained. Therefore, there is the risk that using two standard bulk material properties to extract a third parameter of the system could lead to significant inaccuracies.

- Fig. 5.7 (d) shows a discontinuity on the resistance at mid range of the input currents. This could be due to a particular morphology of the thin metallic layer that passes from one state to another (in terms of voids or mismatch between the polymer and metal) as the temperature increases. Should the values of standard material properties be valid for before as well as after the discontinuity?

- A final remark is that this method does not provide spatial resolution in the temperature measurement or any other indication of the temperature distribution within the cold and flexure arms which do not contain a resistor. Accurate knowledge of these temperatures is, however, of crucial importance for the validation of the models and the prediction of the deflection which relies on

'asymmetric heating' i.e. the difference in temperature between hot and cold/flexure arms.

All of this justifies the need for an independent method to measure the temperature. This is treated in the next section.

5.3. Temperature experiment

In order to be able to electrothermally characterise the different microgrippers it is necessary to find a technique that can provide reasonably good temperature measurements along the different parts of the devices.

5.3.1. Background

In recent years, there has been considerable progress in thermographic techniques for the characterisation of microdevices and their constituent materials. These techniques can be categorised depending on whether they employ electrical or optical signals. They all have advantages and disadvantages, and their relevance to a particular measurement will be highly dependent on the desired resulting data, the material under study, and the dimensions of the features. This section gives a general overview of the techniques that have been applied to thermal actuators, and presents IR thermography as a good solution for the thermometry of the polymeric microgripper.

5.3.1.1. Electrical methods

Electrical resistance thermometry requires relatively simple experimental set ups and is one of the most popular methods. As explained earlier, it relies on the measurement of the temperature dependence of resistance. This is an attractive technique for situations where spatial temperature distributions are not important. In certain thermal actuators this averaged type measurement is enough to characterise their electrothermal behaviour. In the case of a chevron actuator the overall deflection depends on the average temperature increase of the whole structure. As the structure itself is also the resistor, once calibrated, the device temperature can be directly extrapolated from the measurement of the resistance change [272]. In the case of standard U-shaped actuators, however, the deflection depends on the temperature difference between the hot and cold arms. Therefore electrical thermometry will only give a significant measurement when

one can assume that in the cold arm the resistance does not contribute significantly to the resistance change (noting that in standard U shaped actuators the resistor is on both arms). In this case, the increase in temperature in the hot arm can be extrapolated using equation (4.2).

The major advantage of this technique does not lie in static measurements but in its use for dynamic measurements where a temporal resolution in the range of hundreds of nanoseconds is possible. This has been used in the work of Enikov et al. in the analysis of a standard U-shaped actuator [293]. They used a two-level current source to power a thermal actuator and to measure its cooling time. The comparison between modelled and measured time constants used with this technique was in reasonable agreement (within 10%).

As explained earlier the main limitations of this technique is the lack of spatial resolution and the lack of information concerning parts without integrated resistors. Spatial resolution is necessary to localise heated spots, often associated with thermal failure.

Another electrical technique that is becoming increasingly important in micro and nano scale thermometry is scanning thermal microscopy [294] which combines the mechanisms of an atomic force microscope (AFM) or a scanning tunnelling microscope (STM) with a temperature sensing probe. It operates by bringing the sensing probe in close proximity to the sample. This technique has the potential to provide better spatial resolution (30-50 nm [295]) than optical techniques but its application to quantitative measurements still faces many challenges [294]. These calibration techniques are affected by the change in thermal conductance between sample and tip due to topographical features, and the thermal resistance circuit between probe, sample and water meniscus.

5.3.1.2. Optical methods

Optical methods rely mainly on two facts: that some optical properties of materials change with temperature, and that heated bodies emit radiation that can be correlated with their temperature. As opposed to electrical methods, optical techniques provide good spatially resolved temperature distributions. The lower end of the spatial

resolution, d, is limited by diffraction and is directly related to the wavelength of the captured radiation, λ, and the numerical aperture, NA, of the microscope objective used in the system.

$$d = \frac{\lambda}{2NA} \tag{5.4}$$

Some optical methods require interaction with the sample using a laser beam as a probe. Two main techniques of this type, thermoreflectance thermometry and Raman spectroscopy, have attracted a lot of attention.

Thermoreflectance thermometry is based on a calibration of small changes in the optical reflectance with temperature. This technique uses a laser that is reflected with a different reflection coefficient as the temperature changes. The spatial resolution of this technique is limited by the diffraction of the laser probe. As the laser is used at shorter λ based on equation (5.4), better resolution can be obtained [296]. Recently, a spatial resolution of 225 nm has been obtained using a 465 nm LED [297]. Thermal resolution is becoming comparable to other techniques and the best thermal resolution achieved so far is 18 mK. This technique is particularly useful for improving the transient aspect of a point measurement for which ~ns temporal resolutions have been achieved [298].

Thermoreflectance has been used to obtain a 2D thermal mapping of a polysilicon resistor covered with a thin dielectric layer that forms part of a gas sensor [299]. The measurements are in a good agreement with the models and show that the technique is well adapted to measure temperature.

The main disadvantages of this technique are: first, the difficulty of the calibration procedures, especially under focusing conditions that require the control of the distance between the objective and sample [300]. In the measurement of suspended thermal actuators this problem would be difficult to overcome as slight out-of-plane deflections are expected. Second, there are long measurement times associated with this technique.

Micro Raman thermometry has been used to measure the surface temperature distribution on polysilicon thermal actuators [301, 302]. With this technique, the scattered radiation from a probe laser is spectrally resolved and the location, width and

relative intensities of the Raman peaks are used to determine the temperature in the region of the focused probe-laser spot. It provides a very good spatial resolution (~12 μm) with an uncertainty of ±10 K. This provides a very good measurement technique to obtain spatially resolved temperatures in small thermal actuators where the characteristic width is ~3 μm. This technique however has certain limitations. The measurements are taken along the arms of the actuators in 5-10 μm increments, and the Raman spectrum is averaged for 10-60 seconds at each location [301]. Therefore it can take days to measure the temperature distribution of a typical device (beam length 200-2000 μm) for various input currents. In addition, this procedure prevents the measurement of the dynamic thermal behaviour of the actuator.

The dynamic behaviour of thermal actuators has been also analysed on polysilicon thermal actuators using optical techniques [267, 303]. In those cases the movement and therefore heating and cooling of the device is measured by the intensity changes in the light of a reflected laser. With this system an uncertainty of ~16% is obtained. This is due to the minimum size of the laser spot (Ø = 10 μm) and the non-linearity of the measuring system.

Compared to all of these techniques, IR thermography, when used within the right range, can become a very flexible measuring tool in both static and dynamic modes. When the size of the device to be measured is within the spatial resolution of the IR camera (18-30 μm), this technique allows real time accurate 2D surface temperature mappings. In addition, given that the maximum frequency of the camera is 50 Hz, when the time constant is in the order of a few tens of milliseconds, an estimation of the response of the system can be obtained.

5.3.2. Infrared thermography

5.3.2.1. Measurement technique and experimental set-up

Any object with a temperature above 0 Kelvin emits radiation in the infrared range of the electromagnetic spectrum (λ = 1-14 μm). Infrared cameras[11] detect and convert this energy into visible images. The energy emitted by an object is mainly a function of its

[11] The range of detection wavelengths depend on the sensor in the camera

temperature and its emissivity (ε). This makes it possible to calculate and display temperatures. Infrared (IR) thermography is a two dimensional, non-contact technique which transforms the infrared images into radiometric ones, which allows temperature values to be extracted. In order to do this, a set of algorithms have to be incorporated into the infrared cameras.

The law that describes the level of radiation of an object can be expressed by the formula derived by Planck or by its simplified version derived by Wien and shown in equation (5.5).

$$W_{\lambda T}\, d\lambda = \frac{C_1}{\lambda^5 [\exp(\frac{C_2}{\lambda T})]} \tag{5.5}$$

where $W_{\lambda T}\, d\lambda$ is the black body radiation emitted at temperature T [K] between wavelengths λ and $\lambda + d\lambda$; C_1 is Planck's first constant = 3.74 x10^{-16} W m^2; and C_2 is Planck's second constant = 1.4388 x10^{-2} m K.

Equation (5.5) describes the energy radiated from a blackbody which is the maximum value radiated by a body at a given temperature. Real bodies almost never comply with the definition of a blackbody, i.e. a perfect absorber and emitter, and they tend to radiate less energy than a blackbody at the same temperature. The ratio between the energy radiated by an object at temperature, T, and the one that a blackbody would radiate at the same temperature is known as emissivity ε, and will play a major role in the infrared measurements. Using this definition of emissivity equation (5.5) can be rewritten for a real body as

$$W_{object-\lambda T}\, d\lambda = \varepsilon_{object} \frac{C_1}{\lambda^5 [\exp(\frac{C_2}{\lambda T})]} \tag{5.6}$$

The thermal measurements were carried out using an IR camera ThermaCAM® SC3000 from FLIR systems with an attached microscope lens. This IR system operates in the 8 to 9 μm wavelength range of the infrared spectrum with a gallium arsenide (GaAs) focal plane array detector of 320 x 240 pixels cooled at T = 70 K. The image information is digitally captured by a frame grabber. The image is digitised in the

detector head with an accuracy of 14 bits at a rate up to 60 Hz. The system has a spatial and thermal resolution of 31 μm and 20 mK (at 30 °C) respectively. The fact that the sensor is cooled below the temperature of the ambient is a very important feature of the system as it allows accurate measurements around the ambient temperature.

Fig. 5.8 shows a schematic of the thermography measurement set-up used during the experiments. As can be seen, the total radiation received by the IR camera does not come exclusively from the emitted radiation of the microgrippers and therefore it cannot be used to measure their temperature directly. Other sources of infrared radiation such as the radiation originated in the surroundings, reflected by the object and transmitted through the atmosphere, or the radiation emitted by the atmosphere itself also account for the total radiation captured by the IR sensor.

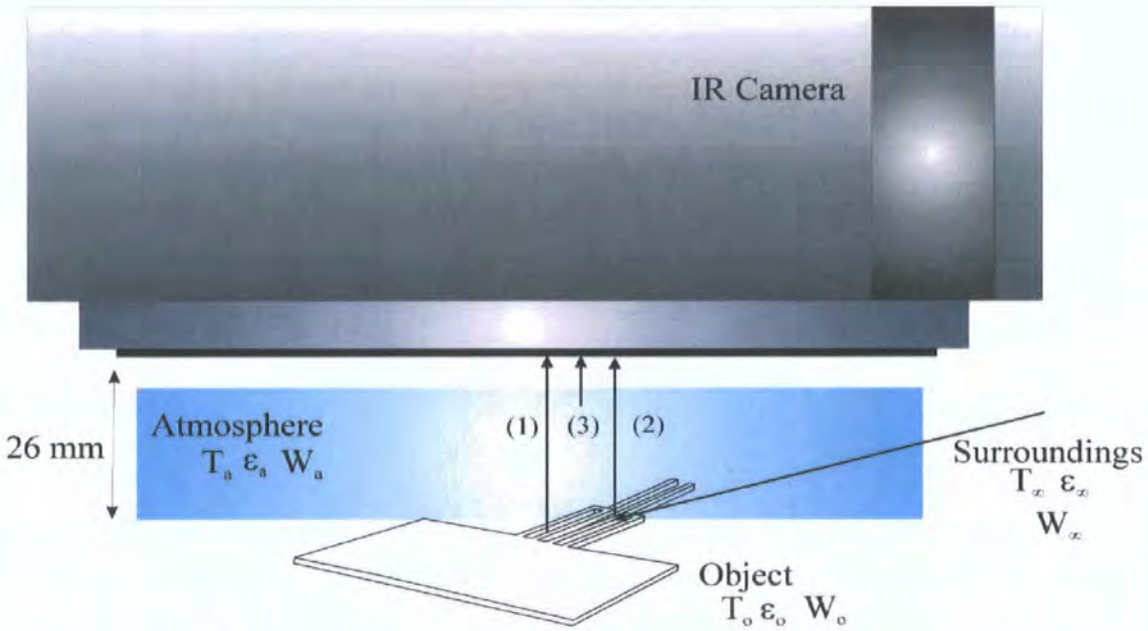

Fig. 5.8: Schematic representation of the general thermography measurement situation. ε = emissivity; τ = transmittance; T = temperature; W = emitted radiation. (1) Emitted radiation from the object (2) Reflected radiation from the environment (3) Transmitted radiation from the atmosphere.

The FLIR IR camera automatically compensates for the effects of these radiation sources, also called background radiation, but the following object and environmental parameters have to be supplied: emissivity of the object (ε); reflected temperature (T_∞); temperature (T_a) and transmittance (τ) of the atmosphere; distance between the object and the camera (d) and relative humidity (Rh).

The object radiation is calculated using equation (5.7) [304].

$$W_{tot} = \varepsilon \tau W_o + (1-\varepsilon)\tau W_\infty + (1-\tau) W_a \tag{5.7}$$

where ε is the emissivity of the object, τ is the transmission of the atmosphere, W_{tot} is the total radiation measured, W_o is the calculated radiation emitted by the object, W_∞ is the theoretical reflected radiation of the surroundings, W_a is the theoretical radiation of the atmosphere.

In this equation the first term on the right, $\varepsilon \tau W_o$, represents the radiation originating in the object and transmitted through the atmosphere (see Fig. 5.8 (1)). The middle term, $(1-\varepsilon)\tau W_\infty$, represents the radiation originated in the surroundings, reflected by the object and transmitted through the atmosphere (see Fig. 5.8 (2)). And the third term, $(1-\tau)\ W_a$, represents the radiation emitted by the atmosphere itself (see Fig 5.8 (3)).

Once the total received energy is quantified, the energy emitted by the object can be calculated. The target temperature displayed in the image is obtained using an internal calibration curve supplied by the vendor. The calibration function has the form

$$W_{tot} = \varepsilon \frac{A}{e^{B/T} - C} \tag{5.8}$$

where W_{tot} is the real amount of energy detected, ε is the emissivity of the object, T is the temperature of the object, and A, B and C are constants that take into account Planck's constant as well as different ambient conditions.

The following assumptions are implicit in the use of equations (5.7 - 5.8):

- That the camera possesses a good linearity, i.e. that the received radiation power from a blackbody source of temperature T_{source} on short distances generates a camera output signal U_{source} that is proportional to the input power (power linear camera).
- That the reflected temperature (T_∞) is the same for all emitting surfaces.

- That the emittance (ε_∞) of the surroundings is 1.
- That the object is an opaque greybody emitter, i.e. its transmittance is zero ($\tau_o = 0$) and that its emissivity does not depend on the wavelength ($\varepsilon(\lambda) = \varepsilon < 1$).

Fig. 5.9 (a) shows a typical 2D thermal map (thermograph) obtained with the FLIR IR camera. Fig. 5.9 (b)-(c)-(d) are the same images with an applied zoom of x2, x4, and x8 magnifications respectively. Numerical data from the images can be extracted with the dedicated software of the camera (ThermaCAM researcher Pro 2.8 RS-1), or by converting the images into a matrix of data points to be treated in separate software such as Excel.

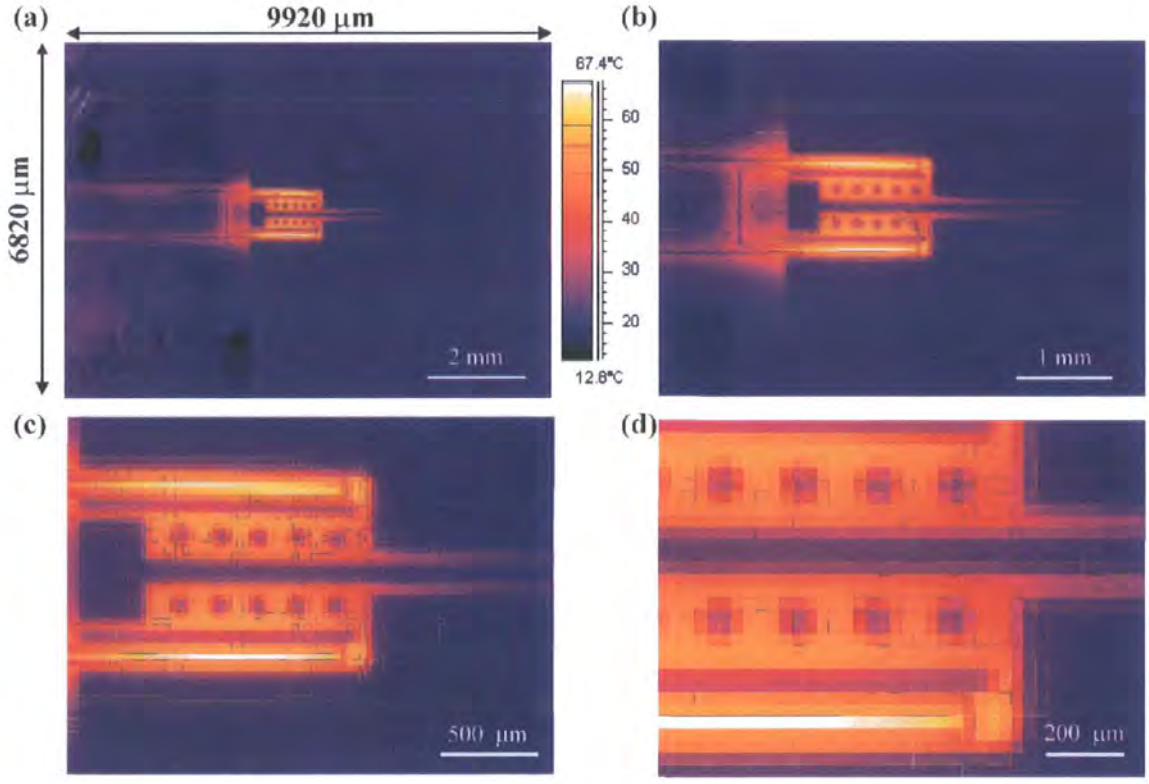

Fig. 5.9: IR image of the absolute temperature of the microgripper design 1_(30) at 30 mA with an $\varepsilon = 0.9$. (a) Maximum field of view of the system (b), (c) and (d) Zoom realised on the images at x2, x4 and x8 increments.

5.3.2.2. Limitations of the measurement technique

The assumptions included in the use of equation (5.8) together with the inclusion of parameters such as ε, τ, T_{refl} or T_{atm} as an input to the thermal images will introduce inaccuracy in the temperature measurements. In this section, a brief analysis of how the

uncertainties in the values of all these parameters will affect the final result is presented. This will give insight into the overall accuracy of the temperature measurement technique.

The experiments were carried out in a temperature controlled environment with an average temperature of 20 ± 2 °C and a relative humidity of 60 ± 10 %. In addition, attention was given to the elimination of radiative (heating) sources in the vicinity of the camera and the sample. Hence the atmospheric (T_a) and reflected temperatures (T_∞) can be considered identical and relatively stable during the course of the experiments. It has been verified using the IR images that fluctuations of up to 4 °C in the input values of the ambient temperature only translates into a variation of 0.40 °C in the final temperature readout. Therefore eventual variations of the cleanroom temperature can be included in the results as a systematic error of approximately ± 0.2 °C.

Due to the small distance separating the sample and the surface of the optics (d = 26 mm), letting the transmittance of the atmosphere, τ, equal to unity is a good approximation and does not introduce inaccuracy in the measurements.

The IR camera does not read temperature directly. The IR detector converts the photon energy captured by the camera optics (measured in watts) into an electrical digital signal. It is assumed that the camera used for the experiments ensures the linearity between the digital value outputs and radiance inputs. The validity of this assumption depends on the quality of the camera and is beyond the scope of this thesis.

A greybody emitter is one whose emissivity remains constant with wavelength. Most of the existing IR cameras (and also the one used here) consider objects as greybodies and include in calculations a constant emissivity know as the greybody emissivity. In practice, emissivities of materials are rarely the same at two different temperatures showing a certain level of non-greyness. For real bodies, however, the greybody emissivity will be temperature dependent and will have to be adjusted if a large range of temperatures are used. Madding [305] studied the effect of the variation of the emissivity with temperatures for the camera used in the experiments and concluded that any changes were relatively small for temperatures up to 500 °C. The operating temperatures of the devices under test were below 170 °C, and therefore a constant

emissivity was enough to guarantee a good result. Moreover, if the temperatures under study are close to the temperature at which the emissivity has been determined, the dependence on temperature is further decreased. The emissivity in the present experiments was calculated at 60 °C, which is close to the middle range of the experiments and should produce accurate results, especially at the low end of the temperature range.

The main difficulty of the IR measurement technique is the calibration of the greybody emissivity of the sample which is required to extract the temperature of the object from its emitted radiation. Measurement errors in the determination of the emissivity will propagate through the calculation of the temperature using equation (5.8) and will become the major contributor to the inaccuracy of the technique. This contribution will be explained in detail in the next section.

Finally, an important limitation of the measurement technique is the lateral resolution of the system (31 μm) which, in some cases, is identical to the size of the device itself. Examples include the flexure arm of models 2_(30) and model 2_(100), and the resistors.

5.3.2.3. Emissivity determination

For the devices under study, the problem of determining the target emissivity becomes particularly difficult due to the semi-transparency of the SU8 polymer to infrared radiation. To the best of my knowledge, there is no published data about the optical properties of SU8 in the infrared range (emissivity, transmittance and reflectance), but the fact that the gold metallisation is 'IR-visible', indicates transparency of the SU8 at the wavelength of the camera (λ = 8-9 μm).

In semi-transparent materials, the emissivity is limited by the transmission and reflections from the surface of the target. The effective emissivity will depend on the sample material, its thickness and, eventually, on the substrate material underneath. The emissivity value will fall with reducing thickness of the semi-transparent film, leading to an increase in transmission from behind the target.

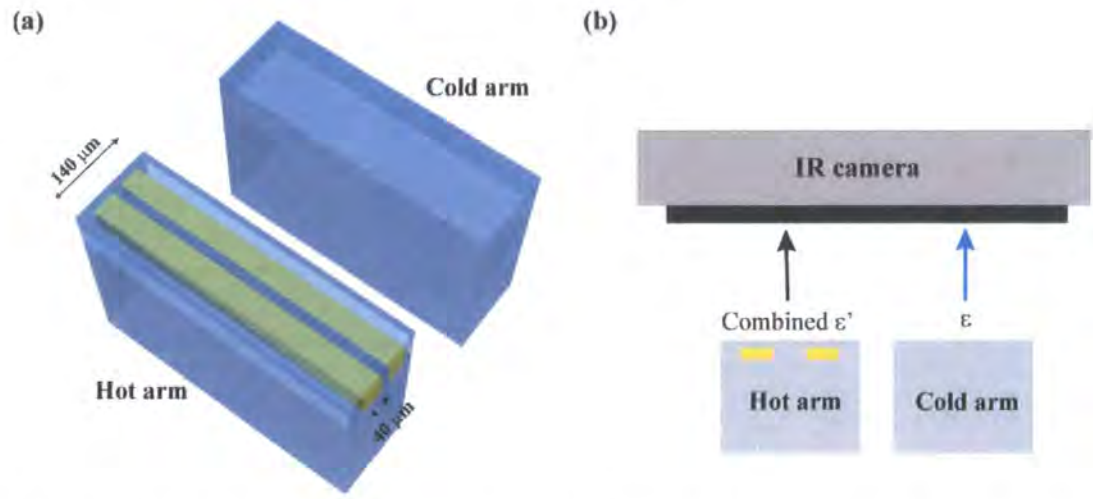

Fig. 5.10: Semi-transparent view of a polymeric actuator with the gold tracks embedded within the polymer beam: (a) 3D view (b) Cross-sectional view.

Fig. 5.10 shows the nature of the sample to be measured. In the cold arm only one material (SU8) is present and, once an effective emissivity is established experimentally, an accurate reading of the temperature should be obtained. The surface of the hot arm, however, is composed in equal parts of SU8 with no substrate underneath (thickness of 30 or 100 µm depending of the sample) and of SU8 (thickness 1.5 µm) with a gold substrate underneath. This implies that within the limits of the spatial resolution of the system (31 µm) we find two material samples. Therefore an effective emissivity for this surface cannot be easily determined and, as noted previously, its determination will become the major contributor to the inaccuracy of the measurements.

The thermograph shown in Fig. 5.9 also reflects the dual nature of the surface of the hot arms where the geometry of the gold circuit can be easily identified in a darker colour. In addition, the gold material with very low emissivity (and therefore high reflectance) is reflecting the infrared radiation emitted by the cooled sensor inside the camera. This radiation is transmitted through the 1.5 µm layer of SU8 and is also captured by the sensor. The reading of the temperature in those areas is expected to be lower than the real temperature. The calculation of the emissivity and its contribution to the error budget in the measurements will now be analysed.

Table 5.3: Emissivities determined experimentally

Emissivities	Anchor	Hot arm	Cold arm
design 1_(30)	0.90	0.56	0.78
design 1_(100)	0.90	0.60	0.85
design 2_(30)	0.90	0.58	0.76
design 2_(100)	0.90	0.61	0.85

To determine the emissivity of the sample the infrared camera and an external reference temperature was used [306]. First, the system was heated to a constant temperature of 60 °C on a calibrated hotplate (±0.1 °C accuracy). The input emissivity was then altered until the reading of the temperature in the thermal images agreed with the temperature indicated by hot plate. This procedure was repeated to obtain the emissivities of the sample on the anchor, the cold arm and the Au_SU8. The values of the emissivities obtained are shown in Table 5.3.

During calibration, it has been observed that the emissivity calculated for the hot arm is affected slightly by the relative position of the objective of the camera and the arm and this is more noticeable at high temperatures when the microgripper is slightly bent outwards. In addition the emissivity has been calculated at a temperature of 60 °C. As the hot arm is likely to reach temperatures of more than 100 °C, a slight change of the emissivity can be expected and larger errors at high temperatures are expected.

5.3.2.4. Temperature corrections

In order to examine how an error in the value of the emissivity is translated into an error in the temperature measurements a simple test has been conducted. Thermal images of the microgripper have been taken at 20, 30 and 40 mA. For each current level, variations of ±3 % around the emissivity determined experimentally (Table 5.3) have been applied. A comparison of the temperature increase from pixel to pixel has been obtained for the average temperature in the hot arm.

The absolute errors associated to a 3% error in the emissivity have been calculated from the images for the average hot arm temperature and are ± 0.9 K at 20 mA, ± 1.8 K at 30 mA, and ± 3.0 K at 40 mA. These errors include the dispersion of the errors along the length of the arms where there is a gradient of temperature. The absolute errors are smaller at lower temperatures and larger at higher temperatures.

This procedure can be repeated for different values of the errors and at different current and temperatures ranges. However this is very time consuming and it has been verified that it gives approximately the same error values as the ones given by equation (5.9) which is commonly used in the IR community.

$$\frac{\Delta T}{T} = \frac{\lambda T}{C_2}\frac{\Delta \varepsilon}{\varepsilon} \tag{5.9}$$

where C_2 is the second Planck's constant expressed in microns Kelvin, T is the absolute temperature of the object expressed in Kelvin [K], λ is the wavelength at which the camera operates, ε is the calculated emissivity, and $\Delta\varepsilon$ and ΔT are the errors of the emissivity and the temperature measurement respectively.

Fig. 5.11 shows the absolute errors in the temperature measurements calculated for different emissivity errors (3, 5 and 8%) on the emissivities of the hot (nominal emissivity = 0.6), and cold (nominal emissivity = 0.85) arms.

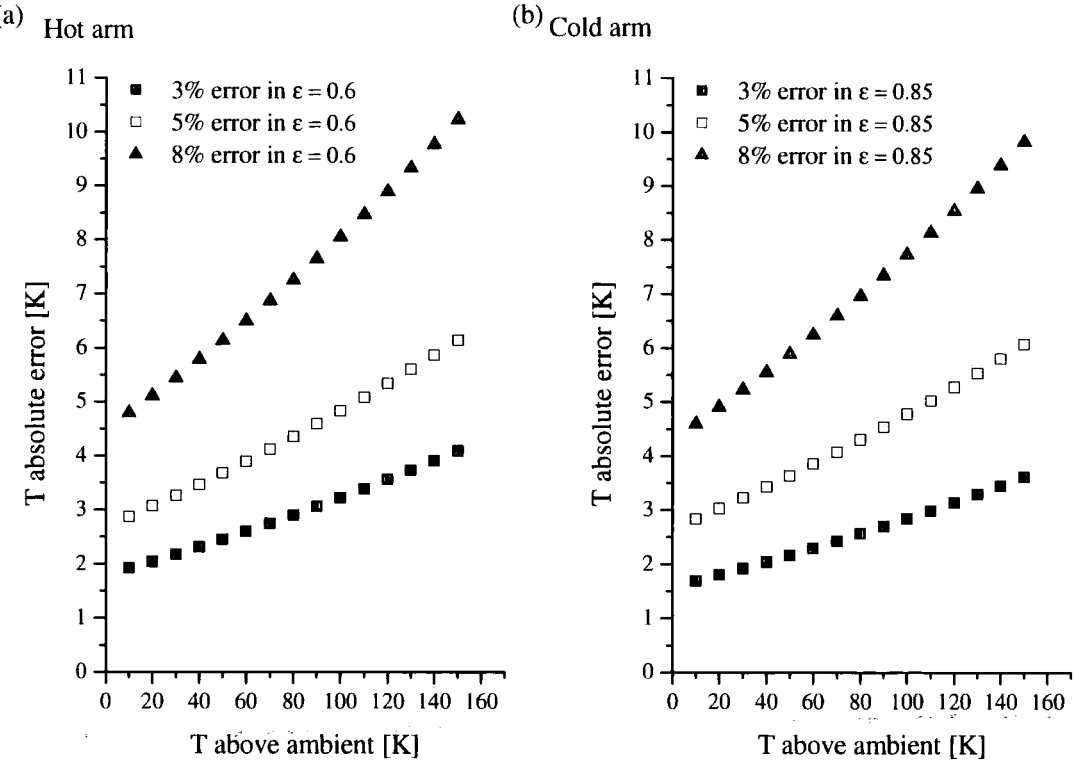

Fig. 5.11: Absolute error in the temperature measurement for different increases of temperature above ambient (10-150 K) and for different emissivity errors (3, 5 and 8%). (a) Simulation of the error due to an error in the hot arm (emissivity = 0.6) (b) Simulation of the error due to an error in the cold arm (emissivity = 0.85).

In the experiments, the emissivity was calculated at a temperature of 60 °C. For the different microgrippers, values of the emissivity of the hot arm between 0.58 and 0.62 were obtained. Thus for temperatures ~60 °C an estimated error of the emissivity of 3% seems to be appropriate. In the case of higher temperatures (>100 °C) a major error in the emissivity could be expected. In this study a 5% error will be used at high temperatures. Fig. 5.11 has been used as a reference for the calculation of the errors.

The errors associated to the emissivity are greater than the accuracy of the camera (±1 K) and the precision (<1 K) and will be added to the results.

5.3.3. Steady-state temperature measurements

In the steady-state experiment, the main goal was to obtain the temperature distribution along the arms of the actuators for a set of different input currents, voltages, or power.

The results shown in this section are organised as follows. First a set of IR images taken for each device at different input currents will be shown. This will give the reader an idea of the spatial resolution and the quality of the thermal images. Then, the temperature data extracted from the IR images will be presented and analysed as a 1D temperature steady-state distribution along the unfolded length of the actuators. The temperature measurements in combination with the electrical experiments will be used to extrapolate two material properties of the metallisation layer: the resistivity and the temperature coefficient of resistance. Finally, IR thermography will be used in dynamic mode to extract transient times during heating and cooling.

5.3.3.1. Device thermal mapping

During the measurements, a constant current source (Keithley 2200) was used to actuate the different microgrippers in air. Current levels ranging from 5 to 40 mA were applied and an IR image was taken for each 2 mA step. The IR images were taken in a non-consecutive manner, guaranteeing the cooling down of the sample in between the current steps.

Once the IR images were obtained, different post-processing actions were needed to guarantee the quality of the temperature measurements. These actions included: the

reduction of the background radiation, the inclusion of the correct emissivities in each area of the image (hot arm and cold arm), and the selection of the areas to be analysed.

In order to minimise the effect of the background radiation, each IR image for a particular current level was individually subtracted from the corresponding IR image taken at 0 mA. This generated a third IR image that does not indicate absolute temperatures but instead increments of temperature above the initial temperature of the device. Hence, unless otherwise indicated, all the data presented in this section will refer to increments in temperature above ambient and will be indicated as T e.g. T_h will denote the average temperature increase of the hot arm.

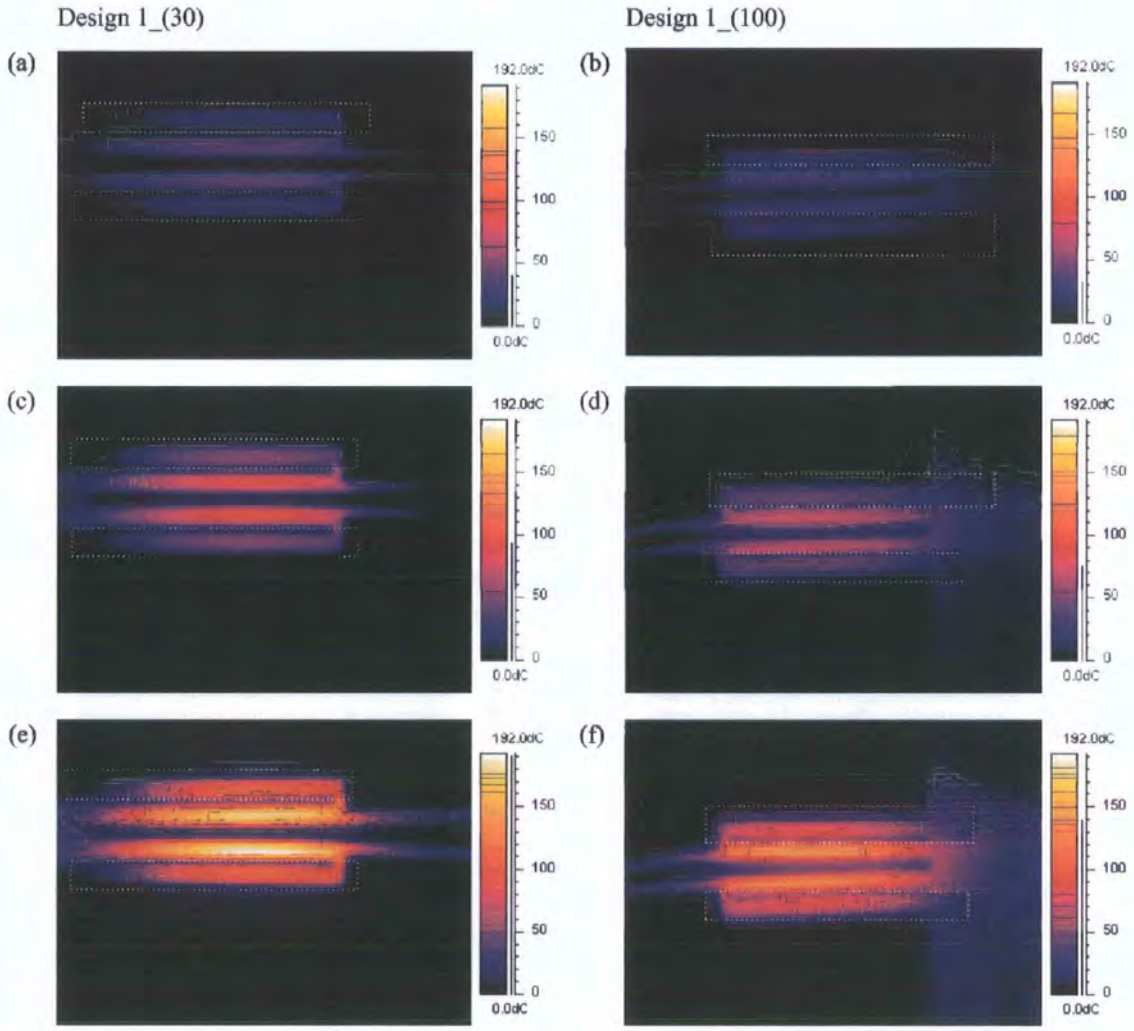

Fig. 5.12: IR images taken at 20 mA, 30 mA and 40 mA from top to bottom, from design 1_(30) (left) and design 1_(100) (right).

This image subtraction procedure was repeated twice. Given the emissivities of the cold and hot arms the temperature data concerning each arm had to be extracted from two

different IR images: one with emissivity of 0.6, another with emissivity 0.78 or 0.85 depending of the model. The use of a single image for both arms with, for example, an emissivity 0.6 would result in an apparent higher temperature of the cold arm, or equivalently a lower temperature difference between the arms.

Fig. 5.12 and Fig. 5.13 show typical IR images taken at input currents of 20, 30 and 40 mA for design 1_(30) and 1_(100), and design 2_(30) and 2_(100) respectively. For illustrative purposes, the two IR images that are processed per microgripper design and per emissivity have been merged in a single photo. The dotted line represents the part of the photo with a different emissivity.

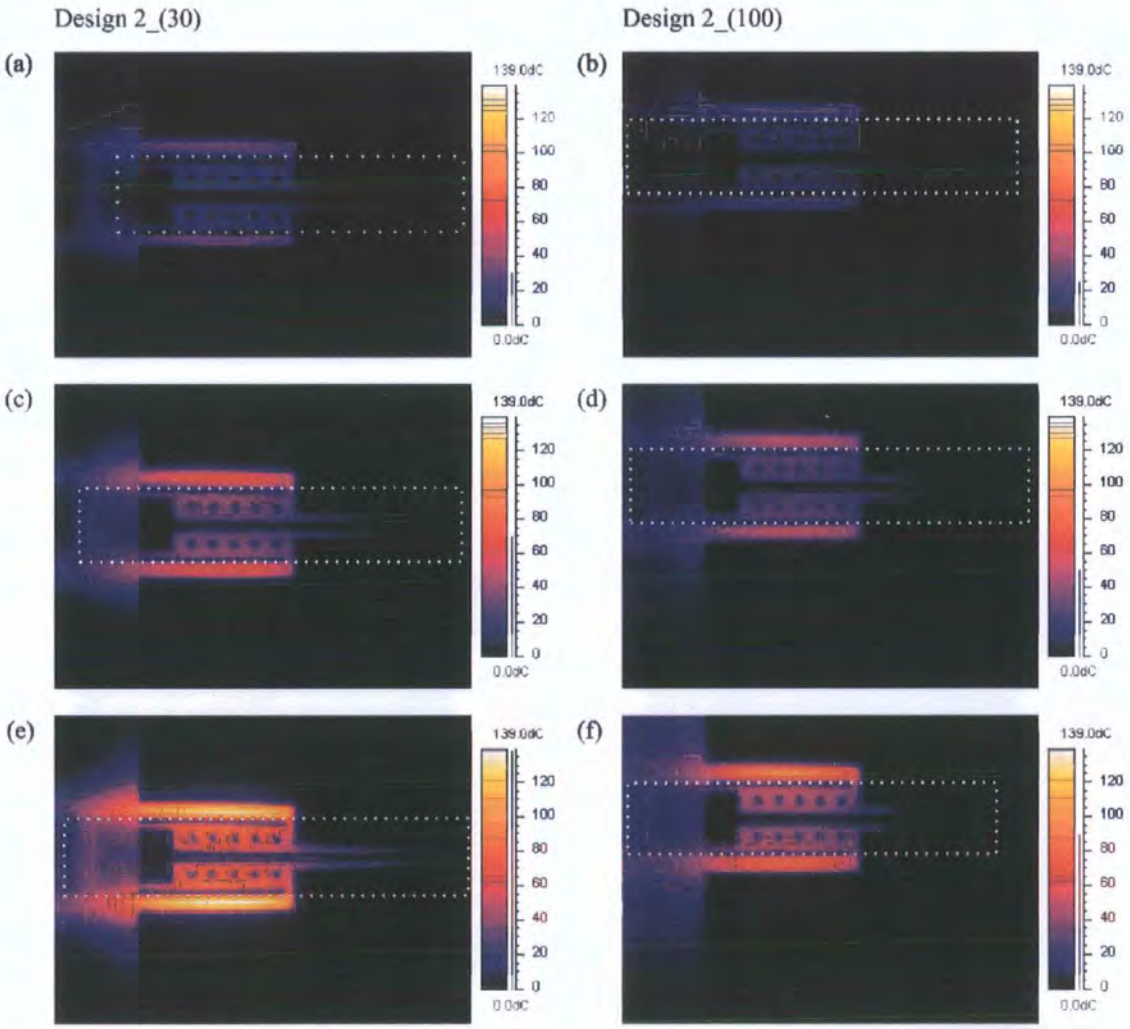

Fig. 5.13: IR images taken at 20 mA, 30 mA and 40 mA from top to bottom, from design 2_(30) (left) and design 2_(100) (right).

The colour scale on the right hand of the images covers the whole range of actuation temperatures for each design in its two different thicknesses. Thus the images in design

1 will go from a increase in temperature of 0 K up to 190 K. The maximum temperature reached within individual images is indicated by a fine black line on the colour scale. For example in design 2_(30) at 30 mA (Fig. 5.13 (c)) the maximum temperature rise is approximately 70 K.

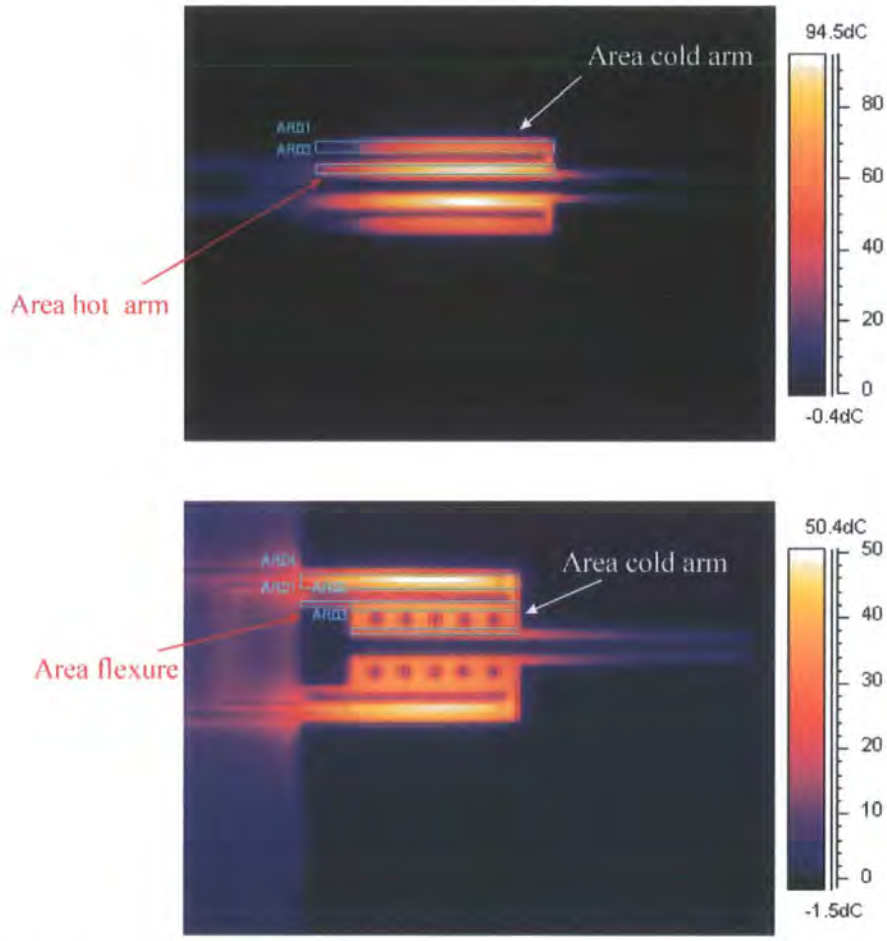

Fig. 5.14: Image processing: areas of analysis in design 1 (top) and design 2 (bottom)

The first thing that can be seen from Fig. 5.12 and Fig. 5.13 is that for the same input current, there are differences between the temperature distributions developed in design 1_(30) compared to design 1_(100), and in design 2_(30) compared to design 2_(100). The reason for that might be twofold: the differences in heat generation per input current due to differences in the metallisation thickness, and different heat losses due to different aspect ratio of the structures. In all the cases, as the current increases the hot arms of the microgrippers heat up and an asymmetric heating is created between the arms of the actuators. The IR images also show that the temperature distribution is symmetric around the central horizontal axis of the images. Thus characterising only one actuator and its corresponding jaw can be considered enough for the

characterisation of the whole microgripper. Once the IR images have been processed, predefined areas on the images can be used to extract the temperature data of the arms. The areas used for each design are indicated in Fig. 5.14 with a blue square: AR01 (cold) and AR02 (hot) for design 1 and, AR01- AR02- AR03 (cold) and AR04 (hot) for design 2. In the case of design 2, the cold arm has been divided into three regions to minimise the possible impact that the presence of the holes of the arms can have on the measured radiation.

From the images it is interesting to point out that, even though the spatial resolution of the camera is not good enough to provide accurate deflection measurements, it permits the visualisation of the opening and closing of the jaws as the temperature changes.

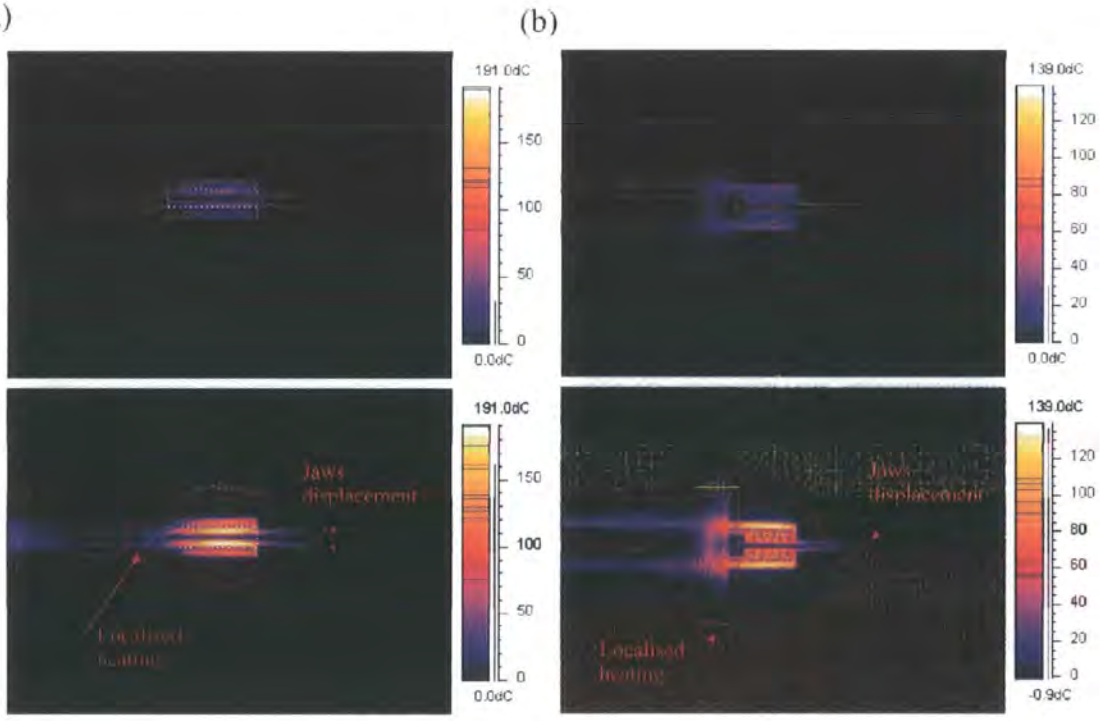

Fig. 5.15: (a) Microgripper design 1_(30) actuated at 20 mA (top) and 30 mA (bottom); (b) Microgripper design 2_(30) actuated at 20 mA (top) and 40 mA (bottom).

This is shown more in detail in Fig. 5.15. The jaws of design 1_(100) have been omitted since they were accidentally interlocked during the experiments and the physical opening was not possible[12]. A deformation in the jaws can be seen in Fig. 5.12 (d)-(f).

[12] After the IR images were taken, higher currents were applied and the jaws unlocked without inducing any damage to the structure that continued to operate correctly.

The large field of view of the IR camera also allows the assessment of the different thermal conditions present at the anchors and jaws of the devices. As can be seen from Fig. 5.15, localised heating is observed in the area surrounding the connection of the actuators with the anchor. As argued in the previous chapters, this can be explained by the thermal insulation that the thick SU8 polymer provides at the anchors.

Moreover, in the case of design 1_(30), the relatively good resolution of the image permits the detection of a fabrication inaccuracy. This is shown in Fig. 5.16, as a misalignment between the PCB, the glue, and the anchor of the microgripper. This will have an impact in the results of design 1_(30) since its total length has been effectively shortened.

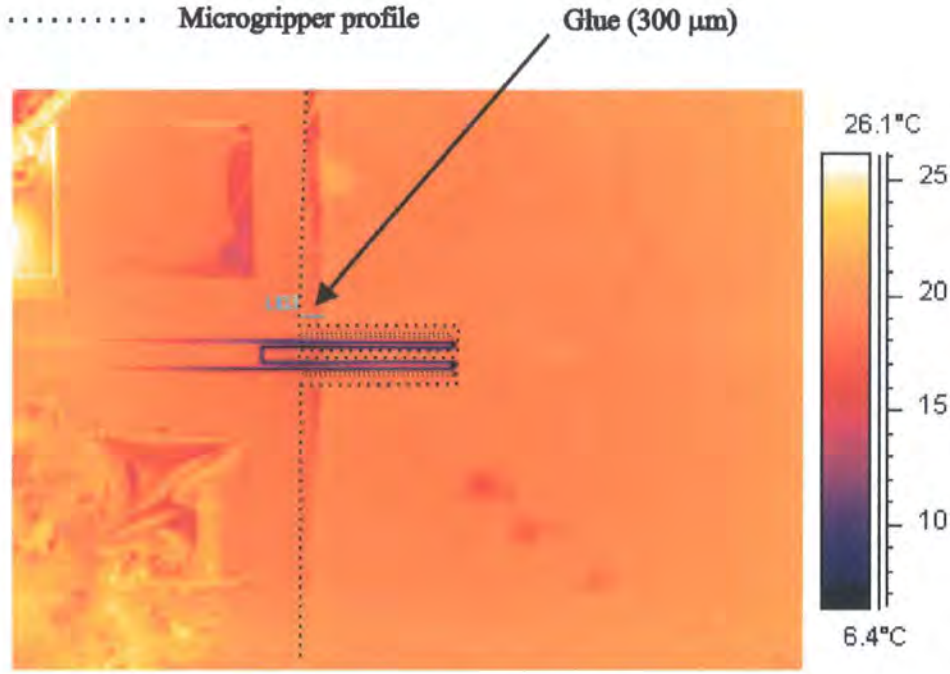

Fig. 5.16: Detail of the misalignment between the anchor of the microgripper and the PCB.

Furthermore the assumption that the jaws remain at ambient temperature has been verified. In the IR images taken at 40 mA, a temperature of approximately 3 °C has been measured at the jaw tips. However, it is possible that this temperature is caused by the distortion of the IR measurement due to the out-of-plane bending of the microgripper, more than due to a real temperature value.

5.3.3.2. 1D thermal distributions

Fig. 5.17 shows the coordinate reference system used in the presentation of the results. The x coordinate covers the full unfolded length of the actuator. For both designs the x = 0 coordinate is taken at the beginning of the hot arm and, depending on the device design, finishes at the end of the cold arm (Fig. 5.17 (a)) or flexure (Fig. 5.17 (b)). In the graphs presenting the experimental data the coordinate system will be presented unfolded, as in Fig. 5.17 (c).

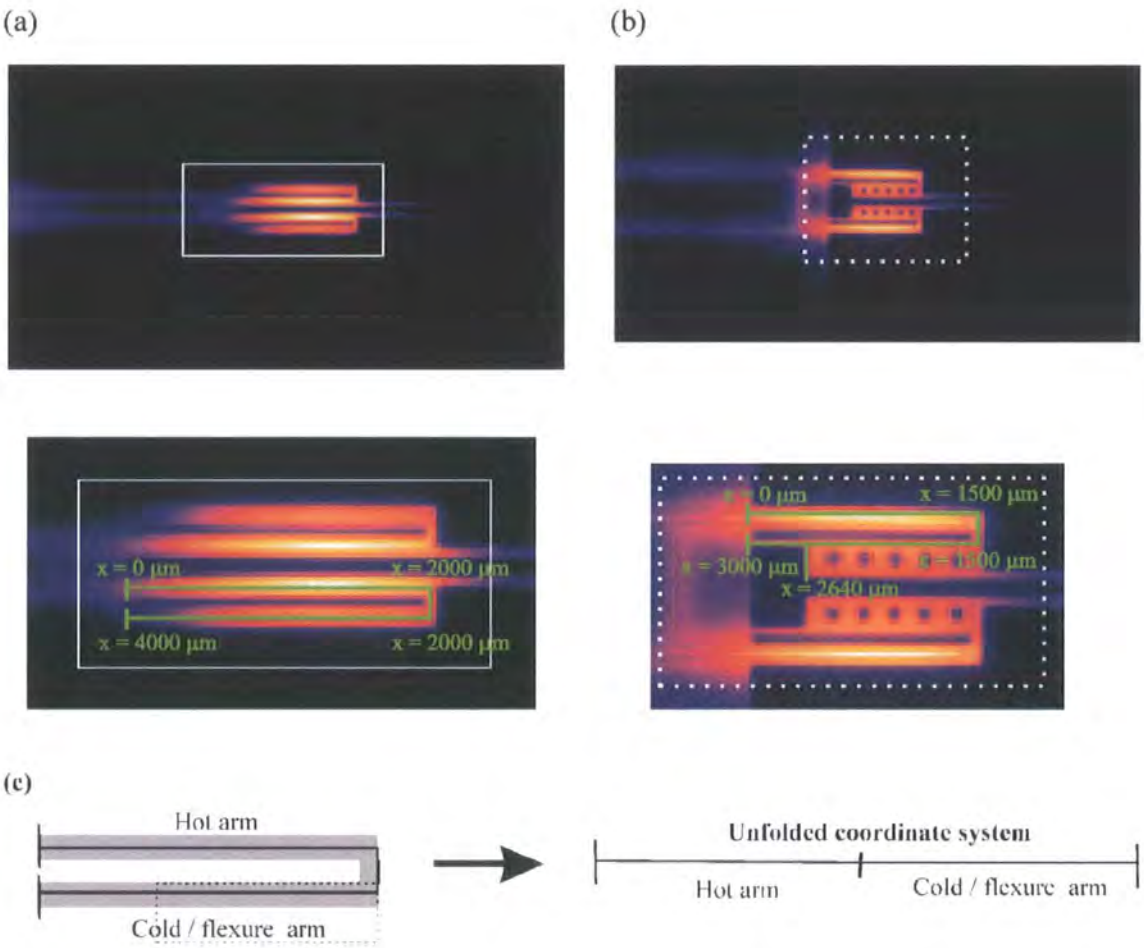

Fig. 5.17: Definition of the x coordinate system (a) design 1 (b) design 2 (c) Unfolded coordinate system used in the graphs.

Fig. 5.18 to Fig. 5.21 show the 1D temperature distribution along an individual actuator of each microgripper design. Each data point is the result of the averaging of six sets of measurements. The error bars shown on some data points combine the standard deviation (<1 K in most of the cases) with the error associated with a 3% (or 5%) error in the emissivity (see section 5.3.2.3).

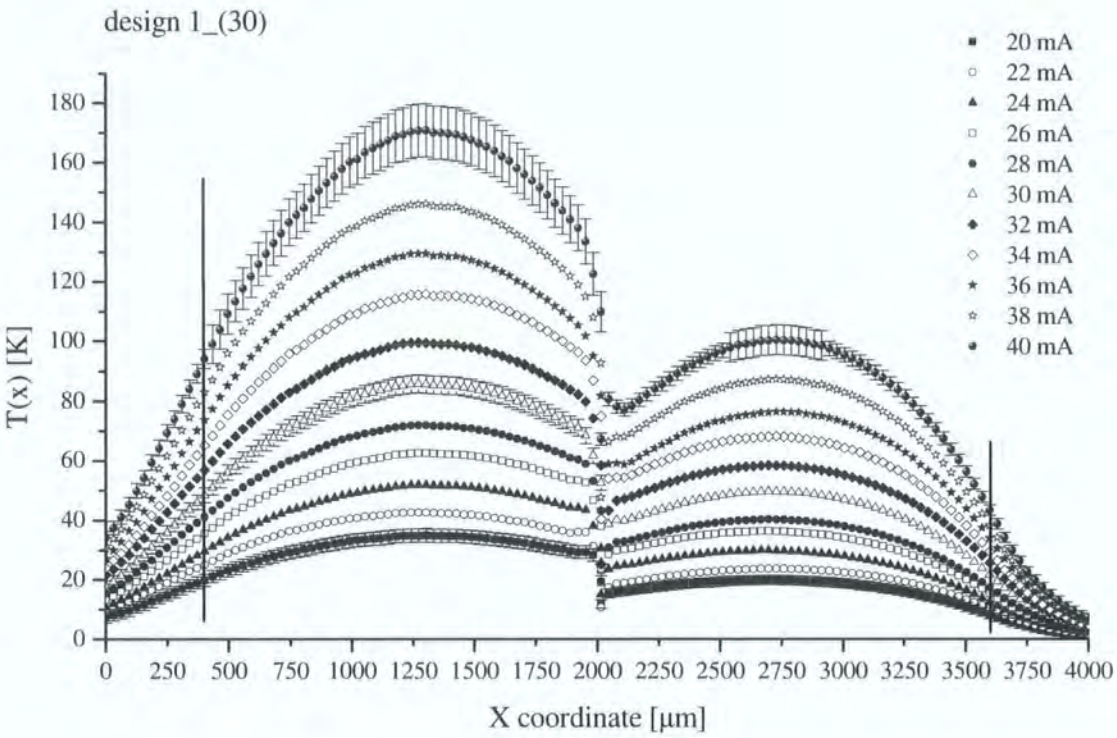

Fig. 5.18: Temperature distribution relative to ambient along the arms of an actuator of the microgripper (design 1_(100)) for different input currents.

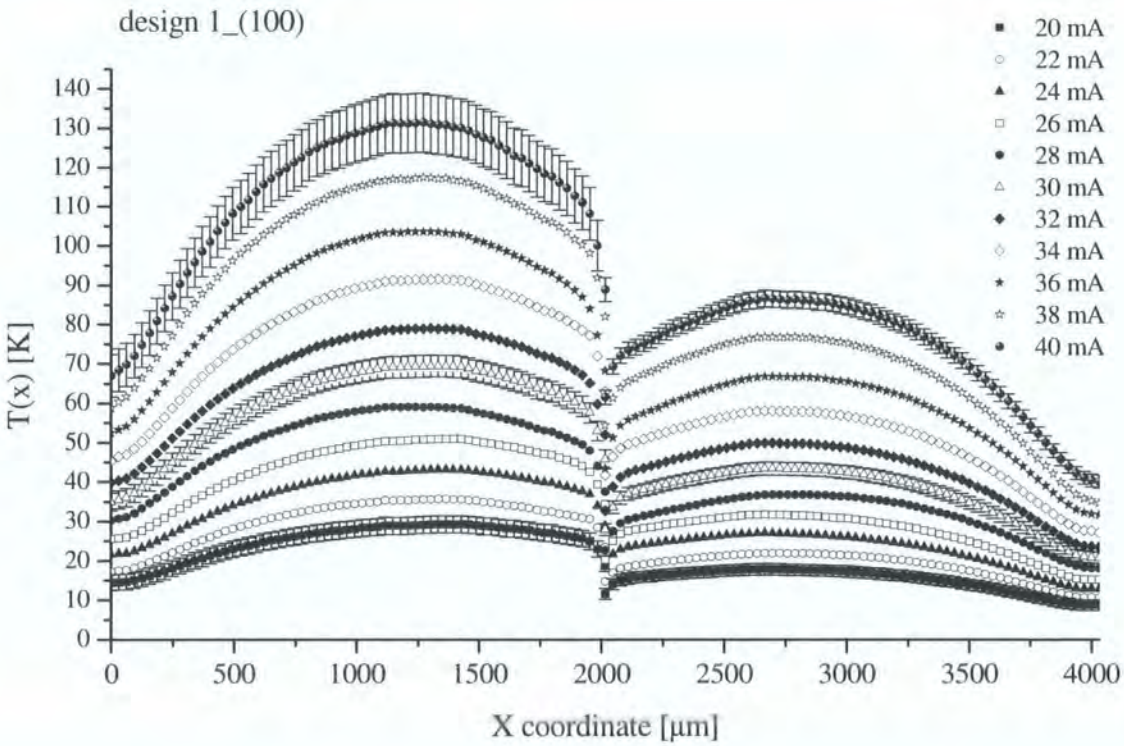

Fig. 5.19: Temperature distribution relative to ambient along the arms of an actuator of the microgripper (design 1_(100)) for different input currents.

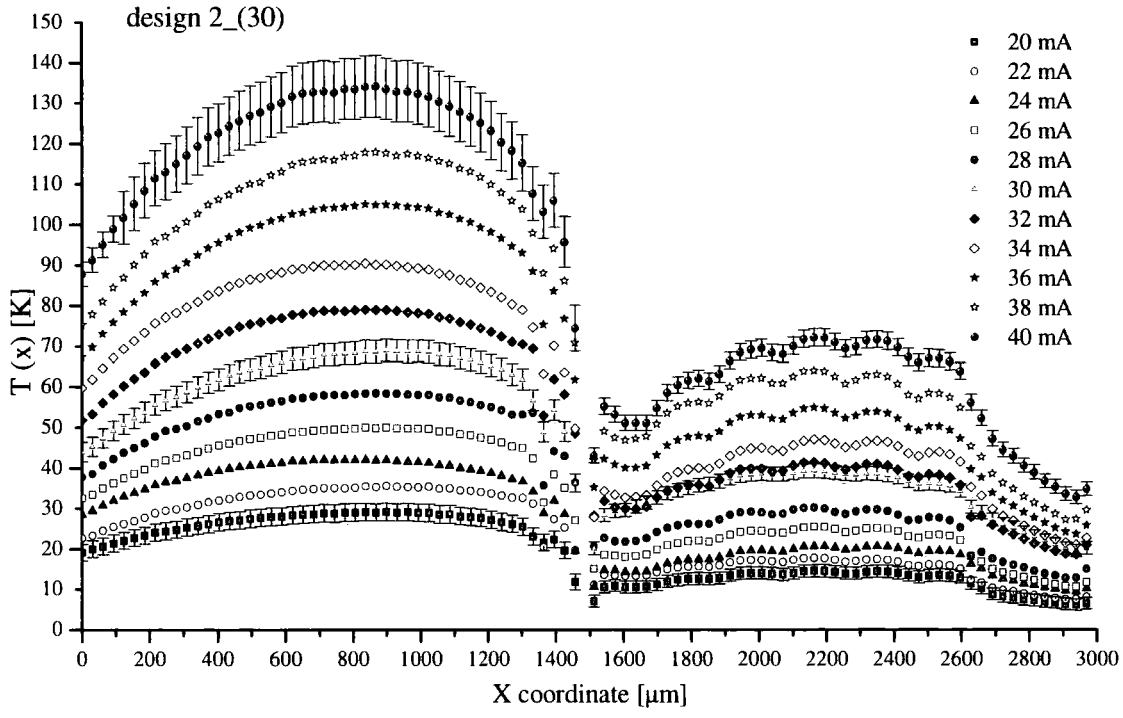

Fig. 5.20: Temperature distribution relative to ambient along the arms of an actuator of the microgripper design 2_(30) for different input currents.

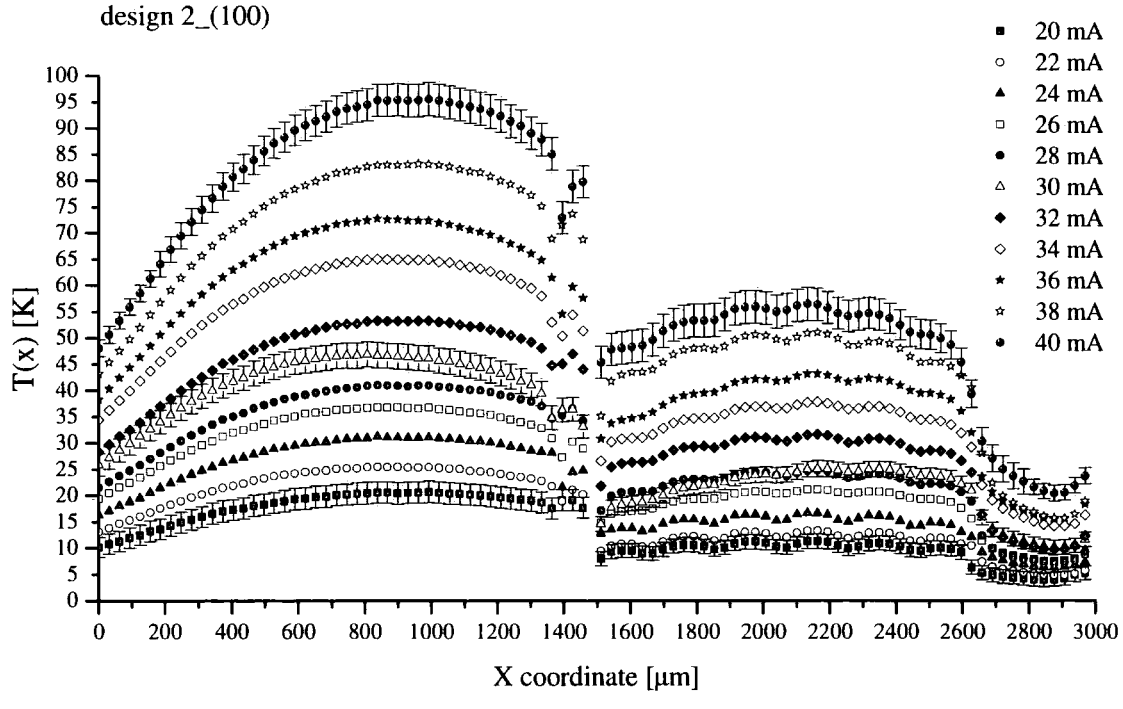

Fig. 5.21: Temperature distribution relative to ambient along the arms of an actuator of the microgripper design 2_(100) for different input currents.

5.3.3.3. Observations and discussion

The interesting aspect of having a temperature measurement technique that enables spatial resolution is that it permits the observation and evaluation of aspects of the system that cannot be seen with averaged results. Some of these aspects are, for example, the thermal conditions at the anchors, the thermal coupling between the cold and hot arms or particular environmental conditions that could affect the measured results.

From all of the temperature profiles, it can be seen that the temperature of the cold arm is consistently above ambient and that the profile increases in overall temperature as the current increases. In addition, it can also be observed that the temperature distribution along the cold arm shows a maximum in approximately the middle part of the arm. This indicates that the cold arm, apart from losing heat via the atmosphere and conduction to the anchors, also receives heat. Fig. 5.22 simulates the curve of a cold arm in equilibrium by losing heat to the atmosphere and to the anchors only (blue line) and by receiving heat from the hot arm (red line).

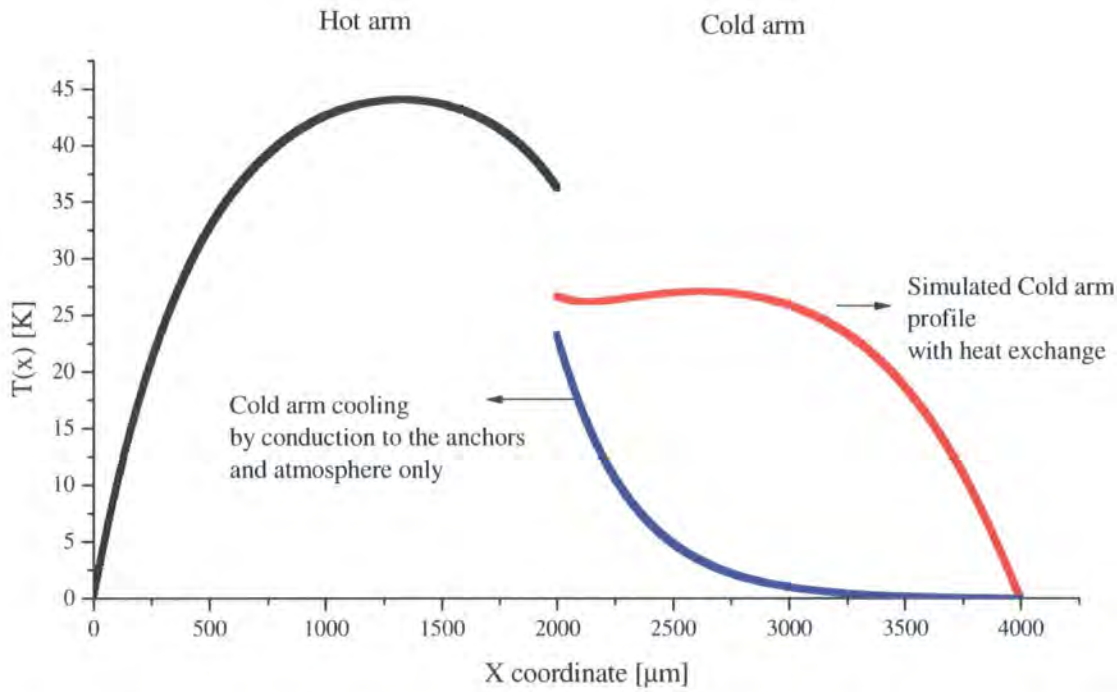

Fig. 5.22: Representation of the profile of the cold arm at equilibrium when no heat exchange is considered between the arms (blue line) and when heat exchange is considered (red line).

The temperature measurements alone do not allow an estimation of the magnitude of the heat exchange but corroborate the hypothesis presented in Chapter 4 that a heat exchange between the arms probably exists.

It can also be observed that, in all the cases, temperatures different to ambient temperature (T= 0 in the graphs) are measured at the beginning of the arms of the actuator i.e. at x = 0 μm, and x = 4000 (design 1) or 3000 μm (design 2). The value of these temperatures increases with the input current which indicates a relationship with the driving power. This contribution could also be included in the models as a boundary condition and will be treated quantitatively in more detail during the validation of the models in chapter 6.

Fig. 5.18 is particularly interesting because it shows how the boundary conditions at the anchors affect the overall temperature measurements. In that case the temperature of the cold arm at the connection with the anchor (x = 4000 μm) seems to be near the ambient temperature for all input currents. This is something not observed in the rest of the profiles. The x coordinate in the figure covers the unfolded length of one of the actuators of design 1_(30). However, as observed in Fig. 5.16, it would be more appropriate to consider the length as being effectively shortened by at least 300 μm. This effective shortening can be seen in the profiles of Fig. 5.18 where two vertical lines at x = 300 μm and at x = 3700 μm indicates the area where the actuator is effectively released from the PCB board. For design 1_(30) an effective length of 3400 μm will be used from now on.

Fig. 5.18 also gives information about the active length of the resistors in the anchors. It can be seen that in design 1_(30) the cold arms placed in the exterior of the microgripper cool down after ~400 μm. All of this will have some implications for the rest of the design and will affect, for example, the modelling of the material properties of the metallisation layer.

5.3.3.4. Extrapolation of the material properties of the metallisation

Having measured the total resistance across the device and the average increase in temperature of the hot arm for different input currents, it is now possible to apply

equation (5.3) to obtain two material properties of the metallisation layer: the resistivity, ρ_0, and the temperature coefficient of resistance, *TCR*. A least squares linear fit to the data presented in Fig. 5.23 and Fig. 5.24 have been used to determine the slope, m, and the intersect, b for each device. Reorganising equation (5.3) shows that

$$\rho_0 = \frac{ba}{L_T} \tag{5.10}$$

$$TCR = \frac{ma}{\rho_0 L_{M+R_3}} \tag{5.11}$$

where a is the section of the resistor, and L_T and L_{M+R3} are respectively the lengths of the whole resistor and the length of the active heaters (see Fig. 5.2).

From Fig. 5.24 (d) it is evident that in some cases the resistance is not continuous or linear with temperature. Even though the linear regression has been applied to obtain the material properties, non linear effects of resistance should be studied in high accuracy models.

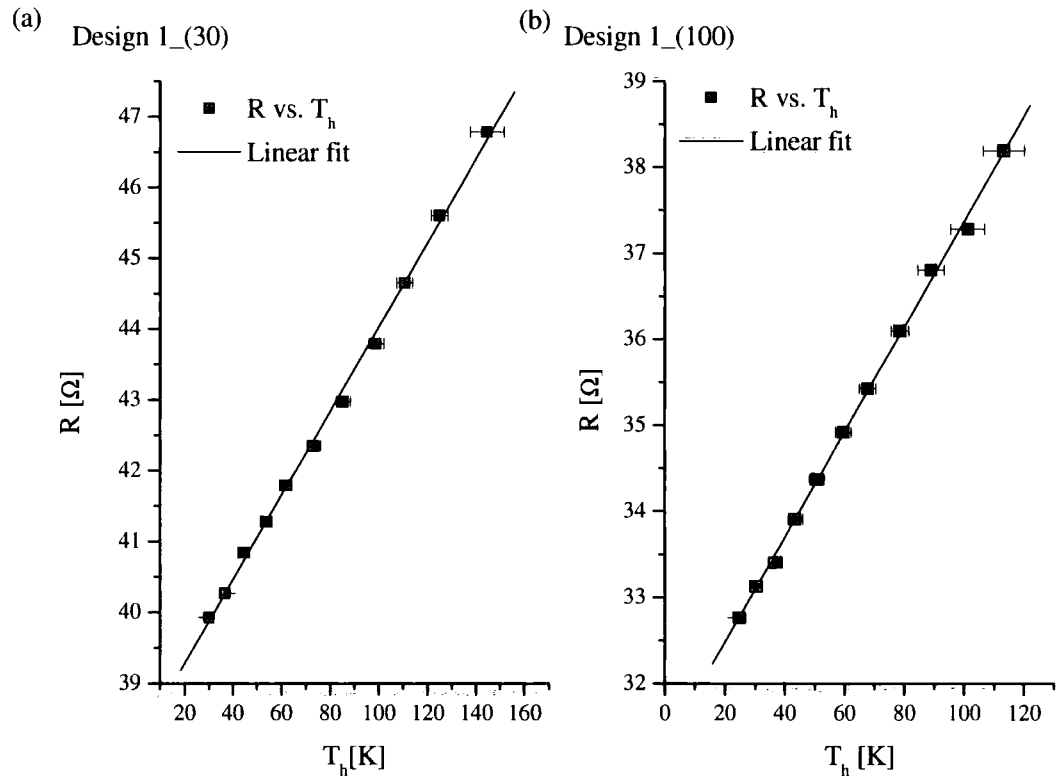

Fig. 5.23: Resistance vs. hot arm temperature (relative to ambient): (a) design 1_(30) (b) design 1_(100)

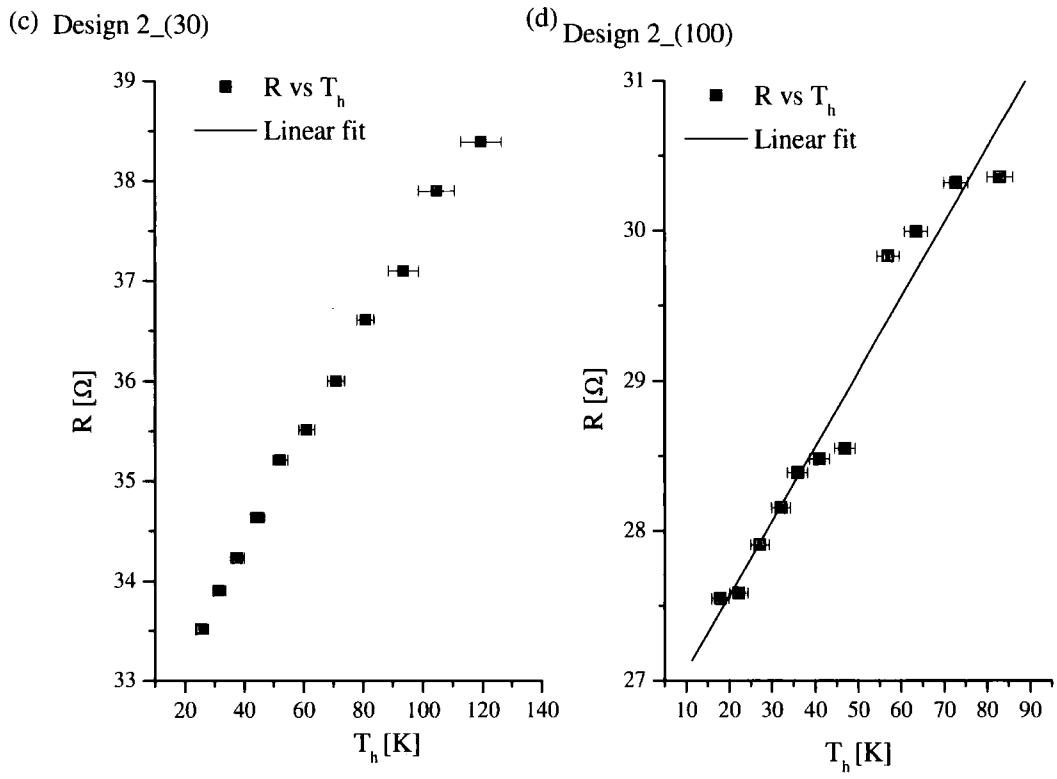

Fig. 5.24: Resistance vs. hot arm temperature (relative to ambient): (c) design 2_(30) (d) design 2_(100).

Table 5.4 shows the resistivity and TCR values calculated for design 1_(30), design 1_(100), design 2_(30),and design 2_(100).

Table 5.4: Material properties extrapolated from the electrical and thermal measurements.

	Effective resistivity [Ω*m]	Temperature coefficient of resistance TCR [K^{-1}]
design 1_(30)	1.990E-08	0.00385
design 1_(100)	2.050E-08	0.00384
design 2_(30)	2.000E-08	0.00384
design 2_(100)	2.080E-08	0.00398

The numerical values obtained for the resistivity and the temperature coefficient of resistance in all of the cases are comparable to the standard values given for thin film gold resistors (2.04×10^{-8} Ω m [292] 0.0037 K^{-1} [45]). In addition, the gold metallisation seems to have slightly lower resistivity than the bulk property and slightly a higher temperature coefficient of resistance coefficient than the bulk property, which is

consistent with the expectation from thin films. These results are also an indication of the good quality of the temperature measurements. It also tells us that, if only the average temperature in the hot arm is necessary, equation (5.3) would be valid using relatively standard material properties for thin films. This is important because IR imaging systems are not standard testing equipment.

5.3.4. Transient temperature measurements

To measure the thermal response of each microgripper, the IR camera is set up to take consecutive IR images at a frequency of 50 Hz. This represents a photo taken every 20 ms which should be enough to capture the response time of the microgrippers. Fig. 5.25 shows an example of the level of detail that can be obtained with this measuring technique. It shows the cooling profile for design 1_(100) with starting temperatures given by different input currents: 20, 30 and 40 mA.

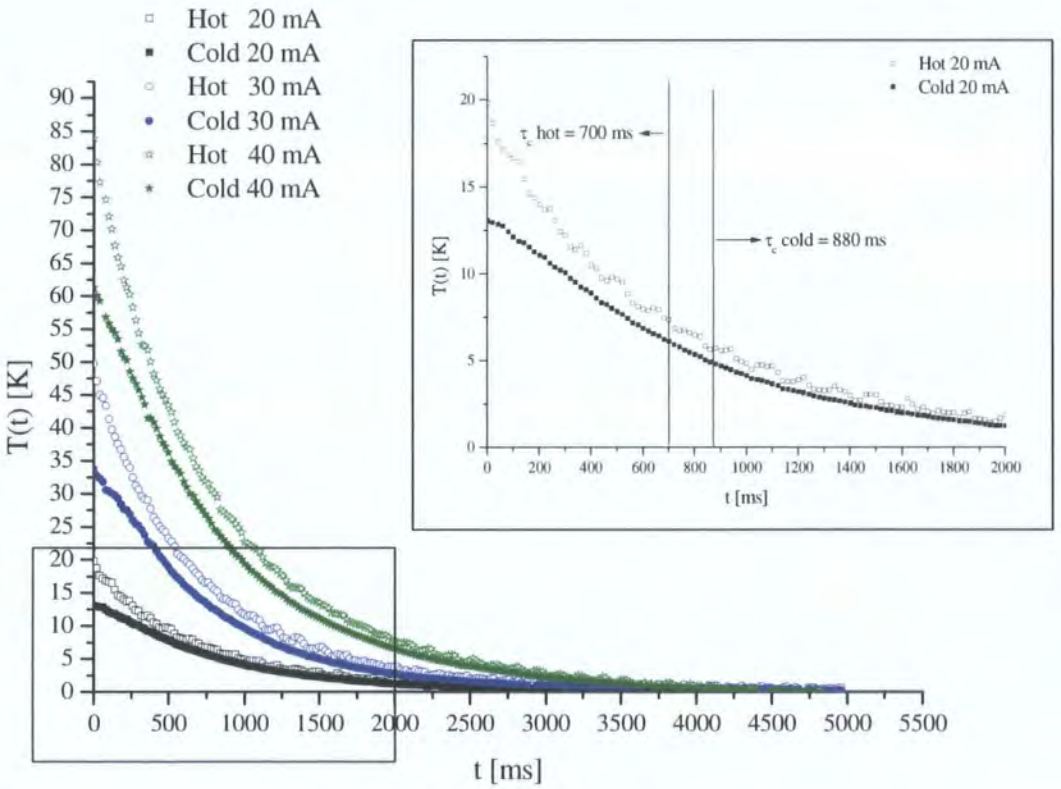

Fig. 5.25: Cooling profile for design 1_(100) with different initial temperatures(relative to ambient) given by initial currents of 20 mA, 30 mA and 40 mA.

The thermal response of a 'beam system' such as the microgripper is primarily governed by the size of the cross section. Therefore, in the microgrippers, beams with

different cross sections such as the hot arm, cold arm and flexure, are expected to respond differently. The response time is also dependent on other factors such as the mass of the beam, the specific heat of the material and the coefficient of heat transfer. Therefore, in the design where the cold and hot arms have identical cross sections, but different constituent materials (SU8+gold, and SU8), a variation in the cooling can be expected.

It is important to distinguish the response time of a system, τ_R, from the time constant, τ_C. The response time is defined as the time required to reach 99% of the theoretical thermal equilibrium. The time constant is defined as the time required reaching 63% of the steady state temperature imposed at a given input power.

Both the time constant and the response time for all of the microgrippers have been obtained from the dynamic measurements of temperature during heating and cooling. The numerical values are given in Table 5.5.

Table 5.5: Cooling thermal response and constant for the different microgrippers

Cooling time [s]		20 mA	30 mA	40 mA
design 1_(30)	**τ_c hot**	0.172	0.138	0.165
	τ_c cold	0.275	0.213	0.267
design 1_(100)	**τ_c hot**	0.700	0.655	0.727
	τ_c cold	0.975	0.848	0.878
design 2_(30)	**τ_c hot**	0.180	0.137	0.186
	τ_c cold	0.253	0.245	0.298
	τ_c flexure	0.180	0.189	0.268
design 2_(100)	**τ_c hot**	0.490	0.497	0.470
	τ_c cold	0.913	0.950	0.892
	τ_c flexure	0.750	0.727	0.655

As can be seen from the transient data, the bandwidth limiting process for the microgrippers is always the cooling of the cold arm which has the longest response times and constants.

The longest cooling response time is 4 seconds in air. This seems to be a relatively long time even for a human operator. However, the microgripper is intended to be used in a liquid environment where the heat losses are over 20 times higher. This would reduce

the response time considerably. The longest response time during heating is much lower and is less than a second in air.

The data in table 5.5 also allows one to check some of the assumptions made during the development of the models. The first thing that can be seen is that thinner beams (design 1_(30), and design 2_(30)) cool faster than thicker beams (design 1_(30), and design 2_(30)). This was justified by the difference in mass and diameter of the beam. It can also be seen that the hot arm of the design 1_(100) cools down slower than the cold arm of design 2_(100). The diameter and morphology of these two arms are identical, and very similar time constants should be expected. A justification for that could be the configuration of the microgripper. In design 2_(100) the hot arms are in the external part of the microgripper and it is possible that the effective cooling is higher in those beams compared to similar beams in the interior of the structure. The difference in response time between the beams in design 1, i.e. τ_R is higher for the cold arm than for the hot arm, could be due to two factors: the difference in material composition and the heat exchange between the arms that could results in an extra heating of the cold arm during cooling.

5.4. Deflection experiment

The main goal of the deflection experiments is to measure the opening/closing of the different microgrippers for a set of different input powers and voltages. The results shown in this section are organised as follows: First, the deflection of the devices – design 1_(30), design 1_(100), design 2_(30), and design 2_(100) – will be measured in air and the results will be presented as a function of the input power. Next, using design 3_(100), the deflection is measured in air and compared with the deflection measured in a liquid environment for the same input power. Then aspects concerning the repeatability of the actuation and the lifetime will be presented. Finally a set of manipulation experiments will be presented.

5.4.1. Deflection measurements in air

Current levels ranging from 5 to 40 mA in 2 mA steps were used to power the different microgrippers under an optical microscope. The voltage drop was measured simultaneously using a voltmeter, and the displacement was recorded using a CCD

camera attached to the microscope. The post processing of the digital images (Fig. 5.26 (a)) enabled the net and absolute deflection of the jaws to be measured.

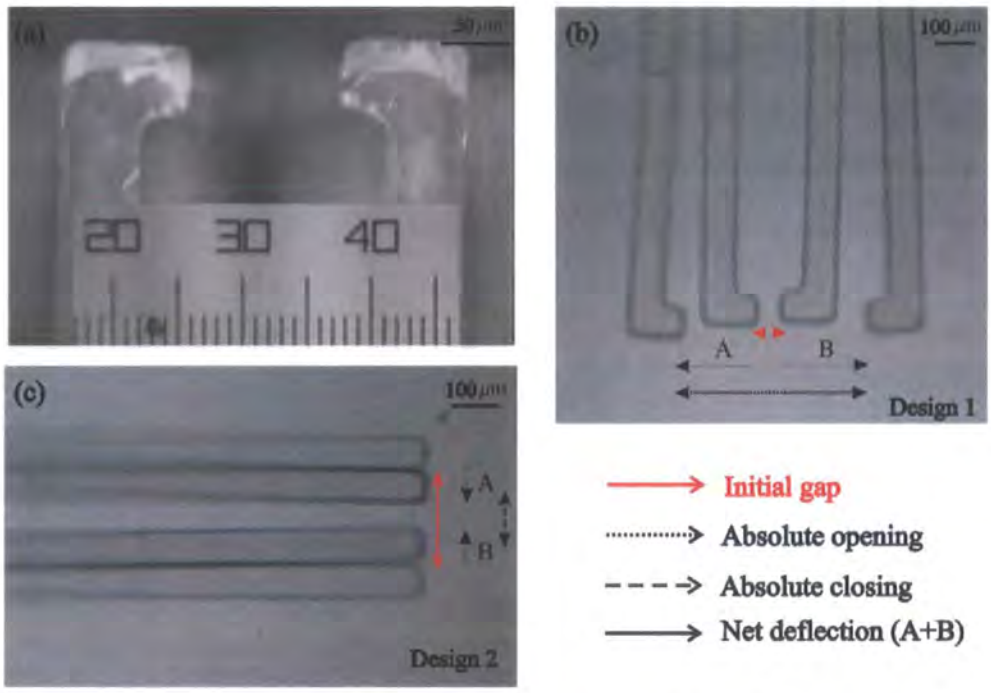

Fig. 5.26: Set of digital images taken during the experiments. (a) Magnification used for the measurements (b) Reference for the measurements of the normally close microgripper (design 1) (c) Reference for the measurements of the normally open microgripper (design 2)

The measurement procedure is depicted in Fig. 5.26 (b) for the microgrippers operating in a closed mode, and in Fig. 5.26 (c) for the microgrippers operating in open mode. The resolution of the images is 0.6 microns (1 pixel), but a certain level of blurriness in the images (due to out-of-plane deflection and focus adjustment) results in an estimated accuracy of ± 3 pixels. This has been included in the deflection data as a systematic error of ±1.8 μm.

The deflection of each microgripper in air versus input power and voltage is plotted in Fig. 5.27 to Fig. 5.30. In each of these graphs, the left and right axes indicate respectively the deflection of the microgripper from its initial position, and the total spacing between the jaws. The latter corresponds to (1) the absolute opening of the microgrippers for the designs operating in open mode (i.e. design 1_(30) and design 1_(100)) and (2) to the absolute closing of the microgrippers for the designs operating in open mode (i.e. design 2_(30) and design 2_(100)). As explained in the design chapter the initial separation between the jaws ultimately determines the range of sizes that can

be manipulated by each design. The initial separation between the jaws is given in each of the figures.

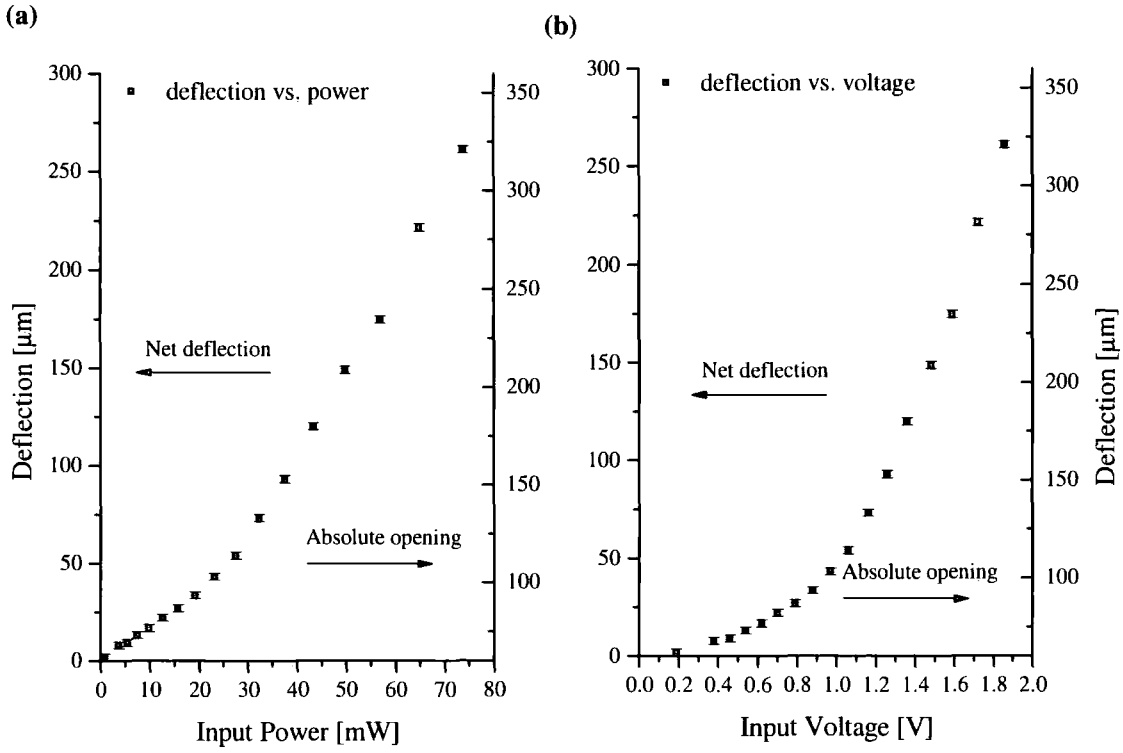

Fig. 5.27: Design 1_(30) (initial gap = 60 μm) (a) Deflection versus input power (b) Deflection versus input voltage.

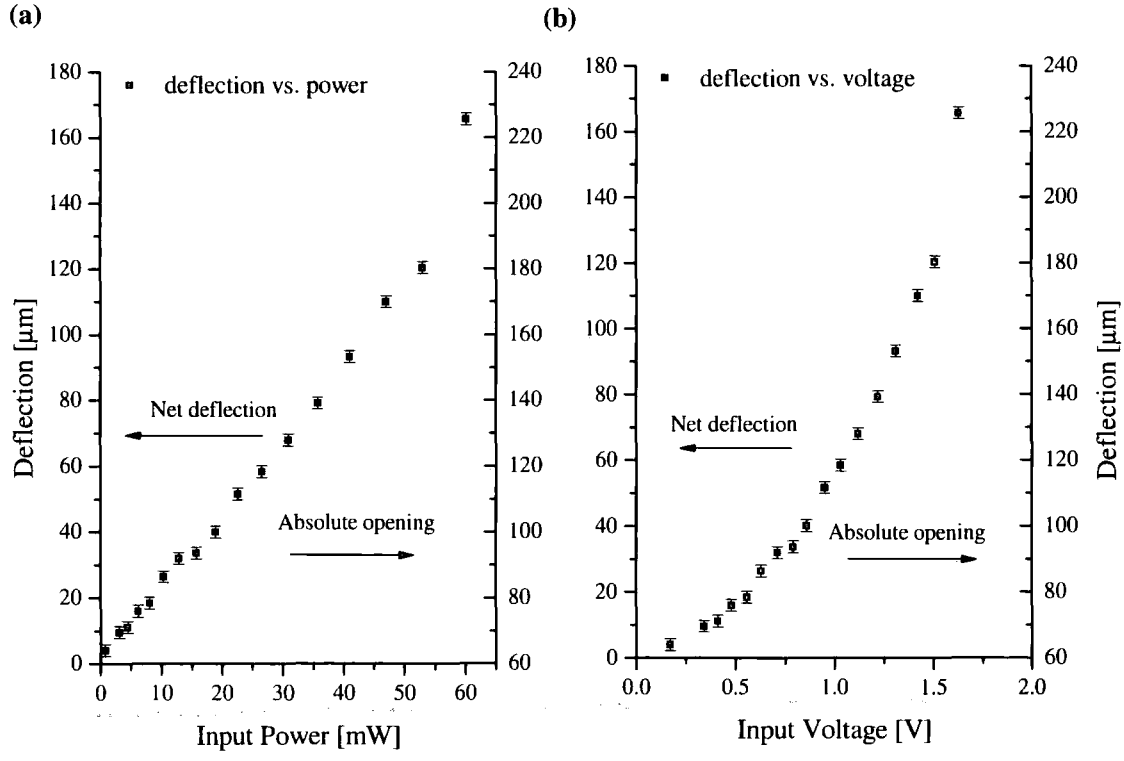

Fig. 5.28: Design 1_(100) (initial gap = 60 μm) (a) Deflection versus input power (b) Deflection versus input voltage.

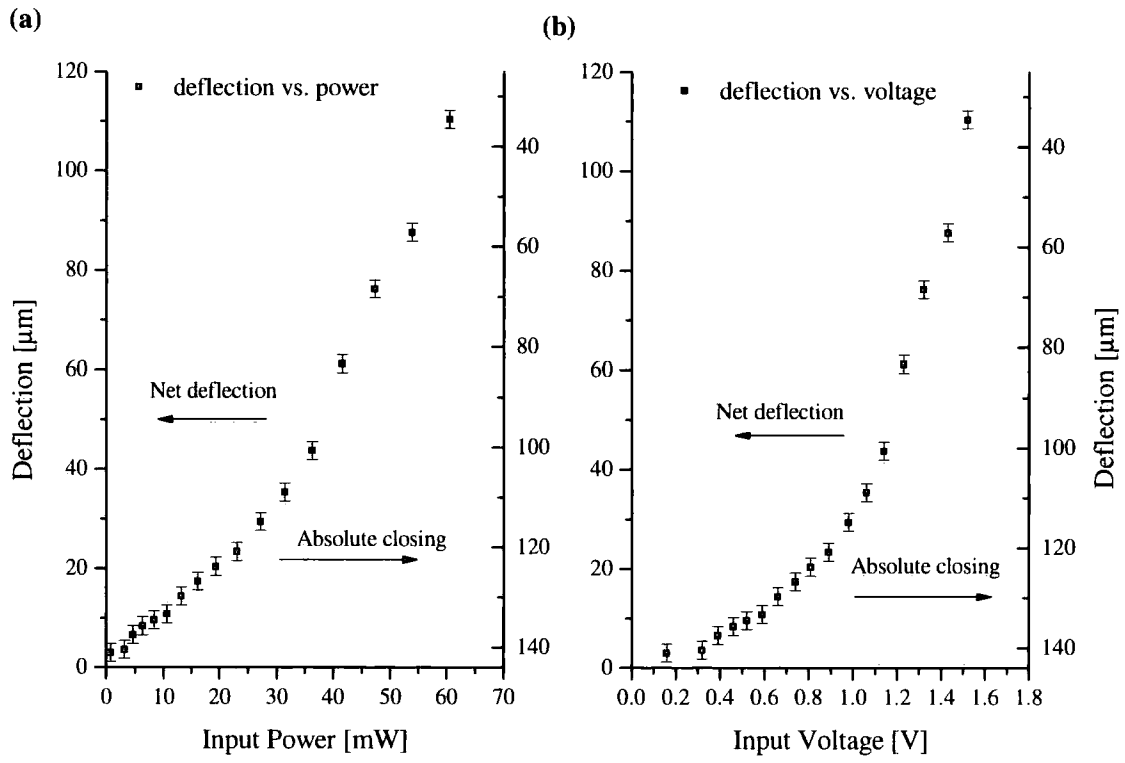

Fig. 5.29: Design 2_(30) (initial gap = 144 μm) (a) Deflection versus input power (b) Deflection versus input voltage.

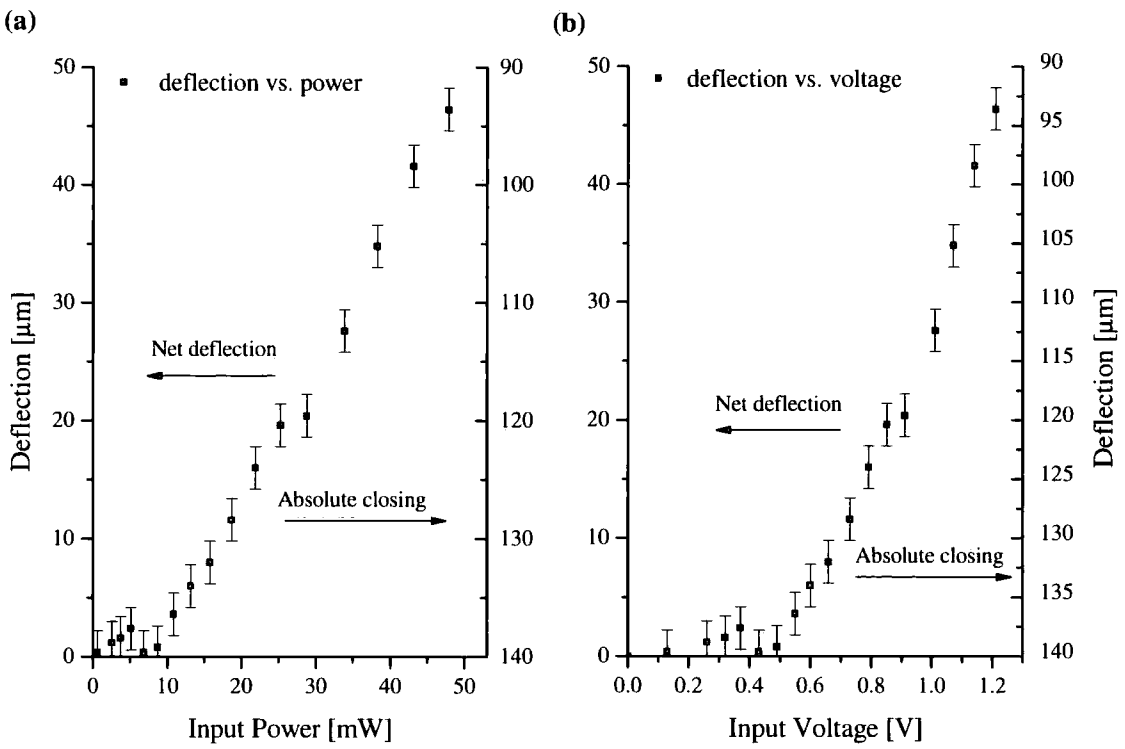

Fig. 5.30: Design 2_(100) (initial gap = 140 μm) (a) Deflection versus input power (b) Deflection versus input voltage.

5.4.2. Deflection measurements in liquid environment

The microgrippers are intended to work mainly in biological media; therefore it is important that the viability of the prototypes is also verified in liquids.

Design 3_(100) was used to measure the deflection in both air and DI water. The measurements in water were performed in two ways: with the device partially submerged in water 9, and with the device entirely submerged in water. Both results are shown in Fig. 5.31. During the measurements in air and with the microgripper partially submerged, a current from 10 to 40 mA in steps of 2 mA was applied. During the measurements in DI water with the microgripper completely submerged, voltages from 0 V to 6.5 V were applied until thermal failure occurred.

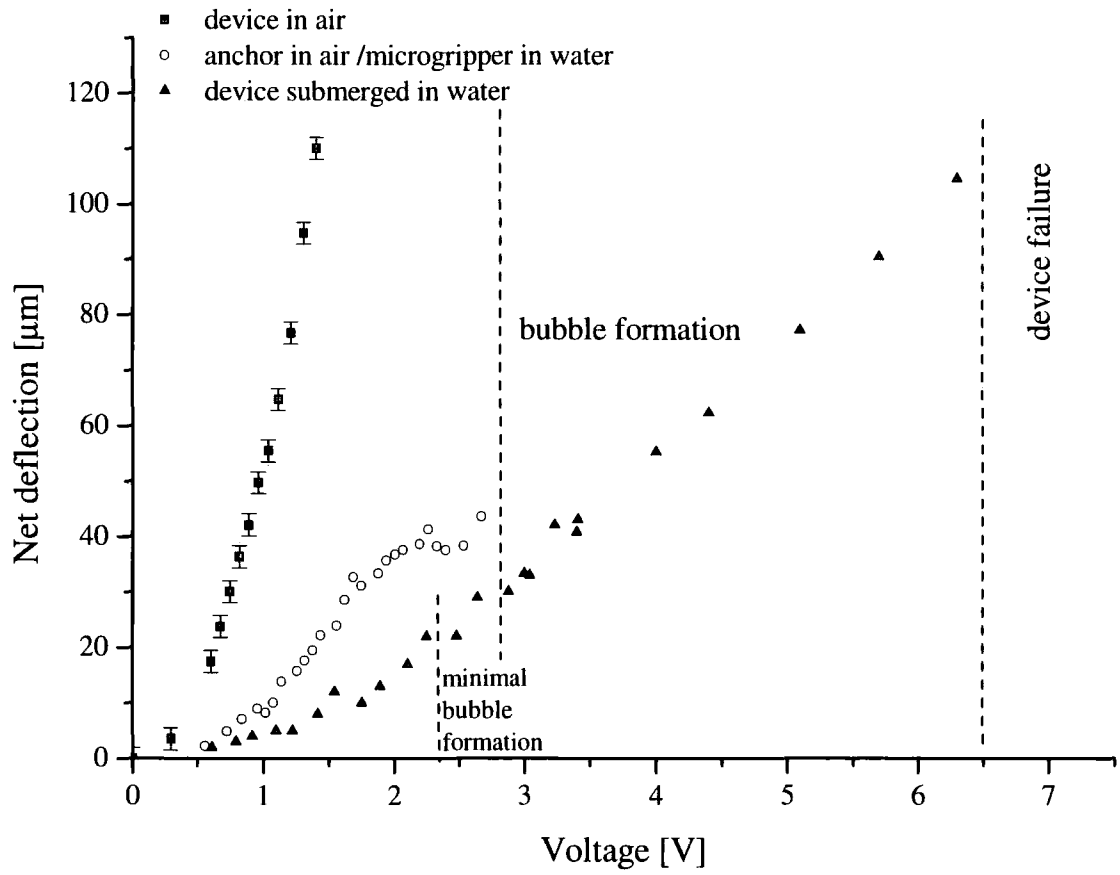

Fig. 5.31: Comparison between the microgripper actuated in air (black square); partially submerged i.e. anchor in air and actuator under water (circle), and completely submerged (triangle).

As expected, due to the difference in heat loss coefficients, the deflections measured in air are larger than the deflections measured in any of the two cases in water for the same

input power. It can also be observed, that the deflection of the device partially submerged in water is larger than the deflection when the device is entirely submerged in water.

Based on these results, the operation of the microgripper partially submerged in water seems to be more favourable. First, because larger deflections are possible for the same input power and second, because leaving the anchor (and electrical contact pads) out of the water eliminates the requirement for low input voltages. From a practical point of view it might be difficult to maintain this working configuration; however for skilled human operators it could always be a way to maximise the capabilities of a particular microgripper design.

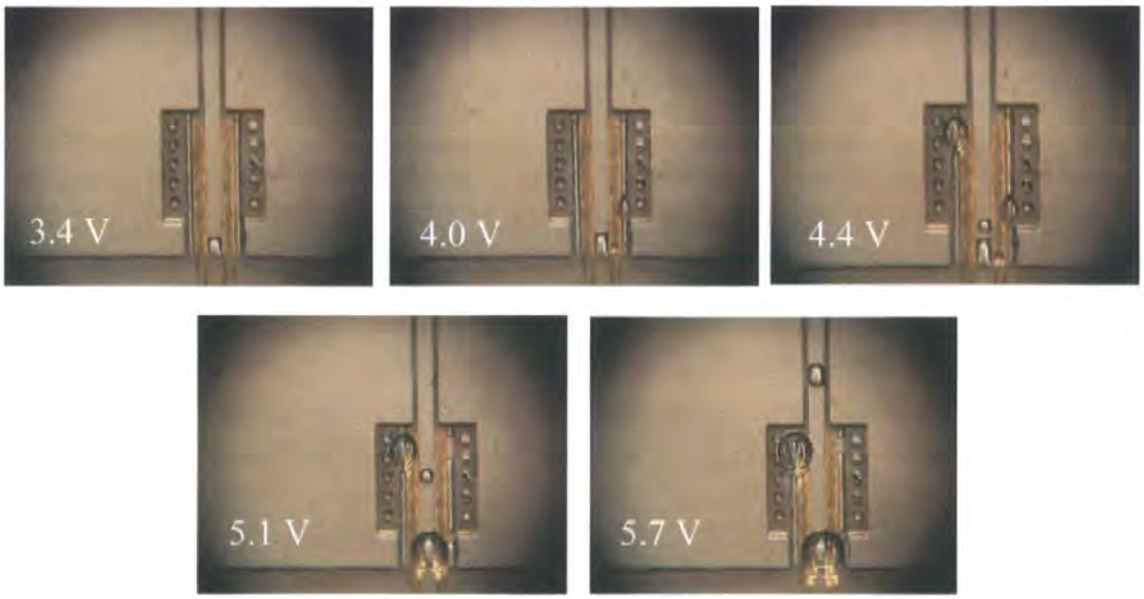

Fig. 5.32: Bubble formation with increasing applied voltage (3.4–5.7 V)

Fig. 5.32 shows some optical images of the microgripper completely submerged in water during actuation. Electrolysis starts occurring at approximately 2.5 V. Initially the bubble formation is minimal and far away from the microgrippers jaws. As the voltage is increased more air bubbles start appearing in different areas of the microgripper and move towards the jaws. At 6.5 V the bubble formation finally induces thermal failure of the device. This is shown in Fig. 5.33.

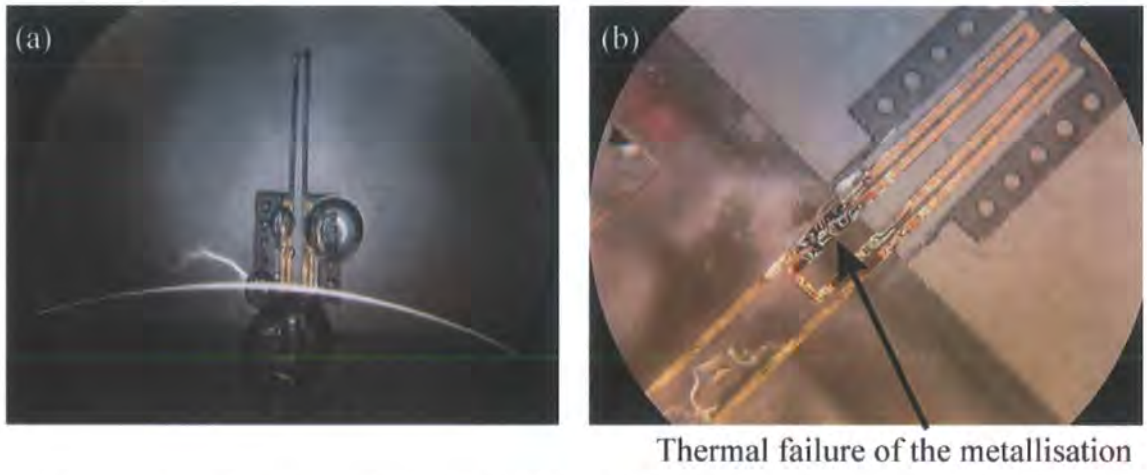

Fig. 5.33: Thermal failure experienced by the device design 3_(100) when actuated under DI water at 6.5 V.

The most likely reason why the thermal failure has occurred in this case is due to the large air bubble created at the beginning of the actuators. The air bubble creates a point where heat losses are drastically reduced (air environment compared to water) and where high localised temperatures can develop.

During the validation of the models in Chapter 6 (section 6.3.1) an estimate of the temperature of the actuators under water will be given.

5.4.3. Repeatability and life time experiments

Design 3_(100) has also been used to assess the repeatability of the operation of the microgrippers. During the experiment current levels from 10 to 40 mA in 2 mA steps were applied. The voltage drop was measured simultaneously.

The results are shown in Fig. 5.34. The experiments show a good repeatability in terms of deflection for a given voltage. The maximum absolute dispersion of the data occurs at the highest voltage and is 7 μm. This represents a dispersion of 3.5 μm per actuator and jaw combination and is equivalent to the error associated to the measurement method. There is also a slight dispersion in the values of the voltage for the same input current. This could be due to a reorganisation of the metallisation layer as the temperature increases.

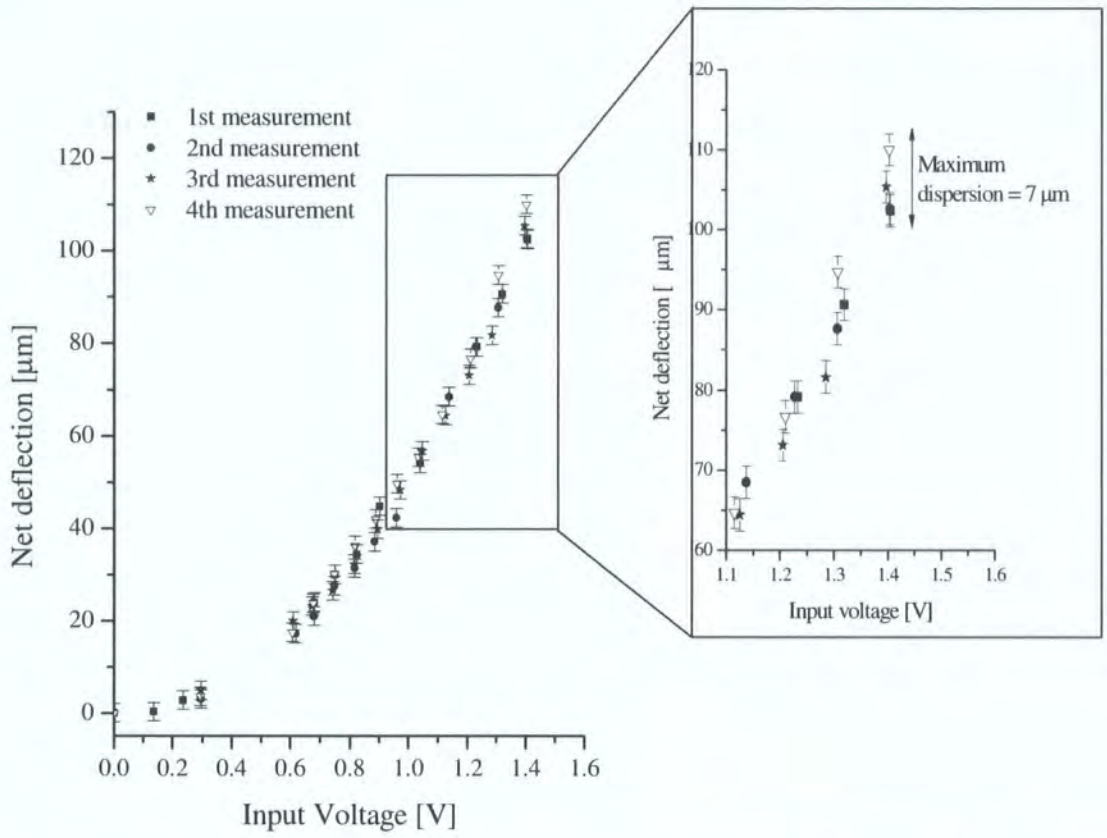

Fig. 5.34: Deflection measured in air during 4 consecutive experiments from design 3_(100).

The short-term operation of the microgripper seems to be very reliable. The microgripper was actuated in air with a square current step of amplitude of 32 mA and duration of 3 s. After 1 hour (1200 cycles) no degradation in performance was observed.

The only failure mechanism detected during the experiments has been due to thermal failure of the metallisation layer (see example Fig. 5.35). This temperature has been calculated to be approximately 220 °C. This temperature is also very close to the melting temperature of the SU8. Therefore it could be possible that the failure occurs due to two simultaneous factors: the overheating of the metallisation and the melting and burning of the SU8.

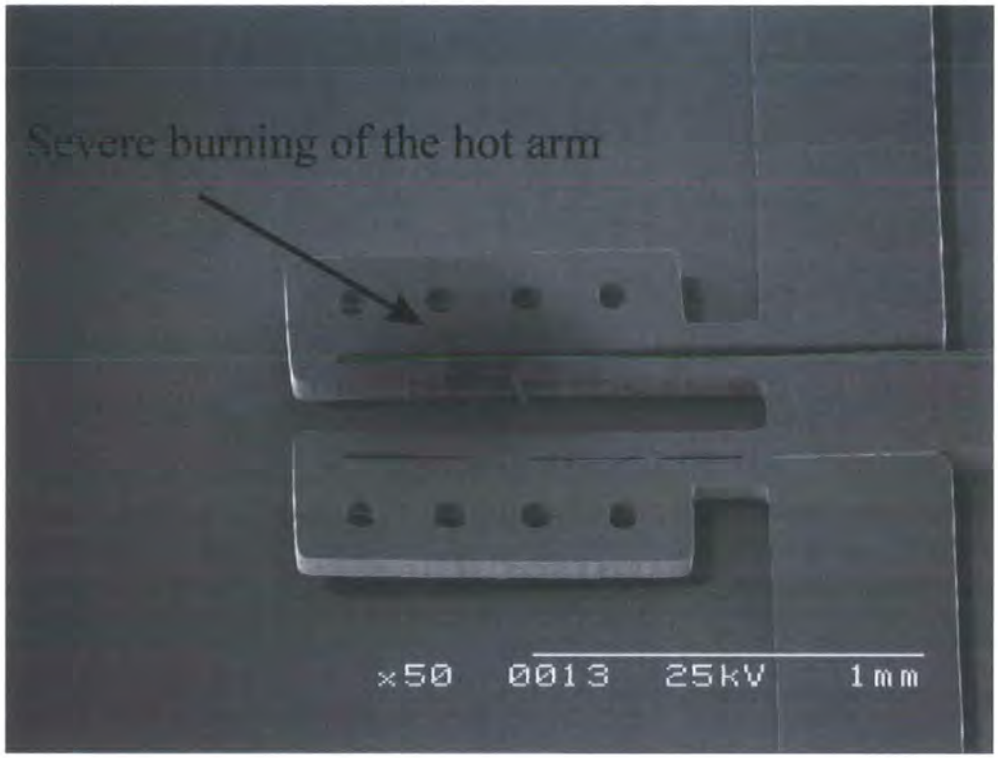

Fig. 5.35: SEM picture of a microgripper after thermal failure occurs.

5.4.4. Manipulation experiments

Manipulation experiments in air and in water environments have been conducted under an optical microscope.

In the air experiments, the microgripper was attached to an x-y-z micromanipulator and a substrate with gold coated SU8 rods was placed on an x-y stage. This provided the operator will full three dimensional micropositioning control of the gripper. Fig. 5.36 shows a sequence of still images from the air-based microrods manipulation experiment. The gripper successfully picked up each rod in turn, moved it and then placed it in a new position.

In the water experiments, underwater illumination permitted the detection and manipulation of biological specimens (clusters of cheek cells).A video with both examples of manipulation can be seen in

http://www.dur.ac.uk/engineering/microsystems.technology/projects/microgripper/.

Fig. 5.36: Manipulation sequence. From left to right and top to bottom 5 gold coated microrods (∅ = 100 μm) are picked and placed

5.5. Electrothermomechanical characterisation: key performance parameters

The DC current, *I*, or voltage, *V*, are directly controlled by the user and determine the Joule heating in the devices. All of the electrical power, *P*, is dissipated in the form of heat and is required to maintain the deflection, *d*, in the whole structure. This in turn is dependent on the asymmetrical temperature profiles developed along the arm of the actuators, i.e. T_h, T_c, T_f and ultimately ΔT. The maximum temperature that the device can attain, T_{max}, is limited by the melting temperature of the devices, environmental conditions or application requirements.

5.5.1. Deflection Performance

The deflection is the ultimate performance indicator of the microgrippers. For a given geometry, the in-plane flexibility and absolute tip deflection will increase with overall length. Therefore, in order to be able to compare the performance of the different microgrippers with different lengths a normalised deflection, d_N, has been used which is the ratio of in-plane deflection compared to the initial device length.

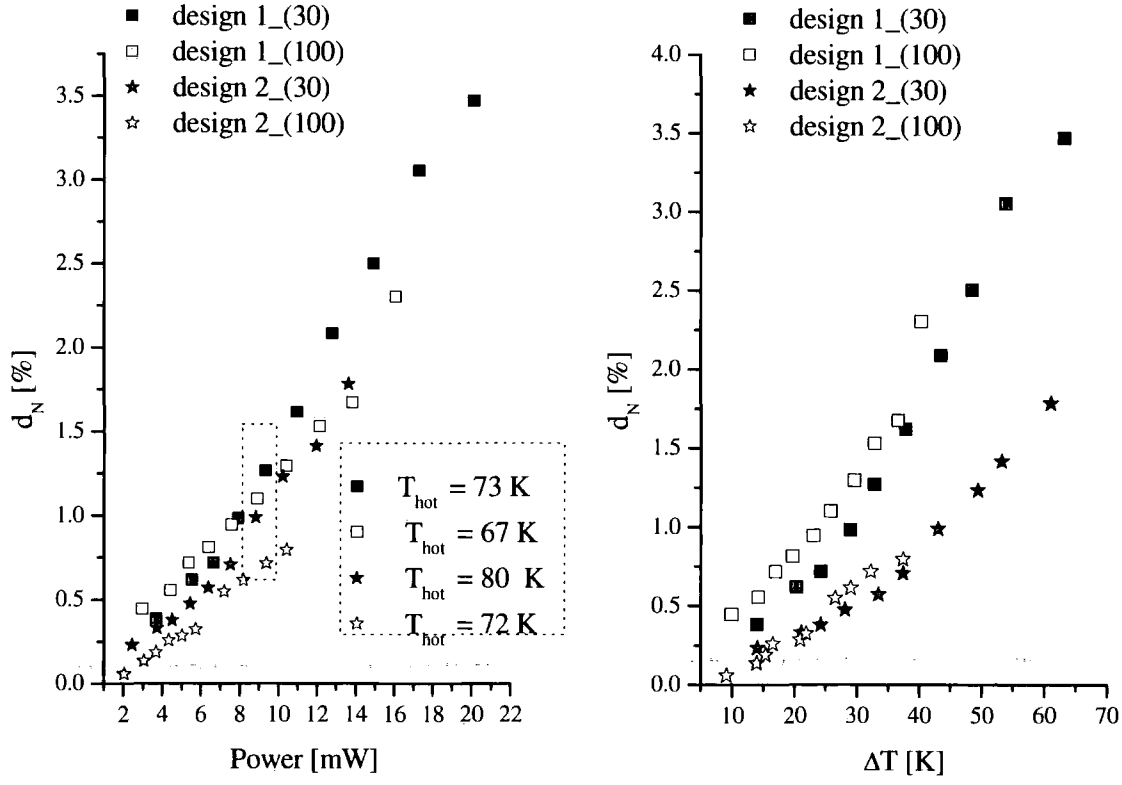

Fig. 5.37: Power consumption (left) and ΔT (right) versus d_N.

From Fig. 5.37 (left), it can be seen that the best performing design in terms of deflection achieved is design 1 in its two thicknesses. Design 2_(30) seems to give similar results in terms of power versus deflection but at the expense of higher temperatures in the hot arm (Fig. 5.38). For example to obtain a 1% normalised deflection, design 2_(30) requires 80 K of temperature increase in the hot arm versus approximately 60 K in design 1.

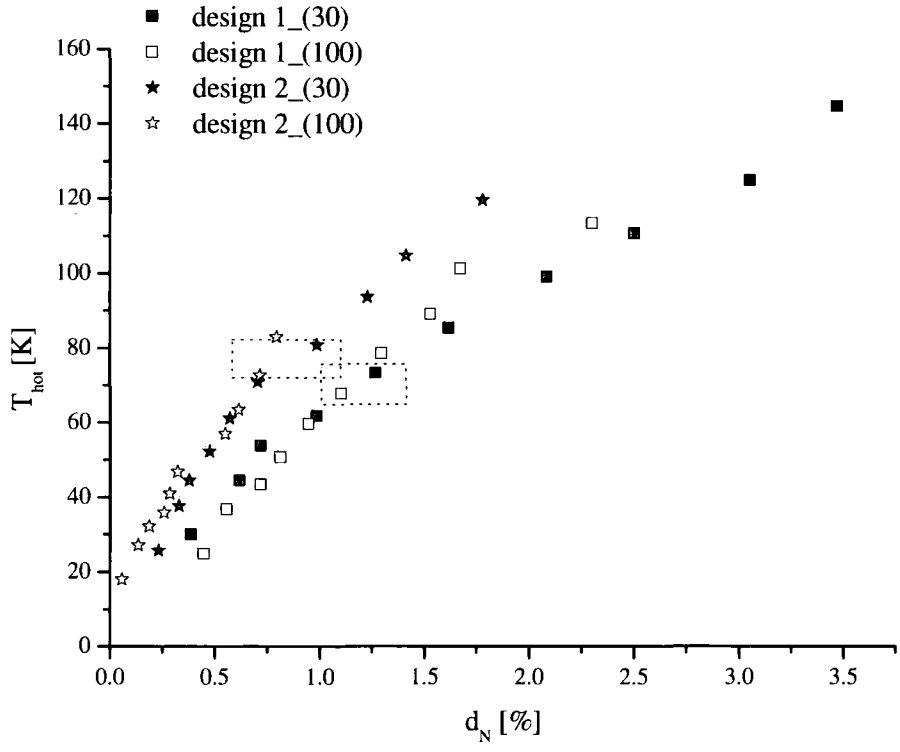

Fig. 5.38: Temperature in the hot arm relative to ambient required to obtain a deflection d_N.

5.5.2. Thermal efficiency

ΔT denotes the asymmetric heating attained in the structure and is ultimately responsible for the deflection. In addition, ΔT is the parameter that decouples the electrothermal from the mechanical problem. Hence ΔT is an important parameter. The thermal efficiency of the system is defined as $\Delta T/T_h$. A value of unity indicates that all the heat generated in the hot arm is invested in a net differential expansion (the cold arm remains at ambient T), but a small value indicates that the heat generated in the hot arm increases the temperature of the whole device, reducing the overall deflection. In order to obtain a microgripper that is able to operate at low absolute temperatures it is necessary that $\Delta T/T_h$ is as high as possible.

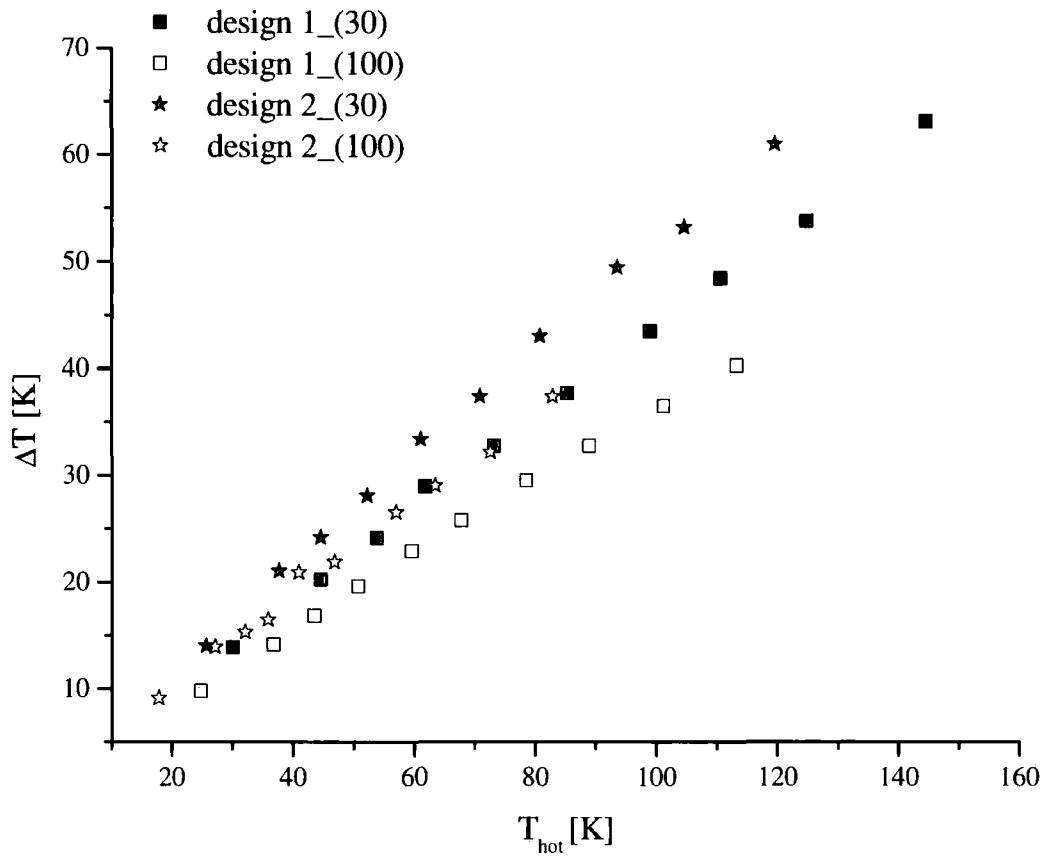

Fig. 5.39: Difference in temperature between hot and cold arm ΔT, versus average hot arm temperature T_{hot}.

Fig. 5.39 shows a fairly linear relationship ΔT versus T_{hot}. The values of the ratio are $\Delta T/T_h = 0.44$ for design 1_(30), $\Delta T/T_h = 0.36$ for design 1_(100), $\Delta T/T_h = 0.52$ for design 2_(30), and $\Delta T/T_h = 0.46$ for design 2_(100).

From these results it can be seen that thinner devices (design 1_(30) and design 2_(30))are more thermally efficient than their corresponding thicker devices (design 1_(100) and design 2_(100)). These results confirm the theory that a higher heat exchange coefficient is expected between thicker beams. This can also be seen in the higher requirements of design 2 in terms of power per unit length (Fig. 5.40 (left)). In addition, for the same T_{hot}, design 2 gives higher values of ΔT than design 1 at lower total power (Fig. 5.40 (right)).

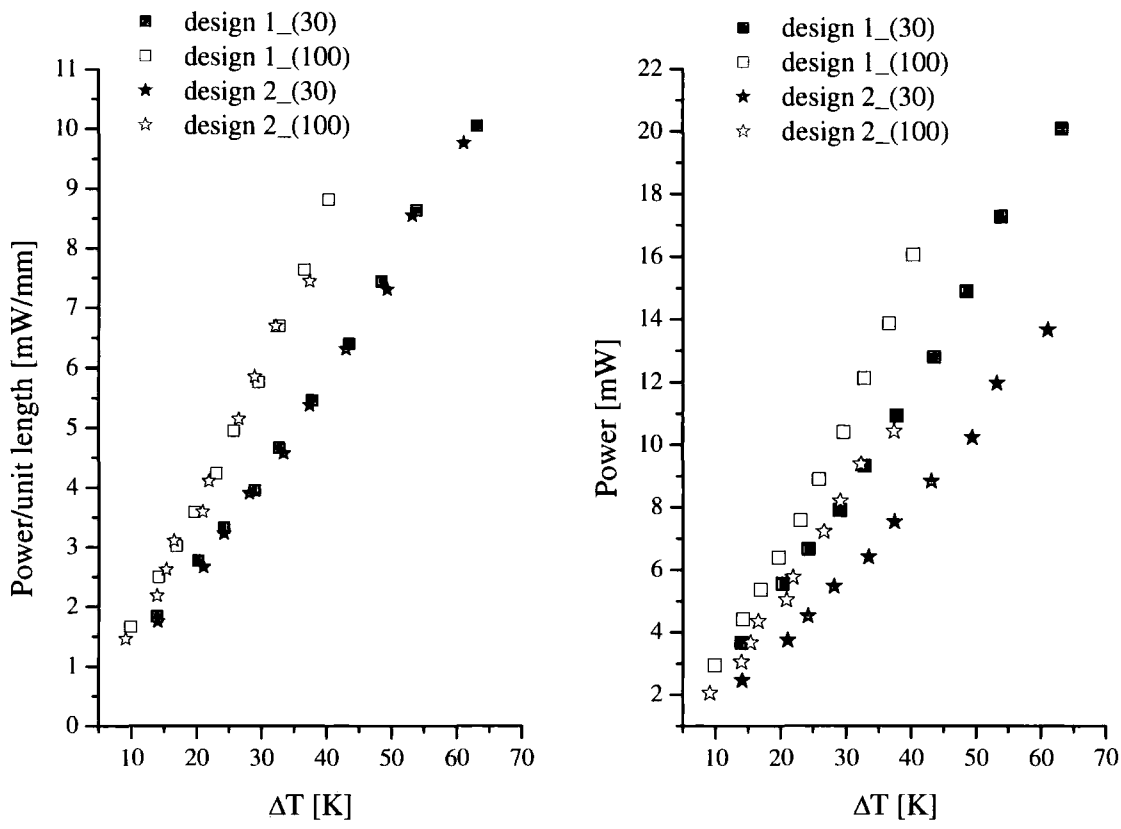

Fig. 5.40: Difference in temperature ΔT versus power per unit length (left) and total power consumption (right).

5.5.3. Homogeneity of the temperature of the hot arm

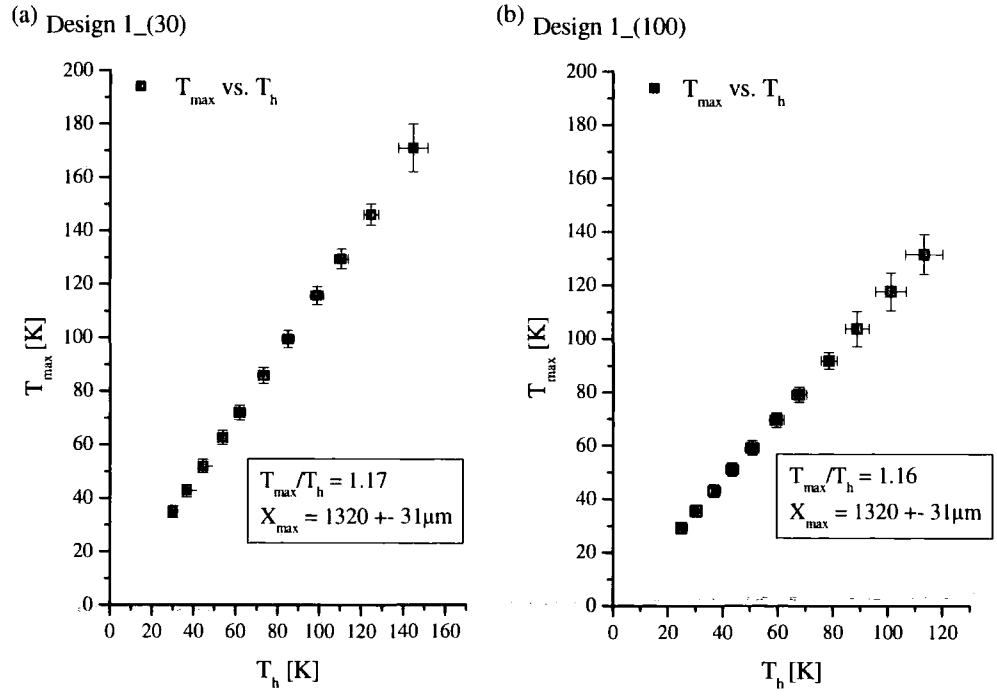

Fig. 5.41: Maximum temperature vs. hot arm temperature (relative to ambient): (a) design 1_(30) (b) design 1_(100).

The homogeneity of the temperature in the hot arm is also a parameter of interest. This is given by the ratio between the maximum temperature and the temperature developed in the hot arm. The more homogenous the temperature is, the higher the overall temperatures and achievable deflections are possible prior to thermal failure of the device. As can be seen from Fig. 5.41 and Fig. 5.42, the four designs show a good homogeneity.

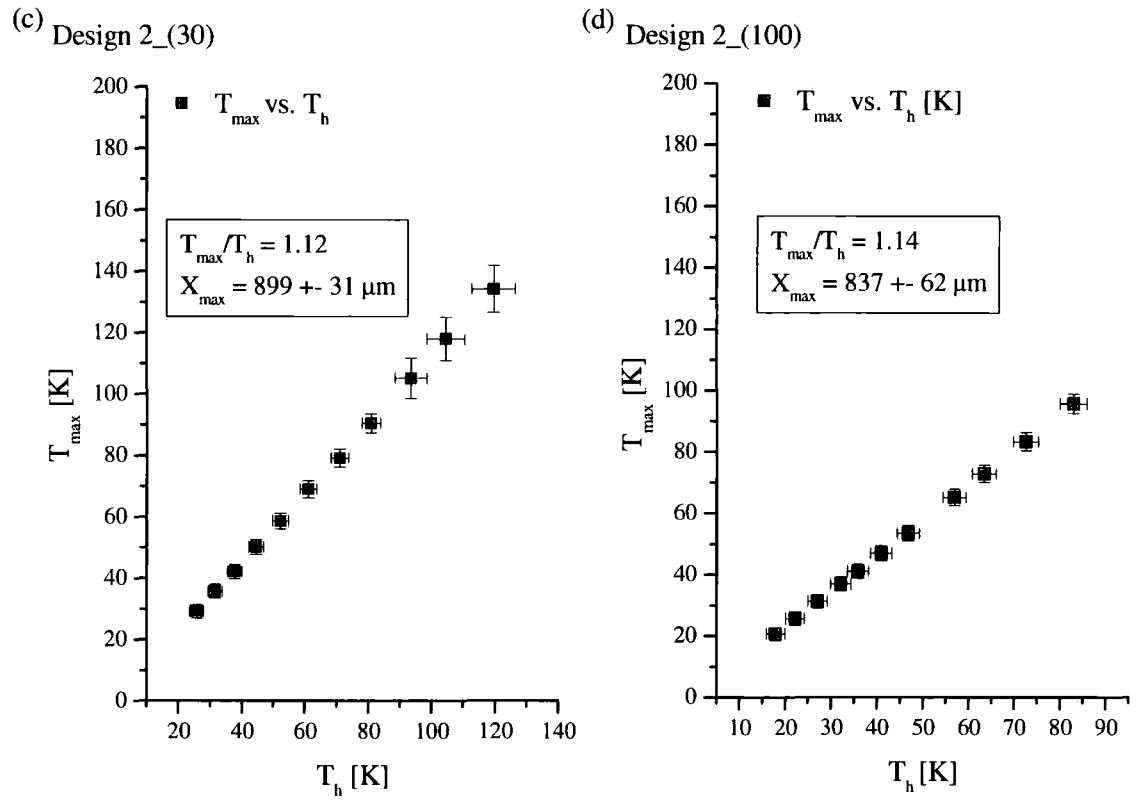

Fig. 5.42: Maximum temperature vs. hot arm temperature (relative to ambient): (a) design 1_(30) (b) design 1_(100) (c) design 2_(30) (d) design 2_(100).

5.6. Summary

In this chapter the devices fabricated in chapter 3 — design 1_(30), design 1_(100), design 1_(30), design 2_(100), and design 3_(100) — have been tested. Four kinds of experiments have been conducted:

- electrical
- IR thermography
- deflection in air and liquid environments
- manipulation in air and in liquid environments

IR thermography has provided accurate two dimensional mappings of the surface temperature of the microgrippers and, in the context of the present work; it has proven to be a very fast and versatile tool for thermal characterisation experiments.

The manipulation experiments have shown that the microgripper, in any of the proposed designs, is a functional device fit for the purpose of holding, grasping and positioning microsized object in air and liquid environments.

All of the microgrippers tested in this chapter have been shown to function within the design requirements in terms of voltage (< 1.5 V), temperatures, and deflections range (Fig. 5.27-Fig. 5.30, and Fig. 5.38).

The different designs have been compared and the best performance has been highlighted. However, the performance comparisons are only valid for these specific geometries and configurations, and general design rules are difficult to extract. The next chapter will use a simulated based approach, involving the models and the experimental results, to identify key design rules.

CHAPTER 6

Validation of the models and simulation based predictions

In this chapter, the analytical models — electrothermal and thermomechanical — developed in Chapter 4 are validated against the experimental data provided in Chapter 5.

The first part of the chapter deals with the validation of the heat transfer geometrical factors, f_i, f_{ex}, proposed in Chapter 4 through a simulation-based technique, i.e. by combining electrothermal analytical simulations with experimental data. Different simulation scenarios, based on various thermal boundary conditions and system configurations, will be compared with the experimental data until good agreement is achieved. In order to accurately validate the proposed electrothermal model, the material properties that affect the results have to be as accurate as possible. Thus experimental and semi-empirical values for the resistivity of the metallisation layer and the thermal conductivity of the air will be obtained and fed into the models.

In the second part of the chapter, the thermomechanical model will be validated against experimental data. The difference in temperature between hot and cold arm, ΔT, obtained from the electrothermal model will be used as an input parameter. Comparison of the thermomechanical model and the measured deflections will indicate that there is a

variation of the coefficient of thermal expansion (CTE) of the polymeric material as the temperature increases and approaches the glass transition temperature of the polymer, T_g. The model provides very good results, within the experimental error, at temperatures below T_g. If the variation of the CTE with temperature is also included, good agreement between the simulations and the experiments is obtained for all of the temperature range tested.

Once the analytical tool takes into account the validated heat transfer geometrical factors, and the dependency of the CTE with temperature, the virtual prototyping tool is created and the optimisation process can start. The analytical tool creates a deterministic link between the microgripper design parameters — geometry, materials and input power — and the microgripper performance in terms of temperature (average, maximum, distribution) and deflection. In the last part of the chapter, how different parameters affect the overall performance will be studied.

6.1. Experimental validation of the electrothermal analytical model

6.1.1. Modelling scenarios

In Chapter 4, a conduction model was proposed to describe the thermal behaviour of half of the microgripper, i.e. an actuator plus an extended jaw. Two kinds of heat transfer phenomena were considered simultaneously:

- a heat loss mechanism, based on conduction, where the hot and cold arms of the actuator lose heat jointly to the ambient by their external, exposed, surfaces. This heat loss is governed by a heat loss coefficient defined as $C_i = f_i \kappa_\infty$, where f_i (i = h, c, f) is a geometrical factor that depends on the geometry of the hot, cold and flexure arms of the actuators, and κ_∞ (the thermal conductivity of the media surrounding the device) (section 4.3.4.4).

- a heat exchange mechanism, based also on conduction, where heated parts of the device (hot arm) exchange heat with cooler parts of the device (cold/flexure arm) that are separated by a small fluid gap. This heat loss is characterised by a heat exchange coefficient defined $C_{ij} = f_{ij} \kappa_\infty$ where f_{ij} (= f_{ex}) is a geometrical

factor that depends on the geometry of the beams, the separation between the arms (*gap*), and the thermal conductivity of the media that fills the gap, κ_∞ (see section 4.3.4.5). The notation ij indicates that the arm i conducts heat to the arm j which is facing, e.g. f_{hc} is the geometrical factors that govern the heat exchange when the hot arm is facing the cold arm. Equivalently f_{hf} is the geometrical factors that govern the heat exchange when the hot arm is facing the flexure arm.

Table 6.1 shows the values of the individual conduction geometrical factors f_i calculated for the different arms of the geometries tested — design 1_(30), design 1_(100), design 2_(30), design 2_(100) —. In the case of design 2 there is the need to specify two sets of geometrical factors: one for the envelope formed by the hot and flexure arm (Fig. 4.17 section 1) and another for the envelope formed by the hot arm and cold arm (Fig. 4.17 section 2) which is considerably larger.

Table 6.1: Individual geometrical factors calculated for the different microgrippers' models

	f_h	f_c	f_h	f_f
design 1_(30)	1.24	1.24	-	-
design 1_(100)	1.25	1.25	-	-
design 2_(30)	1.04	1.77	1.58	0.56
design 2_(100)	1.08	1.70	1.51	0.72

Table 6.2 and Table 6.3 show the geometrical factors that govern the heat exchange between the hot and cold arms. The geometry and spacing of the beams can affect the heat exchange between them. Three ways of calculating the geometrical factors were proposed in Chapter 4: one for geometries where the spacing between the beams, *gap*, is larger than the thickness of the beams (Table 6.2) which would be the case of design 1_(30) and design 2_(30), and one for geometries where the thicknesses of the beams are larger that the *gap* (Table 6.3(a) and Table 6.3 (b)). This would be the case for design 1_(100) and design 2_(100).

Table 6.2: Geometrical heat exchange factors calculated for the microgripper models where gap > thickness of the device.

	f_{hc}	f_{hf}
design 1_(30)	1.49	-
design 2_(30)	1.49	1.49

gap > thickness t

Table 6.3: Geometrical factors calculated for the microgripper models where gap < thickness of the device. (a) Values calculated using the nominal thickness of the device (t); (b) Values calculated using an effective larger thickness (t') for the device.

	(a)		(b)			
	f_{hc}	f_{hf}	t_{hc}'	f_{hc}	t_{hf}'	f_{hf}
design 1_(100)	1.66	-	140.82	2.35	-	-
design 2_(100)	1.66	1.66	144.72	2.41	131.08	2.18
	gap < thickness (t)		**gap < thickness (t')**			

The difference between Table 6.3 (a) and Table 6.3 (b) is that in the first table the thickness included in the calculations is the real value of the thickness of the beam (nominally 100 μm) whilst in the second table an effective larger thickness is used. The reason for that is explained in more detail in section 4.3.4.5.

Implicit in the use of the geometrical factors shown in Table 6.1 to Table 6.3 is the assumption that each actuator, composed of two beams (hot and cold/flexure arm), does not have any other body in close proximity. However, the microgripper considered as a whole device is composed of two such actuators (A and B in Fig. 6.1) placed together and separated by a distance, G, sometimes comparable to the size of the *gap* between the arms of the actuators. In my case, G (~ 140 μm) is approximately double the size of the gap (~ 60 μm). The analytical model will also be able to describe this slightly complex configuration.

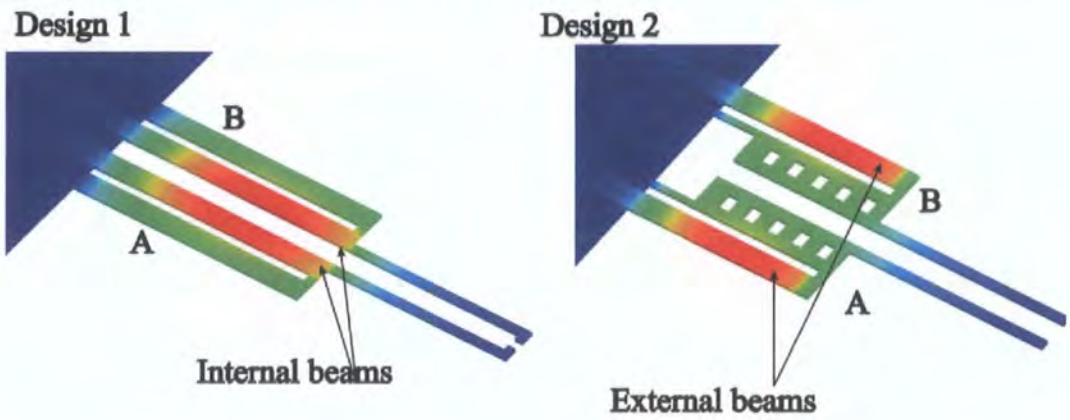

Fig. 6.1: Microgripper configuration for design 1 and design 2. Reference for the location and definition of internal and external arms of the microgripper structure.

Fig. 6.1 shows the two microgripper types that have been tested in Chapter 5. Design 1 has the hottest arms placed in the internal part of the microgripper whilst design 2 has

the hottest arms in the external part of the structure. Looking at these two configurations, it could be envisaged that arms that are placed in the exterior of the structures will be subject to higher heat losses than the ones placed in the interior. The reason for this is that the beams placed in the interior will benefit from the relative thermal insulation provided by the structure of the microgripper itself which would prevent air flowing within the internal gaps of the device or, in other words, that would prevent natural convection in the internal parts of the device. Therefore, in order to understand the nature of the heat transfer processes taking place in a real situation, three modelling scenarios (Fig. 6.2) are proposed and compared with the experimental results.

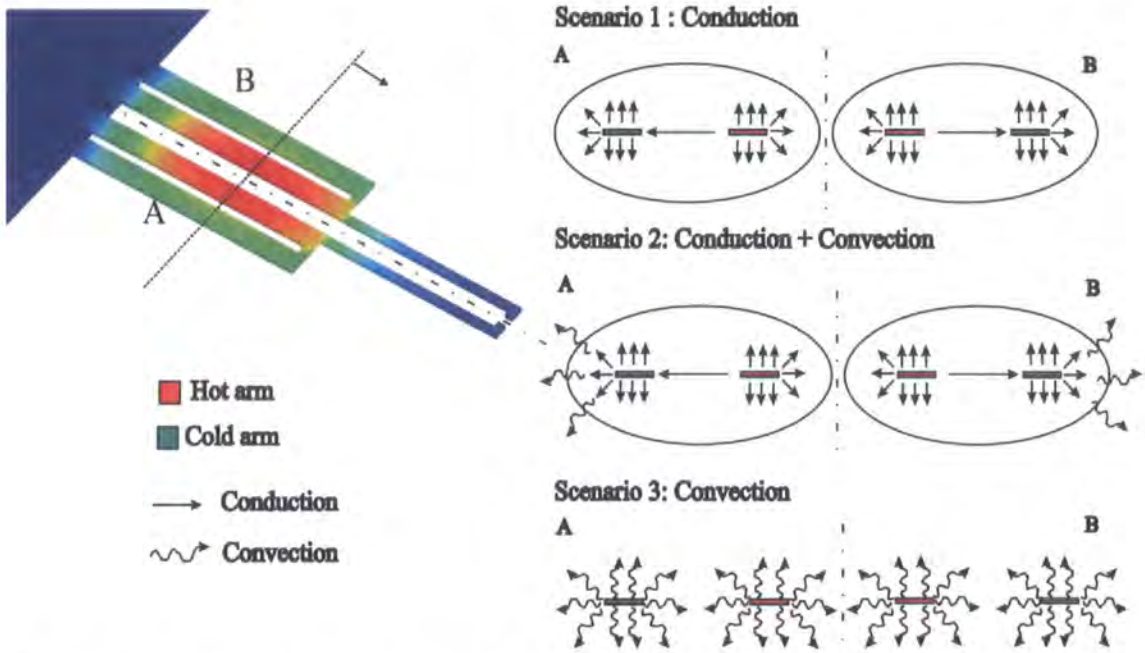

Fig. 6.2: Different heat loss scenarios: conduction only (Scenario 1), conduction and convection (Scenario 2), and convection only (scenario 3).

Scenario 1 (top, Fig. 6.2) will consider that each actuator of the microgripper loses heat to the surrounding ambient by conduction only. This means that internal as well as external beams will exchange heat with the environment by a conduction mechanism only governed by the heat transfer coefficients and geometrical factors given in Table 6.1 to Table 6.3. In the case of design 1_(100) and design 2_(100), two options are possible for f_{ij} depending on the choice of thickness nominal (t) versus effective (t'):

- scenario 1.1, when using Table 6.7 (a) for f_{ij},
- scenario 1.2, when using Table 6.7 (b) for f_{ij}.

Scenario 2 (middle, Fig. 6.2) will consider that each actuator of the microgripper loses heat to the surrounding ambient by conduction and convection. The internal beams of the microgripper will lose heat by conduction only, whilst the external beams will lose heat by conduction and convection. In the latter case a natural convection heat transfer coefficient with a standard value of 40 W/m^2 K in air will be added to the conduction heat losses.

Scenario 3 (bottom, Fig. 6.2) will consider that each beam of the microgripper loses heat to the surrounding ambient by convection only. In this case the beams do not thermally 'see' each other and no heat exchange between beams occurs, i.e. $f_{ij} = 0$.

6.1.2. Dependency of the heat transfer coefficients with temperature

When dealing with conduction heat transfer (Scenario 1) the dependency with temperature of the heat transfer coefficients is taken directly into account through the use of a thermal conductivity of air dependent on temperature.

The conductive heat transfer coefficient is then defined as

$$C_i(T) = f_i \, \kappa_{air}(T) \tag{6.1}$$

where i = h, c, and f. The dependency of $\kappa_{air}(T)$ is explained in section 6.1.5.

When dealing with conduction/convection heat transfer (scenario 2), the heat transfer coefficients will be given by Table 6.1 to Table 6.3 for the internal beams, and by C'(T) in the external beams.

$$C_i'(T) = C_i\big|_{scenario1} + h\, p_i \tag{6.2}$$

where h is a macroscopic heat transfer coefficient applied to the exposed faces of the external beams with an estimated value of 40 W m^{-2} K^{-1}, and p_i is the perimeter of the exposed surface of the external beams. The dependency with temperature is included in $C_i\big|_{scenario\ 1}$.

Finally, when dealing with (microscale) convection heat transfer only (scenario 3), the dependency of the heat transfer coefficients will be given by the dependency of the Grashof number with temperature, $G_r(T)$ (section 4.3.4.2). The heat transfer coefficient used in the convective model is then given by the product of the convection coefficient, $h_i(G_r(T))$, and the perimeter of the exposed area, p_i by

$$C_i(T) = h_i(T) * p_i \tag{6.3}$$

where i = h, c, and f. The convection coefficients calculated for each model at each current level are given in Table 6.4 to Table 6.7.

Table 6.4: Convection coefficients calculated for design 1_(30). T_c and T_h are experimental values measured by IR thermography.

Current [mA]	T_h [K]	T_c [K]	h_{hot} [W/m^2 K]	h_{cold} [W/m^2 K]	C_{hot} [W/m K]	C_{cold} [W/m K]
20	30	16	126	122	0.043	0.041
22	37	19	127	123	0.043	0.042
24	45	24	129	124	0.044	0.042
26	54	30	130	126	0.044	0.043
28	62	33	132	127	0.045	0.043
30	73	40	133	128	0.045	0.044
32	85	48	134	129	0.046	0.044
34	99	56	136	131	0.046	0.044
36	111	62	137	132	0.047	0.045
38	125	71	138	133	0.047	0.045
40	145	81	139	134	0.047	0.046

Table 6.5: Convection coefficients calculated for design 1_(100). T_c and T_h are experimental values measured by IR thermography.

Current [mA]	T_h [K]	T_c [K]	h_{hot} [W/m^2 K]	h_{cold} [W/m^2 K]	C_{hot} [W/m K]	C_{cold} [W/m K]
20	25	15	94	91	0.045	0.044
22	30	18	95	92	0.046	0.044
24	37	23	96	93	0.046	0.045
26	43	27	98	94	0.047	0.045
28	51	31	99	95	0.047	0.046
30	60	37	100	96	0.048	0.046
32	68	42	101	97	0.048	0.047
34	79	49	102	98	0.049	0.047
36	89	56	103	99	0.049	0.048
38	101	65	104	100	0.050	0.048
40	113	73	105	101	0.050	0.049

Table 6.6: Convection coefficients calculated for design 2_(30). T_c and T_h are experimental values measured by IR thermography.

Current [mA]	T_h [K]	T_c [K]	h_{hot} [W/m^2 K]	h_{cold} [W/m^2 K]	$h_{flexure}$ [W/m^2 K]	C_{hot} [W/m K]	C_{cold} [W/m K]	$C_{flexure}$ [W/m K]
20	26	12	125	79	259	0.042	0.044	0.036
22	31	14	126	80	261	0.043	0.045	0.037
24	38	17	128	81	262	0.043	0.045	0.037
26	44	20	129	82	264	0.044	0.046	0.037
28	52	24	130	83	266	0.044	0.046	0.037
30	61	28	131	84	267	0.045	0.047	0.037
32	71	33	133	85	270	0.045	0.048	0.038
34	81	38	134	86	271	0.046	0.048	0.038
36	94	44	135	87	273	0.046	0.049	0.038
38	105	51	136	88	274	0.046	0.049	0.038
40	119	59	138	89	276	0.047	0.050	0.039

Table 6.7: Convection coefficients calculated for design 2_(100). T_c and T_h are experimental values measured by IR thermography.

Current [mA]	T_h [K]	T_c [K]	h_{hot} [W/m^2 K]	h_{cold} [W/m^2 K]	$h_{flexure}$ [W/m^2 K]	C_{hot} [W/m K]	C_{cold} [W/m K]	$C_{flexure}$ [W/m K]
20	18	9	92	65	139	0.044	0.045	0.039
22	22	11	93	66	141	0.045	0.046	0.039
24	27	13	95	67	142	0.045	0.047	0.040
26	32	17	96	68	144	0.046	0.047	0.040
28	36	19	96	69	145	0.046	0.048	0.040
30	41	20	97	69	145	0.047	0.048	0.041
32	47	25	98	70	146	0.047	0.049	0.041
34	57	30	100	71	148	0.048	0.050	0.041
36	63	34	100	72	149	0.048	0.050	0.042
38	73	40	101	73	150	0.049	0.051	0.042
40	83	46	102	73	151	0.049	0.051	0.042

6.1.3. Dependency of the material properties with temperature

A set of tables that relate the input currents used in the different experiments and the corresponding IR temperatures with the values of the resistivity and the thermal conductivity of the ambient have been constructed.

The experimental determination of the material properties is only required for the initial validation of the models. Once the validity of those coefficients has been checked, the modelling technique proposed in section 4.4.6, could be used for the remaining simulations of the chapter.

6.1.4. Resistivity of the metallisation $\rho = \rho(T)$

The values of the resistivity for each current level have been calculated based on the material properties obtained in 5.3.3.4 (Table 5.4) and the values of the temperatures measured with IR thermography. Table 6.8 and Table 6.9 shows the values obtained for design 1_(30), design 1_(100), design 2_(30) and design 2_(100).

Table 6.8: Dependency with temperature of the resistivity of the gold metallisation at different input currents for design 1_(30) and design 1_(100).

Design 1_(30)

Current [mA]	T_h [K]	Resistivity [Ω m]
	0	1.99E-08
19.82	30	2.214E-08
23.79	45	2.322E-08
25.79	54	2.391E-08
27.77	62	2.451E-08
29.75	73	2.537E-08
31.74	85	2.627E-08
33.7	99	2.729E-08
35.7	111	2.816E-08
37.7	125	2.922E-08
39.7	145	3.07E-08

Design 1_(100)

Current [mA]	T_h [K]	Resistivity [Ω m]
	0	2.047E-08
19.82	25	2.242E-08
23.79	37	2.336E-08
25.79	43	2.388E-08
27.77	51	2.445E-08
29.75	60	2.515E-08
31.74	68	2.579E-08
33.7	79	2.664E-08
35.7	89	2.746E-08
37.7	102	2.849E-08
39.7	113	2.937E-08

Table 6.9: Dependency with temperature of the resistivity of the gold metallisation at different input currents for design 2_(30) and design 2_(100).

Design 2_(30)

Current [mA]	T_h [K]	Resistivity [Ω m]
	0	1.996E-08
19.82	26	2.194E-08
23.79	38	2.284E-08
25.79	44	2.337E-08
27.77	52	2.396E-08
29.75	61	2.464E-08
31.74	71	2.539E-08
33.7	81	2.615E-08
35.7	94	2.713E-08
37.7	105	2.798E-08
39.7	119	2.912E-08

Design 2_(100)

Current [mA]	T_h [K]	Resistivity [Ω m]
	0	2.082E-08
19.82	18	2.23E-08
23.79	27	2.307E-08
25.79	32	2.348E-08
27.77	36	2.38E-08
29.75	41	2.421E-08
31.74	47	2.47E-08
33.7	57	2.555E-08
35.7	63	2.608E-08
37.7	73	2.685E-08
39.7	83	2.77E-08

6.1.5. Thermal conductivity of the surrounding media $\kappa_\infty = \kappa_\infty(T)$

The dependency of the thermal conductivity of the surrounding media (air) with temperature will also be taken into account in the models.

Direct measurement of the thermal conductivity of air around the microgripper is not possible; however, the IR temperature measurements obtained in Chapter 5 can be used to construct semi-empirical tables that relate the different input currents, with the temperature of the cold arm and the thermal conductivity of the air. The latter can be calculated using the linear relationship given by [307]

$$\kappa_{air} = 0.025642 + (T_{air} * 0.000072) \tag{6.4}$$

where T_{air} has been taken as the temperature of the cold arm.

Table 6.3 and Table 6.4 show $\kappa_{air} = \kappa_{air}(T)$, and relate it to the different current levels used for design 1_(30), design 1_(100), design 2_(30) and design 2_(100).

Table 6.10: Dependency with temperature of the thermal conductivity of air at different input currents for design 1_(30) and design 1_(100)

design 1_(30)

Current [mA]	T_c [K]	Thermal conductivity of air [W / m K]
	0	0.0256
20	16	0.0268
22	19	0.0270
24	24	0.0274
26	30	0.0278
28	33	0.0280
30	40	0.0286
32	48	0.0291
34	56	0.0296
36	62	0.0301
38	71	0.0307
40	81	0.0315

design 1_(100)

Current [mA]	T_c [K]	Thermal conductivity of air [W / m K]
	0	0.0256
20	15	0.0267
22	18	0.0270
24	23	0.0273
26	27	0.0276
28	31	0.0279
30	37	0.0283
32	42	0.0287
34	49	0.0292
36	56	0.0297
38	65	0.0303
40	73	0.0309

Table 6.11: Dependency with temperature of the thermal conductivity of air at different input currents for design 2_(30) and design 3_(100)

design 2_(30)

Current [mA]	T_c [K]	Thermal conductivity of air [W / m K]
	0	0.0256
20	12	0.0265
22	14	0.0267
24	17	0.0268
26	20	0.0271
28	24	0.0274
30	28	0.0276
32	33	0.0281
34	38	0.0284
36	44	0.0288
38	51	0.0293
40	59	0.0299

design 2_(100)

Current [mA]	T_c [K]	Thermal conductivity of air [W / m K]
	0	0.0256
20	9	0.0263
22	11	0.0265
24	13	0.0266
26	17	0.0269
28	19	0.0270
30	20	0.0271
32	25	0.0274
34	30	0.0278
36	34	0.0281
38	40	0.0286
40	46	0.0289

6.1.6. Boundary conditions

6.1.6.1. Boundary conditions at the anchor attachment

In the simulations in Chapter 4 (4.4.5) it was considered that the microgripper was attached to a thermal sink with a constant temperature equal to the ambient. In this case a large portion of the heat generated within the actuators is lost by conduction through the beams itself to the anchors that are kept at ambient temperature. However overall higher temperatures are expected in thermal actuators where the anchors are insulated from a thermal ground [187].

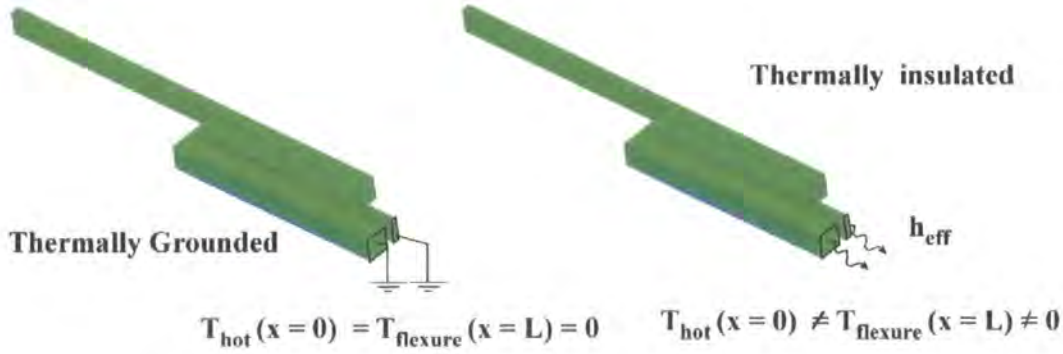

Fig. 6.3: Boundary conditions at the anchors.

Given the design and mounting of the microgripper, it is likely that a certain level of insulation is provided by the SU8 of the anchors (the gold contacts are mounted on the top surface) and the glue used to attach the microgripper to the PCB. A finite heat loss at the anchors can be integrated in the models by applying an effective heat transfer coefficient, h_{eff} (Fig. 6.3), at the base of the each actuator beam (x = 0) in the hot arm and at x = L (≡ total length in the cold/flexure arms) which simulates the insulation provided by the polymer. Depicted in Fig. 6.4 is the one dimensional heat transfer circuit used to estimate the insulation provided by the SU8 at the anchors.

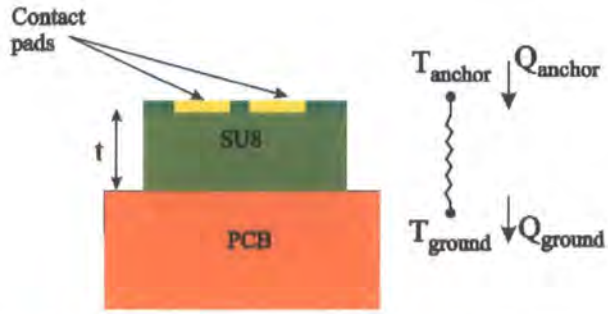

Fig. 6.4: Estimation of the heat loss at the anchors: one-dimensional circuit.

Continuity of heat flux gives that $Q_{anchor} = Q_{ground}$

$$Q_{anchor} = Q_{ground} \tag{6.5}$$

where Q_{anchor} is the heat flux rate through the anchor to a thermal ground.

$$Q_{anchor} = h_{eff}\,(T_{anchor} - T_{ground}) \tag{6.6}$$

The heat conducted through a layer of SU8 of thickness, t, is given by

$$Q_{ground} = \kappa_{SU8}\left(\frac{T_{anchor} - T_{ground}}{t}\right) \tag{6.7}$$

Combining equations (6.5), (6.6), and (6.7) it can be seen that

$$\frac{t}{\kappa_{SU8}} = \frac{1}{h_{eff}} \tag{6.8}$$

The effective convection coefficients calculated for the anchor of the hot arm of thicknesses 30 μm and 100 μm are respectively 6666 and 2000 W/m^2K.

In order to check how this insulation affects the final results of the models, a fourth modelling scenario (Scenario 4) will be considered. In this case the anchors of the actuators will be considered heat sinks, and the $T_{anchor\_hot} = T_{anchor\_cold} = T_\infty = 0$. (in the rest of the scenarios $T_{anchor\_hot} \neq T_{anchor\_cold} \neq T_\infty$).

6.1.6.2. Boundary conditions at the end of the actuators

All of the heat transfer coefficients calculated so far have assumed beams with an infinite length. The beams have a finite length and in some geometries (especially high aspect ratio ones) an extra heat loss path has to be considered in the balance of the heat losses. Fig. 6.5 depicts that situation where a finite heat loss is assumed at the end connection of the beams. The heat loss coefficients can be calculated assuming heat loss by convection of an infinite vertical plane [276].

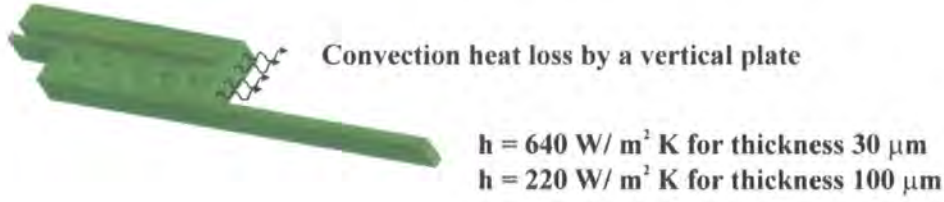

Fig. 6.5: Heat losses at the end of the actuators.

The convection coefficients calculated for the thicknesses of 30 μm and 100 μm are respectively 640 and 220 W/m^2K and are introduced in the electrothermal model by adding an extra heat loss path to the boundary conditions (Table 4.13)

6.1.7. Validation of the electrothermal model in air

In this section, different outputs of the model for different case scenarios (see Table 6.12) will be compared with the experimental results obtained in Chapter 5: the average temperatures of the arms of the actuators (ΔT and T_h), the maximum temperature (T_{max}), and the detailed temperature distribution measured along the length of the actuators when a current is applied at the outputs of interest.

Table 6.12: Summary of the different heat loss mechanisms and thermal boundary conditions considered in each scenario.

	Heat loss to the ambient by	Heat exchange between beams	Boundary condition the anchor	Boundary condition the of the actuator
Scenario 1	Conduction	Yes (Conduction)	Insulated	Yes
Scenario 2	Conduction + Convection[(*)]	Yes (Conduction)	Insulated	Yes
Scenario 3	Convection	No	Insulated	Yes
Scenario 4	Conduction	Yes (Conduction)	Grounded	Yes

[(*)] Convection applied to the external beams only ($h = 40$ W m^{-2} K^{-1})

6.1.7.1. Average temperatures: ΔT, T_h and T_{max}

ΔT is one of the main input parameters for the mechanical model, i.e. for the calculation of the deflection; therefore it is the output parameter of interest of the electrothermal model. For a given ΔT and geometry, it is also important to know the values of T_h and T_{max} as these parameters will ultimately determine if there is a risk of thermal failure (due to the delamination of the metallisation layer or the degradation of the polymer) or whether the microgripper can be used in biological environments where low temperatures are required.

Fig. 6.6 to Fig. 6.13 show the comparison between modelling and experimental results. Evident from all the figures is that Scenario 3 systematically overestimates the average temperatures developed along the arms and, more importantly, that it overestimates the difference in temperature ΔT. These results highlight the importance of considering the heat exchange between the arms in addition to the heat loss from individual beams. The other three scenarios give reasonably good predictions in terms of ΔT, but provide slightly different results when comparing the hot and maximum temperatures developed in the hot arm. For design 1 it seems that scenario 1 gives the most accurate results (even if scenario 2 is also reasonably close). For design 2, it is only scenario 2 that gives accurate results. The reason for that can be the hot arms are the external beams and do not benefit from the internal insulation of the hot arms in design 1. Finally the grounded case, scenario 4, provides results relatively close to the experiments but always shows overall lower average temperatures. The next section will give an idea of the temperature profiles $T(x)$ developed in each case.

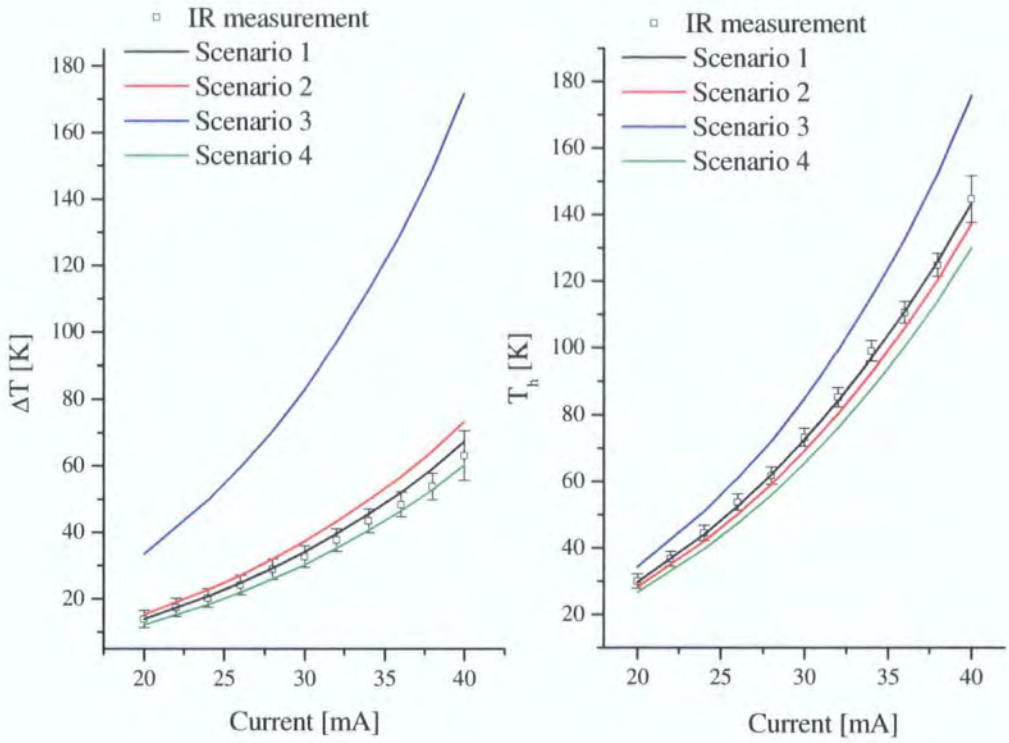

Fig. 6.6: Design 1_(30); ΔT and T_h versus input current. Comparison between experimental data measured using IR thermography and the outputs of the model for scenarios 1 to 4.

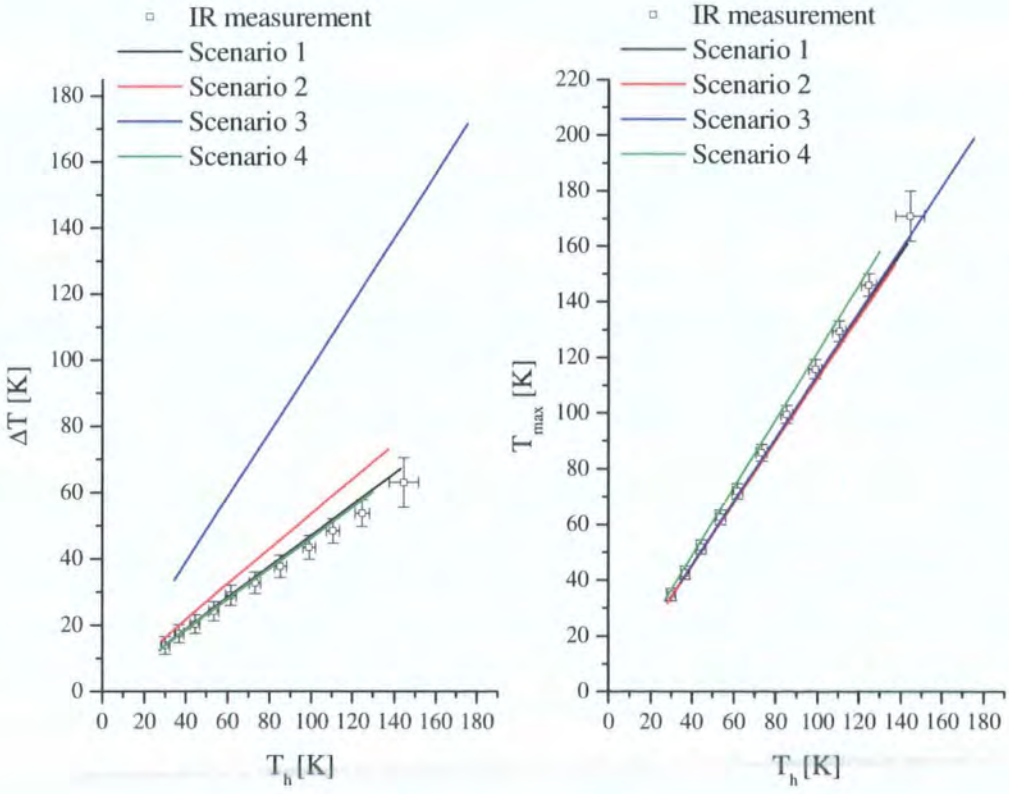

Fig. 6.7: Design 1_(30) ΔT and T_{max} versus T_h. Comparison between experimental data measured using IR thermography and the outputs of the model for scenarios 1 to 4.

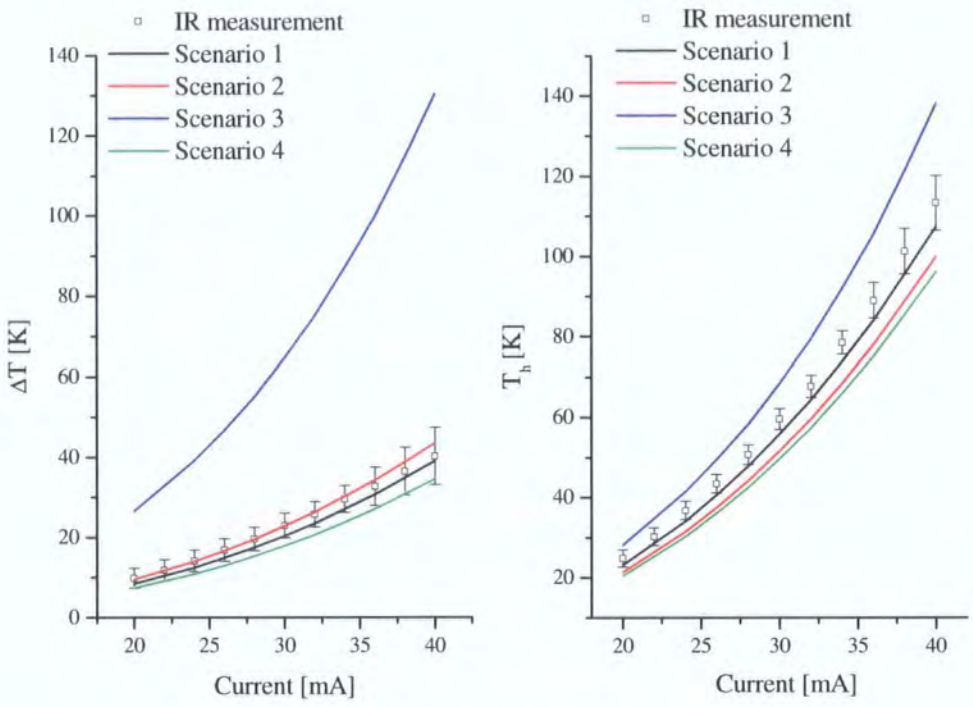

Fig. 6.8: Design 1_(100) ΔT and T_h versus input current. Comparison between experimental data measured using IR thermography and the outputs of the electrothermal model for scenarios 1 to 4 (f_{ij} in the models has been calculated using t' (Table 6.3)

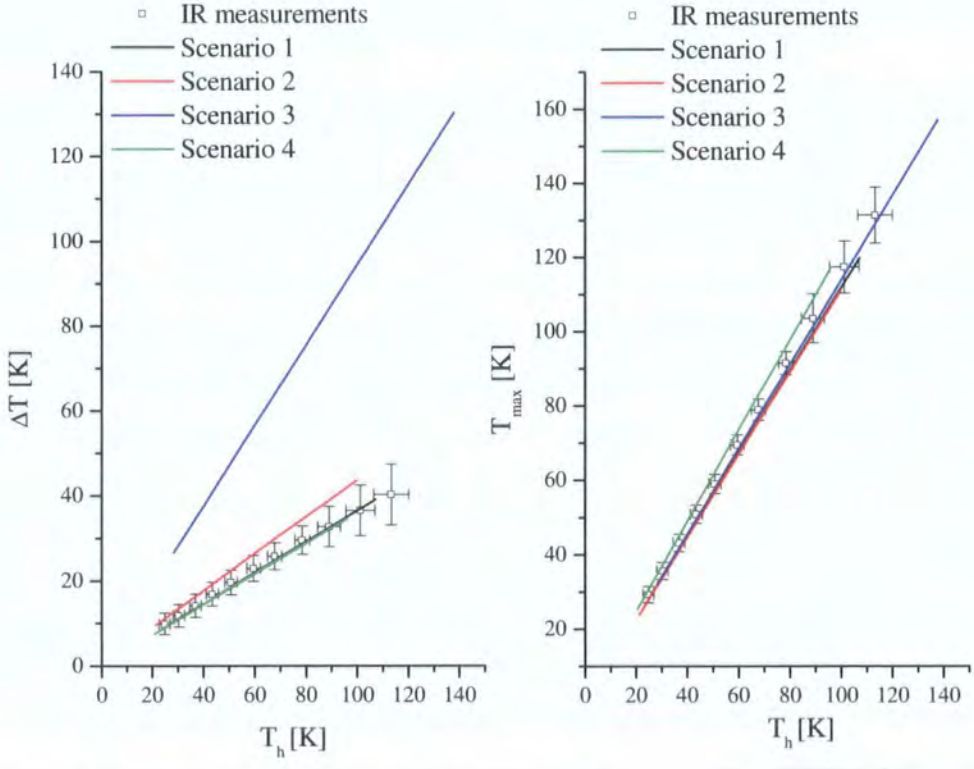

Fig. 6.9: Design 1_(100) ΔT and T_{max} versus T_h. Comparison between experimental data measured using IR thermography and the outputs of the model for scenarios 1 to 4.

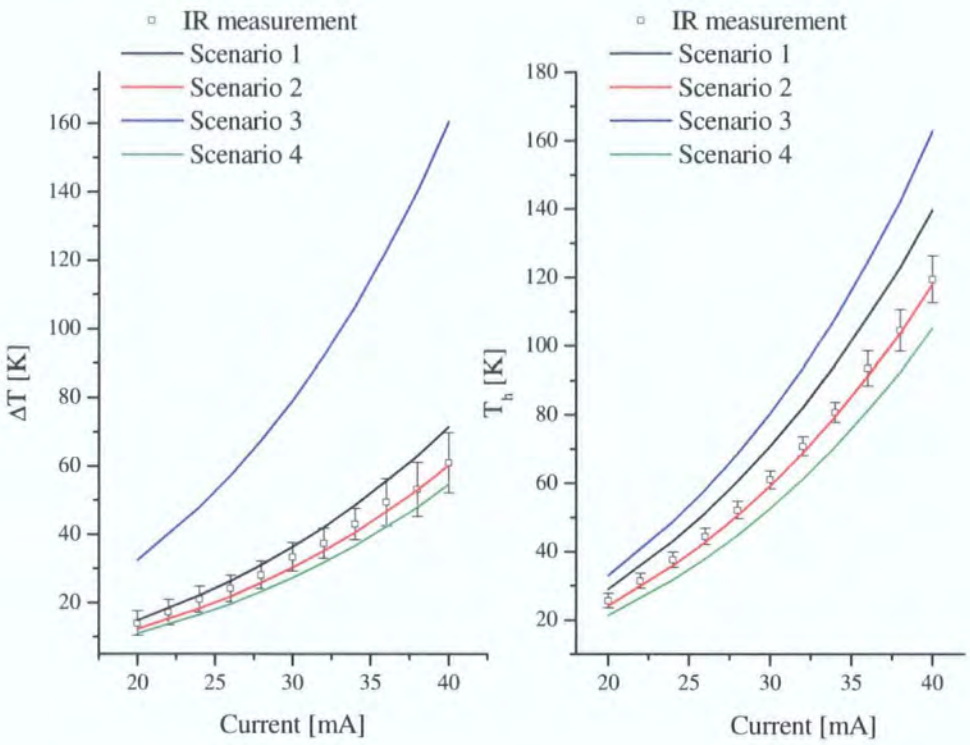

Fig. 6.10: Design 2_(30) ΔT and T_h versus input current. Comparison between experimental data measured using IR thermography and the outputs of the model for scenarios 1 to 4.

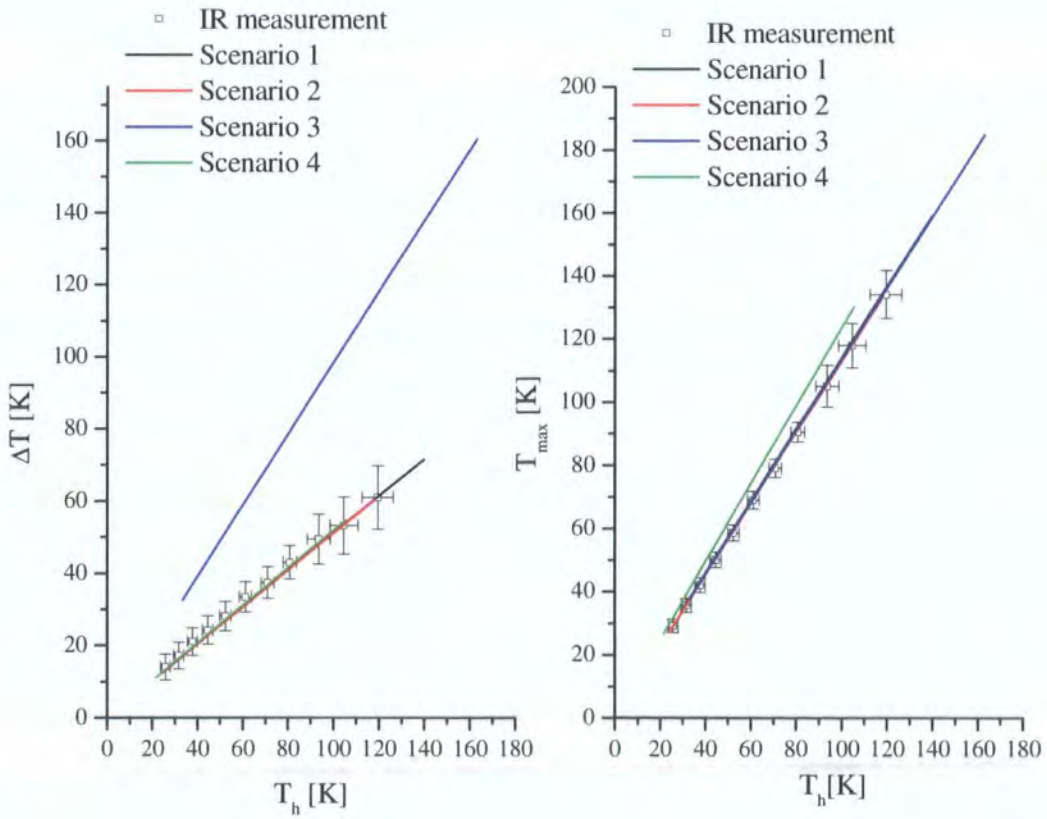

Fig. 6.11: Design 2_(30) ΔT and T_{max} versus T_h. Comparison between experimental data measured using IR thermography and the outputs of the model for scenarios 1 to 4.

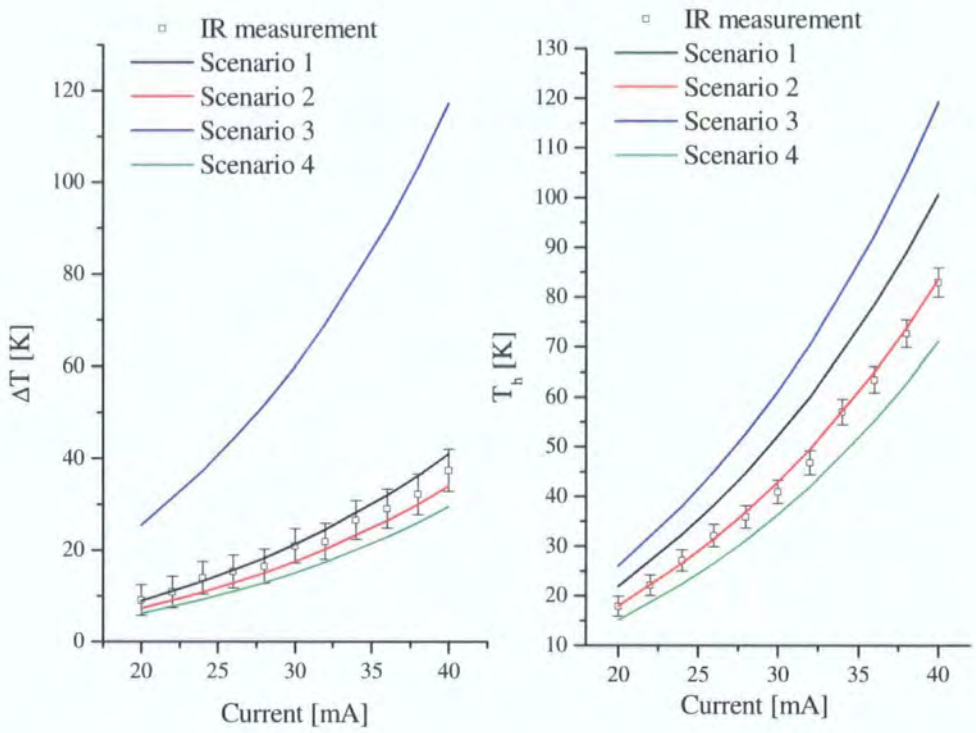

Fig. 6.12: Design 2_(100) ΔT and T_h versus input current. Comparison between experimental data measured using IR thermography and the outputs of the model for scenarios 1 to 4. (f_{ij} in the models has been calculated using t' (Table 6.3)

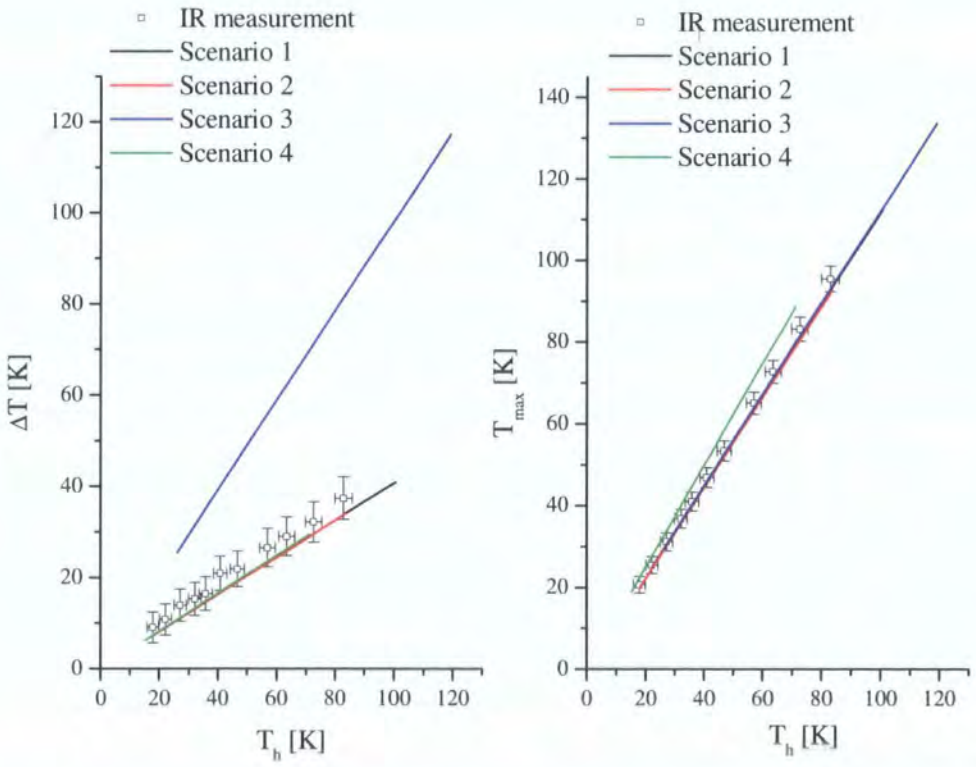

Fig. 6.13: Design 2_(100) ΔT and T_{max} versus T_h. Comparison between experimental data measured using IR thermography and the outputs of the model for scenarios 1 to 4.

6.1.7.2. Temperature distribution T(x)

Once the validation of the models has been performed based on average temperatures, it would be interesting to see how well the models predict the temperature profiles developed along the arms relative to ambient. The graphs presented in this section (Fig. 6.14 to Fig. 6.17) will show the comparison of experimental and modelling results at two representative current levels 30 mA and 40 mA.

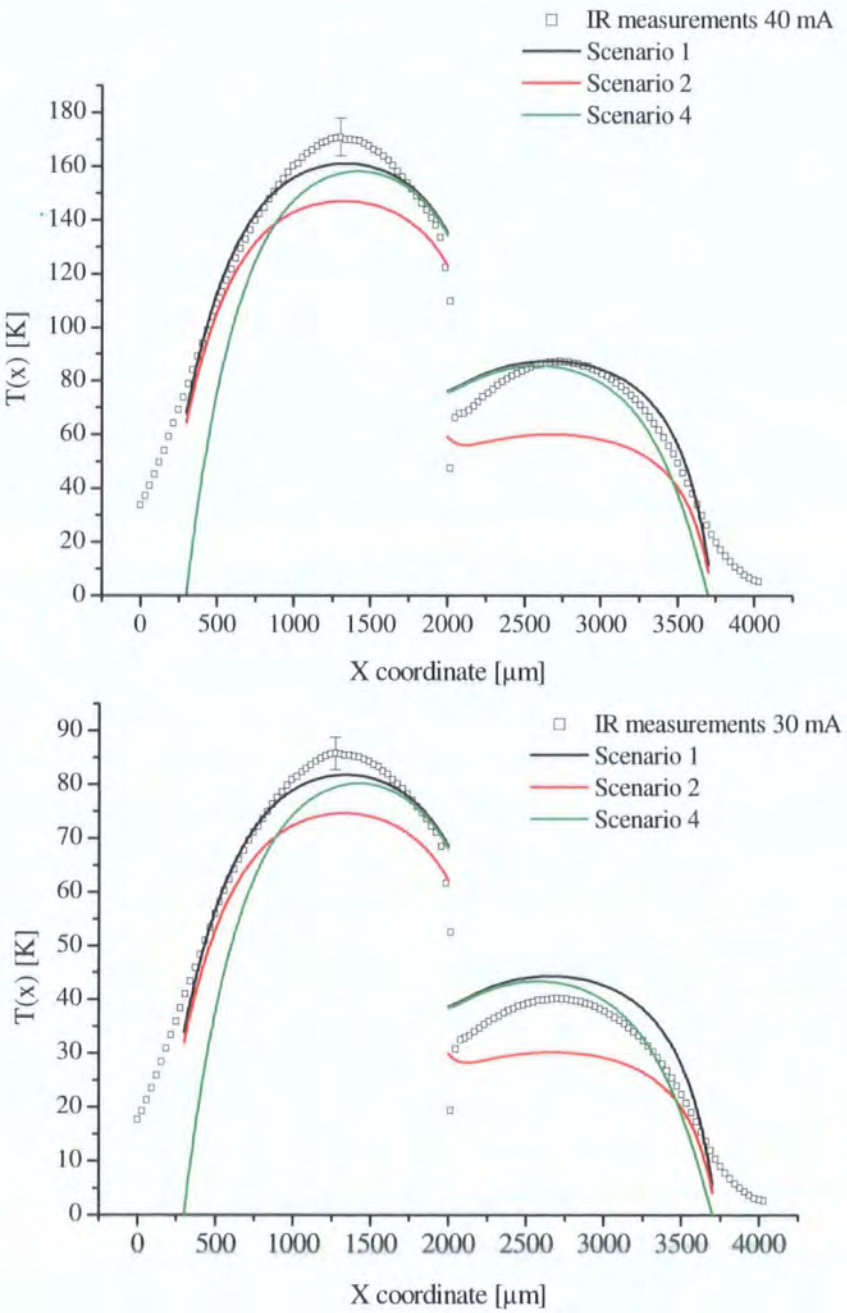

Fig. 6.14: Design 1_(30); experimental data versus modelled profiles developed along the arms of the actuator: scenario 1, scenario 2 and scenario 4.

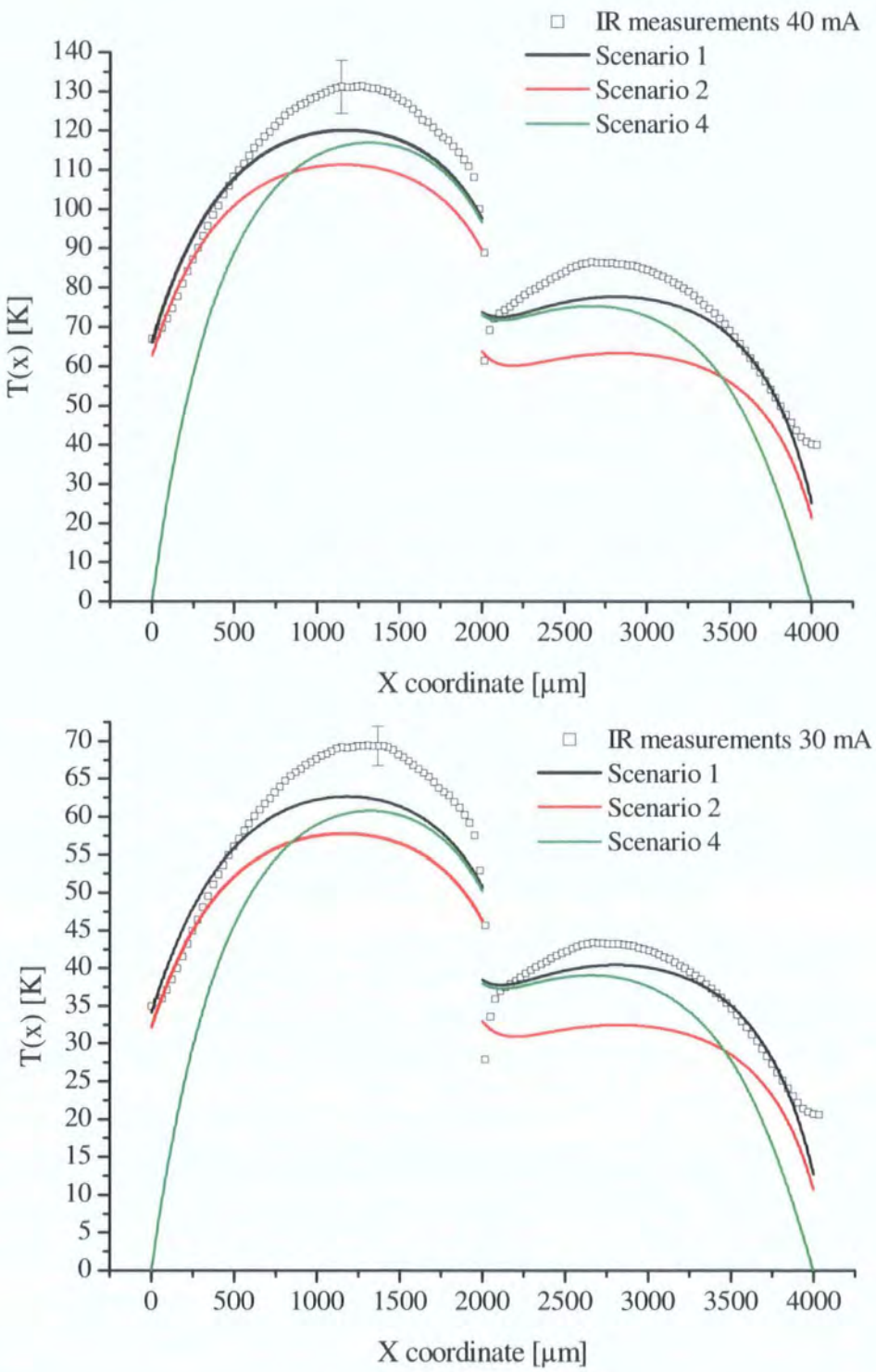

Fig. 6.15: Design 1_(100) experimental data versus modelled profiles developed along the arms of the actuator: scenario 1, scenario 2 and scenario 4.

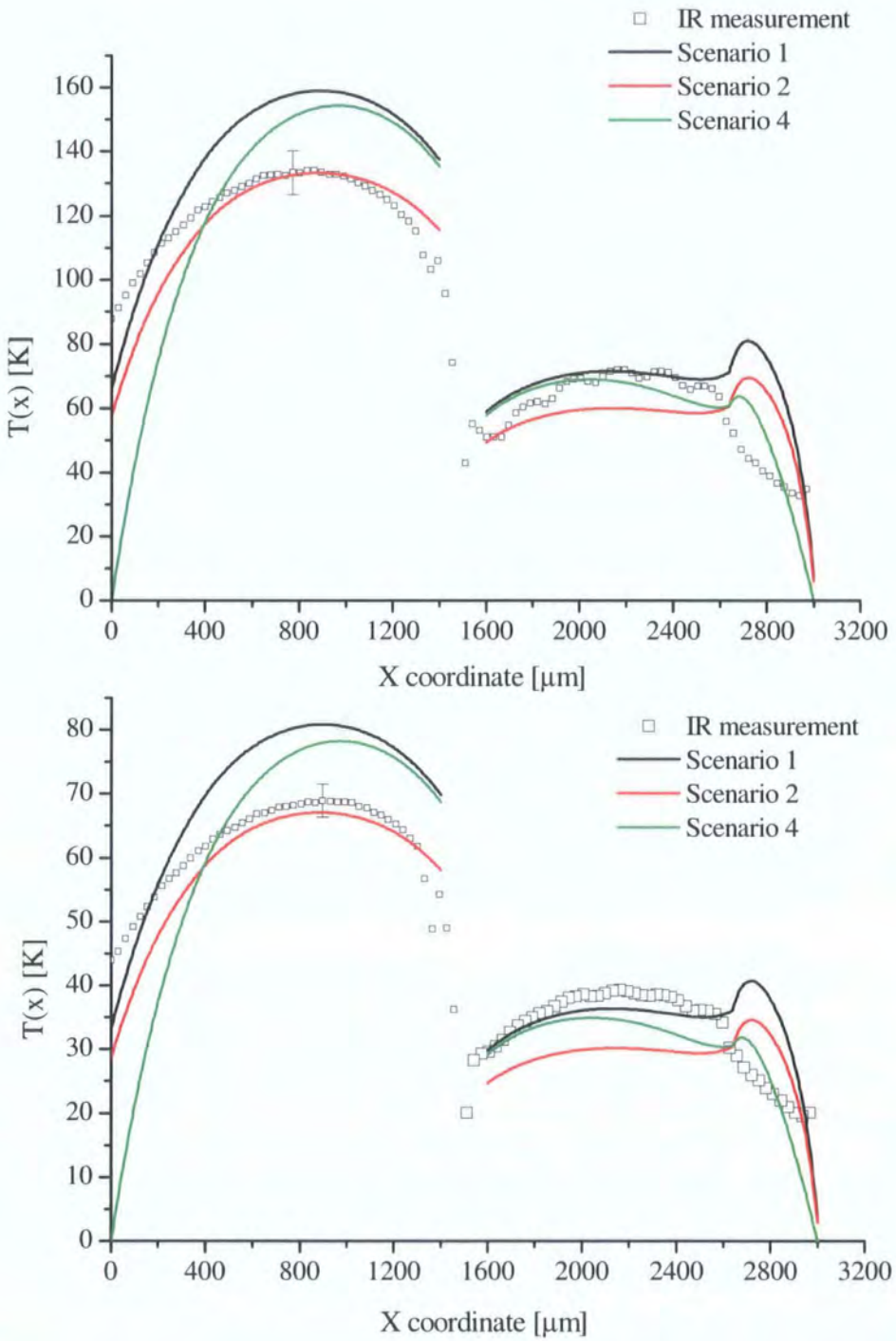

Fig. 6.16: Design 2_(30); experimental data versus modelled profiles developed along the arms of the actuator: scenario 1, scenario 2 and scenario 4.

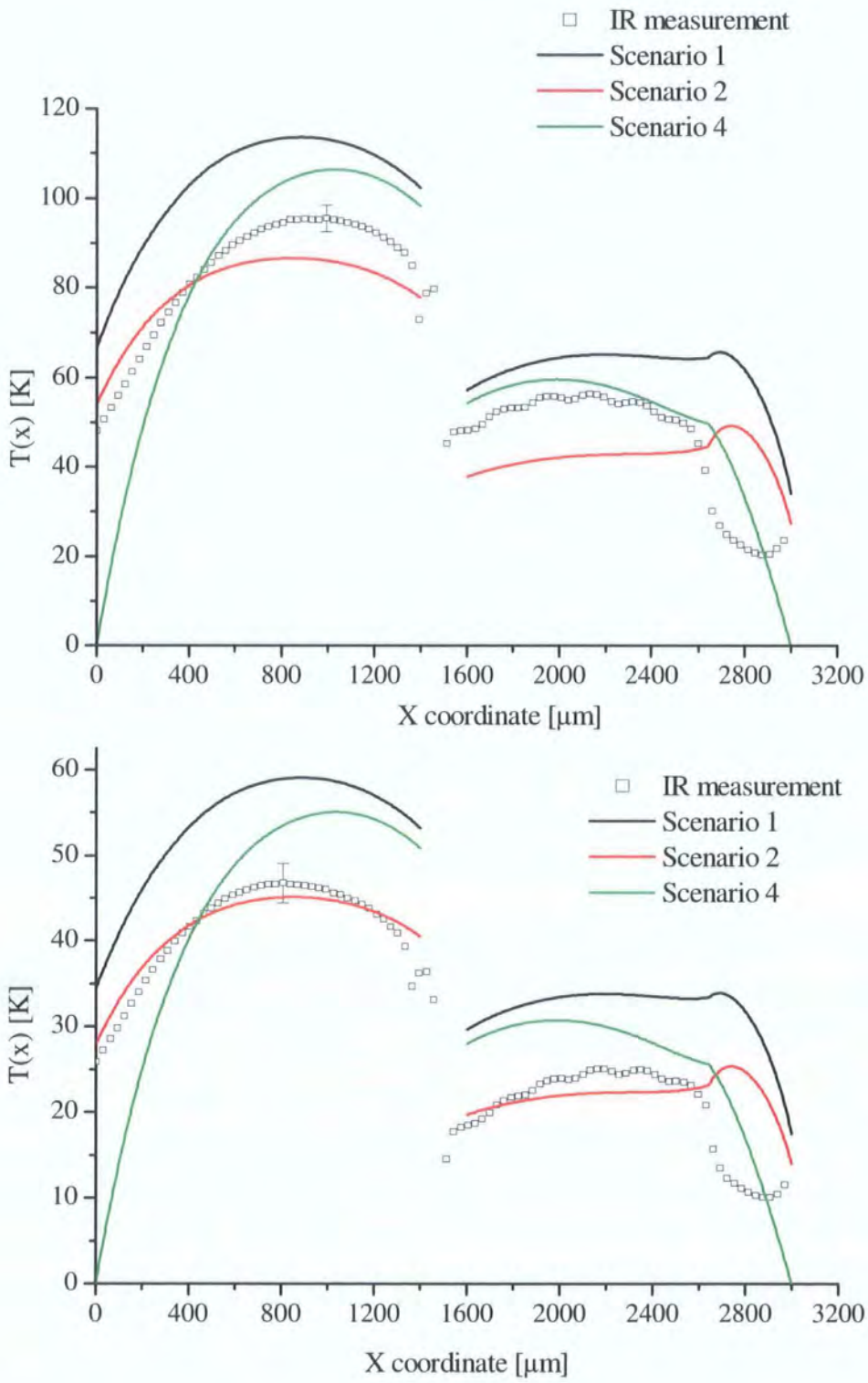

Fig. 6.17: Design 2_(100); experimental data versus modelled profiles developed along the arms of the actuator: scenario 1, scenario 2 and scenario 4.

As can be seen, the scenarios that consider a finite heat loss at the anchors (scenario 1 and scenario 2) predict initial temperatures (see graphs at x = 0 and x = 4000 or x = 3000) similar to the ones measured by IR. These results validate the theory that a

thermal insulation is provided by the presence of the SU8 and that it seems to vary with the thickness of the anchor and power. For example in the case of design 1_(30) the ratio between the initial temperature of the arms and their average temperature is 0.27 while the same ratio in design 1_(100) is 0.58. This is consistent with a higher insulation provided by a thicker anchor.

In section 6.1.7.1 it was concluded that the scenario that best described the behaviour of design 1_(30) and design 1_(100) was number 1. However, it can be seen that scenario 1 generally underestimates the temperature of both the hot and cold arms while maintaining the same value of ΔT as the experiments. This could be explained by the close proximity of the two internal hot arms (Fig. 6.1) that somehow would reduce the heat losses from the hot arms and increase the overall temperature of the device.

In the case of design 2_(30) and design 2_(100), scenario 2 predicts reasonably well the temperature profiles of the hot arms. However, the temperature of the cold arm seems to be underestimated, and overestimated for the flexure. The possibility of the two internal cold arms thermally seeing each other could be a plausible explanation for the higher temperatures shown by the experiments. In the case of the flexure, it is possible that the proximity of the anchor, and the larger gap between the two internal flexure beams (360 μm versus 140 μm between the two cold arms) increases the heat losses from the flexure adding, for example, a convection component.

6.2. Validation of the thermomechanical model in air

In order to validate the mechanical model it is necessary to obtain the values of the deflection at the end of the actuators instead of at the end of the jaws (grasping point). These values, although not measured directly, can be extrapolated from the previous measurements by applying a reduction factor to the overall deflection. This factor depends on the geometry of the microgripper and on the structural thickness of the device and has been obtained for each microgripper by using a set of mechanical FEA simulations.

As depicted in Fig. 6.18, a simple trigonometric extrapolation of the deflection (see dotted line) is likely to overestimate the deflection by at least 30%.

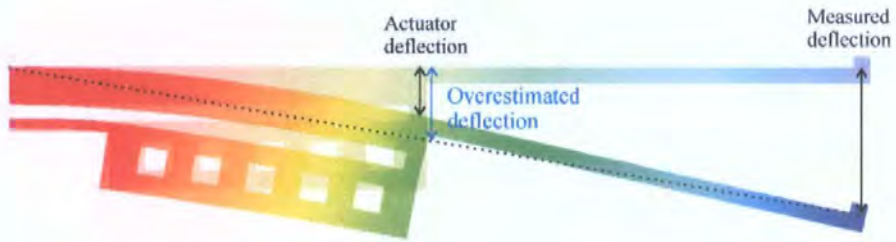

Fig. 6.18: FEA simulation of the deflection (deformation magnification x3)

6.2.1. Deflection versus ΔT

The deflections extrapolated from the measurements compared to the deflections obtained from the mechanical model using the calculated ΔT as an input are shown in Fig. 6.19 to Fig. 6.22. The figures on the left show the experimental values of the deflection compared with the values obtained from the mechanical model when using a constant value of the coefficient of thermal expansion, *CTE*. The value assigned to the *CTE* has been 52 ppm/K for design 1, and 64 ppm/K for design 2 [198, 215]. The figures on the right show the experimental values of the deflection compared with the values obtained from the mechanical model when using an adjusted *CTE* that varies with temperature.

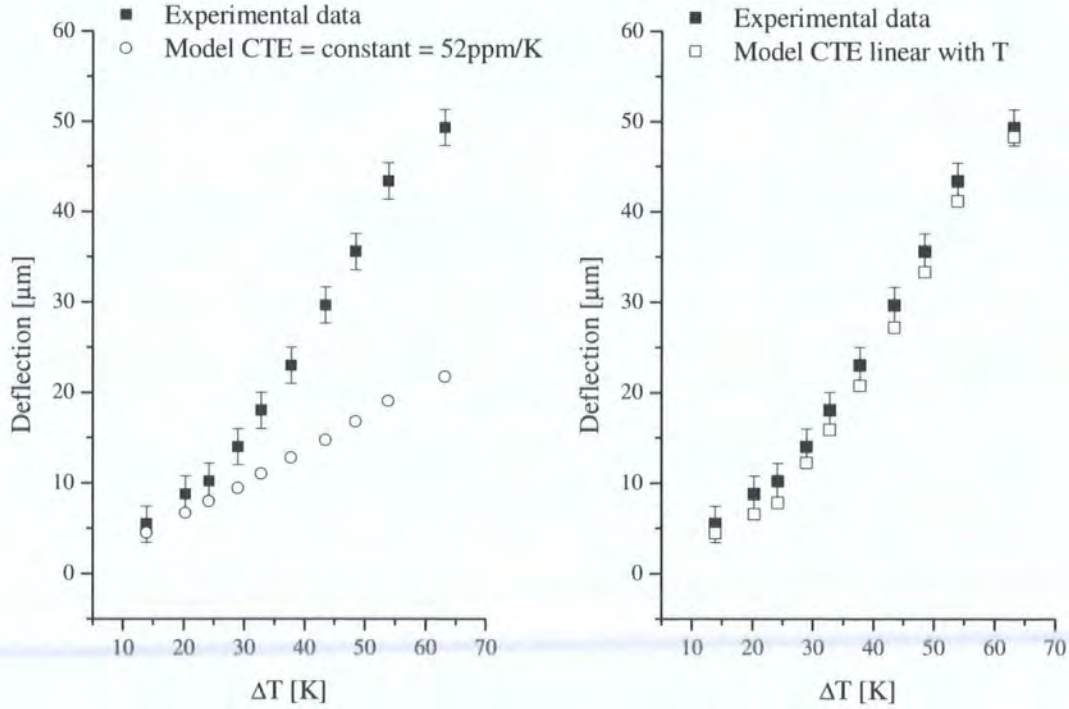

Fig. 6.19: Design 1_(30) (a) Experimental and modelled deflections (CTE = 52 ppm/K) versus ΔT (b) Experimental and modelled deflection (CTE = CTE(T)) versus ΔT.

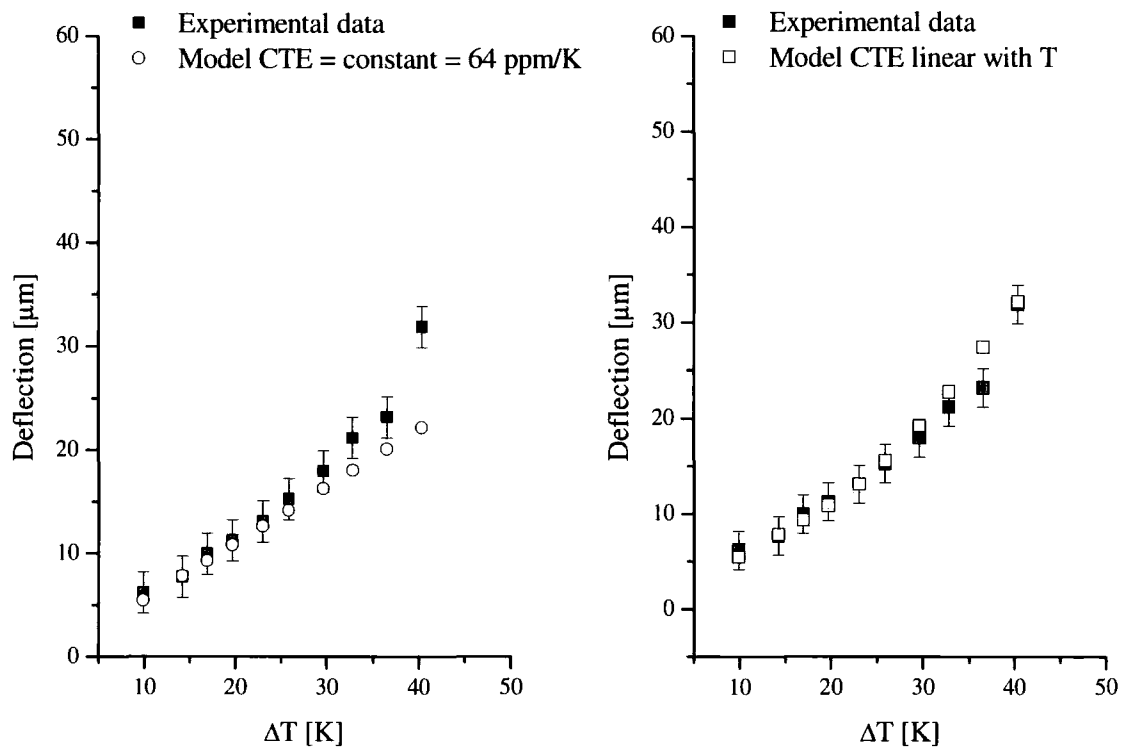

Fig. 6.20: Design 1_(100) (a) Experimental and modelled deflections (CTE = 64 ppm/K) versus ΔT (b) Experimental and modelled deflections (CTE = CTE(T)) versus ΔT.

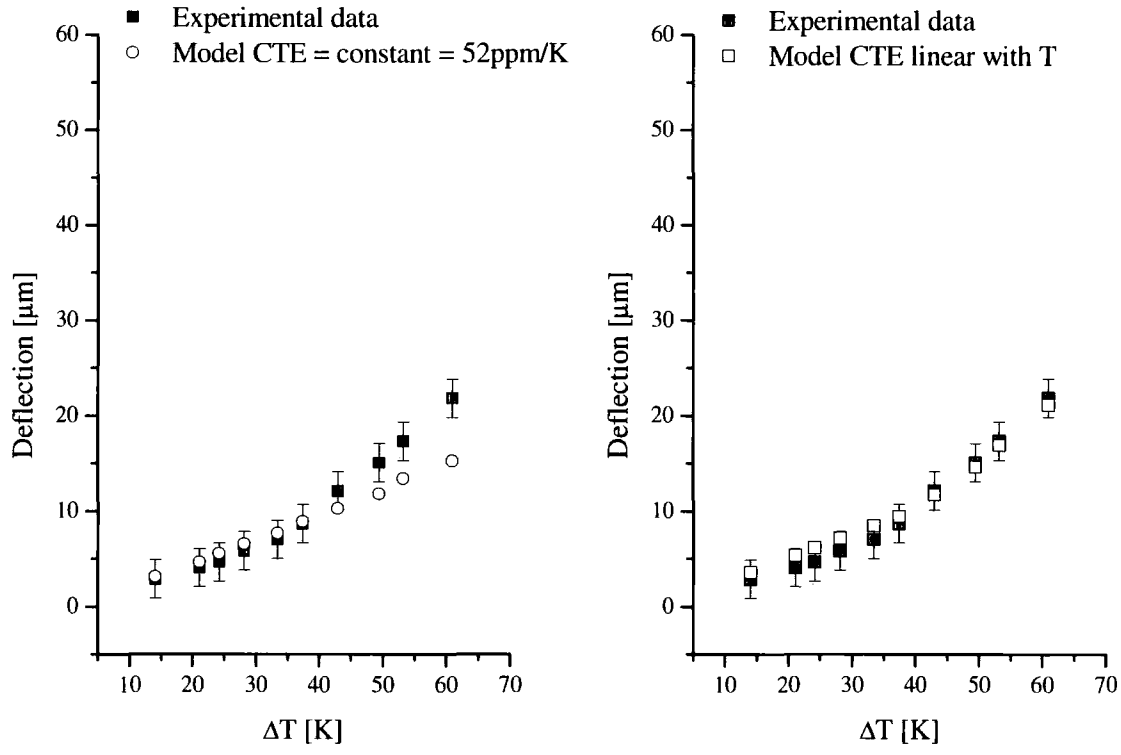

Fig. 6.21: Design 2_(30) (a) Experimental and modelled deflections (CTE = 52 ppm/K) versus ΔT (b) Experimental and modelled deflections (CTE = CTE(T)) versus ΔT.

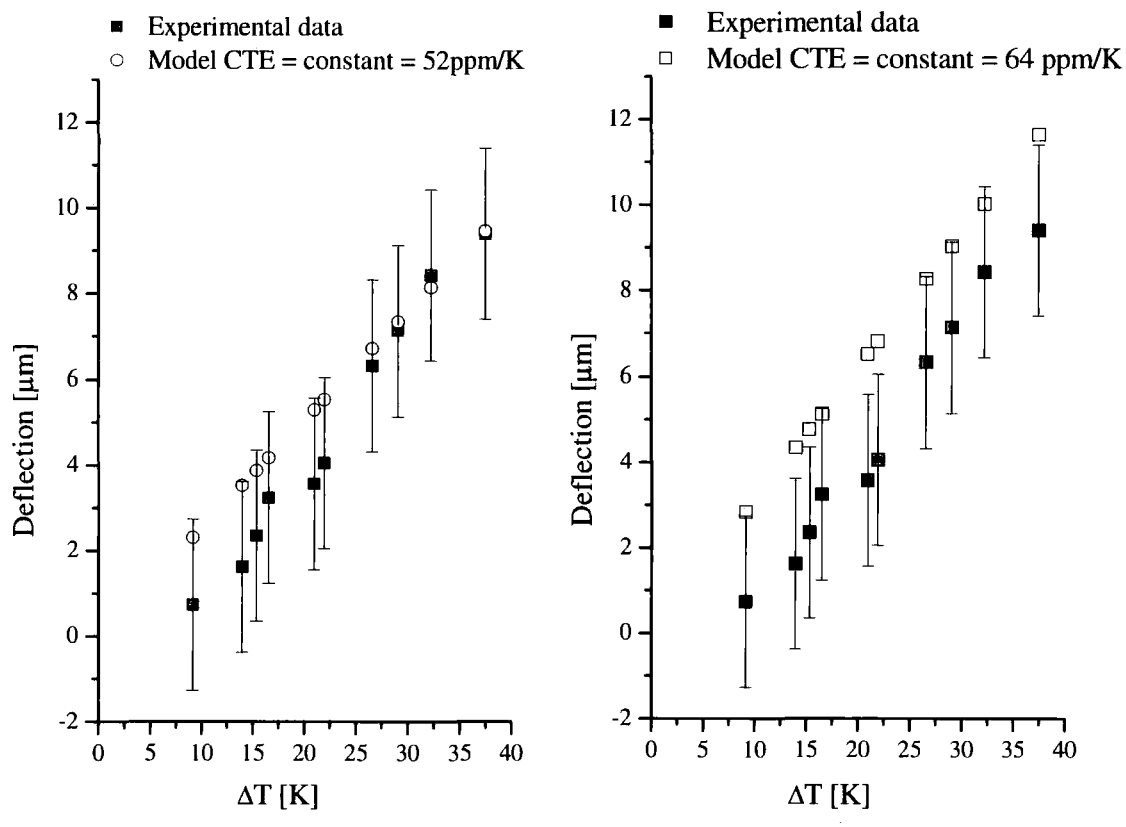

Fig. 6.22: Design 2_(100) (a) Experimental and modelled deflections (CTE = 52 ppm/K) versus ΔT (b) Experimental and modelled deflections (CTE = 64 ppm/K) versus ΔT.

6.2.2. Discussion

As can be seen from the left hand side graphs of Fig. 6.19 to Fig. 6.22, the analytical thermomechanical model predicts a linear relationship between ΔT and the deflection. Even though this gives reasonably good results at low temperatures; the model underestimates the deflection at higher values of T. The reason for that could be the variation of the material properties with temperature.

In the development of the mechanical model, the temperature dependence of material properties such as the Young's modulus or the coefficient of thermal expansion was not taken into account. The Young's modulus, E, dropped out from the 1D analytical model equations (see 4.5) and should not be the cause of the disparity. The impact of its variation with temperature, however, has been analysed by a set of FEA simulations. As expected, the results indicate that the variation of in-plane deflection due to the variation of E is minimal (up to 3 µm for a factor of two in E and a temperature difference of 70 K), and that E is not a strong driver for the system.

The disparity in the results could derive from the variation of the CTE with temperature which in turn results from a variation of processing conditions. Different values of the *CTE* for the SU8 photoresist have been reported previously, e.g. 52 ppm/K [198, 215], 87.1 ppm/K [229] and 102 ppm/K [216]. In each case, the value of the *CTE* was estimated below the glass transition temperature (T_g), and the *CTE* showed a constant value. However, in the results presented here, the deflection of the microgripper occurs at temperatures below and above T_g. The latter is fixed by the processing conditions [216] and has been estimated to be ~95-100 °C. When heating the SU8 microgripper above T_g, polymerisation will continue and the material properties will change [215]. As in other polymers [271, 308], the *CTE* of the SU8 could show a different value before and after T_g, with a linear change between the two material states.

This dependence of the *CTE* with temperature has been simulated as follows. At low temperatures it has been considered a constant value of the *CTE* whilst at temperatures around the T_g a linear variation of the *CTE* has been considered. The slope of the linear variation was chosen to adjust each set of experimental data.

For the design 1_(30) two ranges of the CTE have been considered as a function of the increase in temperature experienced by the hot arm (T_h):

$$CTE(T)\,[ppm/K] = \begin{cases} 52 & if\ T_h < 55K \\ 3.73 + 0.877\,T_h & if\ T_h > 55\ K \end{cases} \tag{6.9}$$

Equivalently, for the design 1_(100)

$$CTE(T)\,[ppm/K] = \begin{cases} 64 & if\ T_h < 60K \\ 37 + 0.491\,T_h & if\ T_h > 60\,K \end{cases} \tag{6.10}$$

For the design 2_(30)

$$CTE(T)\,[ppm/K] = \begin{cases} 52 & if\ T_h < 70K \\ 23.737 + 0.397\,T_h & if\ T_h > 70\ K \end{cases} \tag{6.11}$$

For the design 2_(100), due to the restricted range of data available, only one range of the CTE has been considered.

$$CTE(T)\,[ppm/K] = 64 \quad if\ T_h < 82\,K \tag{6.12}$$

The introduction in the simulations of *CTE (T)* was carried out in an iterative manner. First, the average increase in temperature of the hot arm (T_h) for each input current was measured by IR thermography. This value was then used to estimate the temperature dependent value of the CTE. .For example, as indicated in Table 6.13 when in design 1_(30) an increase in temperature of T_{hot} = 61.7 K is observed, a value of 58 p.p.m/K is considered in the mechanical model. The difference in temperature between hot and cold arms was also measured by IR (ΔT) and, together with the value of the CTE, is used as an input to the mechanical model.

Table 6.13: Values of the coefficient of thermal expansion CTE as a function of the values of T_h for the different designs.

design 1_(30)

ΔT [K]	T_h [K]	T_h Absolute [°C]	CTE [ppm K^{-1}]
13.9	30.0	50.0	52
20.3	44.5	64.5	52
24.2	53.8	73.8	52
29.0	61.7	81.7	58
32.8	73.2	93.2	68
37.8	85.3	105.3	79
43.5	99.0	119.0	91
48.5	110.6	130.6	101
53.8	124.8	144.8	113
63.1	144.6	164.6	131

design 2_(30)

ΔT [K]	T_h [K]	T_h Absolute [°C]	CTE [ppm K^{-1}]
14.0	25.7	45.7	52
21.1	37.7	57.7	52
24.2	44.5	64.5	52
28.1	52.2	72.2	52
33.4	61.1	81.1	52
37.4	70.9	90.9	52
43.0	80.8	100.8	56
49.4	93.6	113.6	61
53.2	104.6	124.6	65
61.0	119.5	139.5	71

design 1_(100)

ΔT [K]	T_h [K]	T_h Absolute [°C]	CTE [ppm K^{-1}]
9.8	24.8	44.8	64
14.2	36.8	56.8	64
16.9	43.5	63.5	64
19.6	50.7	70.7	64
23.6	59.6	79.6	66
25.9	67.3	87.3	70
29.6	78.5	98.5	76
32.4	89.0	109.0	81
36.7	102.1	122.1	87
40.3	113.3	133.3	93

design 2_(100)

ΔT [K]	T_h [K]	T_h Absolute [°C]	CTE [ppm K^{-1}]
9.1	17.9	37.9	64
13.9	27.1	47.1	64
15.3	32.1	52.1	64
16.5	35.9	55.9	64
20.9	40.9	60.9	64
21.9	46.8	66.8	64
26.6	57.0	77.0	64
29.0	63.4	83.4	64
32.2	72.6	92.6	64
37.4	82.9	102.9	64

The good agreement between the fitted CTE and the experimental and literature data indicates that we have a plausible explanation for the non-linear behaviour of the

mechanical model versus ΔT at temperatures around T_g. It is also important to highlight the differences in the value of the temperature at which the *CTE* starts growing for the different devices and the difference in slope. This could be due to a variation in processing and structural factors: the differences in baking times between the devices, the difference in the level of solvent trapped in each layer or non-homogeneities of the exposure across the wafer. These results indicate that a deeper characterisation of the thermal material properties have to be performed when using SU8 in thermally actuated devices. For this task a direct measurement of the temperature, for example using IR thermography, is essential.

6.3. Completion of electrothermomechanical modelling technique

The experimental validation of the thermomechanical model enables the completion of the modelling technique presented in section 4.4.6. There, the first four points were intended to calculate the difference in temperature between the arms of the actuator for various input currents whilst considering the dependency of the resistivity and the thermal conductivity of the air with temperature. Here, the next two points will enable the calculation of the deflection of the actuator whilst considering the dependency of the *CTE* with temperature.

1. Two input parameters are fed into the thermomechanical model for each current level. These will be the average temperature of the hot arm, T_h, and the temperature difference between the arms, ΔT. T_h will be used to determine the temperature dependent coefficient of expansion $CTE = CTE\ (T_h)$. For example, for absolute temperatures below 80 °C (i.e. slightly before the T_g = 95 °C) a constant value equal to 52 ppm/ K for the *CTE* of the SU8 in design 2_(30) will be included. At temperatures above 80 °C a linear variation of *CTE (T)* will be considered. The nature of this variation and the upper limit of the temperature associated to it has to be verified experimentally (it is likely that a second constant value of the *CTE* will be achieved at temperatures well above T_g). Once the CTE has been calculated, ΔT will be used to obtain the deflections.

2. The same procedure can be repeated until the upper limit of input currents for the simulations is reached.

As noted previously, a spreadsheet is used to calculate the solutions to both models and obtain the deflection of the microgripper fro different input currents (or voltages). Fig. 6.23 shows a diagram with the complete modelling technique proposed. The current, the geometry and the material properties of the microgripper, the thermal conductivity of the ambient and the configuration of the system are the inputs for this spreadsheet. The heat losses to the anchor and at the end of the actuators, the geometrical factors (f_i), are calculated automatically based on the geometry of the microgripper and the configuration of the system. The material properties or parameters dependent of temperature (resistivity, thermal conductivity of the ambient, heat transfer coefficients, and coefficient of thermal expansion) are calculated in an iterative manner using the outputs of the models.

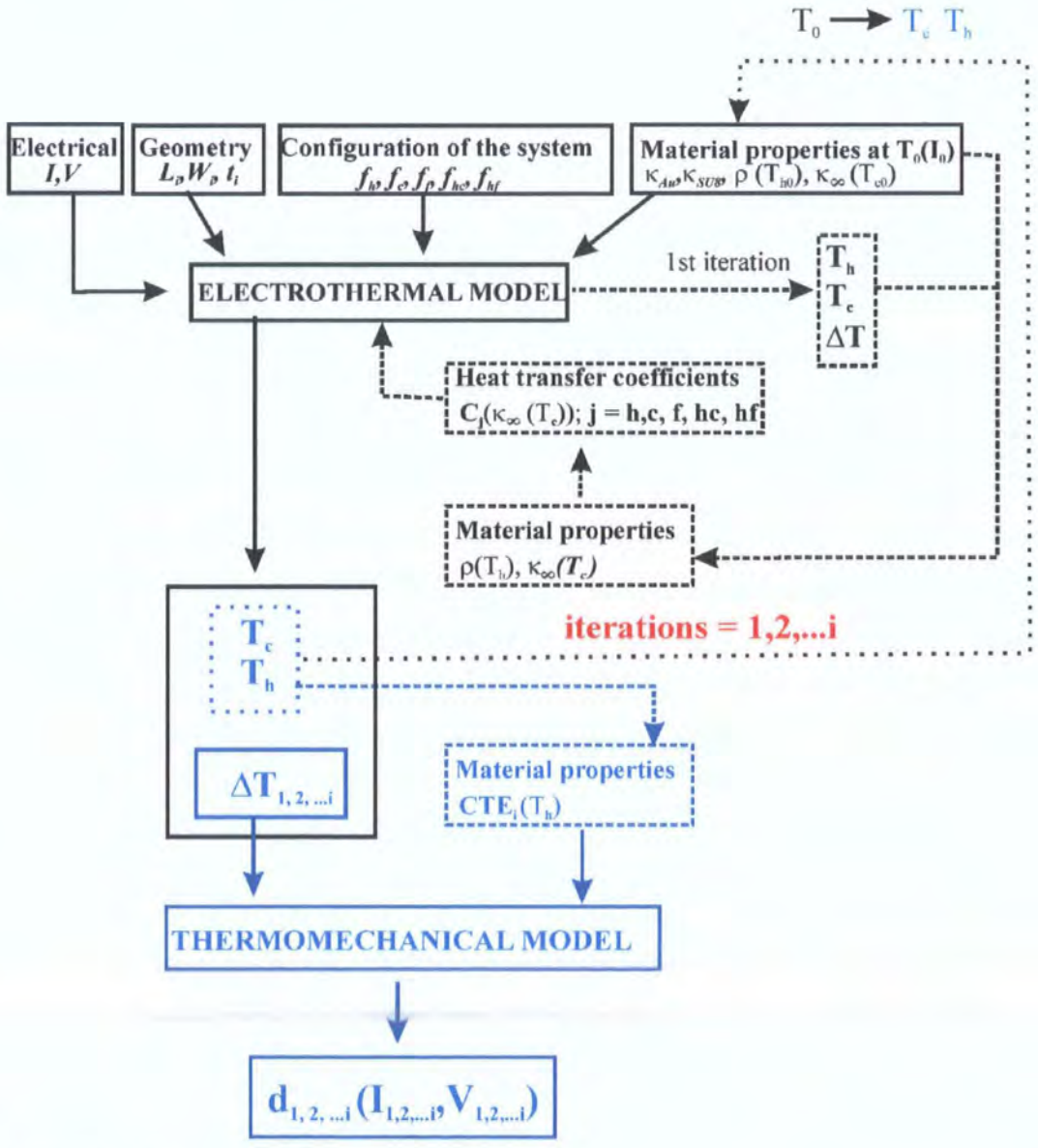

Fig. 6.23: Modelling technique.

6.3.1. Validation of the modelling technique in air and water environments

The proposed modelling technique can be now used to predict the thermal and mechanical performance of another microgripper, design 3_(100) (Fig. 5.1 with dimension in Table 5.1), that has not been measured using infrared thermography but for which electrical and deflection measurement have been taken.

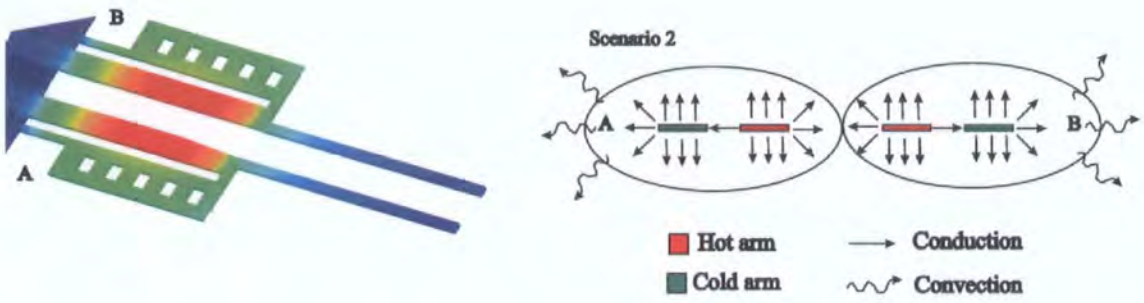

Fig. 6.24: Schematic of Design 3 and the associated heat losses.

The configuration of design 3 (Fig. 6.24) is such that the arms that are placed on the external part of the microgripper are the flexure and cold arm. Following the conclusions derived from the validation of the models, the choice of parameters of the models is as follows:

- The internal beams of the structure, in this case the hot arms; will lose heat to the environment by conduction only. The heat loss coefficients will be given by Table 6.1 and equation (6.1).

- The external beams of the structure will lose heat by conduction and convection. The natural convection coefficients are considered 40 W/m^2 K for air and 200 W/m^2 K for water. The heat loss coefficients will be given by equation (6.2) and Table 6.1.

- There will be a heat exchange between the arms of the actuators governed by a heat exchange factor that takes into account the finite width of the beams, i.e. a thickness *t'* (Table 6.3 (b)).

- The thermal conductivity of the surrounding medium will be considered variable with temperature in the case of air (equation (6.4)), and of a constant value of 0.6 W/m K for water.

In addition it will be assumed that the electrical properties of the metallisation layer are identical to the properties of design 2_(100), i.e. $\rho_0 = 2.08 \times 10^{-8}$ Ω m and TCR = 0.00398 K^{-1} (Table 5.4). Table 6.14 and Table 6.15 summarise the parameters and materials properties of the model.

Table 6.14: Heat transfer geometrical factors used in the simulations

Beam	f_i geometrical factor	f_{ij} geometrical exchange factor
Hot Arm to Ambient[1]	1.51	-
Flexure to Ambient	0.72	-
Flexure to Hot Arm (exchange)	-	2.18
Hot Arm to Ambient[2]	1.08	-
Cold Arm to Ambient	1.70	-
Cold Arm to Hot Arm (exchange)	-	2.41

[1]In section 1 (hot facing flexure)

[2]In section 2 (hot facing cold)

Table 6.15: Material properties used in the simulations

Material property	Value	Units
Resistivity Gold	2.08×10^{-8}	Ω m
TCR	0.00398	K^{-1}
Thermal conductivity Gold	297	$W m^{-1} K^{-1}$
Thermal conductivity SU8	0.2	$W m^{-1} K^{-1}$
Thermal conductivity air(*)	0.0256	$W m^{-1} K^{-1}$
Thermal conudctivity water	0.6	$W m^{-1} K^{-1}$

(*) Variable with temperature as in equation (6.4)

Fig. 6.25 shows the deflections measured in air at different input currents compared with the deflections predicted by the analytical models. The outputs from the thermal and mechanical models are summarized in Table 6.16.

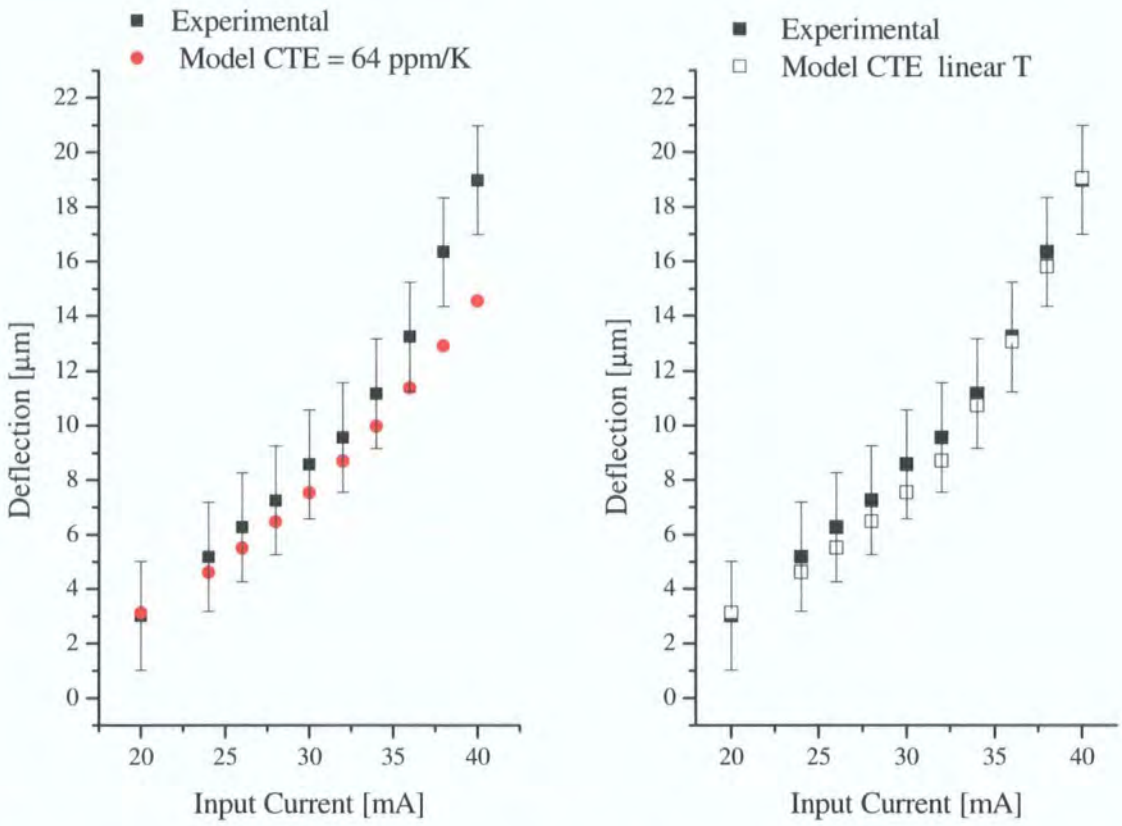

Fig. 6.25: Current versus experimental and modelled deflection for design 3: (left) Scenario 2 with a constant value of CTE (CTE = 64 ppm/K) (Right) Scenario 2 with CTE dependent on temperature (CTE as in equation (6.2)).

Table 6.16: Summary of the outputs of the analytical models presented in Fig. 6.25.

Electrothermal model			Thermomechanical		
Current [mA]	**T_{hot} [K]**	**ΔT [K]**	**Deflection CTE =constant* [μm]**	**Deflection CTE (T_{hot}) linear [μm]**	**CTE = CTE (T_{hot})* [ppm/K]**
20	20.15	10.09	3.13	3.13	64
24	29.78	14.88	4.62	4.62	64
26	35.48	17.70	5.50	5.50	64
28	41.78	20.81	6.47	6.47	64
30	48.73	24.23	7.53	7.53	64
32	56.39	27.99	8.70	8.70	64.69
34	64.82	32.10	9.98	10.73	68.83
36	74.06	36.59	11.38	13.04	73.36
38	84.17	41.49	12.90	15.79	78.33
40	95.22	46.81	14.55	19.05	83.76
			* 64 p.p.m/K		* equation (6.2)

As can be seen, there is a good agreement between the deflections predicted by the model and the deflections measured in air. The mechanical model that considers a constant value of the CTE (= 64 ppm/K) over the whole range of actuation works well at low temperatures but starts to diverge slightly at temperatures (T_h = 55 K i.e. T_h = 75 °C) close to the glass transition temperature (~95 °C). If a linear variation of the CTE when T_{hot} > 75 °C (equation 6.3) is considered, the predictions of the model seem to match the non-linear trend of the measured deflections for the whole range of actuation.

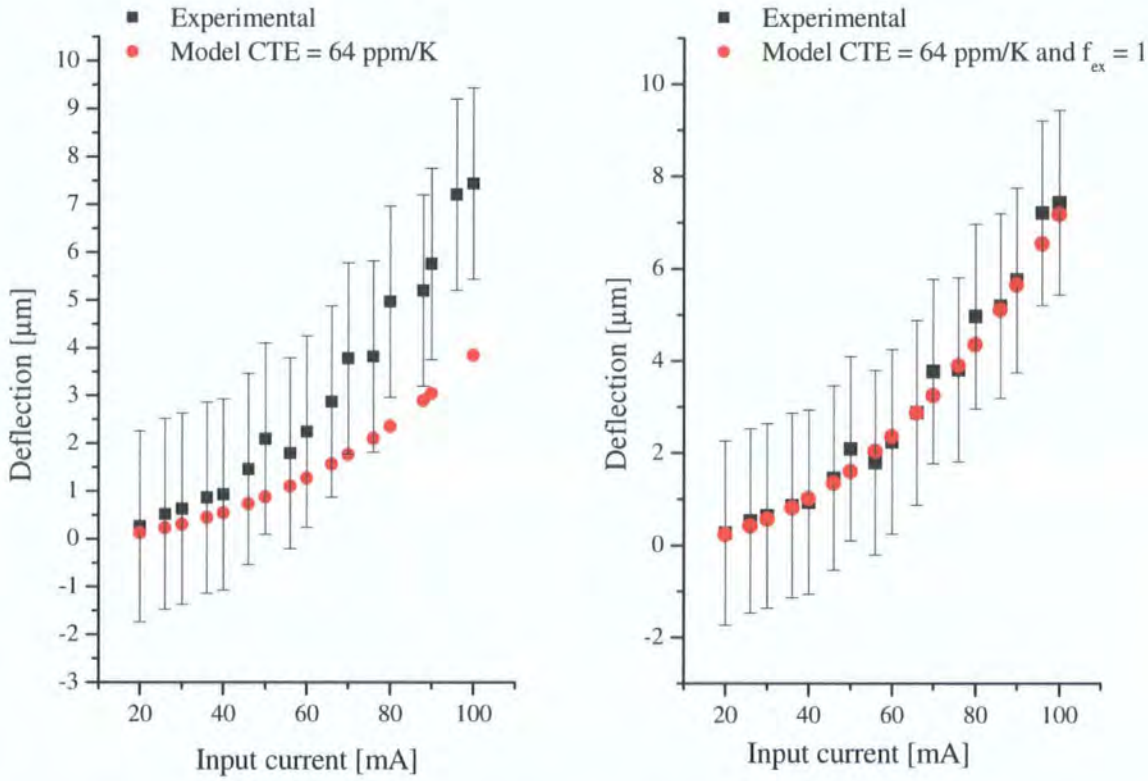

Fig. 6.26: Current versus deflection for design 3: experimental and modelling (CTE = 64 ppm /K) results for the device fully submerged in water.

Fig. 6.26 (left) shows the deflections measured in water at different input currents compared with the deflections predicted by the analytical models. The geometrical factors used in the models are the same as in the case of air and are shown in Table 6.14 and Table 6.15. The outputs from the thermal and mechanical models are summarised in Table 6.17. As in the previous case, the model predicts reasonably well the deflections in water at low currents. At higher currents however, the predictions start to diverge slightly compared to the measured deflections.

Table 6.17: Summary of the outputs of the analytical models used in Fig. 6.26 (Left) model with constant CTE and f_{ex} = 2.18 and 2.41 (right) model with constant CTE and f_{ex} = 1.

Electrothermal model			Thermomechanical
Current [mA]	T_{hot} [K]	ΔT [K]	Deflection CTE =constant* [μm]
20	1.11	0.44	0.13
26	1.89	0.75	0.23
30	2.52	1.00	0.31
36	3.64	1.45	0.45
40	4.51	1.80	0.55
46	6.01	2.39	0.74
50	7.13	2.84	0.88
56	9.00	3.59	1.11
60	10.39	4.14	1.28
66	12.68	5.05	1.57
70	14.35	5.72	1.77
76	17.09	6.81	2.11
80	19.08	7.60	2.36
88	23.44	9.34	2.90
90	24.65	9.82	3.05
100	31.12	12.40	3.85

* 64 p.p.m/K

Electrothermal model			Thermomechanical
Current [mA]	T_{hot} [K]	ΔT [K]	Deflection CTE =constant* and f_{ex} = 1 [μm]
20	1.33	0.81	0.24
26	2.25	1.37	0.43
30	3.01	1.83	0.57
36	4.36	2.65	0.82
40	5.40	3.28	1.02
46	7.19	4.37	1.35
50	8.54	5.19	1.61
56	10.80	6.57	2.04
60	12.48	7.59	2.36
66	15.27	9.29	2.88
70	17.29	10.51	3.26
76	20.63	12.55	3.90
80	23.07	14.03	4.36
86	27.03	16.44	5.11
90	29.92	18.19	5.65
100	37.99	23.10	7.18

* 64 p.p.m/K

In the case of water, the heat losses to the environment are increased considerably and the temperatures of the hot arm are expected to be well bellow the T_g for the range of currents applied. For this reason, it does not seem appropriate to associate the deviation of both set of results to the variation of the *CTE* with temperature. A plausible explanation for the deviation could be the reduction in the thermal coupling between the hot and cold arm due for example to the takeover of natural convection between the arms of the actuators. ΔT in the model is mainly controlled by f_{ex} and the thermal conductivity of the surrounding media. A few simulations have been performed which modify that parameter until convergence between experiments and models has been achieved (Fig. 6.26 (right)). These results indicated that the coupling between the arms in water could be approximately half the value in air.

An interesting consequence of the diminished coupling between the arms in water is that slightly less absolute hot arm temperature is necessary to obtain the same deflection than in air (Fig. 6.27 (left)). This is at the expense of more power consumption (Fig. 6.27 (right)).

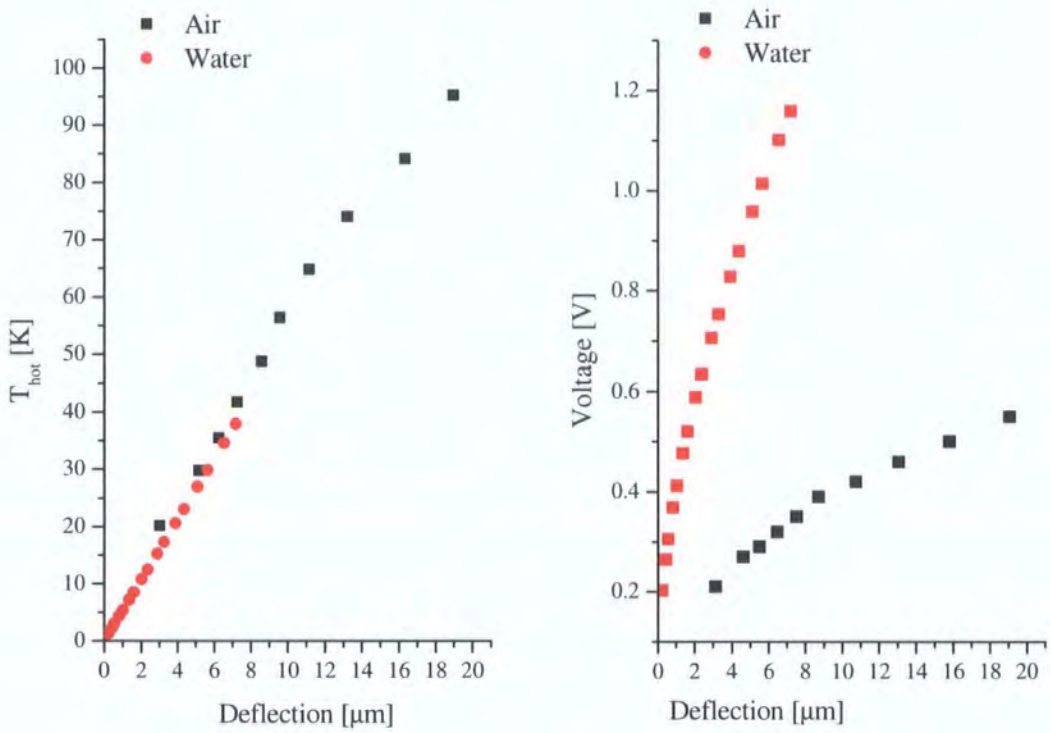

Fig. 6.27: T_{hot} versus deflection and voltage versus deflection in air and liquid environments.

To conclude the validation of the model and the modelling technique, a final verification of the assumptions can be carried out to compare the experimental results between design 2_(100) and design 3. Both have identical overall geometries of the actuators but different configurations (Fig. 6.28). In addition both microgrippers have been fabricated in the same batch and so the value of the material properties can be expected to be fairly similar.

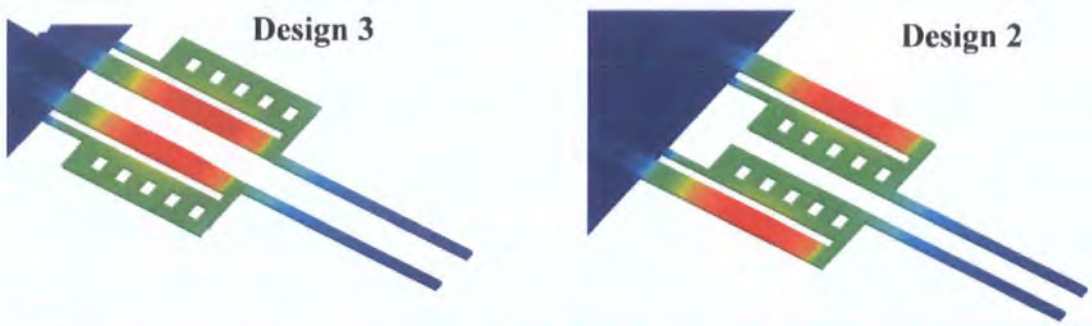

Fig. 6.28: Configuration of design 3 versus design 2

Based on the explanations given so far, what would be expected is that design 3 deflects more for the same input current. If we assume that the heat exchange between the arms

is identical in both cases, then it is expected that for the same input power, the temperatures in the hot arm of design 3 will be higher than in design 2 due to the lower heat losses. This in turn should lead to higher ΔT, and therefore higher deflections due to the linear relationship between the temperature in the hot arm and ΔT These results are summarised in Fig. 6.29. As can be seen the experimental results (current versus deflection (Fig. 6.29)), show a higher deflection of design 3 versus design 2_(100), which is consistent with the theory.

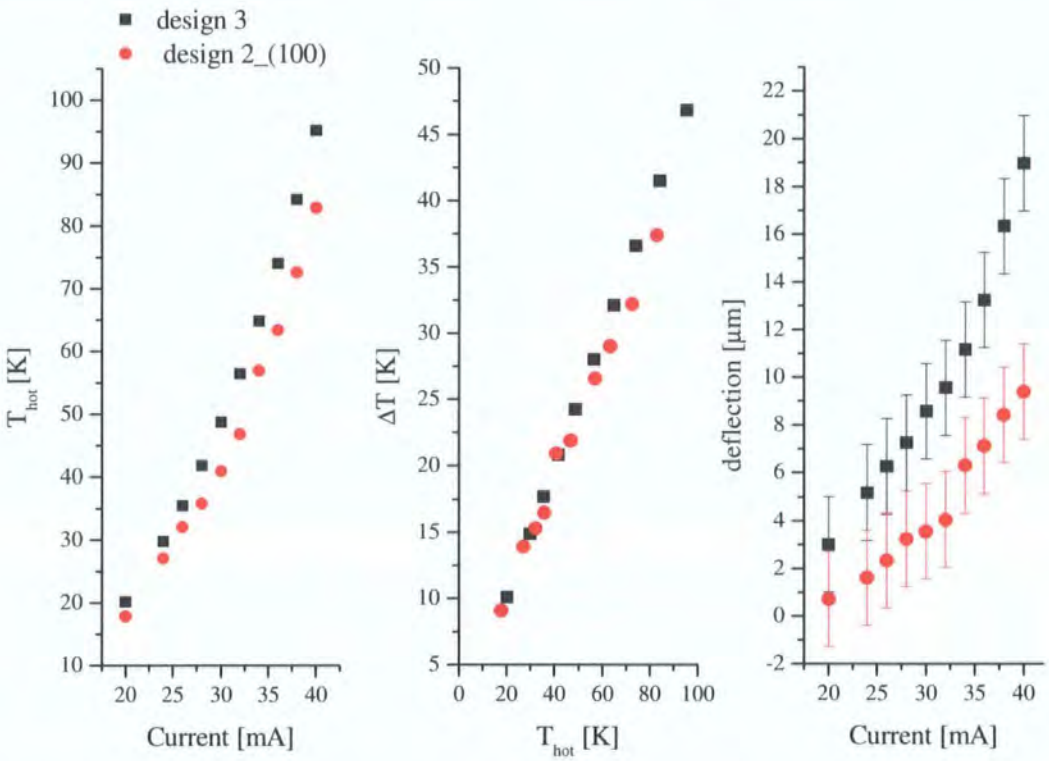

Fig. 6.29: Modelling and experimental comparison between design 3 and design 2_(100).

6.4. Simulation based predictions and optimisation

The good agreement between the experiments and the analytical models has permitted the construction of a "virtual microgripper" over which to perform fast and reliable simulations. As shown previously, these simulations not only enable the interpretation of sometimes limited experimental data, but also enable the exploration of the entire parameter space that influences the performance of the microgripper and therefore its optimisation.

In this section, the virtual prototype tool will be used to assess how different geometrical aspects affect and can improve the performance of a microgripper for a given input voltage and induced temperature. For this kind of study, virtual prototyping is an essential element of the optimisation process.

Three different devices — design 1, design 3, and standard (Fig. 6.30) — in two different scales — meso- and micro- — are used in the simulations. The particular geometries are shown in Table 6.18 and Table 6.19. In all of the simulations it is considered that the anchors are thermally grounded.

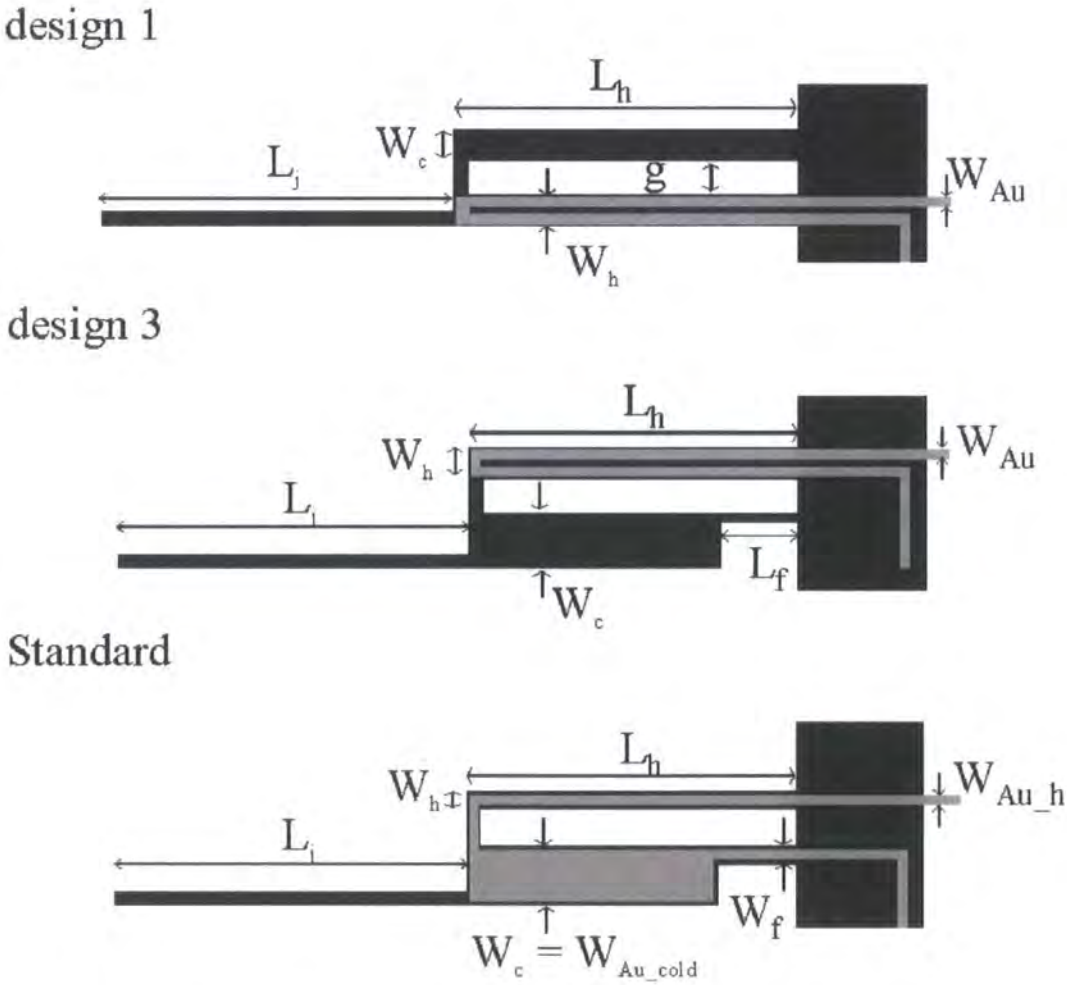

Fig. 6.30: Sketch of the devices to be simulated

Table 6.18: Characteristic dimensions of the mesoscale devices (gap = 60 μm) used in the simulations.

[μm]	w_h	w_c	w_f	L_h	L_c	L_f	L_j	w_{Au}
design 1	140	140	-	1500	1500	-	1600	70
design 3	140	250	80	1500	1140	360	1600	70
standard	140	250	80	1500	1140	360	1600	140

(*) out-of-plane thickness 100 μm

(**) out-of-plane thickness Au = 0.289 μm

Table 6.19: Characteristic dimensions of microscale devices (gap = 11 μm) used in the simulations.

[μm]	w_h	w_c	w_f	L_h	L_c	L_f	L_j	w_{Au}
design 1	7	7	-	200	200	-	450	3.5
design 3	7	22	7	200	140	60	450	3.5
standard	7	22	7	200	140	60	450	6

(*) out-of-plane thickness SU8 = 20 μm

(**) out-of-plane thickness Au = 0.289 μm

6.4.1. Buckling instability and critical temperature

When the characteristic dimensions of thermal actuators are being decided two constraints have to be considered:

1. The critical temperature that the hot arm can resist before thermal failure and melting, $T_{critical}$ *(= 160 K above ambient).*
2. The buckling instability of the hot arm which depends on the geometry of the beam, the CTE of the material, and ΔT.

The critical temperature that the hot arm temperature can resist is given by the characteristics of the structural material. In this work, it has been verified that the critical temperature is not the melting temperature of the SU8 which will be around 250 °C, but the temperature at which the embedded resistor fails, probably due to excess stresses and temperature. In this analysis the absolute critical temperature in the hot arm has been considered to be 180 °C (or equivalently a temperature of 160 K above ambient).

The hot arm is made long and slender to allow for a greater expansion and deflection; however this shape is very susceptible to buckling. Any thermal load experienced by the hot arm above the critical load would most certainly cause its buckling and the failure of

the system. Therefore, apart from the critical temperature, the conditions at which buckling occurs (critical load) at different temperatures also become an inherent constraint of the design.

The critical load for the hot arm is given by [291]

$$F_{critical} = \frac{4\pi^2 E(tw^3/12)}{L^2} \tag{6.13}$$

where E is the Young's modulus, L is the total length, and t and w are the thickness and width of the hot arm respectively.

At the same time, the net thermal load experienced by the hot arm is given by

$$Load_{thermal} = CTE\ \Delta T\ Ewt \tag{6.14}$$

The condition to avoid buckling in any of the arms would be $\mathbf{Load_{thermal} \leq F_{critical}}$ or equivalently,

$$CTE\ \Delta T_{buckling} = \frac{\pi^2 w^2}{3L^2} \tag{6.15}$$

where $\Delta T_{buckling}$ is the maximum temperature difference between the arms of the actuator that the system will be able to sustain.

In this chapter, the results of the simulations will systematically include an indication of the critical load and critical temperature of the actuators.

6.4.2. Design 1 and design 3 versus a standard thermal actuator

6.4.2.1. Equal geometry at the mesoscale

Using the prototype tool developed earlier, one can now compare one of the actuators developed in this thesis, e.g. design 3 (Fig. 6.29), with a standard U-shaped thermal actuator with the same overall dimensions (Fig. 6.29). The deflection results will be presented versus input power, voltage and induced average temperature in the hot arm.

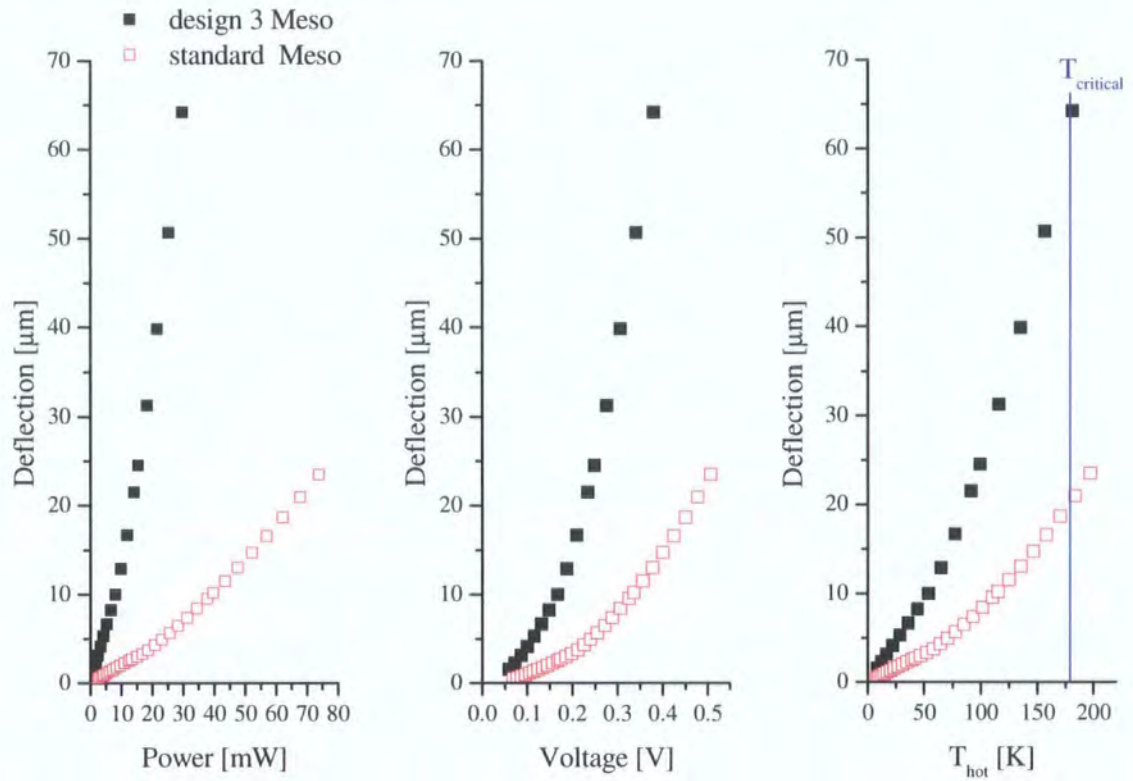

Fig 6.31: Performance comparison between design 3 and standard (Mesoscale)

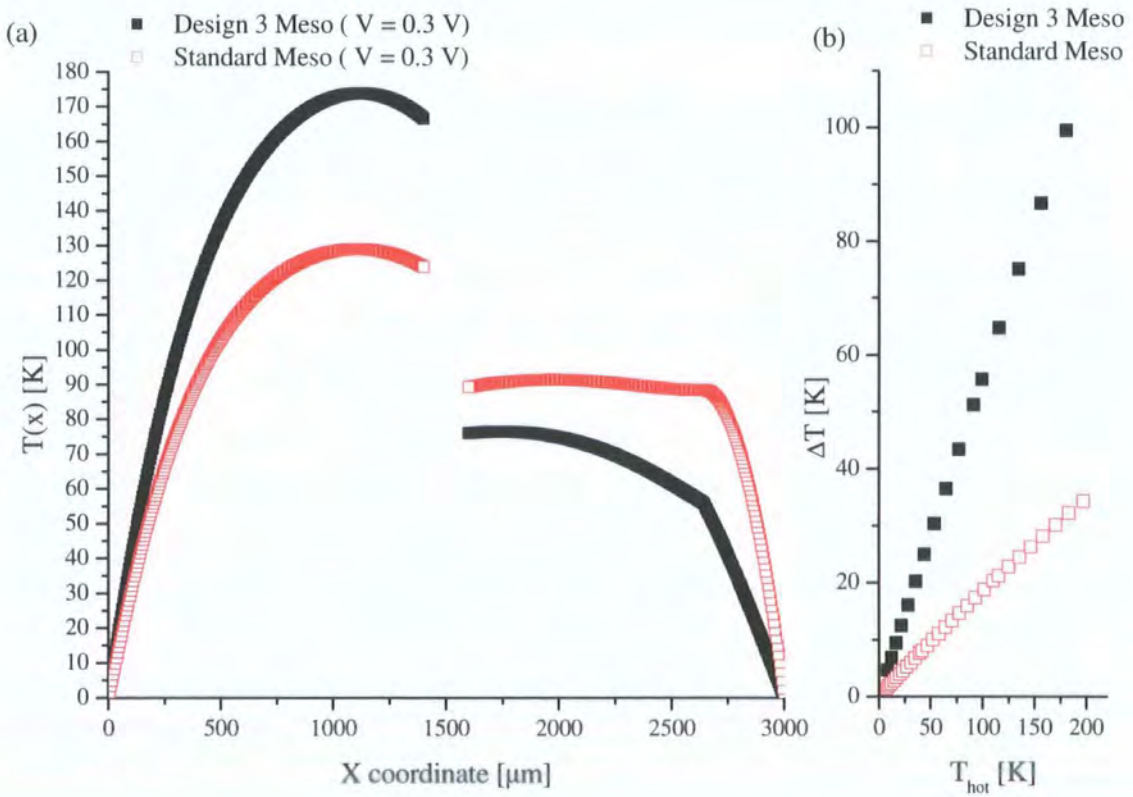

Fig. 6.32: Mesoscale design 3 versus standard (a) Temperature profiles at V = 0.3 V (b) T_{hot} versus ΔT.

As can be seen from the Fig. 6.32, design 3 performs better than an equivalent standard thermal actuator. For an input voltage of 0.3 V, design 3 produces a deflection of 39.8 μm versus a deflection of 8.3 μm produced by the standard actuator. In addition this is done at a lower power. The overall average temperatures of design 3 actuator are higher for the same input voltage (see Fig. 6.33), but still design 3, which only contains the resistor in the hot arm, is more thermally efficient[13] than the standard thermal actuator. For the same hot arm temperature, it is able to produce a larger ΔT and therefore a larger deflection for the same geometry (Fig. 6.33). E.g. for a temperature in the hot arm of approximately 100 K design 3 actuator generates a ΔT = 55.6 K whilst the standard actuator only achieves a ΔT = 18.8 K. The fact that the temperatures in design 3 are higher than the overall temperatures in the standard actuator are not a problem as long as the temperature of the hot arm remains below the critical temperature (= 160 K above ambient). For the geometries of the actuators the $\Delta T_{buckling}$ would be approximately 450 K, well above the range of temperature used and it is not a limiting factor.

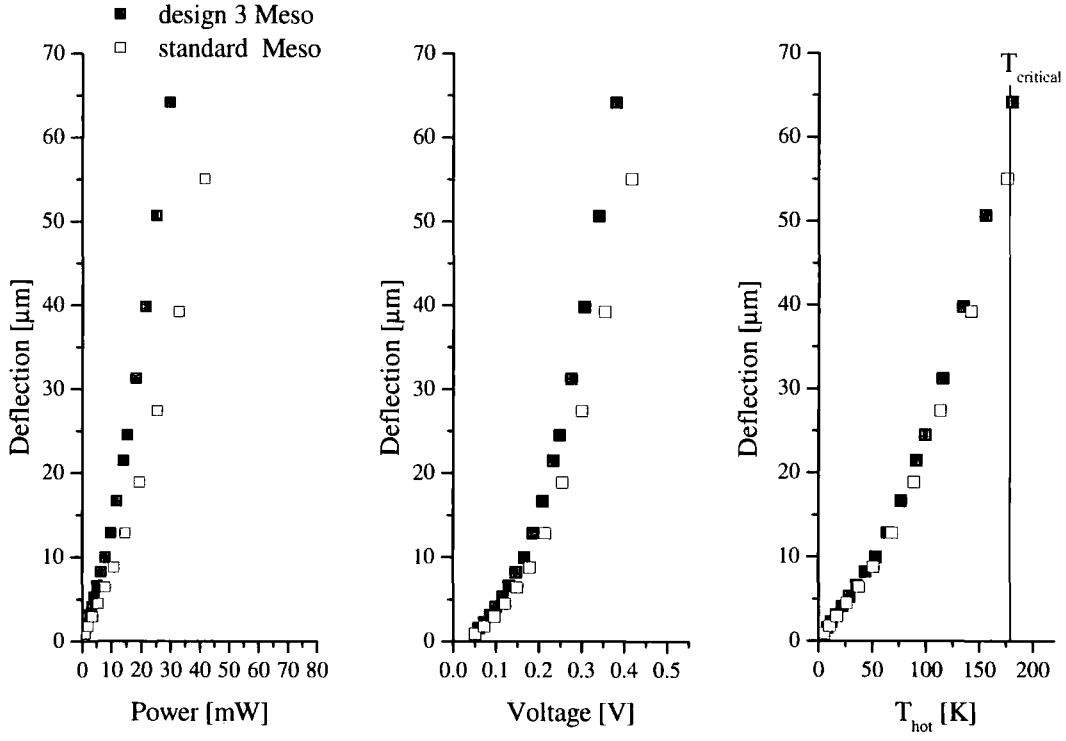

Fig. 6.33: Mesoscale comparison between design 3 and the standard thermal actuator with a reduced hot arm width (W_{hot} = 80 μm) (Left) Voltage versus deflection (Middle) Voltage versus ΔT (right) ΔT versus T_{hot}. ($\Delta T_{buckling}$ = 447 K)

[13] See section 5.5.2.

It could be argued that the need of having two resistors embedded in the hot arm could limit the deflection of design 3 due to the requirement of a wider hot arm. However, as demonstrated in Fig. 6.33, even if the width of the standard actuator is reduced by a factor of two compared to that of design 3, the better performance of design 3 is still maintained.

In addition, when working with standard microfabrication and with a polymeric material such as SU8, the limits of how narrow the SU8 beams can be fabricated is reached well before the limit of the narrowest resistor line is reached, so it is always possible to include two resistors instead of one.

6.4.2.2. Equal geometry at the microscale

The same comparison of results between design 3 and standard can be performed at the microscale (dimension in Table 6.19). The parameters used in the simulations are shown in Table 6.20.

Table 6.20: Heat transfer geometrical factors used in the simulations

Beam	f_i geometrical factor	f_{ij} geometrical exchange factor
Hot Arm to Ambient[1]	0.65	-
Flexure to Ambient	0.61	-
Flexure to Hot Arm (exchange)	-	2.14
Hot Arm to Ambient[2]	0.48	-
Cold Arm to Ambient	0.90	-
Cold Arm to Hot Arm (exchange)	-	2.30

[1]In section 1 (hot facing felxure)

[2]In section 2 (hot facing cold)

As can be seen from Fig. 6.34, design 3 at the microscale also appears to be more thermally and electrically efficient than an equivalent microscale standard actuator. For an input voltage of 0.18 V design 3 produces a deflection of 5.63 μm versus a deflection of 3.98 μm produced by the standard actuator. In addition this is done at a lower power. At the microscale, it is the standard actuator which has overall higher temperatures and therefore, even if buckling might occur at a slightly higher voltage (critical buckling at 0.2 V in standard versus critical buckling at 0.18 V in design 3), its performance is worse than design 3 at the same scale.

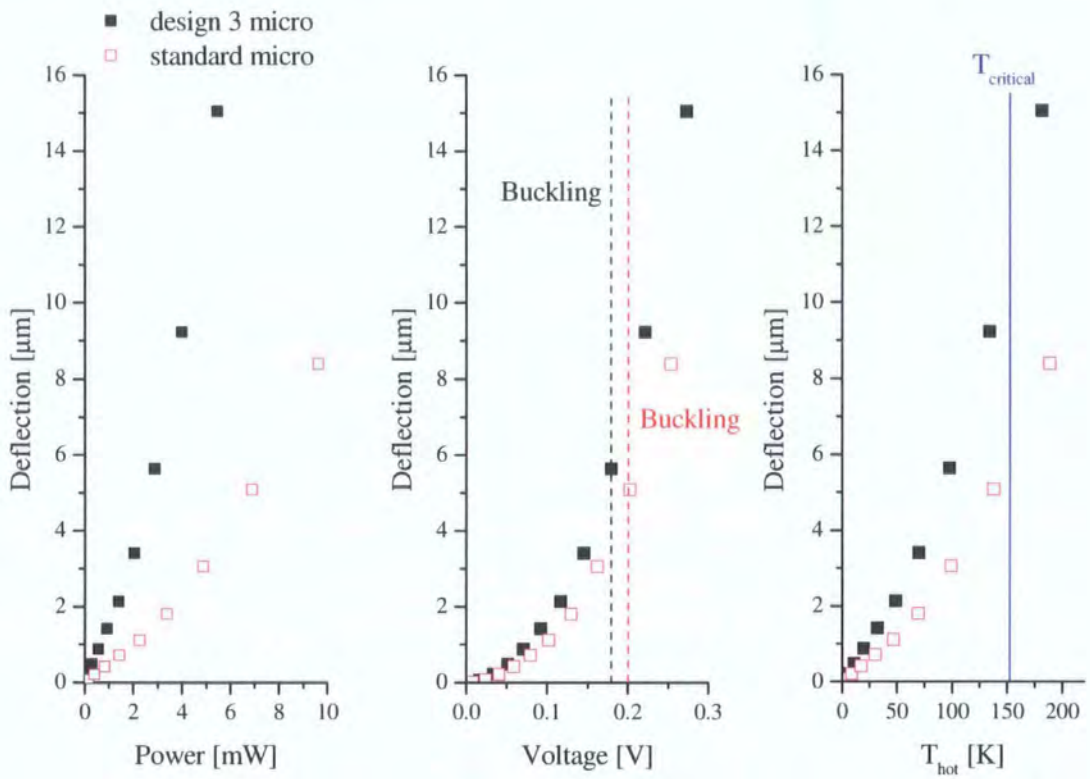

Fig. 6.34: Microscale comparison between design 3 and the standard thermal actuator (Left) Voltage versus deflection (Middle) Voltage versus ΔT (right) T_{hot} versus ΔT.

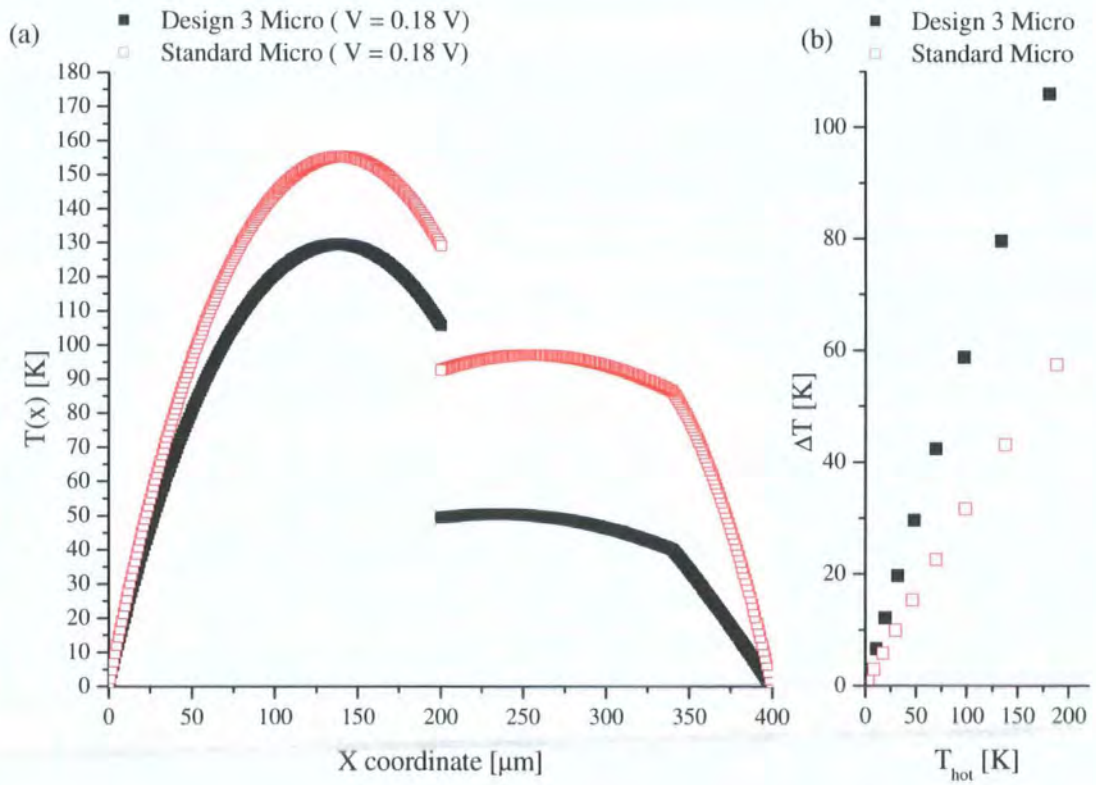

Fig. 6.35: Microscale design 3 versus standard (a) Temperature profiles at V = 0.18 V (b) T_{hot} versus ΔT.

6.4.2.3. Discussion

If we now compare the performance between the meso and micro devices (Fig. 6.35) it can be seen that, for this kind of thermal actuator and this application, reducing the scale of the device does not translate into a better performance measured in absolute terms[14]. Fig. 6.36 compares the power, voltage and temperature requirements at both scales. A general benefit associated with working at larger scales is that the condition of buckling does not limit the actuation of the device, because the device reaches the critical temperature before buckling can occur. As can be seen, design 3 at the mesoscale is the design that provides the best performance. If we compared the results at the limit of the buckling of design 3 micro (V = 0.18 V), it can be seen that design 3 with mesoscale dimensions provides at least twice the deflection of the other models and, equally important, that it does so at a lower temperature in the hot arm (T_{hot} = 64 K). At low deflections it requires a slightly larger amount of energy than design 3 micro but, overall, it is the best performing design.

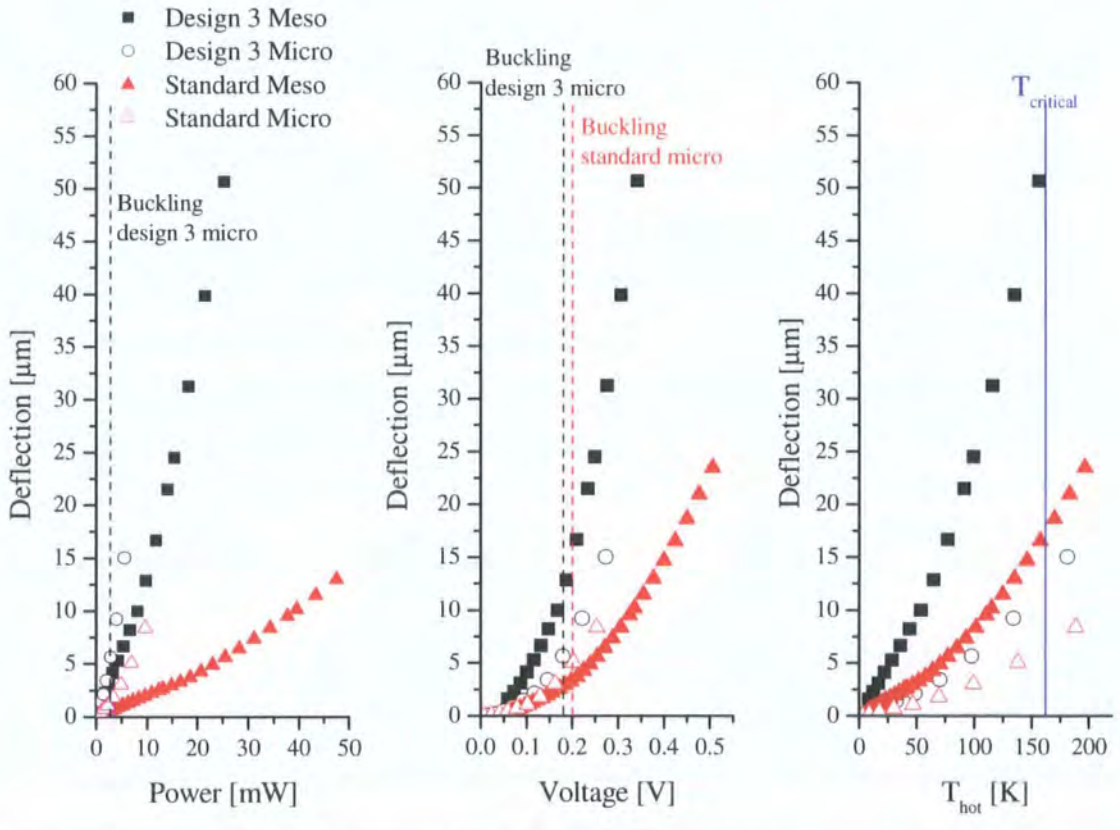

Fig. 6.36: Power, voltage and T_{hot} versus deflection at two different scales.

[14] This discussion is based in absolute deflection and not d_N as defined in section 5.5.1.

6.4.3. Design 1 versus design 3

One of the reasons for design 1 (composed of two identical beams) was to maximise the volume/area of the cold arm in which to integrate complementary active elements such as force sensors or optical waveguides. However it would be interesting to see how this simplified geometry (design 1) compares with the typical flexure/cold arm actuator (design 3).

From Fig.6.37 it can be seen that design 3 with a flexure length of 360 μm will provide higher deflections at the same voltage. Thus, for a voltage of 0.3 V and an T_{hot} = 135 K design 3 produces a deflection of approximately 40 μm, whilst at the same temperature and voltage design 1 will only deflects approximately 33 μm.

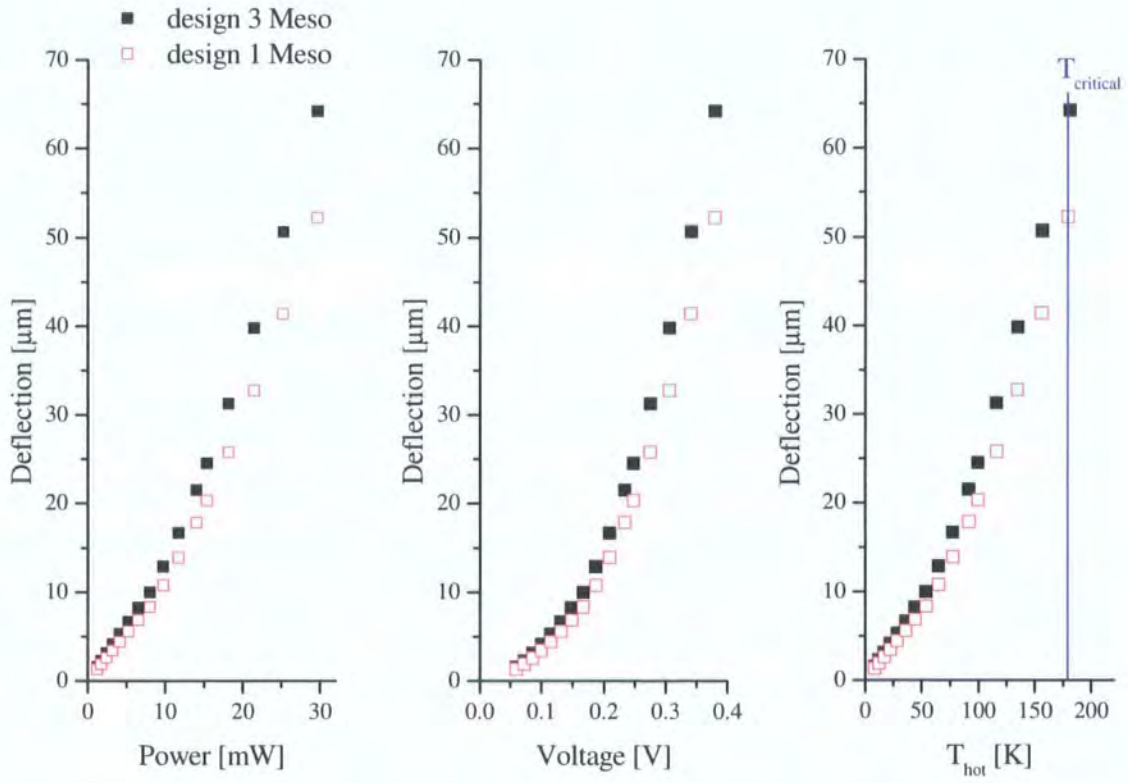

Fig. 6.37: Mesoscale comparison between design 1 and design 3 with a flexure length of 360 μm and a hot arm width of 140 μm (Left) Voltage versus deflection (Middle) Voltage versus ΔT (right) Deflection versus T_{hot}.

Intuitively it could be thought that a reduction of the width of the cold arm of design 1 will improve the deflection. However, as is shown in Fig.6.38, a reduction of this width also increases its temperature, reducing the overall ΔT and therefore the deflection.

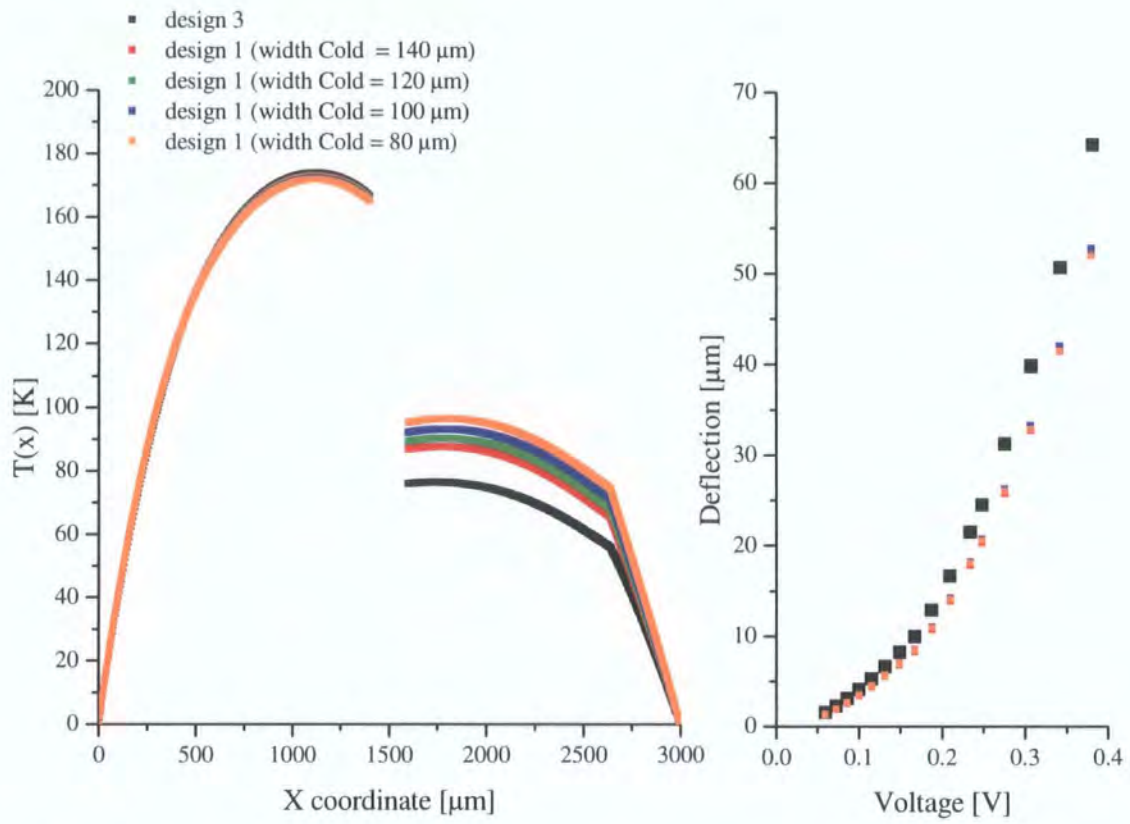

Fig. 6.38: Comparison between design 3 and design 1 at different widths of the cold arm. (Left) T distribution at a voltage V = 0.3 V. (Right) Deflection versus voltage.

6.4.4. Size of the gap

Another parameter of interest is the size of the gap and how it affects the temperature along the arms of the actuators and the deflection. As can be seen from Fig. 6.39 and Fig. 6.40 incrementing the size of the gap increases the deflection for a given input voltage until a limit is reached at a gap size of approximately 140 μm. For gap sizes above 140 μm, the higher ΔT induced between the arms does not contribute to an equivalent increase of the deflection. For an input voltage of 0.2 V the model with a gap of 140 μm will produce a deflection of 18 μm, whilst the model with the smallest gap will produce a deflection of 10 μm. These will be done however at the expense of a higher temperature in the hot arm, i.e. 83 K (gap =140 μm) versus 67 K (gap =30 μm).

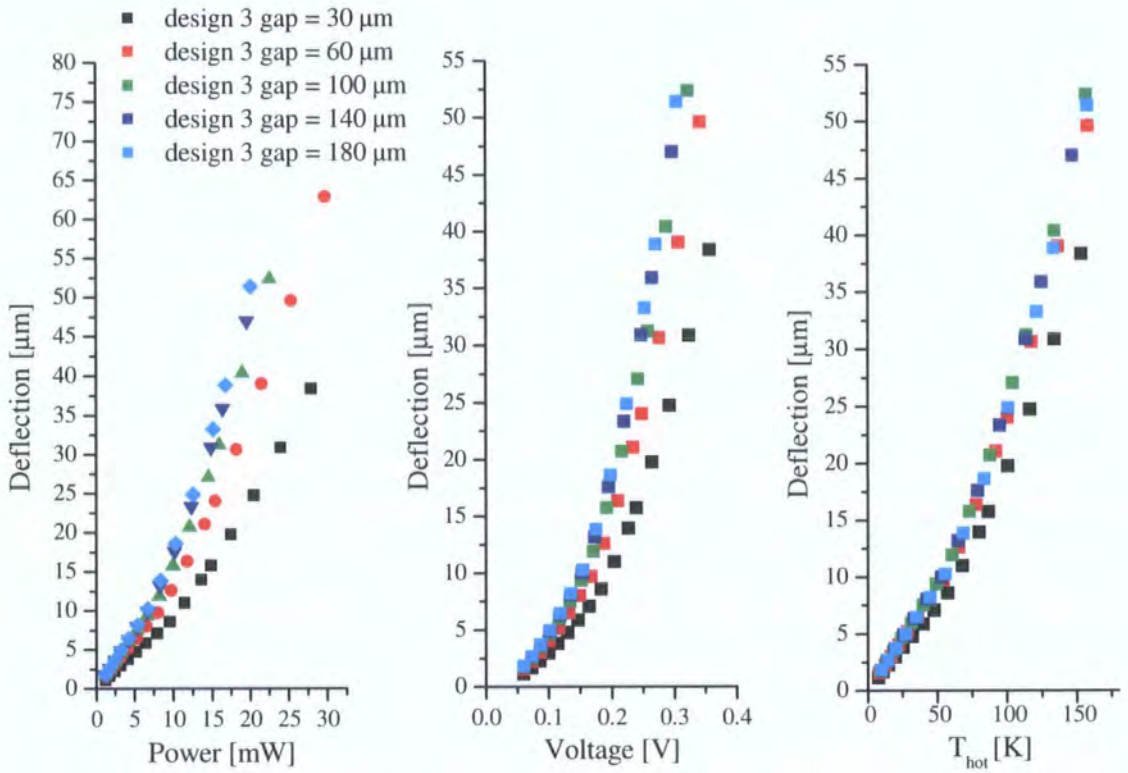

Fig. 6.39: Comparison between designs 3 with different gap sizes. (Left) Voltage versus deflection (Middle) Voltage versus ΔT (right) Deflection versus T_{hot}.

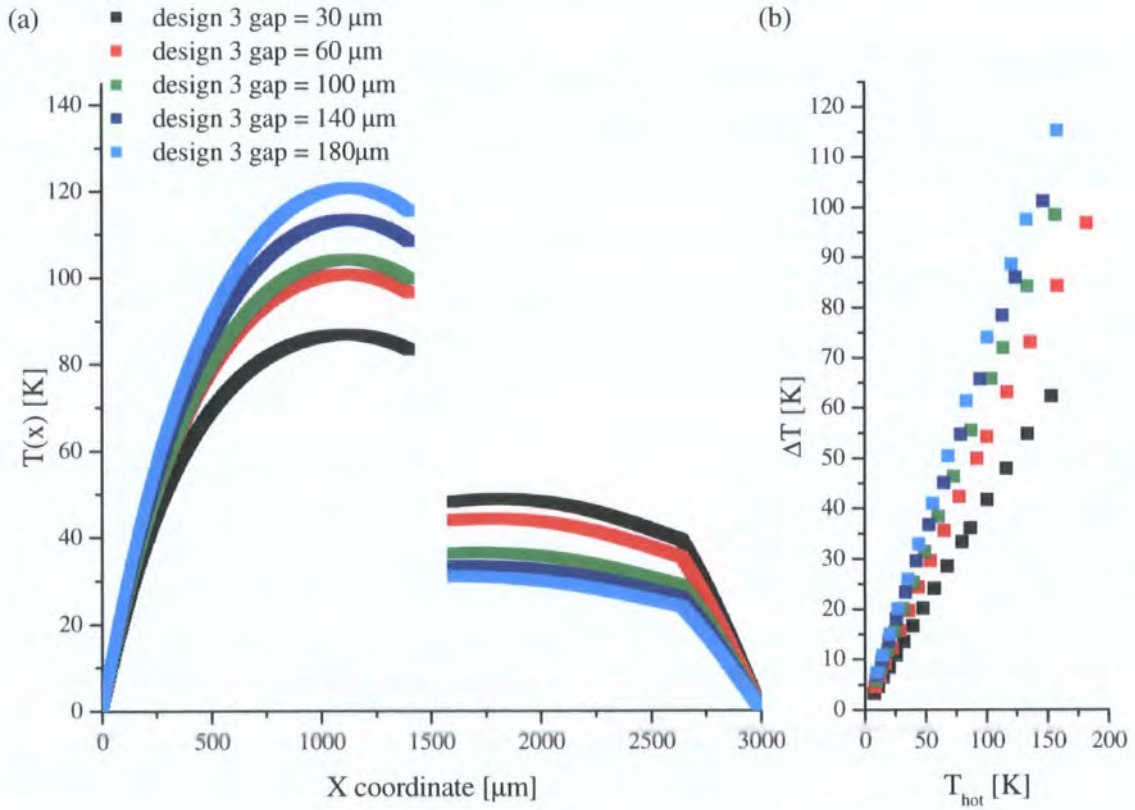

Fig. 6.40: Design 3 for different gap sizes (a) Temperature profiles at V = 0.20 V (b) T_{hot} versus ΔT.

Finally, it is worth investigating what would happen if the size of the gap is large enough to prevent the heat exchange between the arms, i.e. a simulation in which $f_{ij} = 0$. Fig. 6.41 and Fig. 6.42 show the comparison between the performances of design 3 when gap = 140 μm and design 3 when gap = 300 μm and $f_{ij} = 0$.

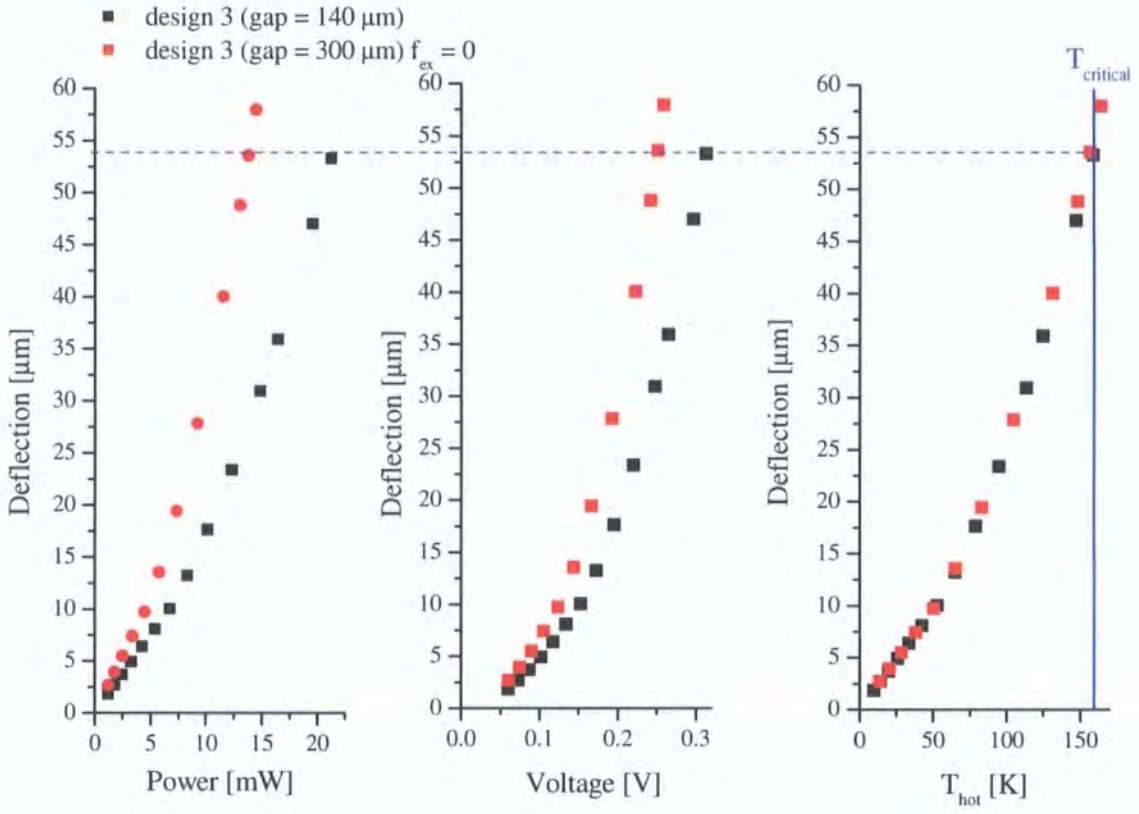

Fig. 6.41: Comparison between designs 3 with a gap of 140 μm and a gap of 300 μm assuming that there is not heat exchange between the arms. . (Left) Voltage versus deflection (Middle) Voltage versus ΔT (right) Deflection versus T_{hot}.

As can be seen, the maximum deflection that can be achieved with both systems, 53.5 μm, is limited by the maximum temperature that the hot arm can sustain. If the results are compared in terms of voltage the design with a 300 μm gap which should be large enough to prevent heat exchange between the arms performs better in producing the highest deflection, only requiring a voltage of 0.25 V compared to 0.31 V in the other model. However, if the parameter of interest is the temperature of the hot arm then both models have the same performance. From these results it can be concluded that, if there is no heat exchange, a gap of approximately 300 μm would be the gap that would produce the maximum deflection at minimum voltage. The benefits of a larger gap (>60

μm) for this length scale of actuators are increased in water as reduced thermal coupling between the arms is expected (section 6.3.1), i.e. where $f_{ij\_water} < f_{ij\_air}$.

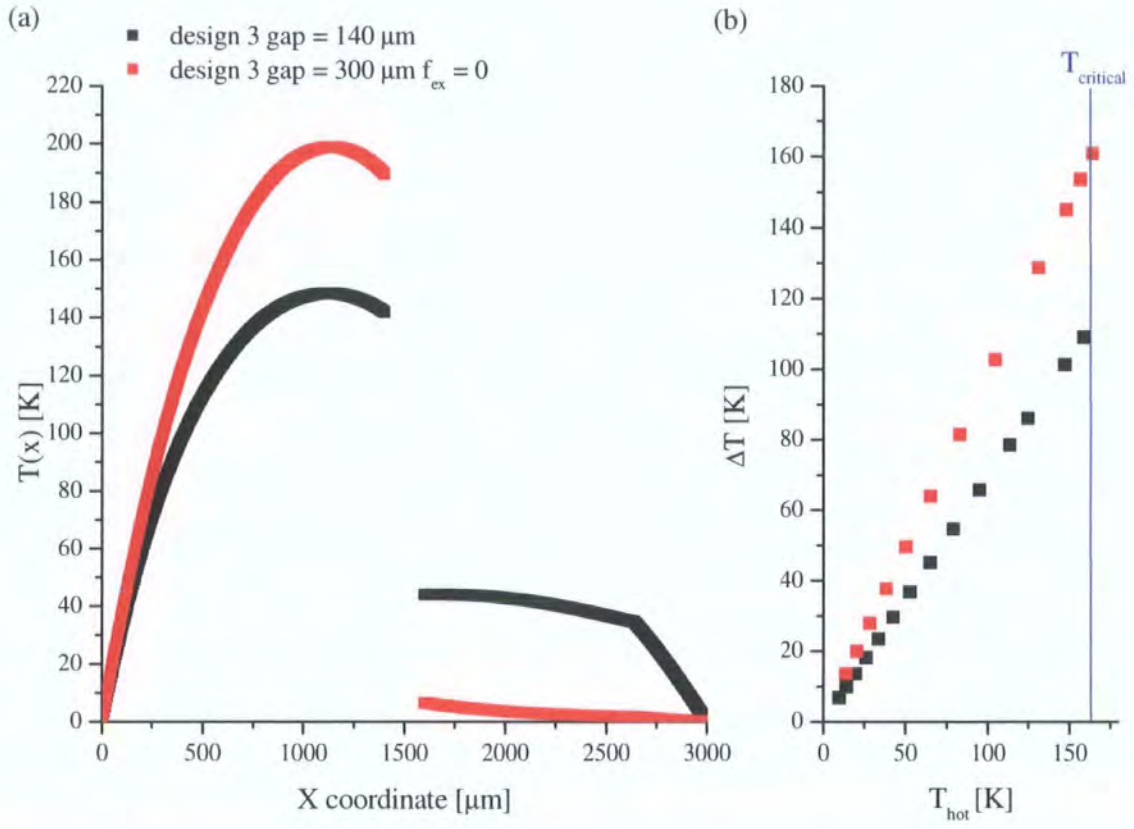

Fig. 6.42: Design 3 for different gap sizes: 140 μm and 300 μm (assuming that there is no heat exchange between the arms i.e. $f_{ex} = 0$ (a) Temperature profiles at V = 0.24 V (b) T_{hot} versus ΔT.

6.5. Design guidelines

Different design guidelines can be extracted from the simulations and used for future design optimisation processes. For the same total length:

- Design 3 (or equivalently design 2) and design 1, actuators that embed the resistor only in the hot arm, perform better than a standard actuator with equivalent dimensions, at both the meso- and microscale.
- Design 3 and standard with dimensions in the mesoscale perform better than design 3 and standard with dimensions in the microscale, measured in absolute deflection terms.
- Design 3, with a cold/flexure arm configuration, performs better than design 1 with two identical arms.

- That the cold arm of design 1 has to be at least the size of the hot arm if lower temperatures are required for the same deflection.
- That there is an optimal gap size for the geometry of design 3 which is between 140 and 300 μm that provides the best deflection per input power.

6.6. Summary

In this chapter the two analytical models — electrothermal and thermomechanical — developed in Chapter 4 have been validated against experimental data obtained in air as well as in liquid environments.

It has been concluded that:

- The electrothermal model defined in Chapter 4 accurately describes the temperatures developed along the arms of the actuators of the microgripper when
    - The internal beams of the microgrippers lose heat to the environment by conduction only.
    - The external beams of the microgripper lose heat to the environment by conduction and convection (mass transfer) (see scenario 2).
    - A heat exchange between the arms is considered. This heat exchange will be governed by the geometrical factor f_{ij} (section 4.3.4.5) and the thermal conductivity of the media. When the media is water, it seems that the thermal coupling between the arms will be reduced and that f_{ij_water} could be considered half f_{ij_air}.
    - The dependency of the resistivity of the metallisation with temperature is included in the simulations in an iterative manner.
    - The dependency of the thermal conductivity of air with temperature is included in the simulations in an iterative manner.
    - The heat losses at the anchors are considered. If the insulation induced at the anchors is not known, a grounded thermal model (scenario 4) provides a reasonable good prediction of the temperature difference

between the arms. This is important as this is one of the main input parameters to the mechanical model.

- The thermomechanical model defined in Chapter 4, accurately describes the deflection provided by the different microgrippers at low temperatures, but requires the inclusion of the dependency of the *CTE* with T at temperatures around the glass transition temperature T_g.

    - The CTE would vary linearly with temperature.

This chapter also includes the used of the models to compare the performance of the design proposed in this thesis with the standard existing design of U-shaped thermal actuator. It has been demonstrated that

- Any of the actuators proposed in this thesis, containing the resistor only in the hot arm, would perform better than equivalent standard actuators.
- That downsizing the device from the mesoscale to the microscale, does not improve the performance of the system in absolute terms.
- That the gap of future actuators with the same overall length should be increased to at least a value of 140 μm to maximise the performance.

CHAPTER 7

Cell handling experiments

This chapter details the first manipulation experiments performed on live cells using the microgripper technology. The ultimate aim of this work was to use the microgrippers for the manipulation of live cells. The large range of displacements provided by the microgrippers make them ideal for the manipulation of large, as well as small, cells. Two areas of biology and medicine where this is necessary are In-Vitro Fertilisation (IVF) and Stem Cell Research.

7.1. Cell handling experiments

Contacts have been established with Dr. Herbert (Scientific director and senior embryologist) and her team in the Newcastle Fertility Centre [313]. It has been verified that in those areas the biggest cell of the human body, i.e. the egg (oocyte), with a diameter between 130-160 μm, has often to be manipulated together with smaller cells and nuclei, so called donor cells, of diameters between 10 – 20 μm. The same is valid for research in stem cell areas where initial tests are often performed on mouse egg cells with diameters of approximately 100 μm.

The microgripper model (Fig. 7.1) used in this experiment operates in a bidirectional mode with a particular semicircular jaw design to confine the cell. The driver circuit

opens the arms and helps the operator to place the cell between the jaws of the microgripper. When the voltage is removed, the arms recover to their initial gap separation (~100 μm) and encapsulate the cell. The final force is applied on the cell with the secondary circuit that slightly closes the arms.

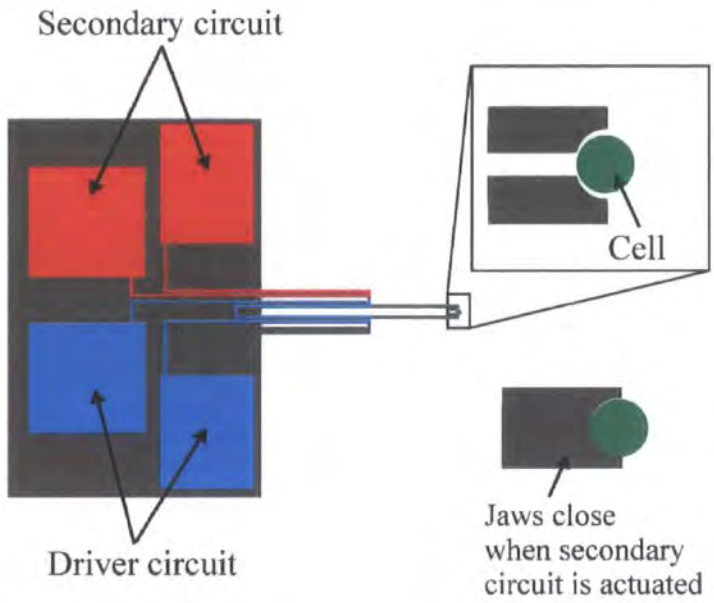

Fig. 7.1: Microgripper design using during the manipulation experiments.

The experiments were conducted in the Newcastle Fertility Centre [313] using mice oocytes (diameter = 100 μm) in a Petri dish culture. The manipulations were carried out on a Nikon Diaphot Eclipse TE300 equipped with Narishige MM0-202N micromanipulators and two holding pipettes with a 30 degree bend [314] (see Fig. 7.2).

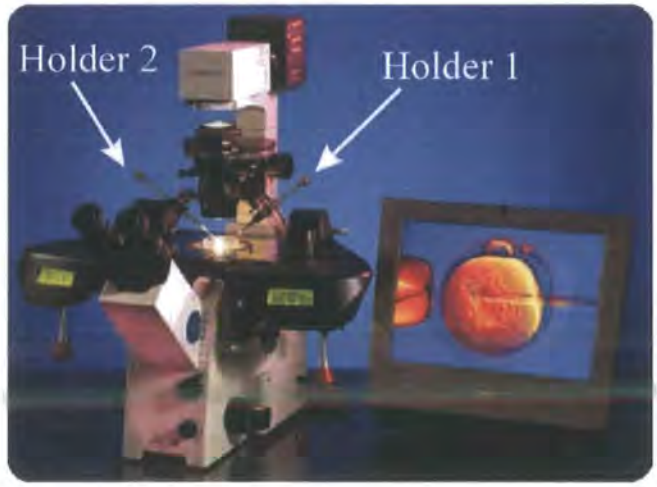

Fig. 7.2: Manipulation station used in the Newcastle Fertility Centre.

The oocytes[15] [315] were manipulated in a culture Petri dish containing microdrops of M2 supplemented with IBMX under mouse embryo tested filtered oil (Sigma). Images were acquired using a Nikon DS Fi-1 CCD camera with a 10x/0.25 NA objective and 0.75x relay lens. Fig. 7.3 shows schematically the experimental set-up.

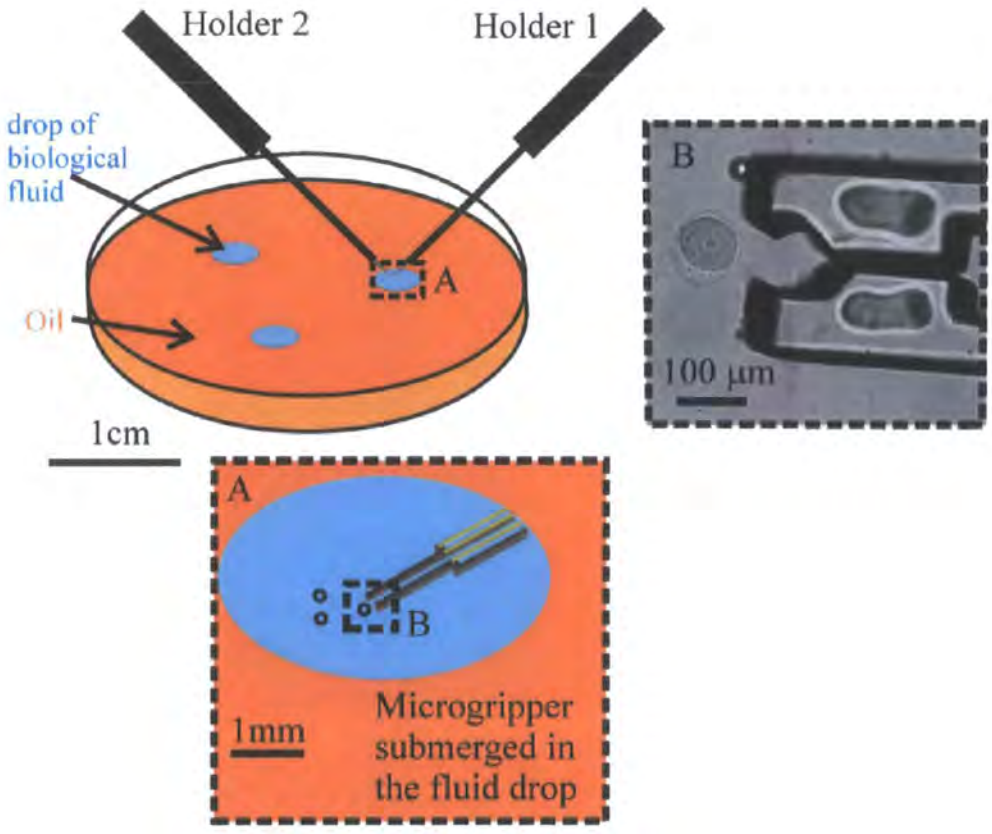

Fig. 7.3: Schematic experimental set-up. During manipulation the microgripper is submerged in the biological drop.

With this set-up the microgripper has been validated as a complementary and unique tool for the single-cell manipulation experiments that are normally carried out by biologists.

Fig. 7.4 shows the images captured during a manipulation experiment where a mouse egg cell is held using a standard glass pipette and a microgripper. The microgripper,

[15] For the manipulation we used 12-16 week old CD-1 mice from which ovaries were isolated 46-48hrs after treatment with 7.5-10 international units of pregnant mares serum gonadotrophin (PMSG). Germinal vesicle (GV) stage oocytes were retrieved from the ovaries by puncturing antral follicles with a fine needle in M2 medium (Sigma) supplemented with isobutylmethylxanthine (IBMX) from Sigma to prevent germinal vesicle breakdown (GVBD) [315].

attached to the holder 1 (see Fig. 7.2) and on the right of the image, is able to grasp and detach the mouse cell from the suction of the pipette in holder 2 on the left of the image. This demonstrates that the grip generated by this microgripper is enough for standard manipulation procedures, or at least the same that are produced by the pipettes.

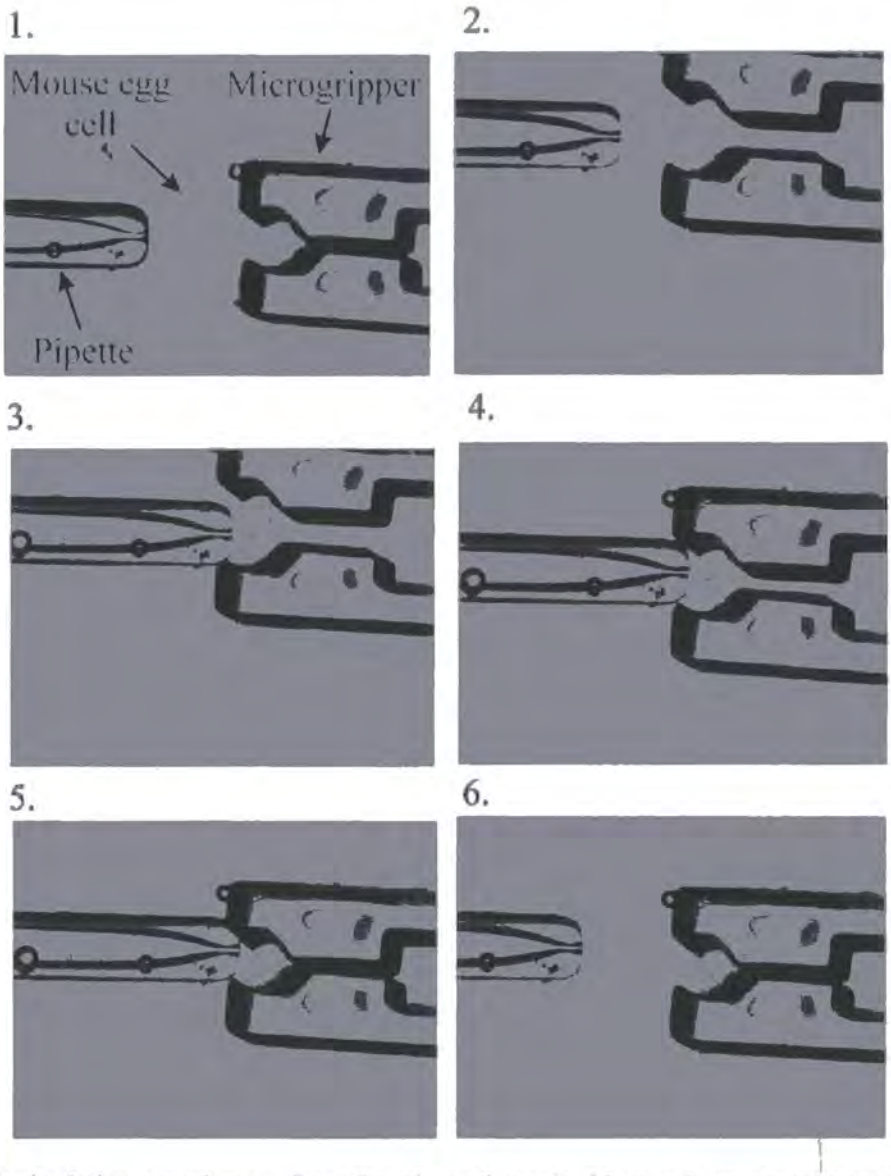

Fig. 7.4: Manipulation experiment where the microgripper is able to release a mouse egg cell (diameter of 100 μm approx.) from the pipette suction.

As can be seen in Fig. 7.5, with this technique the microgripper can hold the cell even if it is detached from the bottom of the Petri dish (see cells on the bottom which are out of focus in the image).

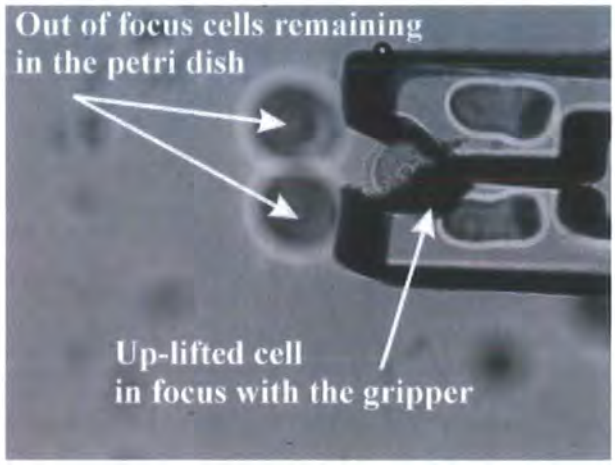

Fig. 7.5: Microgripper holding a cell approximately 1 mm above the bottom of the Petri dish.

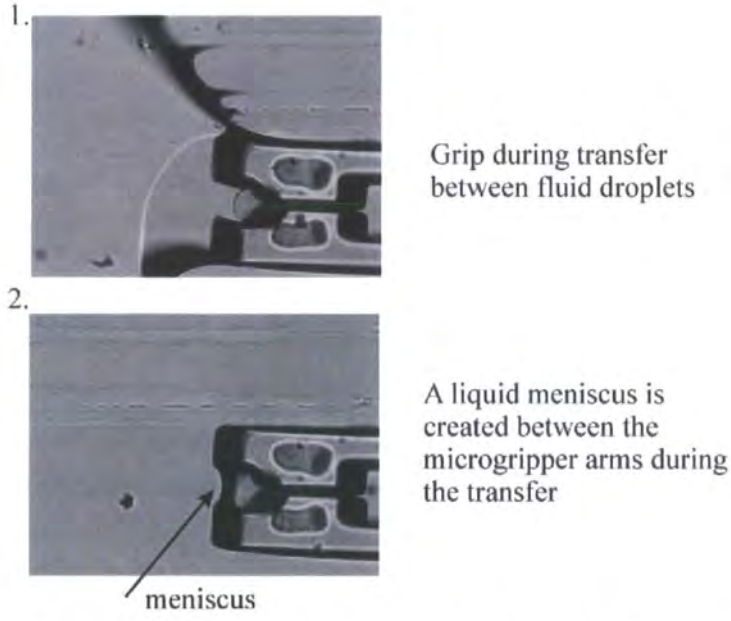

Fig. 7.6: Transfer of a cell from one biological drop to another through the oil media.

The gripping is also strong enough to be able to transport a cell from one drop of biological media to another through the oil media (Fig. 7.6). Standard pipettes lose the grip when leaving the first drop. This makes the microgripper a unique tool for this application.

The future of the microgripper lies in its effective exploitation in the biological arena.

CHAPTER 8

Conclusions and future work

This thesis has presented comprehensive coverage of the development of a polymeric micromachined gripper (microgripper) for the manipulation of biological cells and other microsized objects. The microgripper, which represents the first device of this type at Durham University, has been entirely designed, fabricated and tested in our cleanroom facilities. The device, designed in three different configurations (normally open mode, normally closed mode, and normally open/closed model) has been modelled using two coupled analytical models which have been custom developed for this application. All of the fabrication details have been designed to enable the microgrippers to be released successfully from the substrate and obtain practical prototype devices. Electrical, thermal and mechanical testing of the different designs has allowed the accurate characterisation of the microgrippers as a function of the applied voltage, the induced temperature and the output deflection. This has validated the microgrippers for use in biological environments where operation at low voltage and low temperature is required.

The key result of this thesis is the production of a set of working microgripper prototypes that can be used for the manipulation of biological specimens. As part of this, the following important results have been obtained:

- With the use of polymeric materials and a single heated arm design of a:

    - low voltage in-plane thermal actuator
    - low temperature in-plane thermal actuator
    - bidirectional in-plane thermal actuator

- Design guidelines to produce an efficient in-plane thermal actuator

- The development of cleanroom fabrication techniques for the release of polymer-metallic structures and membranes.

- The development of testing methods such as the use of IR thermography to measure the temperature of polymeric electrothermally heated structures.

- The development of an analytical electrothermal model and a modelling technique that:

    - takes into account the heat losses to the ambient by conduction and the heat exchanged between parts at different temperatures
    - adds a convection heat loss to the beams situated in the external part of the device
    - integrates the variation of the material properties with temperature in an iterative manner.

- The development of an analytical thermomechanical model and a modelling technique that takes into account the variation of the coefficient of thermal expansion of the structural material with temperature.

- 7 journal and conference papers, and a patent.

8.1. Conclusions

In recent years, as demonstrated in Chapter 2, research has been increasingly active in the area of microgrippers and more than 150 different designs have been proposed. However, only very few of them enable the manipulation of biological specimens in

liquid environments. This is mainly due to the restrictive operation conditions when manipulating biological samples at cellular level which demand low actuation voltages for unencapsulated devices (<2 V), low temperatures (<100 °C), and low handling forces (<nN - few μN).

Prior to the start of this work (mid 2004), three main designs of in-plane electrothermally actuated microgrippers had been published and launched to market. These are the HexSil[16] microgripper developed by C.G. Keller and R.T Howe [178] and commercialised by MEMS Precision Instruments [74], and the two microgripper models (BB and SM-BB) developed by T Huang, M. Ellis et al. [175, 176] and commercialised by Zyvex Corporation [79]. The three devices, produced in single crystal silicon or polysilicon, have demonstrated good gripping capabilities and the manipulation of various microsized objects. However they operate at voltages and/or forces and/or temperatures unsuitable for biological manipulation. Table 8.1 and Table 8.2 shows a compilation of the performance of in-plane electrothermal microgrippers published since the launch of the three models cited above.

Table 8.1: Performance of electrothermal microgrippers produced in Si, Poly-Si and metal materials.

Ref.	Year	Material	Actuator type	Model	Max displacement(*) [μm]	Voltage [V]	Current [mA]	Power [mW]	T [°C]	F [mN]
[178]	1997	Silicon	Linear		20	6	18	110	> 250	~ 25
[79]	2003	Silicon	U-shaped	BB	25	10	80	800	-	~ 550
[79]	2003	Silicon	V-shaped	SM-BB	6	6	10	60	-	~ 210
[125]	2004	Nickel	V-shaped	SM-BB	20	3.5	16	56	~ 120	–
[120]	2005	Nickel	Circular-shaped linear		16.3	1.9	840	1596	~ 575	–
[122]	2005	Gold	U-shaped		2	0.23	146	34	–	~ 25
[125]	2006	Nickel	Cascade V-shaped		16.3	1.25	160	200	~ 350	-
[128]	2007	Al + Poly-Si	Bimorph		3.5	-	-	6	~ 220	-
[195]	2007	Silicon	2-hot arm U-shaped		7	4.5	-	40	~ 200	-

(*) Opening/closing measured from initial rest position

Recent advances in the performance of in-plane electrothermal microgrippers have been achieved through the use of: optimised actuation structures (cascaded in-plane V-actuators [125], circular-shaped linear actuators [120], in-plane bimorphs [128], double hot arm U-actuators [195] or a combination of multiple actuators [309]); optimised

[16] HexSil is a microfabrication method of producing high-aspect-ratio parts that involves a combination of DRIE and surface micromachining techniques.

amplification mechanisms [121], and now implemented in some of the models provided by MEMS precision instruments; and finally the incorporation of materials other than silicon and polysilicon e.g. metals an polymers.

Thermal actuators fabricated with metals such as Ni are better than the ones produced in Si and Poly-Si films because, due to the larger coefficient of expansion (e.g. 2.6 ppm K^{-1} for Poly-Si compared to 12.7 ppm K^{-1} for Ni), they can be operated at lower temperatures. In addition they have electrical properties independent of the doping level and with a positive coefficient of resistance. This implies that, at the same power level, the metal actuator consumes most of the power in the hot arm increasing the difference in temperature between the arms and the overall deflection [310]. An example of the incorporation of metals into microgripper designs is [97] where the SM-BB microgripper model from Zyvex is fabricated in nickel. As can be seen in Table 8.1, the nickel version of the microgripper obtains for approximately half of the applied voltage (3.5 V versus 6V) more than double the deflection (20 μm versus 6 μm).

Table 8.2: Performance of electrothermal microgrippers produced in metal-polymer material and actuated in air.

Ref.	Year	Material	Actuator type	Max displacement(*) [μm]	Voltage [V]	Current [mA]	Power [mW]	T [°C]
[120]	2004	SU8 + Pt/Ti	Double hot arm U-shaped	100	10	5	50	< 100
[123]	2005	SU8 + Au/Cr	U-shaped	12	0.45	10	5	< 100
[124]	2006	SU8 + Si	Bimorph	7	2	20	40	~ 130
[311]	2008	SU8 + Si	Bimorph + U-shaped	32	4.5	25	114	~ 180
	2006	SU8 + Au	design 1_(30)	175	1.59	36	57	~ 100
			design 1_(100)	120	1.41	38	54	~ 100
			design 2_(30)	88	1.43	38	54	~ 100
			design 2_(100)	46	1.21	40	48	~ 100

(*) from initial rest position

However, for displacements larger than a few microns, these optimisation efforts still do not correct for the high temperatures and voltages required. In order to reduce these parameters and enable the use of microgrippers in liquid environments it has been essential to incorporate polymeric materials into the designs. These have larger coefficients of expansion than metals (52 ppm K^{-1} for SU8 versus 12.7 ppm K^{-1} for Ni) and therefore require an even lower temperature to produce the same deflection. This has been the design approach used in this work.

Table 8.2 shows four published[17] polymeric microgrippers based on different thermal actuators — double hot arm U-shaped actuator [119], U-shaped [123], and comb-finger [124, 311] — compared to the four microgripper designs demonstrated in this work. In the case of the microgrippers presented here the maximum displacement denotes the maximum distance below 100 °C. As has been shown earlier, failure of these devices occurs at slightly higher displacements and powers.

As can be seen from tables 8.1 and 8.2, all of the microgrippers developed here provide larger displacements at lower voltages and lower temperatures than the rest of the microgrippers. The only competitive microgripper at low displacements would be the one proposed by Chronis et al.[123], which is considerably smaller, with a length of 650 μm compared to a length of 3100 - 3600 μm in the models presented here. However, as explained in section 6.4.2.3, smaller designs of thermal actuators are prone to failure due to buckling at much smaller displacements. This limits the range of actuation possible for this kind of microgripper and makes them suitable only for manipulations where the samples have very little variation in size. In the case of big cells, e.g. the human egg, the variation in size can reach up to 30 μm between samples. In those cases, a useful microgripper would require a minimum opening of 20 microns (per jaw). As shown in Table 8.3 the models (e.g. design 3_(100)) are also comparable to the Chronis model when actuating underwater. As in the air case, at low displacements they both produce similar displacements.

Table 8.3: Performance of electrothermal microgrippers produced in metal-polymer material and actuated in water.

Ref.	Year	Material	Actuator type	Max displacement(*) [μm]	Voltage [V]	Current [mA]	Power [mW]	T [°C]
[123]	2005	SU8 + Au/Cr	U-shaped	12	2	45	91	< 100
	2006	SU8 + Au	design 3_(100)	17	2	66	130	~ 100

(*) from initial rest position

Finally, the designs in this thesis also offer more flexibility since they can produce bidirectional displacements (see section 3.4.2.3) and they offer the possibility to use more efficiently the volume and surface of the cold arm to include active elements such

[17] Zyvex communicated in a note the development of a polymeric model of their MS_BB microgripper model [175].However no quantitative data has been provided. It has never been launch commercially.

as force sensors, electrical sensors and light waveguides [312]. Other issues such as ease of fabrication or cost are difficult to compare.

8.2. Future work

As discussed in Chapter 7, the ultimate aim of this thesis was to provide a reliable and cost effective tool for the manipulation of cells and other biological particles. Now that the technology has been proven, two main directions should be taken to move the development of the microgripper forward: one towards improving manufacturing related issues, a second one towards the inclusion of extra sensor/actuating structures that would enhance the potential of the microgripper as a substitute for existing technologies.

From a manufacturing point of view, the improvement could entail the adaptation of the fabrication flows shown in chapter 3 to a more scalable manufacturing approach. An eventual new process should include, for example:

- The incorporation of a robust anchor (in addition to the SU8) that could be used at the same time as main mechanical attachment to the manipulation station and as robust electrical connection.

- The elimination of the wire bonding step in between the primary device and the new robust anchor.

- Easier dicing of the different microgrippers produced on the silicon chip.

An idea to solve these three problems simultaneously could be the inclusion of a SiO_2 layer between the SU8 and the silicon chip. This layer, acting as a mask and patterned with HF (Hydrofluoric Acid), would help to protect the silicon substrate in the areas of interest. Thus, when finally releasing the microgrippers, the areas of silicon protected by the SiO_2 would define the anchors. Once a silicon anchor is included in the structure, the interconnection from the microgripper to the contact pads (on the silicon anchor) could be achieved with the metallisation step. By using, for example, sputtering techniques the step coverage between the gold, thin SU8 could be guaranteed. Finally, the definition of

thin lines in the SiO_2 mask would facilitate the dicing of the different devices in a reliable manner.

From a functionality perspective, three main options should be explored:

- The incorporation of force sensors in the arms or jaws of the microgripper

- The incorporation of conductive elements in the jaws to eventually apply electrical voltage between the samples. This could be of interest in the emerging field of cell electrofusion.

- The incorporation of an ablation kit. For example by including waveguides in the empty arms that could be used to guide a laser beam.

Finally, it is worth noting that the models developed during this thesis could also be used to further optimise the structure in terms of performance in fluid environments. The displacements in water presented in this work cover a range between 20-40 μm. However, it is my belief that by using the models in combination with optimisation techniques, a more universal microgripper could be produced.

REFERENCES

[1] J. M. Levsky and R. H. Singer, "Gene expression and the myth of the average cell," *Trends in Cell Biology*, vol. 13, pp. 4-6, 2003.

[2] G. Bao and S. Suresh, "Cell and molecular mechanics of biological material," *Nature Materials*, vol. 2, pp. 715-725, 2003.

[3] J. Voldman, M. L. Gray, and M. A. Schmidt, "Microfabrication in Biology and Medicine," *Annual Review in Biomedical Engineering*, vol. 1, pp. 401-425, 1999.

[4] D. L. Polla, A. G. Erdman, W. P. Robbins, D. T. Markus, J. Diaz-Diaz, R. Rizq, Y. Nam, H. T. Brickner, A. Wang, and P. Krulevitch, "Microdevices in medicine," *Annual Review of Biomedical Engineering*, vol. 2, pp. 551-576, 2000.

[5] A. C. R. Grayson, R. S. Shawgo, A. M. Johnson, N. T. Flynn, Y. W. Li, M. J. Cima, and R. Langer, "A BioMEMS review: MEMS technology for physiologically integrated devices," *Proceedings of the IEEE*, vol. 92, pp. 6-21, 2004.

[6] C. Q. Yi, C. W. Li, S. L. Ji, and M. S. Yang, "Microfluidics technology for manipulation and analysis of biological cells," *Analytica Chimica Acta*, vol. 560, pp. 1-23, 2006.

[7] E. W. H. Jager, O. Inganas, and I. Lundstrom, "Microrobots for micrometer-size objects in aqueous media: Potential tools for single-cell manipulation," *Science*, vol. 288, pp. 2335-2338, 2000.

[8] M. Gauthier, B. Lopez-Walle, and C. Clevy, "Comparison between micro-objects manipulations in dry and liquid mediums," presented at IEEE International Symposium on Computational Intelligence in Robotics and Automation, Espoo, Finland, pp. 707-712, June 2005.

[9] J. Desai, A. Pillarisetti, and A. Brooks, "Engineering Approaches to Biomanipulation," *Annual Review in Biomedical Engineering*, vol. 9, pp. 35-53, 2007.

[10] M. E. Chicurel, C. S. Chen, and D. E. Ingber, "Cellular control lies in the balance of forces," *Current opinion in Cell Biology*, vol. 10, pp. 232-239, 1998.

[11] G. Bao, "Molecular Biomechanics," presented at Advances in Biomechanics, Beijing, China, 2001.

[12] K. Yanagida, H. Katayose, H. Yazawa, Y. Kimura, K. Konnai, and A. Sato, "The usufulness of a piezomanipulator in intracytoplsmic sperm injection in humans," *Human reproduction*, vol. 14, pp. 448-453, 1998.

[13] Y. Sun, K. T. Wan, K. P. Roberts, J. C. Bischof, and B. J. Nelson, "Mechanical property characterization of mouse zona pellucida," *IEEE Transactions on Nanobioscience*, vol. 2, pp. 279-286, 2003.

[14] Y. Murayama, J. Mizumo, H. Kamaruka, Y. Fueta, H. Nakamura, K. Akaishi, K. Anazai, A. Watanabe, H. Inui, and S. Omata, "Mouse zona pellucida dynamically changes its elasticity during oocyte maturation, fertilization and early embryo development," *Human Cell*, vol. 19, pp. 119-125, 2006.

[15] K. Nagayama, S. Yanagihara, and T. Matsumoto, "A novel micro tensile tester with feed-back control for viscoelastic analysis of single isolated smooth muscle cells," *Medical Engineering & Physics*, vol. 29, pp. 620-628, 2007.

[16] S. Suresh, "Biomechanics and biophysics of cancer cells," *Acta Biomaterialia*, vol. 3, pp. 413-438, 2007.

[17] A. Ashkin, "Acceleration and Trapping of Particles by Radiation Pressure," *Physical Review Letters*, vol. 24, pp. 156-157, 1970.

[18] A. Ashkin, "History of optical trapping and manipulation of small-neutral particle, atoms, and molecules," *IEEE Journal of Selected Topics in Quantum Electronics*, vol. 6, pp. 841-856, 2000.

[19] M. Praunitz, "Microneedles for transdermal drug delivery," *Advanced Drug Delivery Reviews*, vol. 56, pp. 581-587, 2003.

[20] B. Ma et al., "A PZT insulin pump integrated with a silicon microneedle array for transdermal drug delivery," *Journal of Microfluidics and Nanofluidics*, vol. 2, pp. 417-423, 2005.

[21] CardioMEMS, "CardioMEMS implants first wireless pressure sensor to monitor hypertension," in *News-medical. Net*, 2007.

[22] A. M. Shkel, "An electronic prosthesis mimicking the dynamic vestibular funcion," *Proceedings of IEEE*, vol. 2, pp. 996-1001, Sensors 2003.

[23] *SonionMEMS*, http://www.sonion.com.

[24] W. J. Bennet, P. Krulevitch, A. P. Lee, M. A. Northrup, and J. A. Folta, "Miniature plastic gripper and fabrication method." Patent no US5609608.

[25] *Texas Instruments*, http://www.ti.com.

[26] "STMicroelectronics drives gaming revolution with Nintendo's Wii," http://www.st.com/stonline/stappl/cms/press/news/year2006/t2031.htm.

[27] *Analog Devices*, http://www.analog.com.

[28] P. Hewlett, Hewlett Packard, http://www.hp.com.

[29] T. McMahon, "Size and shape in Biology," *Science*, vol. 179, pp. 1201-1204, 1973.

[30] M. J. Madou, *Fundamentals of Microfabrication*. London: CRC Press, 2002.

[31] W. S. N. Trimmer, "Microrobots and micromechanical systems," *Sensors and Actuators A*, vol. 19, pp. 267-287, 1989.

[32] B. H. Beigl and P. Yager, "Microfluidic diffusion-based separation and detection," *Science*, vol. 283, pp. 346-347, 1999.

[33] "World MEMS fab: an overview of the MEMS industry worldwide," http://www.yole.fr/.

[34] W. S. N. Trimmer, "Microrobots and Micromechanical Systems," *Sensors and Actuators A*, vol. 19, pp. 267-287, 1989.

[35] R. S. Fearing, "Powering 3 dimensional robots: power density limitations," presented at IEEE International Conference on Robotics and Automation, Leuven, Belgium, pp. 1-15, May 1998.

[36] S. T. Smith and R. M. Seugling, "Sensor and actuator considerations for precision, small machines," *Precision Engineering-Journal of the International Societies for Precision Engineering and Nanotechnology*, vol. 30, pp. 245-264, 2006.

[37] J. Judy, "Microelectromechanical systems: fabrication, design and applications," *Smart Materials and Structures*, vol. 10, pp. 1105-1134, 2001.

[38] "Nexus Market Analysis 2006," http://www.nexus-mems.com/iop.asp.

[39] "Ranking of top MEMS companies," http://www.wtc-consult.de/english/home/index.html.

[40] *Canon Technology*, http://www.canon.com.

[41] *Texas Instruments*, http://www.ti.com.

[42] *Bosch Sensortec GmbH*, http://www.bosch-sensortec.com/.

[43] *STMicroelectronics*, http://www.st.com.

[44] "2007-2012 MEMS forecast," http://www.yole.fr/.

[45] Y. development, "2007-2012 MEMS forecast," 2008.

[46] Micronics, "www.micronics.net," 2004.

[47] "European Micro and Nano technologies status: Minanet Analysis," http://www.minatec.com/minatec2003.

[48] E. Mounier and J. C. Eloy, "World MEMS fab: an overview of the MEMS industry worldwide," *Yole Development*, 2004.

[49] S. Yu and B. J. Nelson, "Microrobotic cell injection," presented at IEEE International Conference on Robotics and Automation, Seoul, Korea, pp. 620-625, June 2001.

[50] C. Bustamante, J. C. Macosko, and G. J. L. Wuite, "Grabbing the cat by the tail: Manipulating molecules one by one," *Nature Reviews Molecular Cell Biology*, vol. 1, pp. 130-136, 2000.

[51] S. Yu and J. B. Nelson, "Microrobotic cell injection," presented at IEEE International Conference on Robotics and Automation, Seoul, Korea, pp. 620-625, June 2001.

[52] M. Hengartner, "The biochemistry of apoptosis," *Nature*, vol. 407, pp. 770-775, 2000.

[53] M. Toner, "Integration of living cells into microsystems technology," presented at Second Joint EMBS-BMES Conference 2002, pp.1698-1699, October 2002, 2002.

[54] D. G. Grier, "A revolution in optical manipulation," *Nature*, vol. 424, pp. 810-816, 2003.

[55] M. Lang and S. Block, "Resource Letter: LBOT-1 Laser-based optical Tweezers," *American Journal Physics*, vol. 71, pp. 201-215, 2003.

[56] K. Dholakia and P. Reece, "Optical micromanipulation takes hold," *Nano Today*, vol. 1, pp. 18-27, 2006.

[57] K. C. Neuman and S. M. Block, "Optical trapping," *Review of Scientific Instruments*, vol. 75, pp. 2787-2809, 2004.

[58] M. Durr, J. Kentsch, T. Muller, T. Schnelle, and M. Stelzle, "Microdevices for manipulation and accumulation of micro- and nanoparticles by dielectrophoresis," *Electrophoresis*, vol. 24, pp. 722-731, 2003.

[59] M. Barber, "A new method of isolating micro-organisms," *Journal of Kansas medical Society*, vol. 4, pp. 489-494, 1904.

[60] V. A. Nikitin and E. E. Fesenko, "Biophysical aspects of reconstruction of a single cell by the methods of cell engineering," *Biofizika*, vol. 51, pp. 673-678, 2006.

[61] J. Park, S. H. Jung, Y. H. Kim, B. Kim, S. K. Lee, and J. O. Park, "Design and fabrication of an integrated cell processor for single embryo cell manipulation," *Lab on a Chip*, vol. 5, pp. 91-96, 2005.

[62] Z. Sadani, B. Wacogne, C. Pieralli, C. Roux, and T. Gharbi, "Microsystems and microfluidic device for single oocyte transportation and trapping: Toward the automation of in vitro fertilising," *Sensors and Actuators A-Physical*, vol. 121, pp. 364-372, 2005.

[63] J. Agnus, P. Nectoux, and N. Chaillet, "Overview of microgrippers and design of a micromanipulation station based on a MMOC microgripper," presented at IEEE International Symposium on Computational Intelligence in Robotics and Automation, Espoo, Finland, pp.117-123, June 2005.

[64] M.Gad-el-Hak, *The MEMS Handbook*, vol. 2: Boca Raton, 2006.

[65] A. J. Sanchez-Salmeron, R. Lopez-Tarazon, R. Guzman-Diana, and C. Ricolfe-Viala, "Recent development in micro-handling systems for micro-manufacturing," *Journal of Materials Processing Technology*, vol. 167, pp. 499-507, 2005.

[66] A. Menciassi, A. Eisinberg, I. Izzo, and P. Dario, "From "macro" to "micro" manipulation: Models and experiments," *IEEE-ASME Transactions on Mechatronics*, vol. 9, pp. 311-320, 2004.

[67] J. Cecil, D. Vasquez, and D. Powell, "A review of gripping and manipulation techniques for micro-assembly applications," *International Journal of Production Research*, vol. 43, pp. 819-828, 2005.

[68] P. Dario, M. C. Carrozza, A. Benvenuto, and A. Menciassi, "Micro-systems in biomedical applications," *Journal of Micromechanics and Microengineering*, vol. 10, pp. 235-244, 2000.

[69] E. Smela, "Conjugated polymer actuators for biomedical applications," *Advanced Materials*, vol. 15, pp. 481-494, 2003.

[70] T. Vilkner, D. Janasek, and A. Manz, "Micro total analysis systems. Recent developments," *Analytical Chemistry*, vol. 76, pp. 3373-3385, 2004.

[71] "PillCam™ Capsule Endoscopy for Children," http://www.givenimaging.com.

[72] A. Menciassi, A. Moglia, S. Gorini, G. Pernorio, C. Stefanini, and P. Dario, "Shape memory alloy clamping devices of a capsule for monitoring tasks in the gastrointestinal tract," *Journal of Micromechanics and Microengineering*, vol. 15, pp. 2045-2055, 2005.

[73] G. Hashiguchi, T. Goda, M. Hosogi, K. Hirano, N. Kaji, Y. Baba, K. Kakushima, and H. Fujita, "DNA manipulation and retrieval from an aqueous solution with micromachined nanotweezers," *Analytical Chemistry*, vol. 75, pp. 4347-4350, 2003.

[74] *MEMS Precision Instruments*, http://www.memspi.com.

[75] *Klocke Nanotechnik*, http://www.nanomotor.de.

[76] *Kleindiek Nanotechnik*, http://www.nanotechnik.com.

[77] *Nascatec GmbH*, http://www.nascatec.com.

[78] *Preiser*, http://www.preiser.com.

[79] *Nanoeffector microgripper, Zyvex*, http://www.zyvex.com.

[80] *Bartels Mikrotechnik*, http://www.bartels-mikrotechnik.de.

[81] *PiezoJena*, http://www.piezojena.com/.

[82] C. Kim, A. Pisano, and R. Muller, "Silicon-processed overhanging microgripper," *Journal of Microelectromechanical systems*, vol. 1, 1992.

[83] P. B. Chu and K. S. J. Pister, "Analysis of Closed-Loop Control of Parallel-Plate Electrostatic Microgrippers," presented at IEEE International Conference on Robotics and Automation, San Diego, CA, USA, pp. 820-825, May 1994.

[84] P. Kim and C. M. Lieber, "Nanotube nanotweezers," *Science*, vol. 286, pp. 2148-2150, 1999.

[85] B. E. Volland, H. Heerlein, and I. W. Rangelow, "Electrostatically driven microgripper," *Microelectronic engineering*, vol. 61-61, pp. 1015-1023, 2002.

[86] K. Molhave, T. Hansen, D. Madsen, and P. Boggild, "Towards Pick-and-place assembly of nanostructures," *Journal of Nanoscience and Nanotechnology*, vol. 4, pp. 279-282, 2004.

[87] K. Molhave, T. Wich, A. Kortschack, and P. Boggild, "Pick-and-place nanomanipulation using microfabricated grippers," *Nanotechnology*, vol. 17, pp. 2434-2441, 2006.

[88] R. Wierzbicki, K. Houston, H. Heerlein, W. Barth, T. Debski, A. Eisinberg, A. Mendicassi, M. C. Carrozza, and P.Dario, "Design and fabrication of an electrostatically driven microgripper for blood vessel manipulation," *Microelectronic engineering*, vol. 83, pp. 1651-1654, 2006.

[89] R. Wierzbicki, H. Heerlein, T. Debski, and W. Barth, "Low-voltage driven electrostatic microgripper for biotechnology," presented at MNE 06, Barcelona, Spain, p. 329, September 2006.

[90] F. Beyeler, A. Neild, S. Oberti, D. J. Bell, Y. Sun, J. Dual, and B. J. Nelson, "Monolithically fabricated microgripper with integrated force sensor for manipulating microobjects and biological cells aligned in an ultrasonic field," *Journal of Microelectromechanical Systems*, vol. 16, pp. 7-15, 2007.

[91] O. Millet, P. Bernardoni, S. Regnier, P. Bidaud, E. Tsitsiris, D. Collard, and L. Buchaillot, "Electrostatic actuated micro gripper using an amplification mechanism," *Sensors and Actuators A-Physical*, vol. 114, pp. 371-378, 2004.

[92] F. Arai, D. Andou, Y. Nonoda, T. Fukuda, H. Iwata, and K. Itoigawa, "Integrated microendeffector for micromanipulation," *IEEE-ASME Transactions on Mechatronics*, vol. 3, pp. 17-23, 1998.

[93] R. Salim, H. Wurmus, A. Harnish, and D. Hulsenberg, "Microgrippers created in microstructurable glass," *Microsystems Technology*, vol. 4, pp. 32-34, 1997.

[94] A. Eisinberg, A. Menciassi, S. Micera, D. Campolo, M. C. Carrozza, and P. Dario, "PI force control of a microgripper for assembling biomedical microdevices," *IEE Proceedings-Circuits Devices and Systems*, vol. 148, pp. 348-352, 2001.

[95] J. Park and W. Moon, "The systematic design and fabrication of a three-chopstick microgripper," *International Journal of Advanced Manufacturing Technology*, vol. 26, pp. 251-261, 2005.

[96] J. Park and W. Moon, "A hybrid-type micro-gripper with an integrated force sensor," *Microsystem Technologies-Micro-and Nanosystems-Information Storage and Processing Systems*, vol. 9, pp. 511-519, 2003.

[97] K. Kim, E. Nilsen, T. Huang, A. Kim, M. Ellis, G. Skidmore, and J. B. Lee, "Metallic microgripper with SU-8 adaptor as end-effectors for heterogeneous micro/nano assembly applications," *Microsystem Technologies-Micro-and Nanosystems-Information Storage and Processing Systems*, vol. 10, pp. 689-693, 2004.

[98] S. K. Jericho, M. H. Jericho, T. Hubbard, and M. Kujath, "Micro-electro-mechanical systems microtweezers for the manipulation of bacteria and small particles," *Review of Scientific Instruments*, vol. 75, pp. 1280-1282, 2004.

[99] R. Perez, N. Chaillet, K. Domanski, P. Janus, and P. Grabiec, "Fabrication, modeling and integration of a silicon technology force sensor in a piezoelectric micro-manipulator," *Sensors and Actuators A-Physical*, vol. 128, pp. 367-375, 2006.

[100] R. Perez, J. Agnus, C. Clevy, A. Hubert, and N. Chaillet, "Modeling, fabrication, and validation of a high-performance 2-DoF piezoactuator for micromanipulation," *IEEE-ASME Transactions on Mechatronics*, vol. 10, pp. 161-171, 2005.

[101] C. S. Jeon, J. S. Park, S. Y. Lee, and C. W. Moon, "Fabrication and characteristics of out-of-plane piezoelectric micro grippers using MEMS processes," *Thin Solid Films*, vol. 515, pp. 4901-4904, 2007.

[102] S. K. Nah and Z. W. Zhong, "A microgripper using piezoelectric actuation for micro-object manipulation," *Sensors and Actuators A-Physical*, vol. 133, pp. 218-224, 2007.

[103] M. C. Carrozza, P. Dario, A. Menciassi, and A. Fenu, "Manipulating biological and mechanical micro-objects using LIGA-microfabricated end-effectors," presented at IEEE International Conference on Robotics and Automation, Leuven, Belgium, pp.1811-1816, May 1998.

[104] M. C. Carrozza, A. Eisinberg, and A. Menciassi, "Towards a force-controlled microgripper for assembling biomedical microdevices," *Journal of Micromechanics and Microengineering*, vol. 10, pp. 271-276, 2000.

[105] W. L. Zhou and W. J. Li, "Micro ICPF actuators for aqueous sensing and manipulation," *Sensors and Actuators A-Physical*, vol. 114, pp. 406-412, 2004.

[106] J. W. L. Zhou, H. Y. Chan, T. K. H. To, K. W. C. Lai, and W. J. Li, "Polymer MEMS actuators for underwater micromanipulation," *IEEE-ASME Transactions on Mechatronics*, vol. 9, pp. 334-342, 2004.

[107] K. Yun and W. J. Kim, "System identification and microposition control of ionic polymer metal composite for three-finger gripper manipulation," *Proceedings of the Institution of Mechanical Engineers Part I-Journal of Systems and Control Engineering*, vol. 220, pp. 539-551, 2006.

[108] A. P. Lee, D. R. Ciarlo, P. A. Krulevitch, S. Lehew, J. Trevino, and M. A. Northrup, "A practical microgripper by fine alignment, eutectic bonding and SMA actuation," *Sensors and Actuators A-Physical*, vol. 54, pp. 755-759, 1996.

[109] M. Kohl, B. Krevet, and E. Just, "SMA microgripper system," *Sensors and Actuators A-Physical*, vol. 97-8, pp. 646-652, 2002.

[110] M. Kohl, E. Just, W. Pfleging, and S. Miyazaki, "SMA microgripper with integrated antagonism," *Sensors and Actuators A-Physical*, vol. 83, pp. 208-213, 2000.

[111] J. J. Gill, D. T. Chang, L. A. Momoda, and G. P. Carman, "Manufacturing issues of thin film NiTi microwrapper," *Sensors and Actuators A-Physical*, vol. 93, pp. 148-156, 2001.

[112] S. Buttgenbach, S. Butefisch, M. Leester-Schadel, and A. Wogersien, "Shape memory microactuators," *Microsystem Technologies*, vol. 7, pp. 165-170, 2001.

[113] H. Zhang, Y. Bellouard, T. Sidler, E. Burdet, A. N. Poo, and R. Clavel, "A monolithic shape memory alloy microgripper for 3-D assembly of tissue engineering scaffolds," *SPIE Proceedings vol. 4568*, pp. 50-60, 2001.

[114] I. Roch, P. Bidaud, D. Collard, and L. Buchaillot, "Fabrication and characterization of an SU-8 gripper actuated by a shape memory alloy thin film," *Journal of Micromechanics and Microengineering*, vol. 13, pp. 330-336, 2003.

[115] Z. W. Zhong and C. K. Yeong, "Development of a gripper using SMA wire," *Sensors and Actuators A-Physical*, vol. 126, pp. 375-381, 2006.

[116] C. S. Pan and W. Hsu, "An electro-thermally and laterally driven polysilicon microactuator," *Journal of Micromechanics and Microengineering*, vol. 7, pp. 7-13, 1997.

[117] H. Y. Chan and W. J. Li, "A thermally actuated polymer micro robotic gripper for manipulation of biological cells," in *2003 IEEE International Conference on Robotics and Automation*, pp. 288-293.

[118] J. K. Luo, A. J. Flewitt, S. M. Spearing, N. A. Fleck, and W. I. Milne, "Normally closed microgrippers using a highly stressed diamond-like carbon and Ni bimorph structure," *Applied Physics Letters*, vol. 85, pp. 5748-5750, 2004.

[119] N. Nguyen, S. Ho, and C. Low, "A polymeric microgripper with integrated thermal actuators," *Journal of Micromechanics and Microengineering*, vol. 14, pp. 969-974, 2004.

[120] E. V. Bordatchev and S. K. Nikumb, "Electro-thermally driven microgrippers for micro-electro-mechanical systems applications," *Journal of Microlithography Microfabrication and Microsystems*, vol. 4, pp. 023011, 2005.

[121] Y. C. Tsai, S. H. Lei, and H. Sudin, "Design and analysis of planar compliant microgripper based on kinematic approach," *Journal of Micromechanics and Microengineering*, vol. 15, pp. 143-156, 2005.

[122] K. Molhave and O. Hansen, "Electro-thermally actuated microgrippers with integrated force sensosrs," *Journal of Micromechanics and Microengineering*, vol. 15, pp. 1265-1270, 2005.

[123] N. Chronis and L. Lee, "Electrothermally Activated SU-8 Microgripper for Single cell manipulation in Solution," *Journal of Microelectromechanical systems*, vol. 14, pp. 857-863, 2005.

[124] T. C. Duc, G. K. Lau, J. Wei, and P. M. Sarro, "Silicon-Polymer laterally stacked Bimorph Micro-gripper," presented at MicroMechanics Europe Workshop (MME'06), Southampton, UK, pp. 197-200, September 2006.

[125] M. J. F. Zeman, E. V. Bordatchev, and G. K. Knopf, "Design, kinematic modeling and performance testing of an electro-thermally driven microgripper for micromanipulation applications," *Journal of Micromechanics and Microengineering*, vol. 16, pp. 1540-1549, 2006.

[126] K. Ivanova, T. Ivanov, A. Badar, B. E. Volland, I. W. Rangelow, D. Andrijasevic, F. Sumecz, S. Fisher, M. Spitzbart, W. Brenner, and I. Kostic, "Thermally driven microgripper as a tool for assembly," *Microelectronic engineering*, vol. 83, pp. 1393-1395, 2006.

[127] J. K. Luo, R. Huang, J. H. He, Y. Q. Fu, A. J. Flewitt, S. M. Spearing, N. A. Fleck, and W. I. Milne, "Modelling and fabrication of low operation temperature microcages with a

polymer/metal/DLC trilayer structure," *Sensors and Actuators A-Physical*, vol. 132, pp. 346-353, 2006.

[128] M. S. C. Lu, Z. H. Wu, C. E. Huang, S. J. Hung, M. H. Chen, and Y. C. King, "CMOS micromachined grippers with on-chip optical detection," *Journal of Micromechanics and Microengineering*, vol. 17, pp. 482-488, 2007.

[129] J. Schlick and D. Zuhlke, "Design and application of a gripper for microparts using flexure hinges and pneumatic actuation," in *Microrobotics and Microassembly III*, vol. 4568, *Proceedings of the Society of Photo-Optical Instrumentation Engineers (SPIE)*, 2001, pp. 1-11.

[130] S. Butefisch, V. Seidemann, and S. Buttgenbach, "Novel micro-pneumatic actuator for MEMS," *Sensors and Actuators A-Physical*, vol. 97-8, pp. 638-645, 2002.

[131] S. Mutzenich, T. Vinay, and G. Rosengarten, "Analysis of a novel micro-hydraulic actuation for MEMS," *Sensors and Actuators A-Physical*, vol. 116, pp. 525-529, 2004.

[132] J. Ok, Y. W. Lu, and C. J. Kim, "Pneumatically driven microcage for microbe manipulation in a biological liquid environment," *Journal of Microelectromechanical Systems*, vol. 15, pp. 1499-1505, 2006.

[133] J. S. Lee and S. Lucyszyn, "Design and pressure analysis for bulk-micromachined electrothermal hydraulic microactuators using PCM," *Sensors and Actuators A*, vol. In press, 2006.

[134] J. S. Lee and S. Lucyszyn, "Design and pressure analysis for bulk-micromachined electrothermal hydraulic microactuators using a PCM," *Sensors and Actuators A-Physical*, vol. 133, pp. 294-300, 2007.

[135] Y. Suzuki, "Underwater Performance of Flexible Microgripper and Fine-Particle Manipulation," *Japanese Journal of Applied Physics Part 1-Regular Papers Short Notes & Review Papers*, vol. 33, pp. 6056-6057, 1994.

[136] Y. Suzuki, "Fabrication and Evaluation of Flexible Microgripper," *Japanese Journal of Applied Physics Part 1-Regular Papers Short Notes & Review Papers*, vol. 33, pp. 2107-2112, 1994.

[137] D. H. Kim, M. G. Lee, B. Kim, and Y. Sun, "A superelastic alloy microgripper with embedded electromagnetic actuators and piezoelectric force sensors: a numerical and experimental study," *Smart Materials & Structures*, vol. 14, pp. 1265-1272, 2005.

[138] W. C. Tang, T. C. H. Nguyen, and R. T. Howe, "Laterally Driven Polysilicon Resonant Microstructures," *Sensors and Actuators*, vol. 20, pp. 25-32, 1989.

[139] T. Akiyama, D. Collard, and H. Fujita, "Scratch drive actuator with mechanical links for self-assembly of three-dimensional MEMS," *Journal of Microelectromechanical Systems*, vol. 6, pp. 10-17, 1997.

[140] J. D. Grade, H. Jerman, and T. W. Kenny, "Design of large deflection electrostatic actuators," *Journal of Microelectromechanical Systems*, vol. 12, pp. 335-343, 2003.

[141] M. S. Rodgers, S. Kpt, J. Hetrick, Z. Li, D. Jense, M. Krygowski, S.L., S. M. Barnes, and M. S. Beurg, "A new class of high force, low-voltage, compliant actuation systems," http://www.mems.sandia.gov.

[142] M. Hoffmann, D. Nusse, and E. Voges, "Electrostatic parallel-plate actuators with large deflections for use in optical moving-fibre switches," *Journal of Micromechanics and Microengineering*, vol. 11, pp. 323-328, 2001.

[143] Y. J. Zhao and T. H. Cui, "Fabrication of high-aspect-ratio polymer-based electrostatic comb drives using the hot embossing technique," *Journal of Micromechanics and Microengineering*, vol. 13, pp. 430-435, 2003.

[144] W. Dai, K. Lian, and W. J. Wang, "Design and fabrication of a SU-8 based electrostatic microactuator," *Microsystem Technologies-Micro-and Nanosystems-Information Storage and Processing Systems*, vol. 13, pp. 271-277, 2007.

[145] N. C. MacDonald, L. Y. Chen, J. J. Yao, L. Zhang, J. A. MacMillan, and D. C. Thomas, "Selective chemical vapour deposition of tungsten for micromechanical structures," *Sensors and Actuators*, pp. 123-133, 1989.

[146] J. Breget, S. Henein, R. Mericio, and R. Clavel, "Monolithic piezoceramic flexible structures for micromanipulation," presented at 9th International Precision Engineering Seminar, Braunschweig, Germany, 1997.

[147] C. K. M. Fung, I. Elhajj, W. J. Li, and N. Xi, "A 2-D PVDF force sensing system for micro-manipulation and micro-assembly," in *IEEE International Conference on Robotics and Automation,* 2002, pp. 1489-1494.

[148] M. C. Carrozza, P. Dario, A. Menciassi, and A. Fenu, "Manipulating biological and mechanical micro-objects using LIGA-microfabricated end-effectors," in *1998 Ieee International Conference on Robotics and Automation, Vols 1-4, Ieee International Conference on Robotics and Automation*, 1998, pp. 1811-1816.

[149] D. H. Kim, B. Kim, and H. Kang, "Development of a piezoelectric polymer-based sensorized microgripper for microassembly and micromanipulation," *Microsystem Technologies-Micro-and Nanosystems-Information Storage and Processing Systems*, vol. 10, pp. 275-280, 2004.

[150] H. Janocha, "Application potential of magnetic field driven new actuators," *Sensors and Actuators A-Physical*, vol. 91, pp. 126-132, 2001.

[151] T. Irita and Y. Suzuki, "A drying method using naphthalene for flexible microgripper fabrication," *Japanese Journal of Applied Physics Part 2-Letters*, vol. 35, pp. L1468-L1471, 1996.

[152] Y. Q. Fu, H. J. Du, W. M. Huang, S. Zhang, and M. Hu, "TiNi-based thin films in MEMS applications: a review," *Sensors and Actuators A-Physical*, vol. 112, pp. 395-408, 2004.

[153] A. Johnson, "Vacuum-deposited TiNi shape memnory film: characterisation and applications in microdevices," *Journal of Micromechanics and Microengineering*, vol. 1, pp. 34-41, 1991.

[154] S. Miyazaki and K. Otsuka, "Deformation and Transition Behavior Associated with the R-Phase in Ti-Ni Alloys," *Metallurgical Transactions A-Physical Metallurgy and Materials Science*, vol. 17, pp. 53-63, 1986.

[155] J. Hesselbach and R. Pittschellis, "Shape memory allowys for use in miniature grippers," presented at 2nd Internatioinal conference on Shape memory alloys and superelastic technologies, USA, 1997.

[156] S. Butefisch, G. Pokar, S. Buttgenbach, and J. Hesselbach, "A new SMA actuated miniature silicon gripper fro microassembly," presented at 7th International conference on new actuators, Bremen, 2000.

[157] Q. Chang-jun, M. Pei-sun, and Y. Qin, "A prototype micro-wheeled-robot using SMA actuator," *Sensors and Actuators A-Physical*, vol. 113, pp. 94-99, 2004.

[158] S. Mutzenich, T. Vinay, D. K. Sood, and G. Rosengarten, "Design parameter characterisation and experimental validation of hydrostatic actuation suitable for MEMS," *Sensors and Actuators A-Physical*, vol. 127, pp. 147-154, 2006.

[159] J. S. Lee and S. Lucyszyn, "A micromachined refreshable Braille cell," *Journal of Microelectromechanical Systems*, vol. 14, pp. 673-682, 2005.

[160] G. Alici and N. N. Huynh, "Performance quantification of conducting polymer actuators for real applications: A microgripping system," *IEEE-ASME Transactions on Mechatronics*, vol. 12, pp. 73-84, 2007.

[161] W. Nogimori, K. Irisa, M. Ando, and Y. Naruse, "A laser-powered micro-gripper," presented at IEEE MEMS '97, Nagoya, Japan, pp. 267-271, January 1997.

[162] S. X. Lu, Y. Liu, N. Shao, and B. Panchapakesan, "Nanotube micro-opto-mechanical systems," *Nanotechnology*, vol. 18, pp. 065501, 2007.

[163] D. Petrovic, G. Popovic, T. Petrovic, A. Schneider, E. Huq, H. Detter, and F. Franek, "Micro gripper for handling and assembly in MEMS produced by SU8-technology," *SPIE proceedings vol. 4928*, pp. 63-72, 2002.

[164] D. Petrovic, G. Popovic, E. Chatzitheodoridis, O. Del Medico, A. Almansa, H. Detter, and W. Brenner, "Mechanical gripper system for handling and assembly in MEMS," *SPIE Proceedings vol. 4557*, pp. pp.151-156, 2001.

[165] H. Guckel, J. Klein, T. Christenson, K. Skrobis, M. Laudon, and E. G. Lovell, "Thermo-magnetic metal flexure actuators," presented at Tech Digest IEEE Solid-State Sensor and Actuator Workshop, Hilton Head island, SC, USA, 1992.

[166] J. H. Comtois and V. M. Bright, "Applications for surface-micromachined polysilicon thermal actuators and arrays," *Sensors and Actuators A*, vol. 58, pp. 19-25, 1997.

[167] E. S. Kolesar, S. Ko, J. T. Howard, P. B. Allen, J. M. Wilken, C. Noah, M. Ruff, and R. J. Wilks, "In-plane tip deflection and force achieved with asymmetrical polysilicon electrothermal microactuators," *Thin Solid Films*, vol. 377-378, pp. 719-726, 2000.

[168] Q. A. Huang and N. K. S. Lee, "Analytical modeling and optimization for a laterally-driven polysilicon thermal actuator," *Microsystems Technologies*, vol. 5, pp. 133-137, 1999.

[169] G. Lin, C. J. Kim, S. Konishi, and H. Fujita, "Design, fabrication and testing of a C-shape actuator," presented at Transducers' 95 - Eurosensors IX, Stockholm, Sweden, pp. 416-419, June 1995.

[170] D. Yan, A. Khajepour, and R. Mansour, "Design and modeling of MEMS bidirectional vertical thermal actuator," *Journal of Micromechanics and Microengineering*, vol. 14, pp. 841-850, 2004.

[171] C. Lott, T. McClain, J. Harb, and L. Howell, "Modelling the thermal behaviour of surface micromachined linear-displacement thermomechanical actuator," *Sensors and Actuators A*, vol. 101, pp. 239, 2002.

[172] T. Moulton and G. K. Ananthasuresh, "Micromechanical devices with embedded electro-thermal-compliant actuation," *Sensors and Actuators A*, vol. 90, pp. 38-40, 2001.

[173] S. Prasanna and S. M. Spearing, "Materials selection and design of microelectrothermal bimaterial actuators," *Journal of Microelectromechanical Systems*, vol. 16, pp. 248-259, 2007.

[174] J. K. Luo, A. J. Flewitt, S. M. Spearing, N. A. Fleck, and W. I. Milne, "Three types of planar structure microspring electro-thermal actuators with insulating beam constraints," *Journal of Micromechanics and Microengineering*, vol. 15, pp. 1527-1535, 2005.

[175] M. Ellis, G. Skidmore, A. Geisberger, K. Tsui, N. Sarkar, and J. Randall, "Microfabricated silicon mechanical connectors and micro assembly." Houston, 2002.

[176] T. Huang, E. Nilsen, M. Ellis, C. Goldsmith, K. Kim, G. Skidmore, N. Kumar, and J. Lee, "3-D selfaligned, microassembled, electrical interconnects for heterogenuos integration," presented at SPIE Photonics West, San Jose, 2003.

[177] M. Honnatti and G. Hughes, "Directed cellular manipulation using polymer microgrippers," *Zyvex application note 9720*, 2006.

[178] C. G. Keller and R. T. Howe, "Hexsil tweezers for teleoperated micro-assembly," presented at IEEE MEMS '97, Nagoya, Japan, pp. 72-77, January 1997.

[179] T. L. Sounart, T. A. Michalske, and K. R. Zavadil, "Frequency-dependent electrostatic actuation in microfluidic MEMS," *Journal of Microelectromechanical Systems*, vol. 14, pp. 125-133, 2005.

[180] D. Sameoto, T. Hubbard, and M. Kujath, "Operation of electrothermal and electrostatic MUMPs microactuators underwater," *Journal of Micromechanics and Microengineering*, vol. 14, pp. 1359-1366, 2004.

[181] Y. J. Lai, J. McDonald, M. Kujath, and T. Hubbard, "Force, deflection and power measurements of toggled microthermal actuators," *Journal of Micromechanics and Microengineering*, vol. 14, pp. 49-56, 2004.

[182] J. K. Luo, A. Flewitt, S. Spearing, N. Fleck, and W. I. Milne, "Comparision of microtweezers based on three lateral thermal actuator configurations," *Journal of Micromechanics and Microengineering*, vol. 15, pp. 1294-1302, 2005.

[183] Y. Zhu, A. Corigliano, and H. D. Espinosa, "A thermal actuator for nanoscale in situ microscopy testing: design and characterization," *Journal of Micromechanics and Microengineering*, vol. 16, pp. 242-253, 2006.

[184] L. J. Li and D. Uttamchandani, "Modified asymmetric micro-electrothermal actuator: analysis and experimentation," *Journal of Micromechanics and Microengineering*, vol. 14, pp. 1734-1741, 2004.

[185] Q. A. Huang and N. K. S. Lee, "Analysis and design of polysilicon thermal flexure actuator," *Journal of Micromechanics and Microengineering*, vol. 9, pp. 64-70, 1999.

[186] L. A. Field, D. L. Burriesci, P. R. Robrish, and R. C. Ruby, "Micromachined 1x2 optical-fiber switch," *Sensors and Actuators A*, vol. 53, pp. 311-315, 1996.

[187] N. D. Mankame and G. K. Ananthasuresh, "Comprehensive thermal characterisation of an electro-thermal-compliant microactuator," *Journal of Micromechanics and Microengineering*, vol. 11, pp. 452-462, 2001.

[188] E. Pichonat-Gallois, V. Petrini, and M. Labachelerie, "Design and fabrication of thermal actuators used for a micro-optical bench: application to a tunable Fabry-Perot filter," *Sensors and Actuators A*, vol. 114, pp. 260-266, 2004.

[189] D. Sameoto, S. H. Tsang, and M. Parameswaran, "Polymer MEMS processing for multi-user applications," *Sensors and Actuators A-Physical*, vol. 134, pp. 457-464, 2007.

[190] G. K. Lau, J. F. L. Goosen, F. van Keulen, T. C. Duc, and P. M. Sarro, "Powerful polymeric thermal microactuator with embedded silicon microstructure," *Applied Physics Letters*, vol. 90, pp. 2140103, 2007.

[191] *Microchem SU8 resist*, http://www.microchem.com/products/su_eight.htm.

[192] C. Kim, A. P. Pisano, R. Muller, and M. Lim, "Polysilicon microgripper," presented at Solid-State Sensor and Actuator Workshop, 1990. 4th Technical Digest., Hilton Head Island, SC, USA, 1990.

[193] K. E. Petersen, "Silicon as a mechanical material," *Proceedings of IEEE*, vol. 70, pp. 420-457, 1982.

[194] D.A. Koester, R. Mahadevan, B. Hardy, and K.W. Markus, , . *MUMPs™ Design Handbook Rev. 5*. 3021 Cornwallis Road, Research Triangle Park, NC 27709, 1999.

[195] B. E. Volland, K. Ivanova, T. Ivanov, Y. Sarov, E. Guliyev, A. Persaud, J. P. Zollner, S. Klett, I. Kostic, and I. W. Rangelow, "Duo-action electro thermal micro gripper," *Microelectronic Engineering*, vol. 84, pp. 1329-1332, 2007.

[196] I. Klammer, M. C. Hofmann, A. Buchenauer, W. Mokwa, and U. Schnakenberg, "Long-term stability of PDMS-based microfluidic systems used for biocatalytic reactions," *Journal of Micromechanics and Microengineering*, vol. 16, pp. 2425-2428, 2006.

[197] J. D. Gelorme, R. J. Cox, and S. Gutierrez, "Photoresist composition and printed circuit boards and packages made therewith." USA, 1989.

[198] H. Lorenz, M. Despont, N. Fahrni, N. LaBianca, P. Renaud, and P. Vettiger, "SU-8: a low-cost negative resist for MEMS," *Journal of Micromechanics and Microengineering*, vol. 7, pp. 121-124, 1997.

[199] J. M. Shaw, J. D. Gelorme, N. LaBianca, W. E. Conley, and S. J. Holmes, "Negative Photoresist for optical lithography," *IBM Journal of Research and development*, vol. 41, pp. 81-94, 1996.

[200] H. Lorenz, M. Despont, N. Fahrni, J. Brugger, P. Vettiger, and P. Renaud, "High-aspect-ratio, ultrathick, negative-tone near-UV photoresist and its applications for MEMS," *Sensors and Actuators A-Physical*, vol. 64, pp. 33-39, 1998.

[201] H. Lorenz, M. Despont, P. Vettiger, and P. Renaud, "Fabrication of photoplastic high-aspect ratio microparts and micromolds using SU-8 UV resist," *Microsystem Technologies*, vol. 4, pp. 143-146, 1998.

[202] N. Arana, D. Puente, I. Ayerdi, E. Castano, and J. Berganzo, "SU8 protective layers in liquid operating SAWs," *Sensors and Actuators B-Chemical*, vol. 118, pp. 374-379, 2006.

[203] R. J. Jackman, T. M. Floyd, R. Ghodssi, M. A. Schmidt, and K. F. Jensen, "Microfluidic systems with on-line UV detection fabricated in photodefinable epoxy," *Journal of Micromechanics and Microengineering*, vol. 11, pp. 263-269, 2001.

[204] A. Johansson, M. Calleja, P. A. Rasmussen, and A. Boisen, "SU-8 cantilever sensor system with integrated readout," *Sensors and Actuators A-Physical*, vol. 123-24, pp. 111-115, 2005.

[205] H. Ito, "Chemical Amplification resists: History and development within IBM," *IBM Journal of Research and development*, vol. 44, pp. 119-130, 2000.

[206] L. J. Guerin, "The SU8 homepage," http://www.geocities.com/guerinlj/.

[207] R. Yang and W. J. Wang, "A numerical and experimental study on gap compensation and wavelength selection in UV-lithography of ultra-high aspect ratio SU-8 microstructures," *Sensors and Actuators B-Chemical*, vol. 110, pp. 279-288, 2005.

[208] C. K. Malek and V. Saile, "Applications of LIGA technology to precision manufacturing of high-aspect-ratio micro-components and -systems: a review," *Microelectronics Journal*, vol. 35, pp. 131-143, 2004.

[209] A. Bertsch, H. Lorenz, and P. Renaud, "3D microfabrication by combining microstereolithography and thick resist UV lithography," *Sensors and Actuators A-Physical*, vol. 73, pp. 14-23, 1999.

[210] P. A. Clerc, L. Dellmann, F. Gretillat, M. A. Gretillat, P. F. Indermuhle, S. Jeanneret, P. Luginbuhl, C. Marxer, T. L. Pfeffer, G. A. Racine, S. Roth, U. Staufer, C. Stebler, P. Thiebaud, and N. F. de Rooij, "Advanced deep reactive ion etching: a versatile tool for microelectromechanical systems," *Journal of Micromechanics and Microengineering*, vol. 8, pp. 272-278, 1998.

[211] L. J. Guerin, M. Bossel, M. Demierre, S. Calmes, and P. Renaud, "Simple and low cost fabrication of embedded microchannels by using a new thick-film photoplastic," presented at Transducers 97, Chicago, IL, USA, pp. 1419-1422, June 1997.

[212] G. Genolet, J. Brugger, M. Despont, U. Drechsler, P. Vettiger, N. F. de Rooij, and D. Anselmetti, "Soft, entirely photoplastic probes for scanning force microscopy," *Review of Scientific Instruments*, vol. 70, pp. 2398-2401, 1999.

[213] T. Sikanen, "SU-8 microchips for biomolecule analysis using free zone electrophoresis," in *MICROTAS*. Tokyo, Japan, 2006, pp. 380-382, November 2006.

[214] K. B. Mogensen, J. El-Ali, A. Wolff, and J. P. Kutter, "Integration of polymer waveguides for optical detection in microfabricated chemical analysis systems," *Applied Optics*, vol. 42, pp. 4072-4079, 2003.

[215] H. Lorenz, M. Laudon, and P. Renaud, "Mechanical characterization of a new high-aspect-ratio near UV-photoresist," *Microelectronic Engineering*, vol. 42, pp. 371-374, 1998.

[216] R. Feng and R. J. Farris, "Influence of processing conditions on the thermal and mechanical properties of SU8 negative photoresist coatings," *Journal of Micromechanics and Microengineering*, vol. 13, pp. 80-88, 2003.

[217] T. Anhoj, A., M. A. Jorgensen, D. A. Zaumer, and J. hubner, "The effect of soft bake temperature on the polymerization of SU8 photoresist," *Journal of Micromechanics and Microengineering*, vol. 16, pp. 1819-1824, 2006.

[218] J. D. Williams and W. Wang, "Using megasonic development of SU-8 to yield ultra-high aspect ratio microstructures with UV lithography," *Microsystem Technologies-Micro-and Nanosystems-Information Storage and Processing Systems*, vol. 10, pp. 694-698, 2004.

[219] J. D. Williams and W. J. Wang, "Study on the postbaking process and the effects on UV lithography of high aspect ratio SU-8 microstructures," *Journal of Microlithography Microfabrication and Microsystems*, vol. 3, pp. 563-568, 2004.

[220] J. Zhang, M. B. Chan-Park, J. M. Miao, and T. T. Sun, "Reduction of diffraction effect for fabrication of very high aspect ratio microchannels in SU-8 over large area by soft cushion technology," *Microsystem Technologies-Micro-and Nanosystems-Information Storage and Processing Systems*, vol. 11, pp. 519-525, 2005.

[221] J. Zhang, M. B. Chan-Park, and S. R. Conner, "Effect of exposure dose on the replication fidelity and profile of very high aspect ratio microchannels in SU-8," *Lab on a Chip*, vol. 4, pp. 646-653, 2004.

[222] J. Zhang, K. L. Tan, G. D. Hong, L. J. Yang, and H. Q. Gong, "Polymerization optimization of SU-8 photoresist and its applications in microfluidic systems and MEMS," *Journal of Micromechanics and Microengineering*, vol. 11, pp. 20-26, 2001.

[223] R. A. Lawes, "Manufacturing tolerances for UV LIGA using SU-8 resist," *Journal of Micromechanics and Microengineering*, vol. 15, pp. 2198-2203, 2005.

[224] J. Zhang, K. L. Tan, and H. Q. Gong, "Characterization of the polymerization of SU-8 photoresist and its applications in micro-electro-mechanical systems (MEMS)," *Polymer Testing*, vol. 20, pp. 693-701, 2001.

[225] G. Liu, Y. Tian, and Y. Kan, "Fabrication of high-aspect-ratio microstructures using SU8 photoresist," *Microsystem Technologies-Micro-and Nanosystems-Information Storage and Processing Systems*, vol. 11, pp. 343-346, 2005.

[226] M. Agarwal, R. A. Gunasekaran, P. Coane, and K. Varahramyan, "Scum-free patterning of SU-8 resist for electroforming applications," *Journal of Micromechanics and Microengineering*, vol. 15, pp. 130-135, 2005.

[227] N. LaBianca and J. Delorme, ""High aspect ratio resist for thick film applications"," *in Proc. SPIE*, vol. 2438, pp. 846-852, 1995.

[228] R. Feng and R. J. Farris, "The characterization of thermal and elastic constants for an epoxy photoresist SU8 coating," *Journal of Materials Science*, vol. 37, pp. 4795-4801, 2002.

[229] Y. Zhang and S. Tadigadapa, "Thermal caharacterisation of liquids and polymer thin films using microcalorimeter," *Applied Physic letters*, vol. 86, pp. 034101, 2005.

[230] A. J. Gallant, "The simulation, fabrication and testing of a widely tunable micromachined capacitors," in *PhD Thesis*: Durham University, 2004, pp. 194.

[231] S. Jiguet, A. Bertsch, H. Hofmann, and P. Renaud, "Conductive SU8 photoresist for microfabrication," *Advanced Functional Materials*, vol. 15, pp. 1511-1516, 2005.

[232] N. Y. Zhang, J. N. Xie, M. Guers, and V. K. Varadan, "Chemical bonding of multiwalled carbon nanotubes to SU-8 via ultrasonic irradiation," *Smart Materials & Structures*, vol. 12, pp. 260-263, 2003.

[233] H. Chiamori, J. Brown, E. Adhiprakasha, E. hantsoo, J. Straalsund, N. Melosh, and B. Pruitt, "Suspension of nanoparticles in SU-8 and characterisation of nanocomposite materials," presented at ENS'05, Paris, 2005.

[234] W. Dai, K. Lian, and W. Wang, "A quantitative study on the adhesion property of cured SU-8 on various material surfaces," *Microsystems Technologies*, vol. 11, pp. 526-534, 2005.

[235] F. Ceyssens and R. Puers, "Creating multi-layered structures with freestanding parts in SU-8," *Journal of Micromechanics and Microengineering*, vol. 16, pp. S19-S23, 2006.

[236] G. M. Kim, B. Kim, M. Liebau, J. Huskens, D. N. Reinhoudt, and E. Brugger, "Surface modification with self-assembled monolayers for nanoscale replication of photoplastic MEMS," *Journal of Microelectromechanical Systems*, vol. 11, pp. 175-181, 2002.

[237] S. Mouaziz, G. Boero, R. S. Popovic, and J. Brugger, "Polymer-based cantilevers with integrated electrodes," *Journal of Microelectromechanical Systems*, vol. 15, pp. 890-895, 2006.

[238] G. Voskerician, M. S. Shive, R. S. Shawgo, H. von Recum, J. M. Anderson, M. J. Cima, and R. Langer, "Biocompatibility and biofouling of MEMS drug delivery devices," *Biomaterials*, vol. 24, pp. 1959-1967, 2003.

[239] M. Nordstrom, A. Johansson, E. S. Nogueron, B. Clausen, M. Calleja, and A. Boisen, "Investigation of the bond strength between the photo-sensitive polymer SU-8 and gold," *Microelectronic Engineering*, vol. 78-79, pp. 152-157, 2005.

[240] P. Mandlik, S. P. Lacour, J. W. Li, S. Y. Chou, and S. Wagner, "Fully elastic interconnects on nanopatterned elastomeric substrates," *IEEE Electron Device Letters*, vol. 27, pp. 650-652, 2006.

[241] S. P. Lacour, D. Chan, S. Wagner, T. Li, and Z. G. Suo, "Mechanisms of reversible stretchability of thin metal films on elastomeric substrates," *Applied Physics Letters*, vol. 88, pp. 204103, 2006.

[242] S. P. Lacour, J. Jones, S. Wagner, T. Li, and Z. G. Suo, "Stretchable interconnects for elastic electronic surfaces," *Proceedings of the IEEE*, vol. 93, pp. 1459-1467, 2005.

[243] T. Li, Z. Y. Huang, Z. Suo, S. P. Lacour, and S. Wagner, "Stretchability of thin metal films on elastomer substrates," *Applied Physics Letters*, vol. 85, pp. 3435-3437, 2004.

[244] T. Li, Z. Y. Huang, Z. C. Xi, S. P. Lacour, S. Wagner, and Z. Suo, "Delocalizing strain in a thin metal film on a polymer substrate," *Mechanics of Materials*, vol. 37, pp. 261-273, 2005.

[245] T. Li and Z. Suo, "Deformability of thin metal films on elastomer substrates," *International Journal of Solids and Structures*, vol. 43, pp. 2351-2363, 2006.

[246] T. Li and Z. Suo, "Ductility of thin metal films on polymer substrates modulated by interfacial adhesion," *International Journal of Solids and Structures*, vol. 44, pp. 1696-1705, 2007.

[247] Y. Xiang, T. Li, Z. G. Suo, and J. J. Vlassak, "High ductility of a metal film adherent on a polymer substrate," *Applied Physics Letters*, vol. 87, 161910, 2005.

[248] S. Chiu, J. Leu, and P. Ho, *Journal of Applied Physics*, vol. 76, 5136, 2000.

[249] A. Mata, A. J. Fleischman, and S. Roy, "Fabrication of multi-layer SU-8 microstructures," *Journal of Micromechanics and Microengineering*, vol. 16, pp. 276-284, 2006.

[250] I. G. Foulds and M. Parameswaran, "A planar self-sacrificial multilayer SU-8-based MEMS process utilizing a UV-blocking layer for the creation of freely moving parts," *Journal of Micromechanics and Microengineering*, vol. 16, pp. 2109-2115, 2006.

[251] A. Hartley, R. Miles, N. Dimitrakopoulos, and R. Pollard, "SU-8 beams and membranes," presented at 1st EMRS DTC Technical conference, Edinburgh, 2004.

[252] C. Chung and M. Allen, "Uncrosslinked SU-8 as a sacrificial material," *Journal of Micromechanics and Microengineering*, vol. 15, pp. N1-N5, 2005.

[253] M. Gaudet, J. C. Camart, L. Buchaillot, and S. Arscott, "Variation of absorption coefficient and determination of critical dose of SU-8 at 365 nm," *Applied Physics Letters*, vol. 88, 024107, 2006.

[254] L. Dellmann, S. Roth, C. Beuret, G. Racine, H. Lorenz, M. Despont, P. Renaud, P. Vettiger, and N. Rooij, "Fabrication of high aspect ratio elastic structures for piezoelectric motor," presented at Transducers '97, Chicago, IL, USA, pp. 641-644, 1997.

[255] E. Enikov and K. Lazarov, "Micro-mechanical switch array for meso-scale actuation," *Sensors and Actuators A*, vol. 121, pp. 282-293, 2005.

[256] N. Nguyen and T. Truong, "A fully polymeric micropump with piezoelectric actuator," *Sensors and Actuators B*, vol. 97, pp. 137-143, 2004.

[257] *Brewer Science*, http://www.brewerscience.com/?id=134.

[258] D. Sotiria, P. D, and D. Jenkins, "Comparative assessment of different sacrificial materials for releasing SU8 structures," *Review of Advanced Material Science*, vol. 10, pp. 149-155, 2005.

[259] D. Haefliger, M. Nordstrom, P. A. Rasmussen, and A. Boisen, "Dry release of all-polymer structures," *Microelectronic Engineering*, vol. 78-79, pp. 88-92, 2005.

[260] B. Bohl, R. Steger, R. Zengerle, and P. Koltay, "Multi-layer SU-8 lift-off technology for microfluidic devices," *Journal of Micromechanics and Microengineering*, vol. 15, pp. 1125-1130, 2005.

[261] G. Fedder and R. Howe, "Thermal assembly of Polysilicon Microstructures," presented at IEEE Micro mechanical Systems, Nara, Japan, pp. 63-68, 1991.

[262] C. H. Mastrangelo, "Thermal applications of microbridges," in *PhD Thesis*: Berkeley, University of California, 1991.

[263] L. Lin and M. Chiao, "Electrothermal responses of lineshape microstructures," *Sensors and Actuators A*, vol. 55, pp. 35-41, 1996.

[264] O. Sigmund, "Systematic design of micro actuators using topology optimization," *SPIE Proceedings vol. 3328*, vol. 3328, pp. 23-31, 1998.

[265] J. T. Butler, V. M. Bright, and W. D. Cowan, "Average power control and positioning of polysilicon thermal actuators," *Sensors and Actuators A*, vol. 72, pp. 88-97, 1999.

[266] E. S. Kolesar, P. B. Allen, J. T. Howard, J. M. Wilken, and N. Boysdston, "Thermally-actuated cantilever beam for achieving large in-plane mechanical deflection," *Thin Solid Films*, vol. 355-356, pp. 295-302, 1999.

[267] R. Hickey, D. Samemoto, T. Hubbard, and M. Kujath, "Time and frecuency response of two-arm micromachined thermal actuators," *Journal of Micromechanics and Microengineering*, vol. 13, pp. 40-46, 2003.

[268] L. Lin and A. P. Pisano, "Bubble forming on a micro line heater," *Micromechanical Sensors, actuators, and Systems*, vol. 32, pp. 147-163, 1991.

[269] D. Yan, A. Khajepour, and R. Mansour, "Modeling of two-hot-arm horizontal thermal actuator," *Journal of Micromechanics and Microengineering*, vol. 13, pp. 312-322, 2003.

[270] R. Hickey, M. Kujath, and T. Hubbard, "Heat transfer and optimization of two-beam microelectromechanical thermal actuators," *Journal of Vaccum ScienceTechnology A*, vol. 20, pp. 971-974, 2002.

[271] R. V. Andrews, "Solving Conductive Heat Transfer problems with Electrical-analogue Shape factors," *Chemical Engineering Prog.*, vol. 51, pp. 67-71, 1955.

[272] E. Enikov, S. Kedar, and K. Lazarov, "Analytical Model for Analysis ans Design of V-shaped Thermal Microactuators," *Journal of Microelectromechanical systems*, vol. 14, pp. 788-798, 2005.

[273] R. Cragun and L. Howell, "A constrained thermal expansion microactuator," *Micro-electro-Mechanical systems (MEMS)*, vol. ASME DSC-66, pp. 365-371, 1998.

[274] A. Jungen, M. Pfenninger, M. Tonteling, C. Stampfer, and C. Hierold, "Electrothermal effects at the microscale and their consequences on system design," *Journal of Micromechanics and Microengineering*, vol. 16, pp. 1633-1638, 2006.

[275] X.-G. Liang and Z.-Y. Guo, "The scaling effect on the thermal processes at Mini/Microscale," *Heat Transfer Engineering*, vol. 27, pp. 30-40, 2006.

[276] F. Incropera and D. DeWitt, *Fundamentals of Heat and Mass Transfer*, 4th ed. New York: Wiley, 1996.

[277] A. Artre, "Analysis of out-of-plane thermal microactuators," *Journal of Micromechanics and Microengineering*, vol. 16, pp. 205-213, 2006.

[278] A. Geisberger, N. Sarkar, M. Ellis, and G. Skidmore, "Electrothermal properties and Modeling of Polysilicon Microthermal Actuators," *Journal of Microelectromechanical systems*, vol. 12, pp. 513-523, 2003.

[279] S. Todd and H. Xie, "Steady-state 1D electrothermal modeling of an electrothermal transducer," *Journal of Micromechanics and Microengineering*, vol. 15, pp. 2264-2276, 2005.

[280] A. Jungen, "Thermography on a suspended microbridge using confocal Raman scattering," *Applied Physic Letters*, vol. 88, 191901, 2006.

[281] J. J. Lander, "Measurement of Thomson coefficients for metals at high Temperatures and of Peltier coefficients for solid-liquid interfaces of metals," *Physical Review*, vol. 74, pp. 479-488, 1948.

[282] S. Kasap, *Principles of Electrical Engineering: Materials and Devices*, 1st ed. Boston: McGraw Hill, 1997.

[283] H. H. Bruun, *Hot wire Anemometry, Principles and Signal Analysis*. New York: OUP Inc, 1995.

[284] V. Morgan, "The overall convective heat transfer from smooth circular cylinders," *Advances in Heat transfer*, vol. 11, pp. 199, 1975.

[285] H. Hatton, D. James, and H. Swire, "Combined forced and natural convection with low speed air flow over horizontal cylinders," *Journal of Fluidics Mechanics*, vol. 42, pp. 17-31, 1970.

[286] S. Churchill and H. Chu, "Correlating equations for laminar and turbulent free convection from a horizontal cylinder," *International Journal of Heat and Mass Tranfer*, vol. 18, pp. 1049, 1975.

[287] M. Schneider, "Microstrip lines for microwaves integrated circuits," *The Bell System Technical Journal*, vol. 48, pp. 1421-1444, 1969.

[288] M. Han, X. Liang, and Z. Tang, "Size effect on the heat transfer in micro gas sensor," *Sensors and Actuators A*, vol. 120, pp. 397-402, 2005.

[289] J. Xu, K. Lauger, R. Moller, K. Dransfeld, and I. Wilson, "Heat transfer between two metallic surfaces at small distances," *Journal of Applied Physics*, vol. 76, pp. 720-72169, 1994.

[290] *CoventorWare*, http://www.coventor.com.

[291] P. Beham, R. Crawford, and C. Armstrong, "Buckling instability," in *Mechanics of engineering materials*. London: Prentice hall, 1996, pp. 264-285.

[292] F. Seitz, *The Modern Theory of Solids*. New York, 1987.

[293] E. T. Enikov and K. Lazarov, "PCB-integrated metallic thermal micro-actuators," *Sensors and Actuators A-Physical*, vol. 105, pp. 76-82, 2003.

[294] C. C. Williams and H. K. Wickramasinghe, "Scanning Thermal Profiler," *Applied Physics Letters*, vol. 49, pp. 1587-1589, 1986.

[295] D. G. Cahill, K. Goodson, and A. Majumdar, "Thermometry and thermal transport in micro/nanoscale solid-state devices and structures," *Journal of Heat Transfer-Transactions of the ASME*, vol. 124, pp. 223-241, 2002.

[296] S. Grauby, B. C. Forget, S. Hole, and D. Fournier, "High resolution photothermal imaging of high frequency phenomena using a visible charge coupled device camera associated with a multichannel lock-in scheme," *Review of Scientific Instruments*, vol. 70, pp. 3603-3608, 1999.

[297] P. M. Mayer, D. Luerssen, R. J. Ram, and J. A. Hudgings, "Theoretical and experimental investigation of the thermal resolution and dynamic range of CCD-based thermoreflectance imaging," *Journal of the Optical Society of America A-Optics Image Science and Vision*, vol. 24, pp. 1156-1163, 2007.

[298] Y. S. Ju, O. W. Kading, Y. K. Leung, S. S. Wong, and K. E. Goodson, "Short-timescale thermal mapping of semiconductor devices," *IEEE Electron Device Letters*, vol. 18, pp. 169-171, 1997.

[299] S. Grauby, S. Dilhaire, S. Jorez, and W. Claeys, "Temperature variation mapping of a microelectromechanical system by thermoreflectance imaging," *IEEE Electron Device Letters*, vol. 26, pp. 78-80, 2005.

[300] S. Dilhaire, S. Grauby, and W. Claeys, "Calibration procedure for temperature measurements by thermoreflectance under high magnification conditions," *Applied Physics Letters*, vol. 84, pp. 822-824, 2004.

[301] S. P. Kearney, L. M. Phinney, and M. S. Baker, "Spatially resolved temperature mapping of electrothermal actuators by surface Raman scattering," *Journal of Microelectromechanical Systems*, vol. 15, pp. 314-321, 2006.

[302] J. R. Serrano, L. M. Phinney, and S. P. Kearney, "Micro-Raman thermometry of thermal flexure actuators," *Journal of Micromechanics and Microengineering*, vol. 16, pp. 1128-1134, 2006.

[303] H. Fettig, J. Wylde, T. Hubbard, and M. Kujath, "Simulation, dynamic testing and design of micromachined flexible joints," *Journal of Micromechanics and Microengineering*, vol. 11, pp. 209-216, 2001.

[304] S. FLIR,

[305] R. Madding, "Temperature dependence of the graybody approximation to emissivity for some common materials," *Proceedings of SPIE*, vol. 4710, pp. 37-43, 2002.

[306] R. Madding, "Emissivity measurement and temperature correction accuracy considerations," *SPIE proceedings*, vol. 3700, pp. 393-401, 1999.

[307] *The Engineering Toolbox*, http://www.engineeringtoolbox.com/.

[308] J. E. Mark, *Physical properties of Polymers Handbook*. New York: AIP Press, 1996.

[309] K. Carlson, K. N. Andersen, V. Eichhorn, D. H. Petersen, K. Molhave, I. Y. Y. Bu, K. B. K. Teo, W. I. Milne, S. Fatikow, and P. Boggild, "A carbon nanofibre scanning probe assembled using an electrothermal microgripper," *Nanotechnology*, vol. 18, 345501, 2007.

[310] J. K. Luo, A. J. He, A. J. Flewitt, D. F. Moore, S. M. Spearing, N. A. Fleck, and W. I. Milne, "Development of all metal electro-thermal actuator and its application," *Proceedings of SPIE*, vol. 5344, pp. 201-210, 2004.

[311] T. C. Duc, G. K. Lau, J. F. Creemerl, and P. M. Sarrol, "Electrothermal microgripper with large jaw displacement and integrated force sensors," presented at IEEE MEMS 2008, Tucson, AZ, USA, pp. 519-522, January 2008.

[312] J. A. Martinez, T. Liu, and R. R. Panepucci, "Micro-opto-electro-mechanical system (MOEMS) for microstructure manipulation and optical characterization," *Nanoengineering: Fabrication, Properties, Optics, and Devices IV*, vol. 6645, pp. 664525, 2007.

[313] *Newcastle Fertility Centre at Life*, http://www.nfc-life.com/staff.html.

[314] *Hunter Scientific*, http://www.hunterscientific.com/products.shtml.

[315] G. Greggains, "Preparation of mice oocyte samples." Personal communication, 2008.

PUBLICATIONS

Conference proceedings:

B. Solano and D. Wood, "Low Voltage microgripper for single cell manipulation" 3rd International Conference Smart Materials Structures Systems, Sicily, Italy, in press.

B. Solano and D. Wood, "The use of single manipulation tools in assisted reproduction technologies" Proceedings of 3rd Nanotechnology Transfer Executive Summit in Europe (NanoTransfer 2007), Paris, France, pp. 87, Dec.2007.

B. Solano and D. Wood, "Design and testing of a polymeric microgripper for cell manipulation" Proceedings of Micro and Nano engineering (MNE 2006), Barcelona, Spain, pp. 361-362, Sep. 2006.

B. Solano and D. Wood., "Electro-thermal analytical modelling and virtual prototyping of a polymeric microgripper" Proceedings of Micromechanics Europe (MME '05), Gothenburg, Sweden, pp.136, Sep. 2005.

B. Solano, S. Rolt, D. Wood and P.G. Maropoulos, "CAD framework for the development of a thermally actuated microgripper" Proceedings of Computer Aided Design & Engineering (ECAD/ECAE 2004), Durham, UK, pp.59, Nov. 2004.

Journal papers:

B. Solano and D. Wood, "Design and testing of a polymeric microgripper for cell manipulation" Journal of Microelectronic Engineering, vol. 84 (5-8), 1219-1222, 2007

B. Solano, S. Rolt and D. Wood, "Thermal and mechanical analysis of a SU8 polymeric actuator using IR thermography", Proceedings of the IMechE Part C-Journal of Mechanical Engineering Science, vol. 222, 73-86, 2008

Patent applications:

B. Solano and D. Wood, "Electro-mechanical actuator device and apparatus incorporating such device" Patent application WO 2007/138266 A1

NOMENCLATURE

A	cross-sectional area of the microbeam [m^2]
Bi	Biot number
c_p	constant pressure specific heat of the fluid [J kg K]
C	heat transfer coefficients per unit length [W m^{-1} K^{-1}]
C_1	Planck's first constant [W m^2]
C_2	Planck's second constant [m K]
CTE	coefficient of thermal expansion
d	spatial resolution
dx	differential element of the microbeam [m]
D	equivalent diameter of the microbeam [m]
E	Young's modulus [MPa]
F	conduction shape factor to the substrate
F_{hc}	radiation shape factor
f	conduction shape factor into the ambient from individual beams
f_{ex}	conduction shape factor characterising the intra device heat exchange
g	gravitational acceleration [m s^{-2}]
gap	size of the separation between the hot and cold/flexure arms
GAP	separation between the actuators in the microgripper [m]
Gr	Grashof number
h	convection heat transfer coefficient [W m^{-2} K^{-1}]
I	intensity of the electrical current [A]
J	current density [A m^{-2}]
L	length of the microbeam [m]
L_c	characteristic dimension of the microbeam [m]
NA	numerical aperture
Nu	Nusselt number
p	perimeter length of the microbeam [m]
P	electrical power [W]
q_{COND}	conductive heat rate through the differential element dx of the microbeam [W]
q_{cond}	conductive heat rate into the ambient from the differential element [W]

q_{conv} convective heat rate into the ambient from the differential element [W]

q_{ex} conductive heat exchange between closely spaced bodies [W]

q_{gen} heat generated by Joule heating within the differential element [W]

q_{rad} radiative heat rate into the ambient from the differential element [W]

q_{th} heat generated by Thomson effect within the differential element [W]

Q volumetric heat generation [W m^{-3}]

s separation between the actuator and the underneath substrate [m]

r equivalent radius of the microbeam [m]

R radius of the air cylinder from which convection takes place [m]

R electrical resistance [Ω]

Ra Rayleigh number

Rh relative humidity

t thickness of the microbeam and differential element dx [m]

t' effective thickness of the microbeam [m]

T relative temperature to the ambient [K]

T_{abs} absolute temperature [K]

T_g glass transition temperature [°C]

T_s temperature of the substrate [K]

TCR temperature coefficient of resistance [K^{-1}]

ΔT temperature increase in the differential element dx [K]

u velocity component in the x-direction [m s^{-1}]

U voltage signal [V]

V voltage [V]

w thickness of the microbeam and the differential element dx [m]

W emitted thermal radiation

x,y,z cartesian coordinates [m]

Greek letters

α coefficient of thermal expansion [ppm K^{-1}]

β Thomson coefficient [μV K^{-1}]

δ deflection [m]

δ_T thickness of the thermal boundary layer [m]

ε emissivity

κ thermal conductivity [W m^{-1} K^{-1}]

λ	wavelength [m]
σ	Stefan-Boltzmann constant [W m^{-2} K^{-4}]
τ	transmittance
ν	kinematic viscosity [m^2 s^{-1}]
ρ	electrical resistivity [Ω m]

Subscripts

a	anchor
A	anchor
Au	gold metallization
c, cold	cold arm
eff	effective
f	flexure
FEA	relative to a finite element analysis
h, hot	hot arm
i	integer
j	integer
l	length
M	microgripper
max	maximum
P	parasitic
s	substrate
T	total
th	thermal
SU8	SU8 polymer
∞	ambient

Superscripts

‘	heat per unit length [W m^{-1}]
“	heat per unit area [W m^{-2}]
·	heat per unit volume [W m^{-3}]

(this page has been left intentionally blank)